NATIONAL TECHNICAL UNIVERSITY OF ATHENS

School of Civil Engineering

Department of Water Resources and Environment

Laboratory of Hydrology and Water Resources Management

Development and Implementation of a Methodological Framework for Early Warning of Intense Floods using Innovative Technologies

Apollon D. Bournas

Ph.D. Thesis

Athens, September 2023

NATIONAL TECHNICAL UNIVERSITY OF ATHENS

School of Civil Engineering

Department of Water Resources and Environment

Laboratory of Hydrology and Water Resources Management

Development And Implementation of a Methodological Framework for Early Warning of Intense Floods using Innovative Technologies

Apollon D. Bournas

Ph.D. Thesis

Athens, September 2023

Title: Development and Implementation of a Methodological Framework for Early Warning of Intense Floods using Innovative Technologies
Author: Apollon D. Bournas

This dissertation has been approved by the advisory committee:

Prof. E. Baltas, NTUA, Greece, Supervisor

Prof. A. Stamou NTUA, Greece, Member of the Advisory Committee

Prof. V. Tsihrintzis   NTUA, Greece, Member of the Advisory Committee

Member of the Advisory Committee Members of the Ph.D. Examination Committee:

Prof. E. Baltas

National Technical University of Athens (NTUA), Greece

Prof. A. Stamou

National Technical University of Athens (NTUA), Greece

Prof. V. Tsihrintzis

National Technical University of Athens (NTUA), Greece

Prof. N. Mamassis

National Technical University of Athens (NTUA), Greece

Prof. F. Maris

Democritus University of Thrace (DUTH), Greece

Prof. A. Langousis

University of Patras, Greece

Dr. K. Lagouvardos

National Observatory of Athens (NOA), Greece

Acknowledgments

With the completion of this Ph.D. dissertation, the long cycle of education and continuous learning seems to come to a halt for a minute. Completing this dissertation makes me feel more complete and think that a new exciting journey is yet to begin. This effort would neither have started or finished without the contribution of the following people:

First and foremost, I would like to express my appreciation and special gratitude to my supervisor Prof. Evangelos Baltas for trusting me with completing this dissertation. His continuous support, guidance, and encouragement throughout this research were invaluable. I feel fortunate by our collaboration and his understanding of me as a person. I constantly felt his faith in me during our meetings, even at times when I would derail from our planning due to intense workload.

Secondly, I would like to thank the two members of the advisory committee, A. Stamou, Professor NTUA, and V. Tsihrintzis, Professor NTUA, for their valuable comments, collaboration, and trust in me to complete this dissertation. It would not have been as complete if it was not for them.

I would also like to thank the seven-member examination committee for their positive and valuable comments regarding the content and execution of this dissertation.

Special thanks go to Dr. Konstantinos Lagouvardos, director of the Institute of Environmental Research and Sustainable Development of the National Observatory of Athens (NOA), who provided me with three years of rainfall time series from the NOA rain gauge network; these data were extremely useful for this dissertation.

This research was carried out with the financial support provided by the State Scholarship Foundation (IKY) under an operational program co-financed by Greece and the European Union (European Social Fund-ESF). I hope that the outcome of this research lives up to their expectations. Moreover, I would like to thank the National University of Athens, in general, for providing me with the necessary access and licensing to the software used in this dissertation, such as ArcGIS and MATLAB.

I wish to thank my Ph.D. "family," starting with Dr. Elissavet Feloni, not only for consulting me in my early stages and for our continuous and valuable knowledge-gap-filling conversations but also as a person, for giving me the courage to complete this work. In the same length, special thanks go to the other Ph.D. candidates that I shared my office with, Aimilia-Panagiota Theochary, Maria-Margarita Bertsiou, and Sofia Skroufouta, which made our work space an enjoyable and knowledge-sharing place. Special thanks go also to Nick Dervos who introduced me the NTUA weather radar system, and helped with its installation. I want to also thank Mrs. Panagiota Skarlou from the office institution

Apollon D. Bournas
Athens, September 2023

Abstract

The main scope of this Ph.D. dissertation is the development and implementation of a methodological framework for early warning of intense floods using innovative technologies. The key feature of this research is the collection, analysis, and use of datasets obtained by a newly installed weather radar, the Rainscanner system, located in Athens, Greece. The Rainscanner system is an X-Band weather radar that can obtain reflectivity fields of fine temporal and spatial scales of up to two minutes and 100 m x 100 m, respectively. These high-resolution datasets are essential for understanding the spatial and temporal characteristics of a storm's rainfall fields and are suited for local-based applications, such as small-basin rainfall-runoff modeling and nowcasting. However, weather radar datasets are yet to be widely accepted and used, mainly because of the uncertainty governed by the datasets due to various sources of errors and the scarcity of such data. A weather radar is not a typical/commercial device, and proper handling of the generated raw datasets is required. Considering the above, this dissertation aims to provide a holistic approach to properly managing and using weather radar data for hydrological applications. This approach is divided into two main sections.

The first section includes a review of the weather radar types, formulation, sources of errors, and quality control. To that end, a framework is devised where the raw weather radar datasets are quality-corrected in two phases: a) through the application of clutter-filters derived in a pre-process, such as ground-clutter filtering, gap-filling algorithms and reflectivity thresholds and b) through the cross-correlation with ground rain gauges. Apart from the ground-clutter filtering process, the most critical source of uncertainty is deriving the reflectivity (Z) to rainfall rate (R) transformation equation, the Z-R relationship. It is acknowledged that the Z-R relationship varies in time and space. Therefore, in this thesis, multiple Z-R relationships are derived in varying locations to assess this issue. Fifty-three stations and thirty-eight events in the region of Attica were used for this process, which led to the extraction of interesting findings concerning the Z-R parameter values to the proximity of a location to specific geographical locations and the storm's classification.

The second section of this thesis focused on developing a framework for real-time flood risk assessment as part of a Flood Early Warning System (FEWS). This system is designed to focus on flash flood events characterized by their small duration and intensive rainfall rates. To that end, a gridded rainfall-based FEWS is devised based on the Flash Flood Guidance (FFG) system. In such a concept, all calculations are performed at the grid level, making the system easier to understand, calibrate, operate, and adjust based on the user's needs and available data. The system compares forecasted rainfall with threshold rainfall fields

derived from inverse rainfall-runoff models. For this comparison, a rainfall-runoff model is devised using the time-area diagram theory through Geographical Information Systems (GIS) and the MATLAB programming language. The devised rainfall-runoff model is a gridded hydrological model suitable for small ungauged basins, such as those found in the Attica region. Using this model, one can derive rainfall threshold maps for the entire Attica Region and a peri-urban basin, the Sarantapotamos basin, and perform a sensitivity-based approach to extract the effects of system parameters on the results. The GFFG system is formulated and simulated based on historical events obtained by the weather radar. The effects of system parameters (such as soil moisture conditions before the rainfall event and thresholds derived for flooding) are examined through sensitivity-based simulations. In the final stage, a storm-tracking algorithm uses multiple reflectivity thresholds to provide cell identification and tracking procedures to identify the storm's cell movement in consecutive images. This application uses image analysis and processing, highlighting the usability of weather radars in such applications.

This thesis establishes a comprehensive framework for leveraging weather radar datasets within a Flood Early Warning System. It highlights the significance of meticulous quality control processes and introduces easily configurable operational methodologies to harness the potential of weather radar data effectively.

Keywords: Weather radar; X-Band; Reflectivity; Z-R relationship; Flash flood; Flood Early Warning System; FFG; gridded; rainfall-runoff; storm tracking; Athens; Floods; Rainfall Rate; Sarantapotamos

Development and implementation of a methodological framework for early warning of intense floods using innovative technologies

Table of Contents

Selected Publications

Bournas A, Baltas E (2023) Analysis of Weather Radar Datasets through the Implementation of a Gridded Rainfall-Runoff Model. Enviromental Process 10:7. https://doi.org/10.1007/s40710-023-00621-2

Bournas A, Baltas E (2022) Investigation of the gridded flash flood Guidance in a Peri-Urban basin in greater Athens area, Greece. Journal of Hydrology 610:127820. https://doi.org/10.1016/j.jhydrol.2022.127820

Bournas A, Baltas E (2022) Determination of the Z-R Relationship through Spatial Analysis of X-Band Weather Radar and Rain Gauge Data. Hydrology 9:137. https://doi.org/10.3390/hydrology9080137

Bournas A, Baltas E (2021) Comparative Analysis of Rain Gauge and Radar Precipitation Estimates towards Rainfall-Runoff Modelling in a Peri-Urban Basin in Attica, Greece. Hydrology 8, 29., https://doi.org/10.3390/hydrology8010029

Pappa A, Bournas A, Lagouvardos K, Baltas E (2021) Analysis of the Z-R relationship using X-Band weather radar measurements in the area of Athens. Acta Geophysica, https://doi.org/10.1007/s11600-021-00622-5

Abbreviations

AMC	Antecedent Soil Moisture
ANN	Artificial Neural Network
API	Antecedent Precipitation Index
ARC	Antecedent Runoff Conditions
ARI	Average Recurrence Interval
CN	Curve Number
DEM	Digital Elevation Model
DSD	Drop Size Distribution
EWS	Early Warning System
FEWS	Flood Early Warning System
FFPI	Flash Potential Index
FFG	Flash Flood Guidance
FHRM	Flood Hazard and Risk Maps
FRMP	Flood Risk Management Plan
GFFG	Gridded Flash Flood Guidance
GIS	Geographical Information Systems
IDW	Inverse Distance Weighting
MAP	Mean Areal Precipitation
MBE	Mean Bias Error
NMAE	Normalized Mean Absolute Error
NMB	Normalized Mean Bias
NTUA	National Technical University of Athens
PFRA	Preliminary Flood Risk Assessment
PPI	Plan Point Indicator
QPE	Quantitative Precipitation Estimates
RMSE	Root Mean Square Error
RR	Rainfall-Runoff
SAC-SMA	Sacramento Soil Moisture Accounting Model
TC	Total Cost
UH	Unit Hydrograph

Development and implementation of a methodological framework for early warning of intense floods using innovative technologies

x

Extended Abstract

Introduction

Flash Floods are presently among the most lethal weather-related hazards on a global scale. Their origin diverges from conventional river-driven floods, primarily from abrupt and intense precipitation over a brief duration. Usually confined to local settings, they associate closely with convective storms, limiting their spatial impact (Houze Jr. et al., 2015). Factors influencing flash floods include basin geomorphology, size, slope, soil water retention, and initial moisture conditions events (Merz and Blöschl 2003; Houze Jr. et al. 2015; Velásquez et al. 2020). Sediment loads and altered river cross-sections due to high rainfall, especially in post-fire or developmental areas, can reroute rivers and induce flooding beyond riverbeds. Urbanization, deforestation, and intensified storm events due to climate change drive local-scale flash flooding, reshaping vulnerability events (Alfieri et al. 2012; Gaur and Simonovic 2015; Rogger et al. 2017; Caloiero et al. 2017). This evolving threat transforms previously unaffected regions into flood-prone zones (Bournas and Baltas 2021a). Notably, the Mediterranean region has witnessed substantial economic losses and loss of life from recent flash floods (Diakakis et al. 2012, 2019; Pereira et al. 2017; Feloni 2019; Varlas et al. 2019; Spyrou et al. 2020).

Most research on flood management is focused on understanding the hydrometeorological processes that influence the extreme weather conditions leading to flood events. To that end, one of the main non-structural methods for mitigating flood and flash flood problems is the development and use of a Flood Early Warning System (FEWS). An integrated FEWS consists of various technical and non-technical subsystems concerning a) disaster risk knowledge, b) detection and monitoring analysis, c) forecasting and thresholds of hazards and non-technical components, d) warning dissemination and communication, e) preparedness to respond, and f) response capabilities (Perera et al. 2019). Although the methods used to simulate the hydrometeorological processes are critical, the main uncertainty lies in the chaotic nature of the atmosphere and the lack of sufficient resolution and quality of data (Marchi et al. 2010). Moreover, even in cases with a good level of data, there may be high uncertainty in the modeling of a watershed system, which could lead to incorrectly estimated discharges compared to observed values (Di Baldassarre and Montanari 2009).

The desired spatial and temporal scale to monitor rainfall events that lead to flash floods is higher than the resolution offered by traditional rain gauge networks (Anagnostou et al. 2017). When sufficient data are not obtained, the ability to provide timely warnings is

reduced (Mimikou and Baltas 1996), while in cases where measurements are nearly absent, unreliable, or spatially insufficient, such as in Greece, the problem is exacerbated.

By further deepening the development and organization of FEWS against flood risk, we can expect benefits such as a) improved prediction accuracy, b) quicker response times, and c) better knowledge of potentially flooded areas to strategically plan and execute flood protection measures. Today, the main areas where a FEWS can advance in Greece are a) new technologies concerning data collection and mining and b) more precise and effortless methods that lead to more and higher-quality information for decision-making. Developing an FEWS based on weather radar datasets can lead to significant reductions in the mortality rate and the economic impact of the flood-affected areas. European-wide FEWS, such as the EFAS and ERIC, have limited usage in Greece, mainly because of unavailable datasets and mis-calibrated models required for such systems. Greece is disconnected from Central Europe, where monitoring systems like the OPERA radar composite are in place, while typical river monitoring systems are not as applicable to Greece's small-scale basins.

Greece's diverse geography, extensive coastline, and small basins prone to flash floods face growing threats. Recent events have highlighted this vulnerability (Feloni et al., 2020; Varlas et al., 2021). While forecasting attempts exist (Spyrou et al., 2020; Varlas et al., 2021, 2019), a comprehensive FEWS is absent due to research-operation challenges (Georgakakos et al., 2022, 2021). Instead, the National Hellenic Meteorological Service (NMMS) issues daily forecasts lacking flash flood specifics.

The main goal of this Ph.D. dissertation is the development of a suitable methodology for processing weather radar datasets of high spatial and temporal resolutions. The research questions this dissertation aims to answer are divided into two sections. The first concerns the use of weather datasets: *What are the major factors to consider when utilizing weather radar datasets? Do weather radar datasets provide any benefit compared to rain gauge networks, or are they governed by uncertainty?".* The second question concerns the implementation of a FEWS: *What are the necessary components of an integrated flood early warning system (FEWS) based on weather radar datasets? Can such a system be efficient at an operational level, and how can it be implemented?* To answer these questions, datasets of a newly installed weather radar system, the NTUA X-Band Rainscanner system, were obtained, calibrated, and evaluated against datasets provided by ground-based measurements from meteorological stations.

This dissertation is divided into two main sections. The first section includes a review of the weather radar types, formulation, sources of errors, and quality control. The second section of this thesis deals with developing a framework for an easy-to-use and applied Flood Early Warning System (FEWS). This application is designed to focus on flash flood events characterized by low-duration intensive rainfall.

Overall, this dissertation is structured in five chapters. The first chapter provides an Introduction that situates the thesis context and reviews the characteristics of FEWS and the use of weather radars. The second chapter consists of an analysis of the study area and the data used for this research. The third chapter includes the methodological framework applied. In the fourth chapter, the results for the study area are presented for a series of events between 2018 and 2023. Finally, the fifth chapter provides the conclusions drawn from this research and recommendations for future work.

Study Area and Data Used

The study area is the Attica region, specifically the area defined by the coverage of the Rainscanner system, as shown in Figure 1. The Rainscanner is located in Athens, Greece, within the National Technical University of Athens (NTUA) Zographou campus, featuring an installation elevation of 200 m, overseeing mainly the east side of Athens up to a 50 km distance. The extent of the Rainscanner, as seen in Figure 1, includes the majority of the Attica Prefecture, apart from a small area on the west, beyond Mount Gerania, as well as a small section of the Central Greece prefecture north of Mount Parthitha, a part of the Asopos river basin.
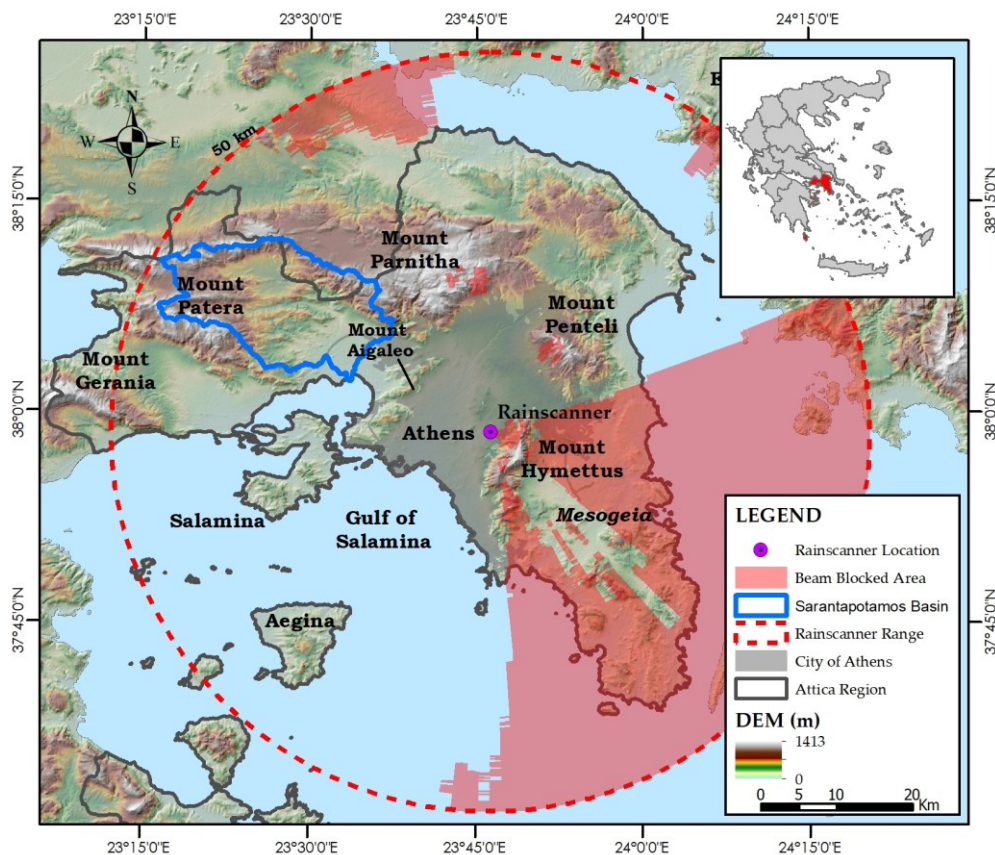
Figure 1: The Study area.

Due to the presence of Hymettus Mountain, the entire southwest area is obstructed and, therefore, cannot be measured by this Rainscanner system. Similarly, the entire "Mesogeia" region, including the Athens "Eleftherios Venizelos" airport, is out of reach. However, the Rainscanner location favors observing precipitation systems with a west-to-east and north-to-southwest direction, which are the majority of systems in the area, making it a viable option for observing and providing nowcasts and forecasts for the city of Athens and its vicinity.

Land use in the Attica region is characterized by a high urban fabric, where 27% of the region is of artificial type, while the rest (73%) is agricultural and forest type. In west Attica lies the largest peri-urban basin, the Sarantapotamos River basin. This basin has a total area of 341 km², of which 231 km² features rural characteristics. A key characteristic of the subbasins formed in the Attica region is a large number of highly urbanized small basins vulnerable to flash flood events due to the lengthy coastline.

The primary datasets used in this research are summarized below:

- Rainscanner Datasets. The X-Band weather radar datasets are generated by the Rainscanner system, featuring a 100 m x 100m spatial accuracy and a 2-minute temporal resolution. The technical specifications of the system are shown in Table 1. The files are provided in georeferenced ASCII text files.

- RainGauge datasets: The National Observatory of Athens Automatic Network (NOAAN) is used (Lagouvardos et al. 2017). Specifically, data from 53 stations in the Attica region are used, as shown in Figure 2, with their respective NOAAN IDs. The datasets consist of 10-minute precipitation measurements that have been quality-controlled concerning spatial and temporal inconsistencies against neighboring stations.

- A Digital Elevation Model (DEM) with a 5m x 5m resolution, provided by the National Cadastre & Mapping Agency S.A. (Copyright © 2012, National Cadastre & Mapping Agency S.A.).

- The CORINE Land Cover (CLC, 2018) and the dataset URBAN Atlas 2018 feature an inventory of land cover—the former for Europe and the latter for the selected urban areas.

- GIS-based datasets were acquired from open-access sources. Boundaries of the administrative regions were provided by geodata.gov.gr, while datasets, e.g., road network, were provided by the OpenStreetMap initiative.

- A list of the rain gauge stations with known Intensity-Duration-Frequency curves (IDF) is used, shown in Figure 2. The IDF curve parameters were derived from the

Flood Risk Management Plans for Greece by the Ministry of Environment, Energy, and Climate Change (SSW-MEECC 2017).

Table 1: Technical Specifications of the NTUA Rainscanner weather radar system

Parameter	Value
Peak Power	25 kW
Wave Length	X- Band 3.2 cm
Frequency	9410 (± 30 MHz)
PRF	833 – 1500 Hz
Pulse Duration	1200 – 500 ns
Rotation Rate	12 rpm
Azimuth & Elevation Beamwidth	2.5o
Azimuth Accuracy	± 0.5°
Scanning Range	50 km
Maximum Spatial Resolution	100 m x 100 m

Figure 2: The Study area, rain gauge network, and the location of the IDF station

Methodological Framework

The methodological framework considered for this research is shown in Figure 3. It consists of five main components: 1) the File Management and Data correction, 2) the Z-R calibration, 3) the Rainfall-Runoff model, 4) the Gridded FFG system, and 5) the Storm tracking algorithm.
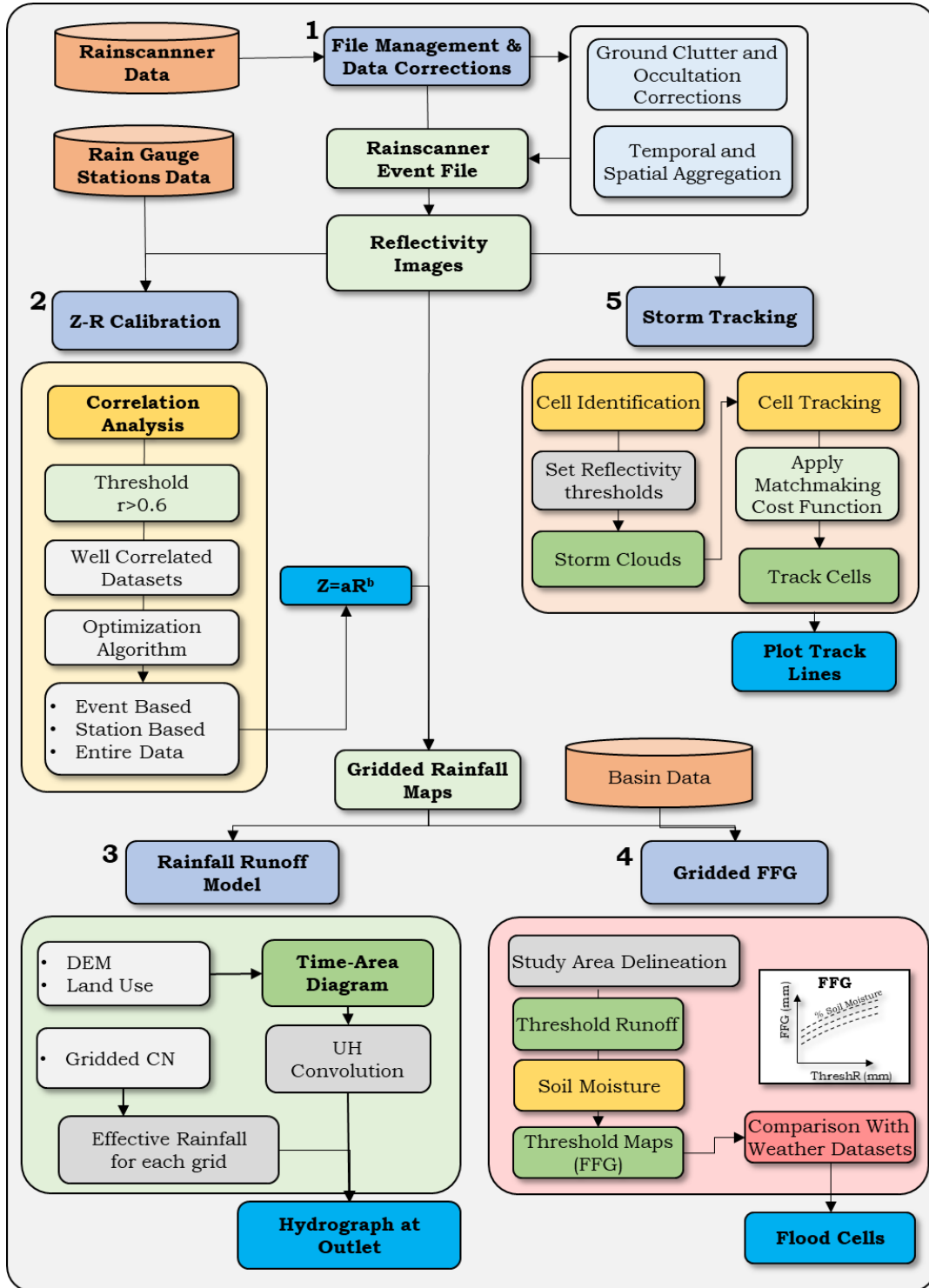
Figure 3: The Methodological Framework

Each component is crucial for the functionality of the entire FEWS. The components belong to two different categories. One category deals with the Rainscanner data quality control and transformation into rainfall, while the other utilizes rainfall maps to produce FEWS products.

1.   The File management and data correction component deals with the pre-processing quality control, where corrections are applied to radar data to address ground clutter and occultation issues. Ground clutter refers to undesired signals from non-rain objects. The ground clutter correction identifies cluttered areas through a clear sky map and employs methods like clutter subtraction or flagging with interpolation. Occultation results from radar signal obstruction. Occultation correction deals with areas where radar signals are blocked, utilizing neighboring data for gap-filling. Spatial and temporal aggregations ensure that the desired resolutions are achieved. The processed data are spatially projected, stored in specific file formats, and named based on timestamp and product type. During post-processing, further quality control checks are performed to address (if any) extreme values and/or temporal inconsistencies.

2.   The Z-R calibration deals with the derivation of the Z-R relationship, which is crucial for converting radar reflectivity (Z) to rainfall intensity (R). A correlation framework is established using rain gauge-Rainscanner data. The conversion aligns spatial and temporal resolutions, with rain gauges serving as "true rainfall." The correlation analysis used the Pearson correlation coefficient to determine the well-correlated datasets used in the optimization. The optimization targets the Z-R parameter values by minimizing the RMSE. Three optimization groups focus on deriving station-based, event-based, and entire dataset relationships. The results are compared with established Z-R equations to reveal spatial-temporal variability and enhance understanding of rainfall characteristics.

3.   The rainfall-runoff model components concern a gridded model. The model is based on the time-area diagram technique, building on the Clarks unit hydrograph model. The model parameters are calculated using GIS tools through a DEM. Excess rainfall is calculated using the NRCS-CN method, with runoff routed through a linear reservoir. A linear relationship is applied to adjust the CN values based on soil moisture conditions. The model is designed for flash flood prediction in small to medium-sized basins and employs the Rainscanner-generated rainfall maps to produce the flow hydrograph for a given position. A series of Z-R relationships are used to determine the impact of the generated runoff characteristics in various rainfall events.

4.   The Gridded Flash Flood Guidance (GFFG) is an FEWS based on rainfall thresholds and the FFG value, defined as the accumulated rainfall over a predetermined duration that will cause minor flooding. The system incorporates hydrological and meteorological conditions to determine areas under risk of flooding for lead times up to 6 hours. The system uses three

parameters: threshold runoff, soil moisture conditions, and forecasted accumulated rainfall over predetermined durations. The first is a static characteristic of a given grid, which is calculated using the five-year rainfall Average Recurrence Interval (ARI). The second is a dynamic variable affecting rainfall losses. The third, the FFG value, is calculated through inverted rainfall-runoff modeling for a given threshold runoff and soil moisture conditions. In this application, the GFFG is applied on a 500m x 500m grid scale, deriving threshold maps for three soil moisture conditions and accumulation periods. The system is applied in flood events using the Rainscanner datasets, marking flood-prone areas.

5. The Storm tracking algorithm involves two processes: cell identification and cell tracking. In cell identification, reflectivity thresholds determine the cell's core boundaries and centroids. Multiple thresholds are used to identify coverage and core cells, with a 25 dBZ appropriate for coverage and a 35 dBZ for the cell cores. A minimum area of 4 km^2 is set to define a cloud cell in either case. The Cell tracking process utilizes motion vectors and cross-correlation between consecutive images. An optimization process matches the cells based on characteristics such as area and fitting ellipse properties. A cost function is utilized to solve the linear assignment problem and to match the past and current cell storms by minimizing total cost. The cost function uses the Euclidean distance between each cell and other cell characteristics. Finally, the Merging and splitting of cells are considered. The algorithm is applied in a series of events to determine its ability to identify and track cells. Different temporal scales are used, such as the tracking of 10-min reflectivity fields between more extended periods. Eventually, areas with high reflectivity, i.e., above 35 dBZ, are identified in multiple events to highlight areas subject to intense rainfall.

Results and Discussion

Z-R Calibration

In this section, a comprehensive Z-R analysis and an optimization process are conducted to enhance the accuracy of the radar-based rainfall estimation. The procedure involves two primary components: a correlation analysis and an optimization process. The aim here is to establish station-based and event-based Z-R relationships, highlighting the variability of the Z-R relationship in time and space.

The correlation analysis is based on Pearson's r correlation coefficient index, which shows whether the same rainfall volume is measured in each timestep by the Rainscanner and the rain gauges. The calculations are performed at the Station level, i.e., the correlation index is calculated between the station's rain gauge timeseries and the designated Rainscanner cell for that station per event. Then, two correlation thresholds, 0.6 or 0.7, are used to distinguish between the well- and poor-correlated stations for 13 events. In Figure 4, the number of events a station exhibits a correlation over 0.6 or 0.7 is shown, which reveals the reliability

of the Rainscanner datasets to the location of each station. Notably, coastal stations and stations within a 10km range from the Rainscanner location present a more often good correlation, whereas stations on high elevation do not. Figure 5 demonstrates the mean correlation coefficients for all events and well-correlated events (r > 0.6). Higher correlation thresholds lead to fewer well-correlated events due to the stringent criteria. The choice of threshold is thus essential, as it must ensure data quality while retaining a substantial dataset for optimization.
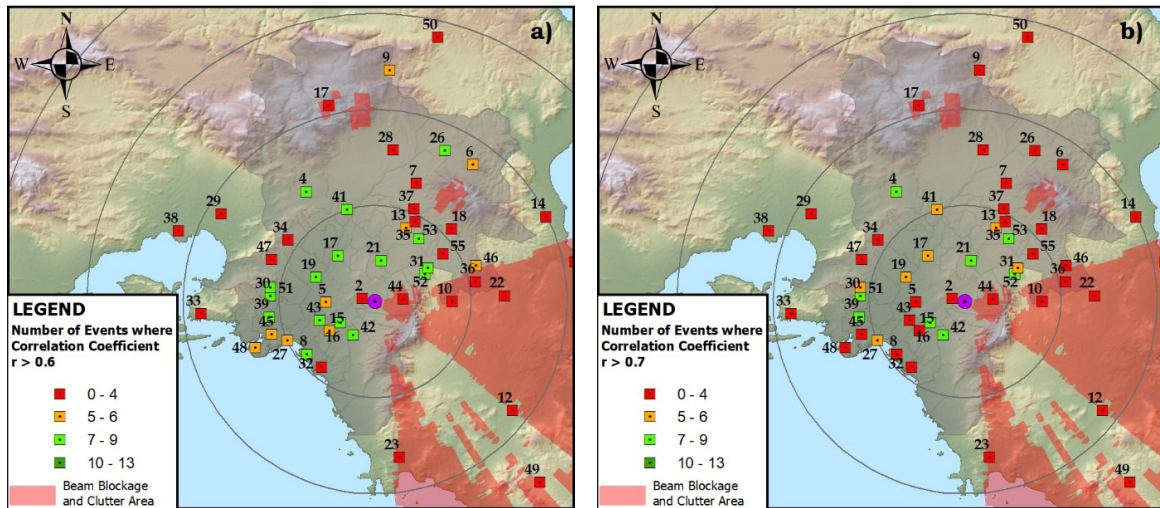
Figure 4. Number of events with a correlation coefficient between Rainscanner and rain gauge datasets: a) higher than 0.6 and b) higher than 0.7. Source: (Bournas and Baltas 2022a)
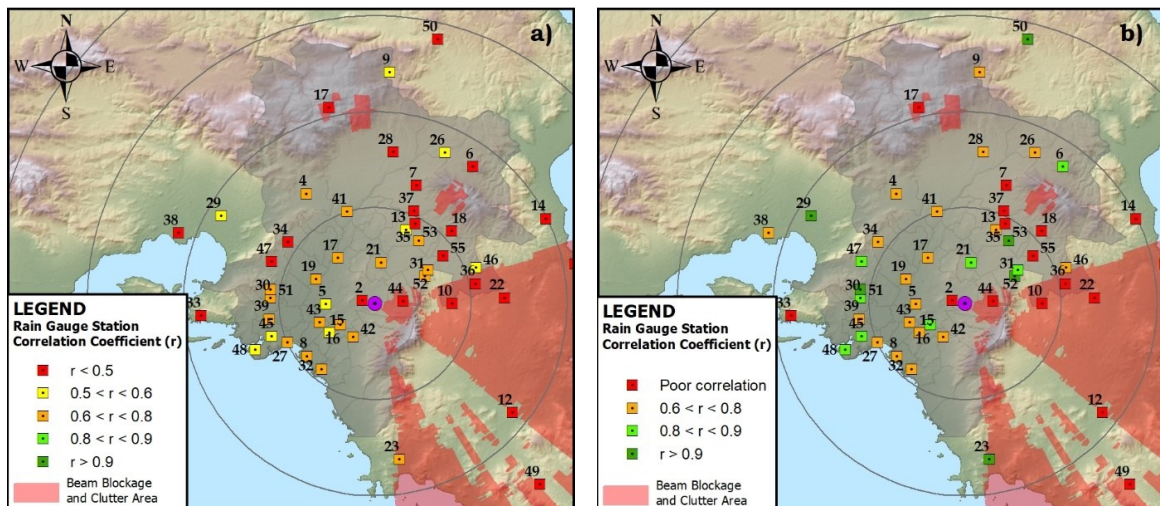
Figure 5. The mean correlation coefficient between the Rainscanner and rain gauge stations for a) all available events and b) utilizing events with an r > 0.6 correlation at each station.
Source: (Bournas and Baltas 2022a)

The assessment of the poorly-correlated station's location within the study area reveals several patterns. Stations near or within cluttered areas, particularly northeast of the

Rainscanner, exhibit consistently low correlations, typically below 0.6, due to the limited number of well-correlated events. Stations within a 10 km radius of the Rainscanner generally have more well-correlated events, except for Ampelokipoi station (ID 2), which is an exception. Coastal front stations also experience a reduction in well-correlated events with higher correlation thresholds. For instance, the Faliro station (ID 8) goes from seven well-correlated events at a 0.6 threshold to just four at a 0.7 threshold. This trend is not found only in coastal areas, as Dionysos station (ID 6) exhibits a similar pattern in the northeast. After testing various thresholds, the 0.6 threshold was considered optimal since it filters out poor correlations while retaining sufficient data for optimization.

Notably, some stations have high correlations in only a limited number of events. This behavior is influenced by storm-based characteristics such as rainfall amount, wind intensity, and possible bright band effects. Such dynamics contribute to correlations and can lead to systematic errors. While this study did not extensively investigate these aspects, it acknowledges their significance. Low correlations are not solely attributed to Rainscanner errors but can indicate systematic errors in certain rain gauge stations.

As previously described, the Z-R optimization process follows the correlation analysis. Three optimization groups define station-based, event-based, and entire dataset Z-R relationships. The findings are discussed based on the values of parameters *a* and *b*, which are derived in each case. In the established Z-R relationships, parameter *a* values ranging from 50 to 250 are suited for stratiform events, while values from 250 to 500 are better suited for convective events. Finally, values over 1000 are derived for snowfall events. The results from each optimization group are described below:

Event-Based Z-R Calibration:

The event-based optimization highlights the variability of the Z-R relationship between events. Furthermore, the derived parameters are used to assess the classification of each storm. Two optimizations are performed, one where both parameters are optimized, and one where parameter *b* is set to 1.60 and parameter *a* is optimized. Both optimizations resulted in high variability of the parameter values in both cases. The most intriguing result was the parameters value of three events when parameter *a* was over 1000. Such values indicate snowfall events, which was the case as revealed by cross-checking with historical information. Therefore, the value of event-based calibration lies in classifying events and removing inappropriate datasets for further processing. Specifically, snowfall events feature different radar parameters and, therefore, are inconsistent with convective or stratiform-based events.

Station-Based Z-R Calibration:

In this approach, the Z-R relationships are calibrated for each rain gauge station, using multiple events after excluding the snowfall events. The results are shown in Figure 6. Each subfigure exhibits the spatial variability of values for parameters *a* and *b*. Furthermore, in Figure 7, the spatial variability of parameter *a* is shown when parameter *b* is set to a constant value.
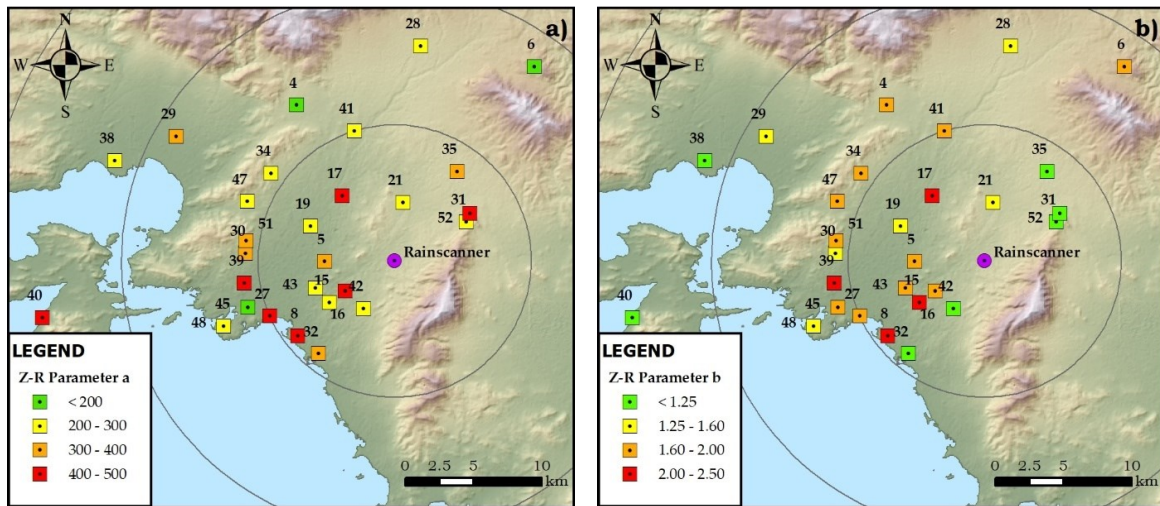
Figure 6: Spatial variability of Z-R parameter, a) for parameter a, b) for parameter b, Source: (Bournas and Baltas 2022a)
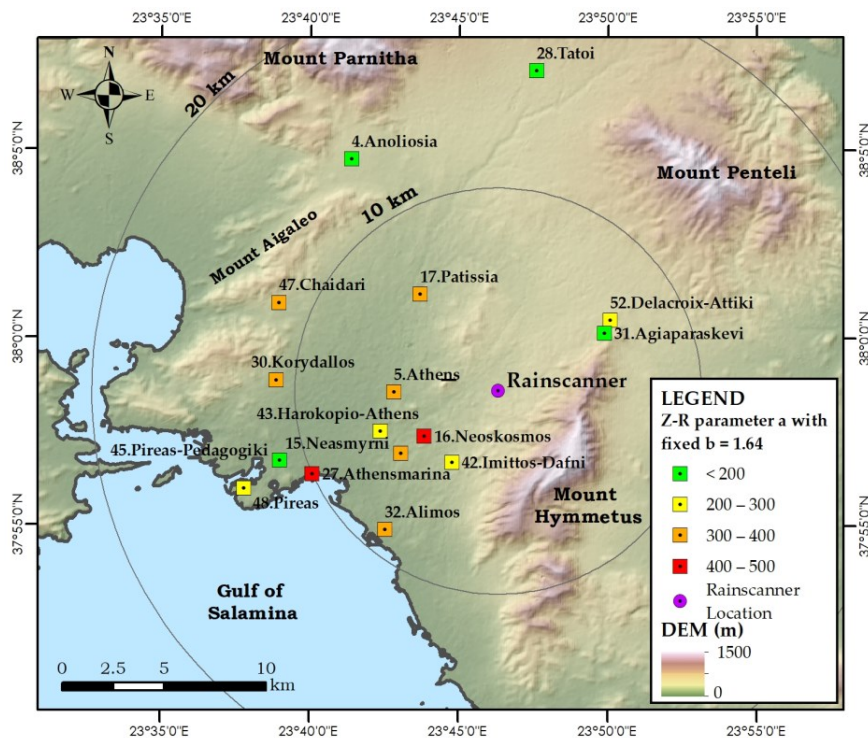
Figure 7: Spatial variability of Z-R parameter a, when a fixed parameter b is used, Source: (Bournas and Baltas 2022a)

As shown in panel a of Figure 6, the higher values for parameter *a* are found in the southwest, at the coastal front of Athens, while the lower values are found in the north section. As previously mentioned, a high value for parameter *a* and a low value for parameter b are found in Z-R relationships better suited to convective-type events. Since the sample includes both convective and stratiform events, this result indicates that higher reflectivity is measured on the coast front and less on the northeast. This finding can also be related to the typical trajectory of rainstorms in Athens. As featured in the studied events, storm cells in Athens tend to have a west-to-east direction. This trajectory usually takes the storm cell above the Gulf of Salamina and towards Mount Aigaleo. Especially in convective events, the storm cell feeds with moisture while it passes the sea, only to discharge when it hits the mainland and the higher elevation that Mount Aigaleo offers. Water discharge, i.e., rainfall, occurs rapidly in the coastal regions, imitating convective-based storm characteristics. From then on, the storm cell keeps discharging until it reaches Athens' city center and then heads to the north due to the presence of Hymmetus Mountain in the east. When it arrives at higher elevation locations, the rainfall intensity has dropped, and stratiform-based rainfall intensities are observed. A lower rainfall intensity does not necessarily mean less rainfall accumulation since the storm cloud may lose its velocity, thus delaying its departure from these regions.

Single Z-R Calibration:

In this optimization, a unified Z-R relationship is derived using the entire correlated dataset. Two approaches are considered: one using all available data and another using a calibration/validation scheme. In the first case, the relationship is $Z=300R^{1.69}$, while in the second case, it is $Z = 321R^{1.53}$. The second relationship was then validated with various stations and showed minimal differences in correlation and RMSE values. Therefore, the second relationship is considered more robust.

The derived relationships are subsequently compared with previously established relationships. Firstly, the comparison is made upon the precipitation and accumulation timeseries per station. Figure 8 shows the rainfall and accumulative rainfall timeseries for the Psychiko station on event 6. Blue bars denote the rain gauge measurements within the figures, while the Rainscanner measurements are presented with lines of different colors based on the Z-R relationship used. Specifically, with green color, the Marshal and Palmar equation, *$Z=200R^{1.6}$*, with red color the all-data calibration equation 5.2, *$Z=321R^{1.53}$*, with purple color the Event-based Z-R, with black color the Station Based Z-R, and with a blue color the optimized relationship when the station dataset for the particular event is used. The optimized relationship is the best-fit relationship since the Z-R parameters are optimized to match the specific data.

The Marshal and Palmer equation shows the higher deviations in all figures. In other words, it leads to overestimating rainfall compared to the rain gauge datasets. The equation closer to the optimized relationship is the station-based equation, followed by the All-data and event-based relationships. Figure 8 (Psychiko station, event 6) shows that while the optimized result fits better in each 10-minute rainfall height interval, the rainfall accumulation does not feature the best result compared to other relationships. This is caused by the gap of the Rainscanner dataset at 02:00, where no data was recorded, disrupting the accumulation time series graph.

Finally, in Figure 9, the RMSE, BIAS, Normalized Mean Absolute Error (NMAE), and Normalized Mean Bias (NMB) indexes between the rain gauge measurements and the rainfall heights are estimated for each Z-R relationship. The optimum relationship is the optimized result of each station per event, featuring the best results that the rest of the relationships should imitate. All indices are set to have zero as their optimum value, while NMAE and BIAS are also allowed to have negative values. Furthermore, apart from the mean value (red line), which should be found to be close to zero, the spread of the sample is also essential. Among the evaluated Z-R relationships, the all-data calibrated one ($Z=321R^{1.53}$) performs the best, followed by $Z=261R^{1.52}$ and $Z=431R^{1.25}$, while the Marshal and Palmer ($Z=200R^{1.6}$) yields the poorest outcome in all metrics. The substantial mean deviation and significant spread in the Marshal and Palmer relationship indicate its limited applicability across most stations. Although $Z=431R^{1.25}$ seems promising, its negative NMB suggests underestimation and suitability mainly for high reflectivity convective events.
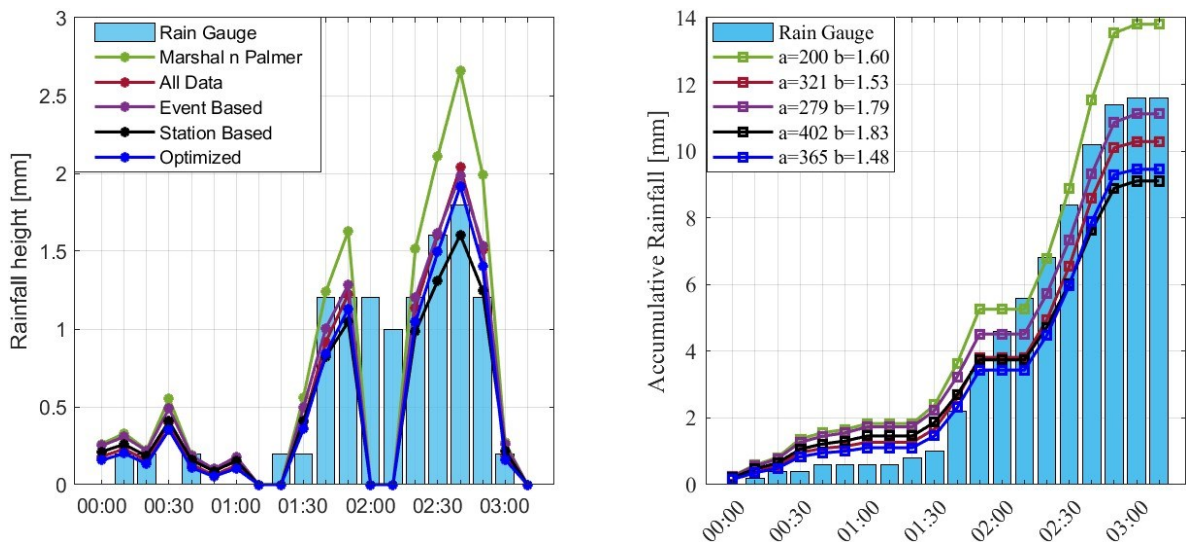
Figure 8. Precipitation and accumulative precipitation for Psychiko, on Event 6.
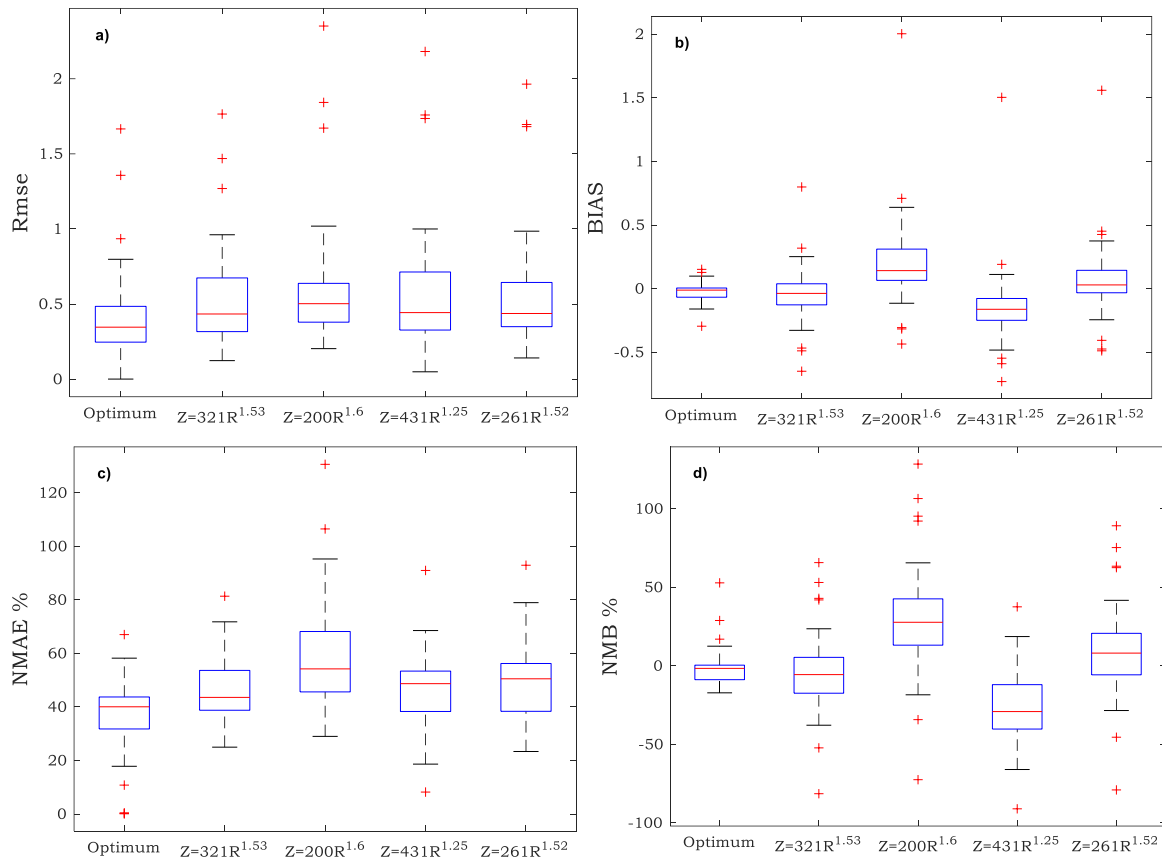
Figure 9. Boxplots of the a) RMSE, b) Bias, c) NMAE, and d) NMB per Z-R relationship

Rainfall-Runoff Model

The gridded rainfall-runoff model is applied to the rural part of Sarantapotamos River, with its outlet at the cross-section with the Attiki Odos freeway, totaling an area of 231.50 km². The time-area diagram is derived from GIS, using a 500 m x 500 m grid size based on the basin size. The grid leads to a total of 1021 grids. Figure 10 shows the gridded slope and CN AMC-II values, while Figure 11 shows the derived time-area diagram of the subbasin. The rainfall-runoff model is applied to six events. The events are shown in Table 2, featuring their duration and the 5-day accumulated precipitation to evaluate the prior soil moisture conditions better.

Table 2: Simulated events and main characteristics; Source: (Bournas and Baltas 2022b)

Event	Start Datetime	End Datetime	Duration (h)	5-Day API (mm)	Mean Area Cumulative Rainfall (mm)
6	17-12-2018 23:40	18-12-2018 13:50	14.2	13.8	25.8
21	24-11-2019 21:40	25-11-2019 08:30	10.8	37.0	30.4
31	01-06-2020 14:00	01-06-2020 20:00	6.0	0.0	20.5
48	09-06-2021 18:00	10-06-2021 02:44	8.7	0.2	25.0
50	12-06-2021 11:50	12-06-2021 19:00	7.2	32.0	26.0
61	23-11-2021 17:30	24-11-2021 07:40	14.2	2.6	26.4

Figure 10. Gridded datasets; a) Slope %, b) Curve Number for AMC-II conditions
Source: (Bournas and Baltas 2022b)
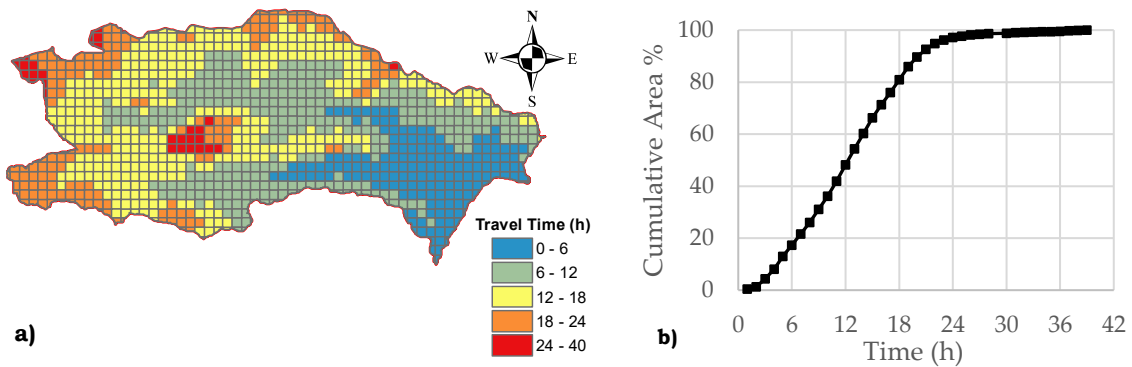
Figure 11. Time-area diagram: a) Time travel raster; b) Cumulative area % per hour at the basin outlet. Source: (Bournas and Baltas 2022b)

The events simulated were both stratiform- and convective-based. Of the simulated events, events 31, 48, and 50 featured convective-based characteristics, i.e., increased rainfall rates with small footprints. The hydrographs of Figure 12 show that in the stratiform events, the selection of the Z-R relationship features minor differences in all events. In contrast, in the convective events, while all relationships estimated 10-20 years return period, a single relationship led to unrealistic rainfall and runoff values, as showcased by the extreme runoff values and the high return period of rainfall as calculated by the IDF curves for the region (the rainfall return period is calculated above 100 years). This warrants caution when using a Z-R relationship since it can lead to unrealistic results.

Furthermore, between the used relationships, it is shown that the typically used Marshal and Palmer relationship leads to the highest amount of generated runoff. In contrast, the convective-based Z-R relationships feature the least generated runoff in the stratiform events but the highest in the convective-based among the rest. This result indicates that a convective-based relationship is preferable for these events, i.e., events with high rainfall intensities. In contrast, for stratiform events, it will probably underestimate the generated

runoff. Therefore, when considering flash flood early warning system implementations, a convective-based relationship should be desired, whereas in continuous rainfall-runoff simulation, where light rain and low runoff are simulated, it should be avoided.
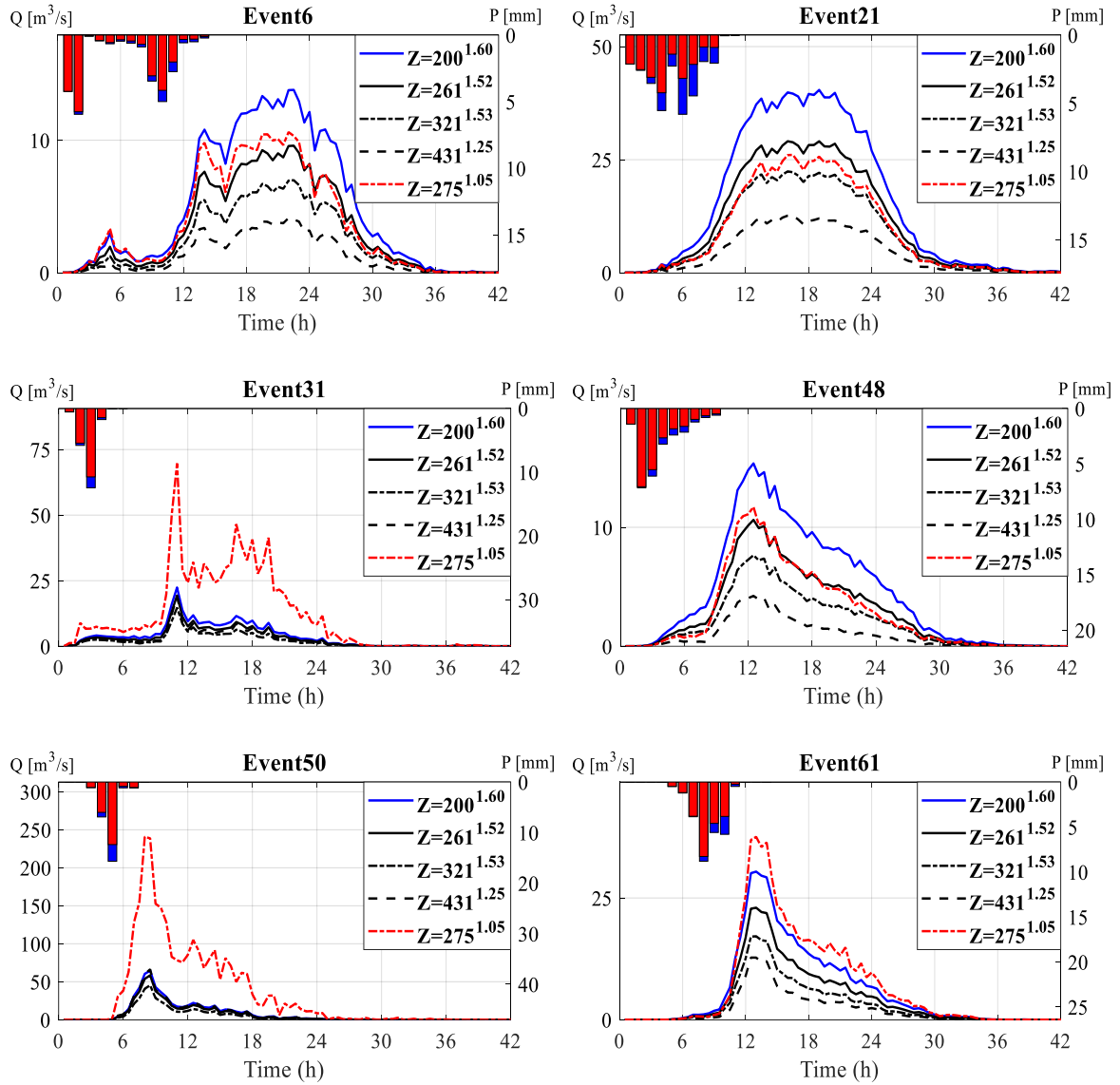
Figure 12. Hydrographs generated for all events. Blue and red bars denote mean area rainfall and rainfall losses, respectively. Source: (Bournas and Baltas 2022b)

Gridded Flash Flood Guidance

The GFFG is applied in the Sarantapotamos basin and Attica region. Firstly, the threshold runoff maps are presented, and the results are discussed. Secondly, the system is applied in a series of rainfall events to extract the potential flood risk in each case.

In Figure 13, the threshold maps for the three accumulation periods, 1-, 3- and 6-hours, are presented for medium saturated soil moisture conditions. Figure 14 shows the threshold runoff for two different soil moisture conditions (medium and saturated). In real-time monitoring, the threshold maps are named the FFG maps when the current soil moisture conditions are used.
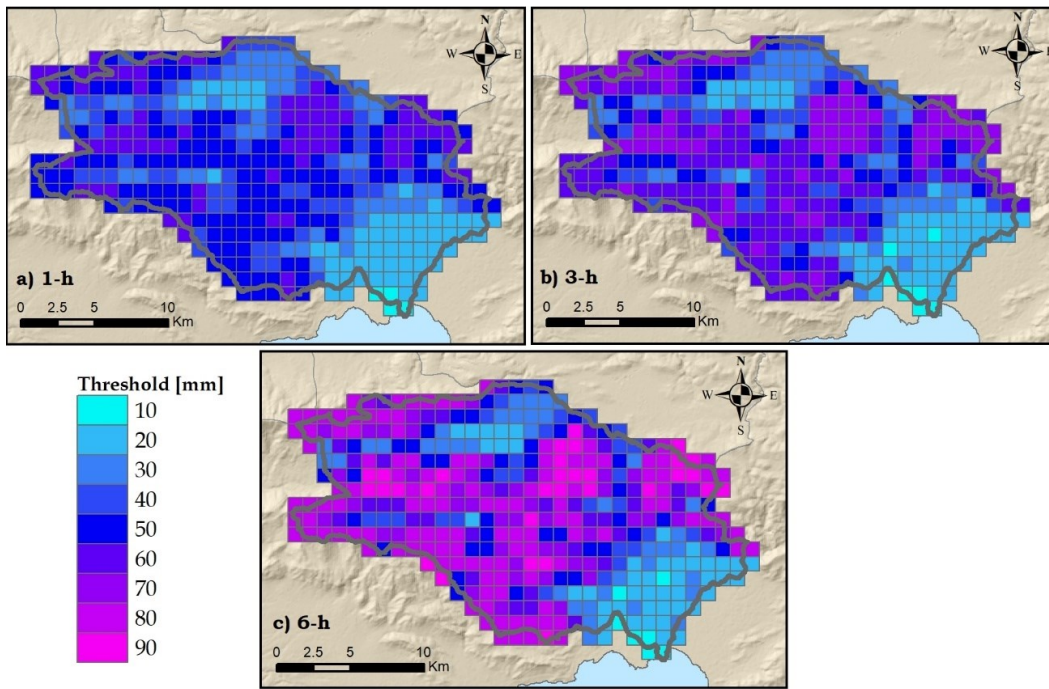
Figure 13: Threshold rainfall values for different rainfall duration: a) 1-h, b) 3-h, and c) 6-h. Source (Bournas and Baltas 2022c)
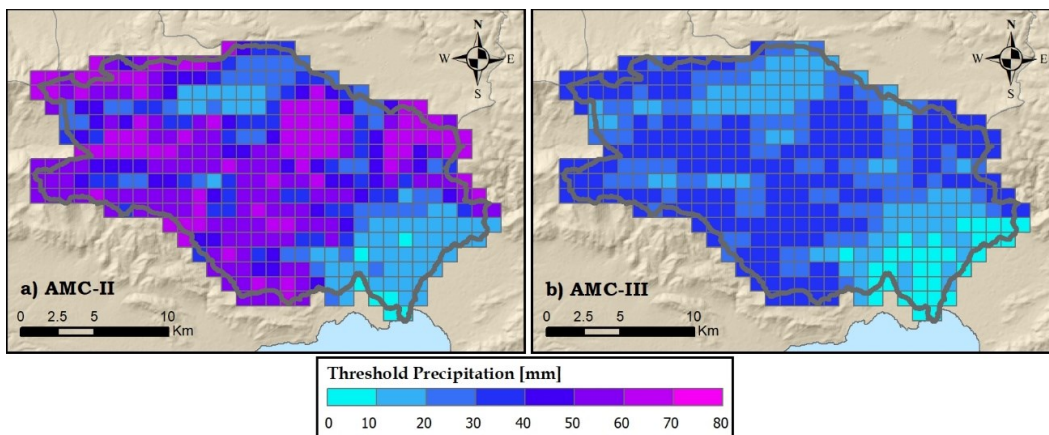
Figure 14: Threshold rainfall for a 3-h accumulation period for a) ACM-II and b) AMC-III conditions; Source (Bournas and Baltas 2022c)

By applying the above methodology, the FFG maps are derived for three accumulation periods (1-, 3-, and 6 hours). The main findings concern the characteristics of generated maps, such as the dependencies of the thresholds to the soil moisture conditions and the accumulation periods. Different accumulation periods aim to be used and assessed through the respective duration forecasted products. This is because a more extended duration provides a longer lead time, however, with increased uncertainty. This is not only due to the uncertainty of the provided forecast but also due to the uncertainty regarding the exact moment flooding will occur within the designated period. More specifically, the system does not warn on the exact time that flooding will occur within the accumulation period. Instead, it warns on whether flooding will eventually occur. The effect of soil moisture on the generated maps is significant since the threshold runoff features lower values during medium or wet conditions. The latter means that less rainfall accumulation is required to create flooding conditions. The results also indicate that the effect of soil moisture is at its maximum in land uses with permeable CN (CN values close to 50). This is because the calculated CN changes dramatically between dry and wet conditions. In contrast, highly impervious areas are less dependent on soil moisture conditions since runoff potential is already high.

Below is the application to the Attica Basin and the Sarantapotamos for flood events. For this extended abstract, Event 50 is presented. This event occurred on 12-06-2021. Figure 15 shows the rainfall maps, with highlighted cells for potential floods. A 3-hour accumulation period is used. As seen in the figure, areas highlighted for flooding were well-correlated with the areas where high rainfall occurred.
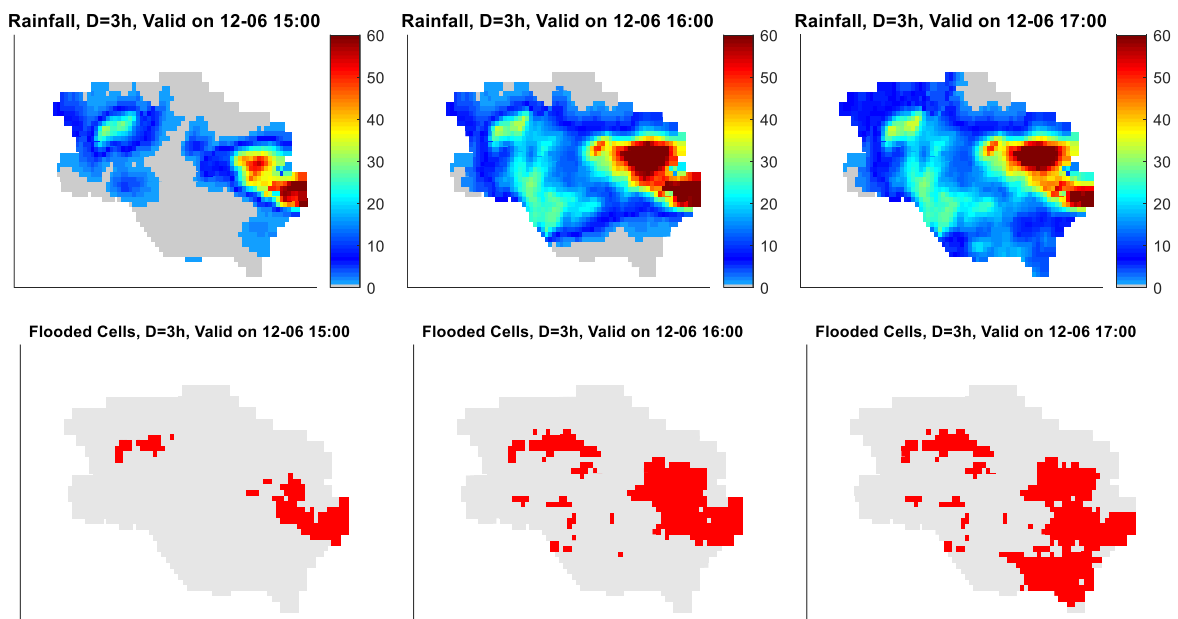
Figure 15: 3-hour Gridded Rainfall, valid per timestamp for Event 50, Sarantapotamos subbasin. The first row shows the rainfall fields; the second row shows the flooded cells.

The difference between the accumulation periods is observed in the rainfall height and extent in each timestamp. The benefit lies mainly in the provided lead time. The 3-h and 6-h durations are the most useful. However, in these cases, the exact time of flooding is unknown, while in the 1-h duration, the uncertainty is less. Figure 16 shows the total flooded cells for each duration for both Sarantapotamos and the Attica Region. As shown, the result is the same regardless of period used (1h or 3h or 6h).
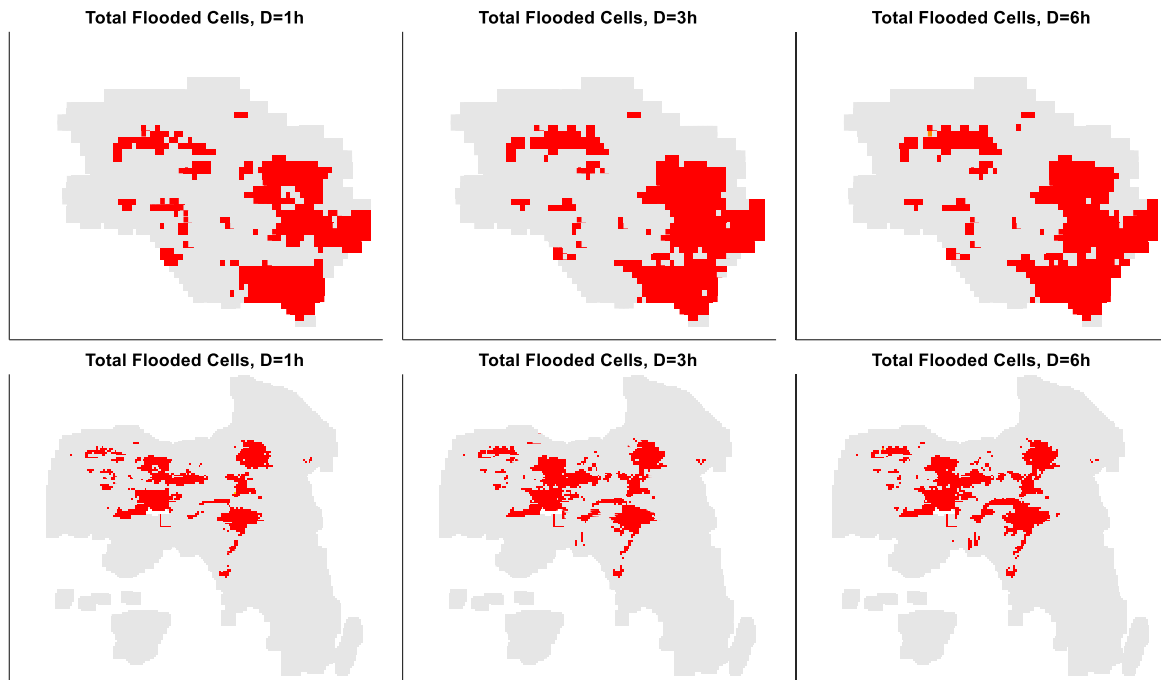
Figure 16: Total Cells flagged for flood based on the GFFG system for Event 50 at the Sarantapotamos basin and Attica Region.

Finally, a sensitivity-based analysis is performed. The main parameters of the system are adjusted, and the result is shown. The main parameters of the system are a) the rainfall return period used to calculate the threshold runoff, b) the soil moisture conditions, and c) the Z-R relationship used to transform reflectivity into rainfall. In Figure 17, different values of the above a, b, c, are used and compared with the 16:00 timeframe shown. In panel (a), the change of the rainfall return period for the calculation of runoff threshold is performed from T=5 years to T=10 years, in panel (b), the soil moisture is changed from 70% to 100%, while in panel (c) the Z-R relationship is changed from the $Z=321R^{1.53}$ to the $Z=200R^{160}$ relationship. Observing Figure 17 and comparing it with the time frame shown, it is shown that the effect of the return period is minimal, while the effect of the soil moisture conditions is the most significant. The change in the Z-R relationship also increases the number of potential cells flagged for flood since the used Z-R results in higher rainfall intensity values, but not as high as the soil moisture conditions.
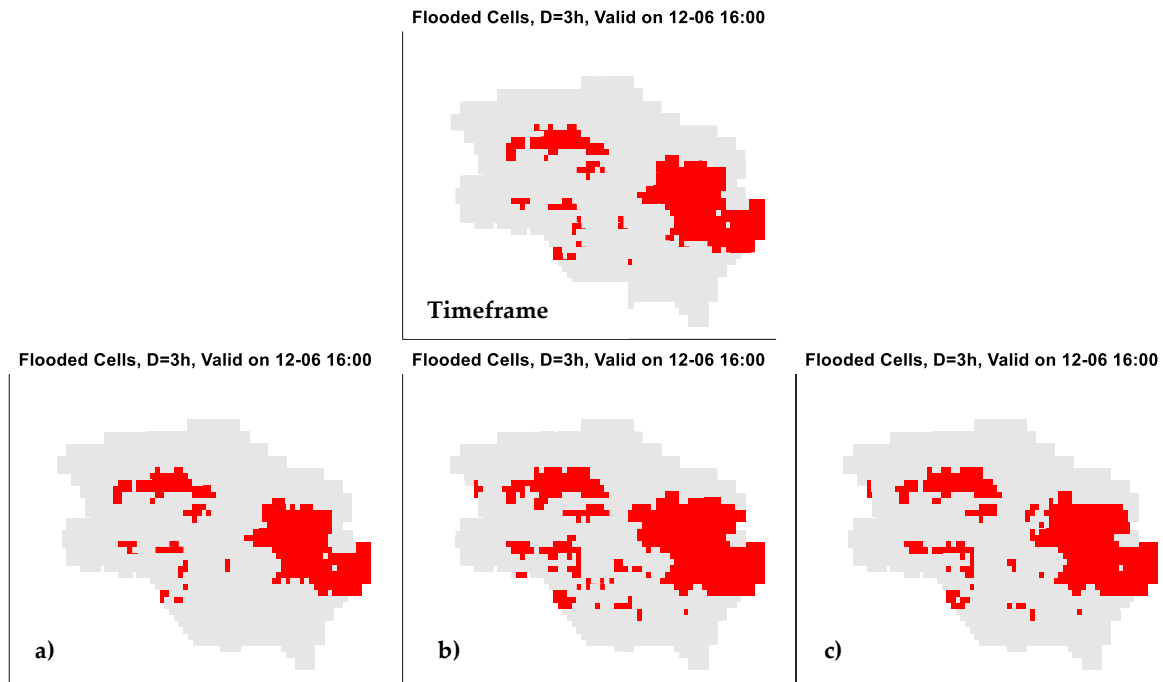
Figure 17: Impact of the number of cells flagged for flood for a selected timeframe, by changing the: a) return period from T=5 years to T=10 years, b) Soil moisture from 70% to 100% and c) the used Z-R from $Z=321R^{1.53}$ to $Z=200R^{1.60}$.

Storm Tracking

The storm tracking algorithm includes the storm cell's identification and tracking procedures. The first case shows the algorithm's ability to track cloud cells. Figure 18 shows the difference between utilizing a different reflectivity threshold and whether a polygon or a fitting ellipse represents the cloud cell's boundaries. The 25 dBZ threshold works well when identifying polygon boundaries but does not work well with a fitting ellipse. By setting a 4 km² area threshold, 11 cells are identified above this threshold. In the 30 dBZ case, the fitting ellipse features better results concerning the core cell identification. Since the emphasis is given on intense rainfall systems, the 30 dBZ with a fitting ellipse is used to identify the cell centroids and store their attributes (e.g., the ellipse characteristics and centroid coordinates). Finally, the 35 dBZ limit highlights areas with higher-than-average rainfall intensities, signifying areas where heavy rain occurred.
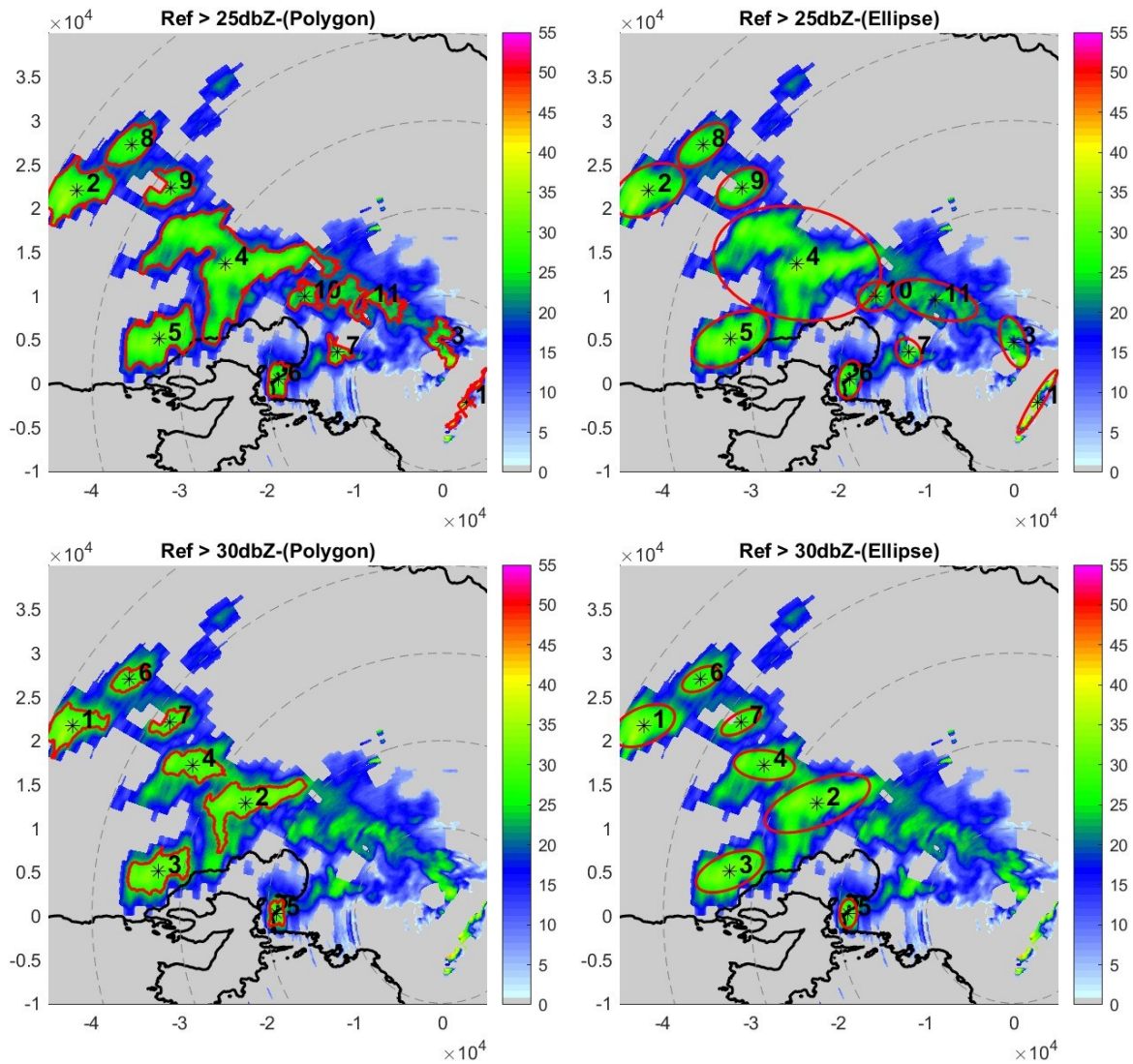
Figure 18: Results of the cell algorithm when a different reflectivity threshold is used; 25-, 30-dBZ shown in each row, and when a polygon or fitting ellipse is used to form the boundaries, each column.

Figure 19 illustrates the application of the cell track algorithm, using 10-min derived reflectivity images in a 10-min temporal interval. Specifically, five 2-min reflectivity images are merged to define the 10-min reflectivity field. Following this, a 10-minute time step is used, and the tracking algorithm is applied to perform the matchmaking of each cell and the merging and splitting of cells. The resulting timeframe cells are shown with red polygons, while the previous ones are dashed black. The objective is to match the centroids of black cells to those of the red cells. The algorithm works well and successfully merges the cells.
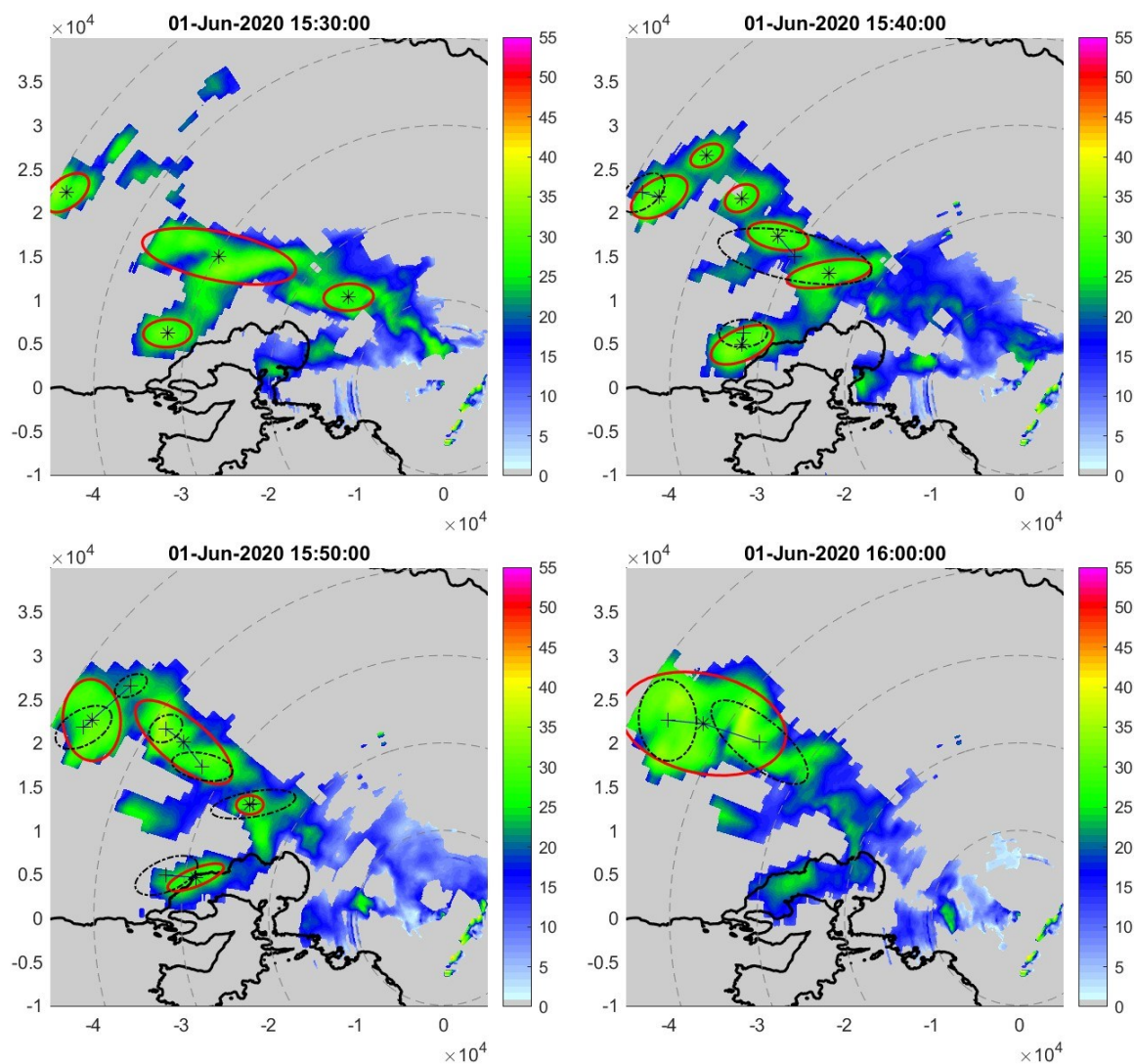
Figure 19: The matchmaking procedure between four timeframes with a 10-minute step

Following this procedure, the algorithm is applied to all events observed by the Rainscanner. In Figure 20, the tracking for events E31 and E50 is shown. In blue borders: the border of a cell whose threshold is above either 35 dBZ (first row) or 40 dBZ (second row). In red polygons: the centroids of cells. In dashed black lines, the tracking. The above 40 dBZ results are more visually appealing due to the fewer identified cells.

In Figure 21, the centroids of the 35 dBZ are shown in red rectangles. The result shows improved clarity regarding the location of the cells and the direction of the storms for events 31 and 50. Similar results for all featured events are shown in Appendix B.
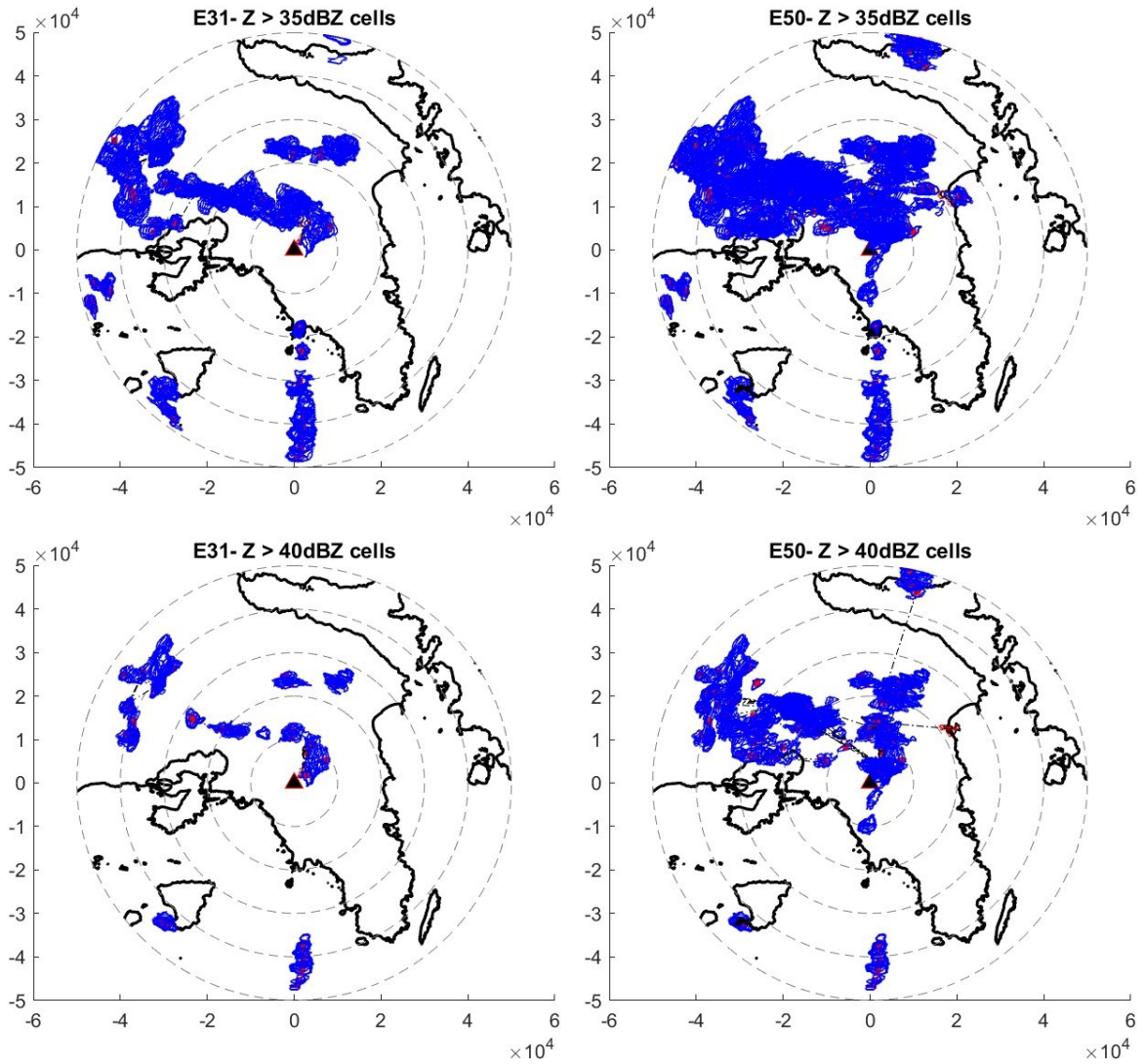
Figure 20: Cells borders of events 31 and 50 for two reflectivity thresholds: over 35 dBZ (first row), over 40 dBZ (second row)
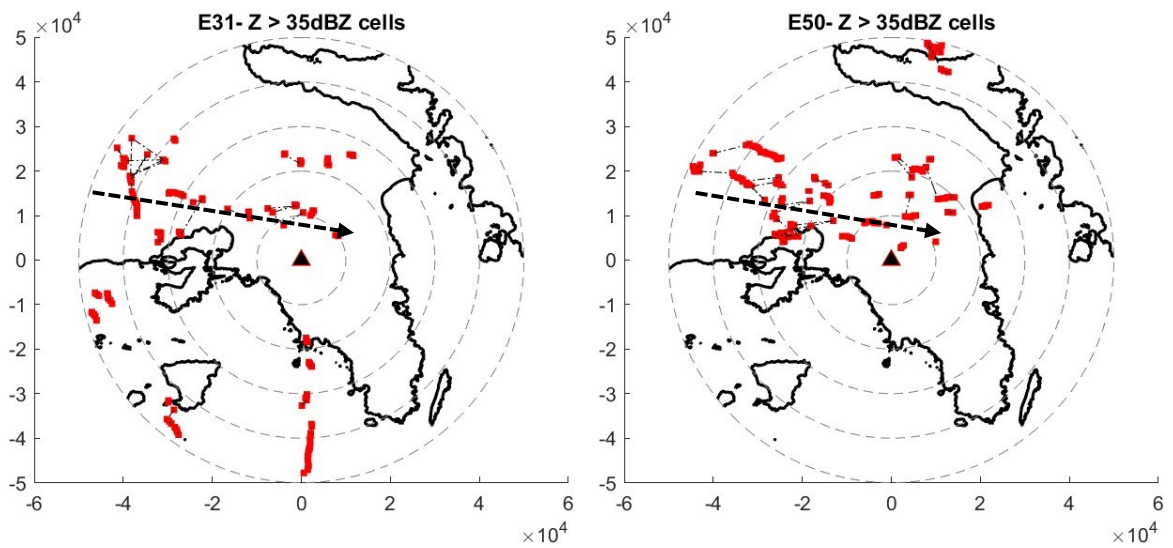
Figure 21: Centroids of storm cells (red rectangles) with a reflectivity threshold > 35 dBZ

The tracking confirmed the west-to-east direction of the storm events, which is featured in most events. Figure 22 shows the main directions of the storms featured in Attica. Most storms have a southwest-to-northeast direction, passing over Athens city center, followed by west-to-east and northwest-to-east directions. South-to-northeast directions are observed mainly with convective-based storms, whereas North-to-south directions are observed during winter, featuring stratiform events characterized by their low velocity and rainfall intensity. Moreover, snowfall events also feature Northeast-to-southwest directions, with the slowest velocity among other events. Convective-based events, i.e., events that showcase the highest reflectivity values, had an east-to-west direction, as featured in the studied events E31 and E50.
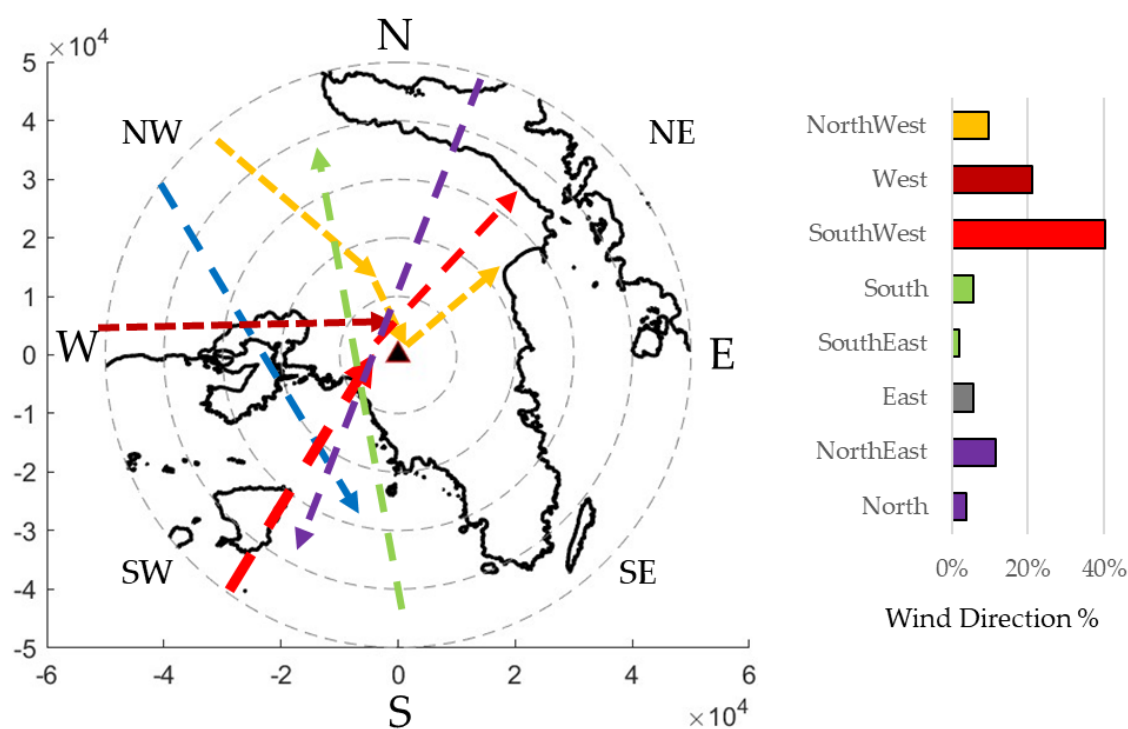
Figure 22: Main directions of storm clouds in Attica Region; Red lines are for storms occurring most often, followed by blue, yellow, and purple.

Conclusions and Future Research

This Ph.D. dissertation focuses on developing and implementing a methodology for early warning of intense floods using innovative technologies, primarily centered around a newly installed weather radar system called the X-Band Rainscanner in Athens, Greece. The high-resolution data from this radar system is crucial for understanding rainfall's spatial and temporal characteristics, especially for local applications like small-basin rainfall-runoff modeling and nowcasting. The dissertation is divided into two main sections. The first section reviews various aspects of weather radar technology, specifically on the variability

of the Z-R relationship, and the second focuses on applying a Flood Early Warning System (FEWS).

Concerning the Z-R variability, it is found that although significant variability is showcased in time and space, several patterns that explain this variability are extracted. Specifically, the location's characteristics within the study area, such as its elevation and proximity from various locations, such as the distance from the weather radar, the coastline, the clutter-affected areas, and the high-elevation areas, affect the Z-R relationship. These characteristics affect the storm's characteristics, which this study was able to extract using high-resolution rainfall fields.

Concerning the application of FEWS, this research showcased the required components and processes to obtain reliable results through an easy-to-apply methodological framework. Through the development of a gridded rainfall-runoff model, the impact of the Z-R relationship on the generated runoff is performed, where it was found that convective-based Z-R relationships work well with respected convective events but tend to lead to underestimation of runoff when used in light rain. On the other hand, caution should be exercised when utilizing a Z-R relationship since this can lead to excessive errors in the generated runoff, highlighted by the difference in the event's return period as calculated by the intensity duration curves derived for the region. The implementation of the GFFG system reached valuable results concerning issuing flash flood warnings using high-resolution modeling and highlighting the impact of the soil moisture conditions prior to the events. Finally, the storm-tracking algorithm showcased the ability of the Rainscanner system to be used for forecasting applications by focusing on identifying and tracking storm cells. The algorithm was able to distinguish and match storm cells in consecutive images, making it a valuable tool for further nowcasting applications. The algorithm was finally applied in a series of events that occurred in Athens, showcasing the west-to-east direction of summer convective events and the north-to-south direction of winter stratiform events.

The dissertation presents a holistic approach to using weather radar-derived datasets for an FEWS implementation in Athens, offering valuable insights into radar technology, Z-R relationships, and flash flood forecasting methodologies. It introduces innovative techniques and contributes to the field of flood early warning systems. Future research aims to extend the findings of this thesis to other regions with different characteristics. Moreover, the assimilation and analysis of additional data such as runoff measurements, satellite data, distrometers data, and other meteorological radars to the individual points of this research, as well as the integration of stochastic methods to quantify and assess the uncertainty of the individual systems is proposed.

Εκτενής Περίληψη

Εισαγωγή

Η εν λόγω διδακτορική διατριβή (Δ.Δ) με τίτλο «Ανάπτυξη και εφαρμογή μεθοδολογίας έγκαιρης προειδοποίησης ισχυρών πλημμυρών με χρήση νέων τεχνολογιών», επικεντρώνεται στην ανάπτυξη και εφαρμογή ενός μεθοδολογικού πλαισίου για την έγκαιρη προειδοποίηση ισχυρών καταιγίδων και πλημμυρών, χρησιμοποιώντας νέες τεχνολογίες και συγκεκριμένα δεδομένα από μετεωρολογικό ραντάρ. Τέτοια συστήματα ραντάρ συναντώνται κυρίως για την αντιμετώπιση αιφνίδιων πλημμυρών οι οποίες αποτελούν μία από τις πιο θανατηφόρες φυσικές καταστροφές σε παγκόσμιο επίπεδο. Τα χαρακτηριστικά των αιφνίδιων πλημμυρών διαφέρουν από τις συμβατικές ποτάμιες πλημμύρες, καθώς προκαλούνται από απότομες και έντονες βροχοπτώσεις, που πραγματοποιούνται σε σύντομο χρονικό διάστημα, ενώ πλήττουν κυρίως αστικές περιοχές. Οι αιφνίδιες πλημμύρες αποτελούν συνήθως επεισόδια περιορισμένης έκτασης, και οφείλονται σε συγκεκριμένου τύπου καταιγίδες (Houze Jr. et al. 2015). Οι παράγοντες που επηρεάζουν την εμφάνιση και την ένταση των αιφνίδιων πλημμυρών, εκτός της έντονης βροχόπτωσης, είναι η γεωμορφολογία της λεκάνης απορροής, όπως το μέγεθος, η κλίση, η υδατοπερατότητα του εδάφους και οι αρχικές συνθήκες υγρασίας (Merz and Blöschl 2003; Houze Jr. et al. 2015; Velásquez et al. 2020). Η μεταβολή της γεωμορφολογίας όπως για παράδειγμα η μεταβολή των διατομών ενός ποταμού λόγω της διάβρωσης και της μεταφοράς ιζημάτων που προκαλείται από ισχυρές βροχοπτώσεις, τείνει να μεταβάλλει τα φυσικά χαρακτηριστικά των ποταμών. Επιπλέον, οι βίαιες αλλαγές χρήσεων γης, όπως η αστικοποίηση, η αποψίλωση των δασών και οι δασικές πυρκαγιές, μεταβάλλουν την τρωτότητα των περιοχών έναντι πλημμυρών και σε συνδυασμό με πιο συχνές υψηλής έντασης καταιγίδες, οδηγούν σε αύξηση των αιφνίδιων πλημμυρών (Alfieri et al. 2012; Gaur and Simonovic 2015; Rogger et al. 2017; Caloiero et al. 2017). Ως αποτέλεσμα περιοχές που στο παρελθόν δεν ήταν επιρρεπείς σε πλημμύρες, πλέον είναι ευάλωτες σε αυτές (Bournas and Baltas 2021a). Στην περιοχή της Μεσογείου, τα τελευταία χρόνια, οι αιφνίδιες πλημμύρες έχουν προκαλέσει όχι μόνο σημαντικές οικονομικές αλλά ακόμα και ανθρώπινες απώλειες (Diakakis et al. 2012, 2019; Pereira et al. 2017; Feloni 2019; Varlas et al. 2019; Spyrou et al. 2020).

Μία από τις κύριες μη-κατασκευαστικές μεθόδους για την αντιμετώπιση των πλημμυρών είναι η ανάπτυξη και η χρήση Συστημάτων Έγκαιρης Προειδοποίησης Πλημμυρών (ΣΕΠΠ). Ένα ολοκληρωμένο ΣΕΠΠ αποτελείται από διάφορα τεχνικά και

μη-τεχνικά υποσυστήματα που αφορούν, α) στην ανάλυση των χαρακτηριστικών που προκαλούν τον κίνδυνο πλημμύρας, β) στην παρακολούθηση και ανάλυση των καιρικών συστημάτων, γ) στην πρόγνωση καιρού και τη θέσπιση ορίων κινδύνου, δ) στη μεταφορά των προειδοποιήσεων, ε) στην προετοιμασία και τις ενέργειες αντίδρασης (Perera et al. 2019). Παρόλο που οι μέθοδοι που χρησιμοποιούνται για την ανάλυση και προσομοίωση των υδρομετεωρολογικών διαδικασιών κατά την διάρκεια μίας έντονης βροχόπτωσης διαφέρουν σε πολυπλοκότητα, η κύρια αβεβαιότητα της εκτίμησης πλημμυρικού κινδύνου έγκειται στη χαοτική φύση της ατμόσφαιρας και την έλλειψη επαρκούς ανάλυσης και δεδομένων υψηλής ποιότητας (Marchi et al. 2010). Ακόμη και σε περιπτώσεις όπου υπάρχει διαθεσιμότητα αξιόπιστων δεδομένων, έχει βρεθεί πως ενδέχεται να υπάρχει υψηλή αβεβαιότητα στην προσομοίωση της απορροής συγκριτικά με τις παρατηρηθείσες τιμές, γεγονός που οφείλεται στην κλίμακα και στις μεθόδους που χρησιμοποιούνται στα υδρολογικά μοντέλα (Di Baldassarre and Montanari 2009). Η επιθυμητή χωρική και χρονική κλίμακα των πεδίων βροχής που οδηγούν σε αιφνίδιες πλημμύρες είναι υψηλότερη από την αντίστοιχη ανάλυση που προσφέρουν τα παραδοσιακά δίκτυα επίγειων βροχογράφων (Anagnostou et al. 2017), ενώ όταν η επιθυμητή ανάλυση των δεδομένων δεν είναι διαθέσιμη, η δυνατότητα παροχής έγκαιρων προειδοποιήσεων μειώνεται σημαντικά (Mimikou and Baltas 1996). Σε περιπτώσεις, όπως συμβαίνει στην Ελλάδα, όπου δεν υπάρχουν διαθέσιμες μετρήσεις, ή η αξιοπιστία των δεδομένων είναι μικρή, το πρόβλημα επιδεινώνεται. Ως αποτέλεσμα, η κλίμακα και η ποιότητα των δεδομένων επιδρούν σημαντικά και στην ποιότητα ενός ΣΕΠΠ.

Στο πλαίσιο συνεχούς ανάπτυξης των ΣΕΠΠ η έρευνα επικεντρώνεται, στην βελτίωση της ποιότητας της πρόγνωσης, στην αύξηση του διαθέσιμου χρόνου αντίδρασης και στην αποτελεσματικότερη διάχυση της πληροφορίας σχετικά με τον χρόνο και τις περιοχές που πρόκειται να πλημμυρίσουν. Οι δύο πρώτες συνιστώσες μπορούν να επιτευχθούν με την εφαρμογή νέων τεχνολογιών που αφορούν στη συλλογή και την επεξεργασία δεδομένων καθώς και στην χρήση πιο προχωρημένων μοντέλων, δηλαδή είναι άρρηκτα συνδεδεμένες με την ανάλυση και την ποιότητα των δεδομένων εισόδου, και κυρίως της βροχόπτωσης. Για παράδειγμα ΣΕΠΠ που επικεντρώνονται σε αιφνίδιες πλημμύρες, δηλαδή σε επεισόδια βροχής υψηλής χωροχρονικής μεταβλητότητας, απαιτούν αντίστοιχης ανάλυσης δεδομένα εισόδου, και συγκεκριμένα για τα δεδομένα βροχόπτωσης βασίζονται σχεδόν αποκλειστικά στην επεξεργασία δεδομένων μετεωρολογικού ραντάρ. Στην Ελλάδα, τα ευρωπαϊκά ΣΕΠΠ όπως το European Flood Awareness System (EFAS), και συγκεκριμένα τα συστήματα ERIC και EPICHA για αιφνίδιες πλημμύρες, έχουν περιορισμένη χρήση που οφείλεται κυρίως α) στη μη διαθεσιμότητα κύριων συστημάτων, π.χ. μη κάλυψη του Ευρωπαϊκού δικτύου

μετεωρολογικών ραντάρ στην περίπτωση του EPICHA στην Ελλάδα, β) της μη διαθεσιμότητας των κατάλληλων δεδομένων για τη βαθμονόμηση των μοντέλων, και γ) στη μεθοδολογία που ακολουθείται καθώς τα αναφερθέντα συστήματα σχεδιάστηκαν για εφαρμογή σε μεγάλα ποτάμια συστήματα και όχι σε μικρές λεκάνες απορροής που απαντώνται στον Ελληνικό χώρο. Ειδικά στην Ελλάδα, η μεγάλη ποικιλομορφία στην γεωγραφία και η μεγάλη ακτογραμμή της, δημιουργεί πολλές μικρές λεκάνες απορροής οι οποίες έχουν αστικοποιηθεί στα πεδινά τμήματα τους, με αποτέλεσμα να είναι ευάλωτες σε αιφνίδιές πλημμύρες, με πρόσφατα επεισόδια να επιβεβαιώνουν την υπόθεση ότι οι περιοχές αυτές είναι ευάλωτες (Feloni et al., 2020; Varlas et al., 2021). Επιπλέον, όπως αναφέρθηκε, η Ελλάδα είναι αποκομμένη από τα περιφερειακά Ευρωπαϊκά δίκτυα συλλογής δεδομένων, όπως αυτά της κεντρικής Ευρώπης, και ως αποτέλεσμα οι περισσότερες έρευνες πάνω στη πρόγνωση έναντι πλημμυρών επικεντρώνονται στην χρήση δορυφορικών δεδομένων, (Spyrou et al., 2020; Varlas et al., 2021, 2019) τα οποία όμως δεν θεωρούνται τόσο αξιόπιστα όσο αυτά των μετεωρολογικών ραντάρ. Ο επίσημος φορέας πρόγνωσης καιρού στην Ελλάδα είναι η Εθνική Μετεωρολογική Υπηρεσία (ΕΜΥ), η οποία εκδίδει ημερήσιες προβλέψεις, με μέγιστο χρονικό βήμα 3-ωρών, οι οποίες δεν έχουν την απαιτούμενη χωρική και χρονική ακρίβεια για την ανίχνευση και αντιμετώπιση αιφνίδιων πλημμυρών σε αστικές και ημιαστικές περιοχές στο πλαίσιο ενός ΣΕΠΠ.

Ο κύριος στόχος της συγκεκριμένης Δ.Δ. είναι η ανάπτυξη μιας μεθοδολογίας εκτίμησης και πρόγνωσης ισχυρών καταιγίδων και πλημμυρών με τη χρήση δεδομένων μετεωρολογικού ραντάρ υψηλής χωρικής και χρονικής ανάλυσης. Τα ερευνητικά ερωτήματα που η Δ.Δ. σκοπεύει να απαντήσει αναλύονται σε δύο ενότητες. Η πρώτη επικεντρώνεται στην συλλογή, επεξεργασία και ανάλυση των δεδομένων από το μετεωρολογικό ραντάρ και απαντά στα εξής ερωτήματα: "*Ποιοι είναι οι κύριοι παράγοντες που πρέπει να ληφθούν υπόψη για τη χρήση δεδομένων μετεωρολογικού ραντάρ; Ποιες είναι οι πηγές αβεβαιότητας και πως μπορούν αν εξαλειφθούν;*". Η δεύτερη ενότητα επικεντρώνεται στην ανάπτυξη μίας μεθοδολογίας εκτίμησης πλημμυρικού κινδύνου σε πραγματικό χρόνο, ως υποσύστημα ενός ΣΕΠΠ και απαντάει στα εξής ερωτήματα: "*Ποια είναι τα απαραίτητα μέρη ενός ΣΕΠΠ βασισμένου σε δεδομένα μετεωρολογικού ραντάρ; Ποιες είναι οι παράμετροι ενός τέτοιου συστήματος και πως αυτές επηρεάζουν την εκτίμηση πλημμυρικού κινδύνου; Τι υδρολογικά εργαλεία απαιτούνται να για υλοποιηθεί ένα τέτοιο ΣΕΠΠ;*".

Για τον σκοπό αυτό, χρησιμοποιούνται τα δεδομένα από ένα νέο εγκατεστημένο σύστημα μετεωρολογικού ραντάρ, τύπου X-Band (Rainscanner - Σαρωτής βροχής) του Εθνικού Μετσόβιου Πολυτεχνείου (ΕΜΠ). Τα δεδομένα αυτά επεξεργάζονται και επαληθεύονται μέσω μιας μεθοδολογίας βαθμονόμησης της σχέσης Z-R, της σχέσης

που συνδέει την μετρούμενη ανακλαστικότητα (Z) σε ένταση βροχής (R), με διαθέσιμα δεδομένα από επίγειους μετεωρολογικούς σταθμούς. Επιπλέον αναπτύσσεται ένα σύστημα εκτίμησης πλημμυρικού κινδύνου, και συγκεκριμένα μια παραλλαγή του συστήματος Flash Flood Guidance (FFG), το Gridded Flash Flood Guidance (GFFG). Στο πλαίσιο εφαρμογής του παραπάνω συστήματος, αναπτύχθηκαν δύο υδρολογικά εργαλεία, ένα κατανεμημένο μοντέλο βροχής-απορροής κατάλληλο για μικρές λεκάνες απορροής, και ένας αλγόριθμος παρακολούθησης καταιγιδοφόρων νεφών (Storm Tracking) που εφαρμόστηκε με σκοπό τον εντοπισμό και την παρακολούθηση των ισχυρών κυττάρων καταιγίδας.

Η Δ.Δ. αποτελείται από έξι κεφάλαια. Στο πρώτο κεφάλαιο (Introduction) παρουσιάζεται το αντικείμενο, ο σκοπός της διατριβής, η βιβλιογραφική ανασκόπηση σε θέματα που αφορούν στα μετεωρολογικών ραντάρ και τα ΣΕΠΠ, και παρατίθενται τα ερευνητικά ερωτήματα που επιδιώκει να απαντήσει. Το δεύτερο κεφάλαιο (Study Area and Data Used) αφορά στην επισκόπηση της περιοχή μελέτης και των δεδομένων που χρησιμοποιήθηκαν. Το τρίτο κεφάλαιο (Methodological Framework) αναφέρεται στο μεθοδολογικό πλαίσιο που εφαρμόστηκε στην Δ.Δ. καθώς και στις επιμέρους μεθοδολογίες που εφαρμόστηκαν για κάθε εργασία, ενώ στο τέταρτο κεφάλαιο (Results and Discussion) παρουσιάζονται τα αποτελέσματα της έρευνας ανά εργασία. Τέλος, στο πέμπτο κεφάλαιο (Conclusions and Future Research) παρουσιάζονται συνοπτικά τα συμπεράσματα της Δ.Δ. καθώς και στόχοι και προτάσεις μελλοντικής έρευνας.

Περιοχή Μελέτης και Δεδομένα

Η περιοχή μελέτης είναι η περιοχή της Αττικής και, συγκεκριμένα, η περιοχή που καλύπτεται από το σύστημα Rainscanner και φαίνεται στο Σχήμα 1. Το Rainscanner βρίσκεται στην Αθήνα, εντός του πανεπιστημιακού χώρου του ΕΜΠ, στον δήμο Ζωγράφου σε υψόμετρο εγκατάστασης 200 μέτρα. Η εμβέλεια του είναι 50 km και όπως φαίνεται στο Σχήμα 1, περιλαμβάνει το μεγαλύτερο τμήμα του Νομού Αττικής, εκτός από μια μικρή περιοχή στα δυτικά, πέρα από το Όρος Γεράνια, ενώ επιβλέπει και ένα μικρό τμήμα βόρεια του όρους Πάρνηθας, μέρος της Λεκάνης Απορροής Ποταμού (ΛΑΠ) Ασωπού. Λόγω της παρουσίας του Υμηττού στα ανατολικά, ολόκληρη η νοτιοδυτική περιοχή είναι αθέατη καθώς η δέσμη του Rainscanner εμποδίζεται από τον ορεινό όγκο. Ως αποτέλεσμα ολόκληρη η περιοχή των Μεσόγειων, συμπεριλαμβανομένου του αερολιμένα Αθήνας, "Ελευθέριος Βενιζέλος", είναι εκτός εμβέλειας. Ωστόσο, η τοποθεσία του Rainscanner είναι ευνοϊκή για την παρακολούθηση συστημάτων βροχόπτωσης, καθώς η πλειοψηφία των συστημάτων αυτών έχουν δυτική και βόρεια διεύθυνση, καθιστώντας την μία καλή επιλογή για την παροχή προγνώσεων για την πόλη της Αθήνας.

Οι χρήσεις γης στην Αττική χαρακτηρίζονται από υψηλό ποσοστό αστικού ιστού, καθώς το 27% της περιοχής είναι αστικοποιημένη, ενώ το υπόλοιπο 73%, είναι γεωργικού και δασικού τύπου. Οι υπολεκάνες απορροής που διαμορφώνονται στην περιοχή της Αττικής είναι γενικά μικρές και υψηλά αστικοποιημένες. Στη δυτική Αττική βρίσκεται η ΛΑΠ Σαρανταπόταμου, η μεγαλύτερη ημιαστική λεκάνη της Αττικής, με συνολική έκταση 341 km², από τα οποία τα 231 km², είναι μη-αστικά με αγροτικά χαρακτηριστικά.
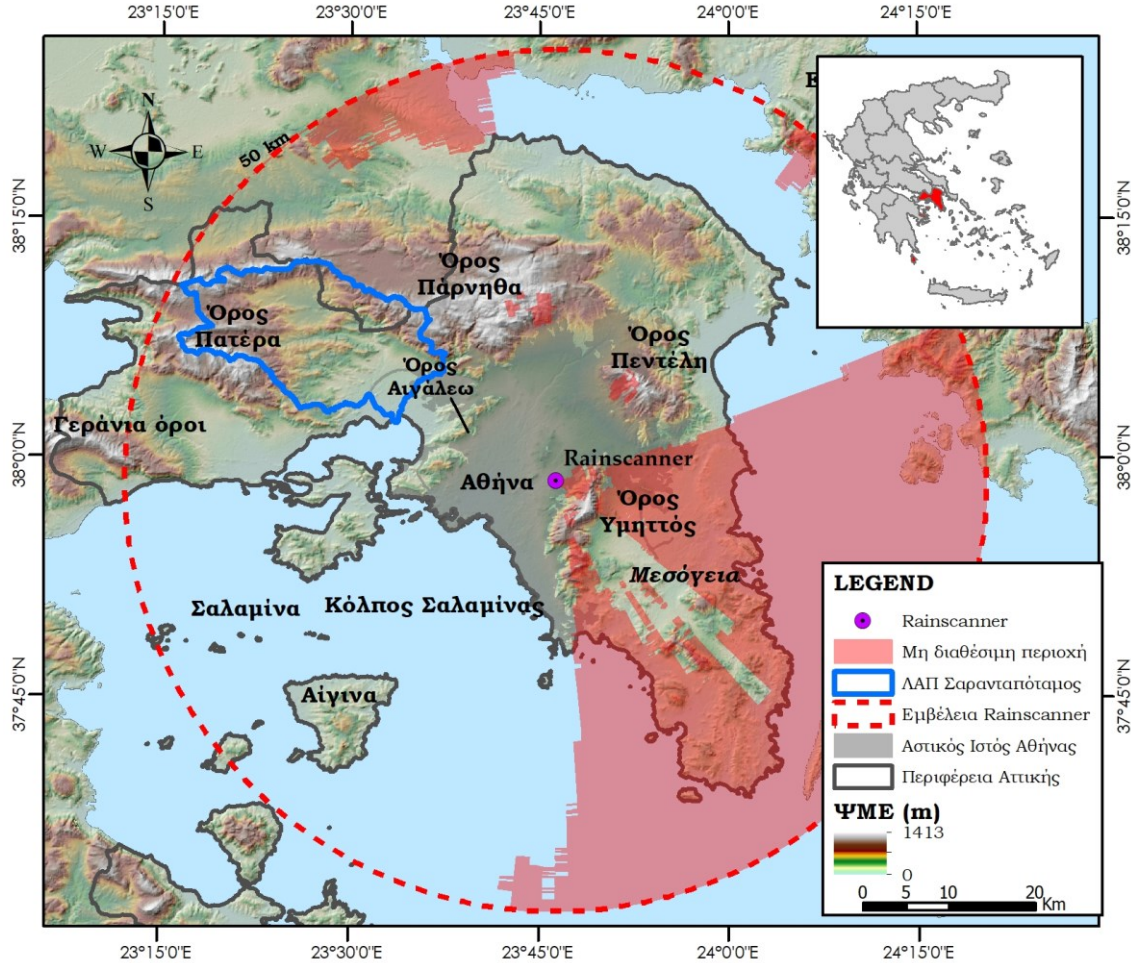
Σχήμα 1: Η περιοχή μελέτης

Τα βασικά δεδομένα που χρησιμοποιήθηκαν στη Δ.Δ. είναι τα εξής:

- Δεδομένα μετεωρολογικού ραντάρ. Τα δεδομένα του Rainscanner διαθέτουν χωρική ακρίβεια 100 m x 100 m και χρονική ανάλυση 2 λεπτών. Τα αρχεία υποβάλλονται σε ένα στάδιο προ-επεξεργασίας για την εξάλειψη ή την μείωση των επιπτώσεων των σφαλμάτων που οφείλονται στο ανάγλυφο του εδάφους (ground clutter) και της εξασθένισης του σήματος. Τα δεδομένα παρέχονται σε αρχεία τύπου ASCII με την αντίστοιχη γεωαναφορά. Τα τεχνικά χαρακτηριστικά του συστήματος Rainscanner παρουσιάζονται στον Πίνακα 1.

Δεδομένα επίγειων μετεωρολογικών σταθμών: Χρησιμοποιήθηκαν δεδομένα από το Αυτόματο Δίκτυο του Εθνικού Αστεροσκοπείου της Αθήνας (ΕΑΑ - ΝΟΑΑΝ), που αποτελείται από 53 σταθμούς για την περιοχή της Αττικής (Lagouvardos κ.ά. 2017). Τα δεδομένα αφορούν μετρήσεις βροχόπτωσης με χρονικό βήμα 10 λεπτά, οι οποίες έχουν υποβληθεί σε έλεγχο ποιότητας, αναφορικά με χωρικές και χρονικές ανακρίβειες. Στο Σχήμα 2, με μπλε χρώμα, παρουσιάζονται οι θέσεις των σταθμών που χρησιμοποιήθηκαν στην Δ.Δ.

• Ψηφιακό Μοντέλο Εδάφους (ΨΜΕ) με ανάλυση 5μ x 5μ, που παρέχεται από την Κτηματολόγιο Α.Ε.

Οι κατηγορίες κάλυψης γης CORINE (CLC, 2018) και τα δεδομένα URBAN Atlas 2018, που περιλαμβάνουν έναν κατάλογο της γεωγραφικής κάλυψης, τον πρώτο για ολόκληρη την Ευρώπη και τον δεύτερο για αστικές περιοχές της Ευρώπης.

• Γεωχωρικά δεδομένα από ανοικτές πηγές, όπως η ιστοσελίδα geodata.gov.gr, όπου παρέχονται τα όρια των διοικητικών περιοχών, καθώς και άλλα δεδομένα, όπως το οδικό δίκτυο, από την πρωτοβουλία OpenStreetMap.

Λίστα των διαθέσιμων σταθμών με γνωστές όμβριες καμπύλες (Intensity-Duration Frequency-IDF) που προέκυψαν στο πλαίσιο σύνταξης των Σχεδίων Διαχείρισης Κινδύνου Πλημμυρών για την Ελλάδα από το Υπουργείο Περιβάλλοντος, Ενέργειας και Κλιματικής Αλλαγής (SSW-MEECC 2017), Σχήμα 2.

Πίνακας 1: Τεχνικά χαρακτηριστικά του μετεωρολογικού ραντάρ Rainscanner

Παράμετρος	Τιμή
Μέγιστη ισχύ	25 kW
Μήκος Κύματος	X- Band 3.2 cm
Συχνότητα	9410 (± 30 MHz)
PRF	833 – 1500 Hz
Διάρκεια Παλμού	1200 – 500 ns
Συχνότητα περιστροφής	12 rpm
Κατακόρυφη και οριζόντια γωνία δέσμης	2.5ο
Οριζόντια ακρίβεια	± 0.5°
Μέγιστη Εμβέλεια	50 km
Μέγιστη χωρική ανάλυση	100 m x 100 m
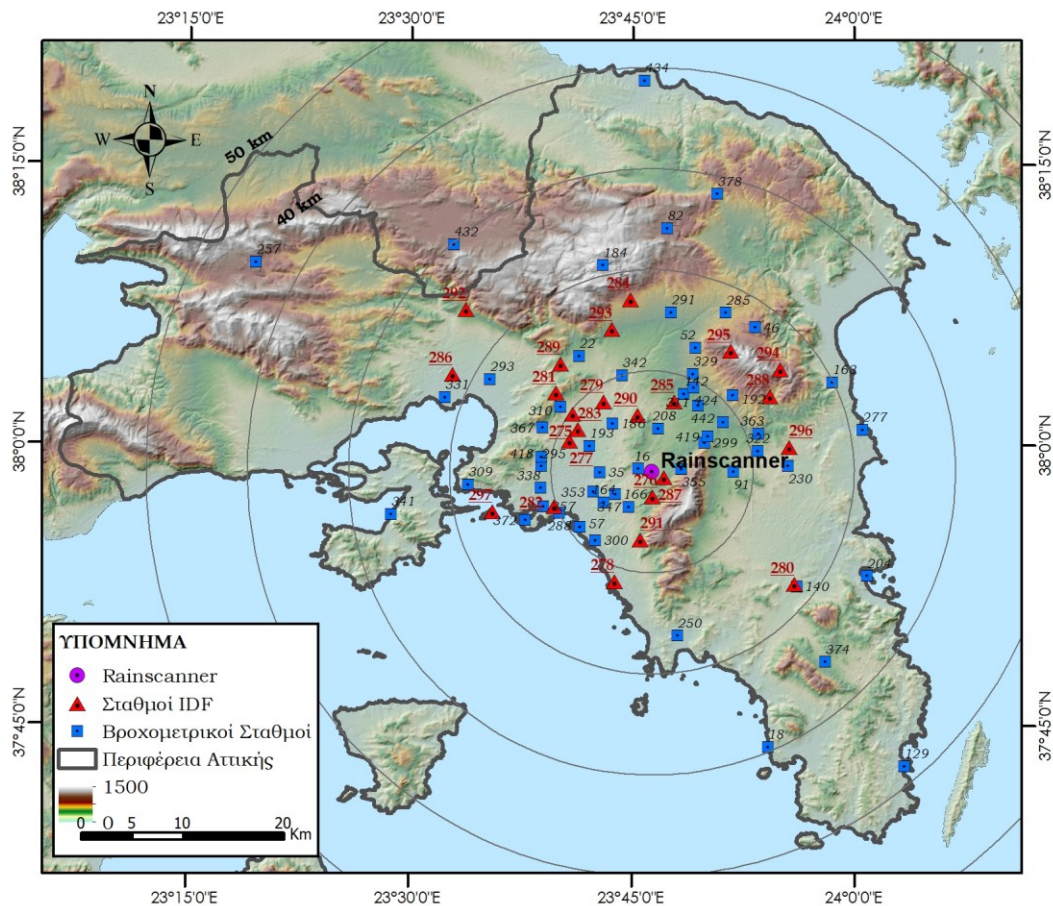
Σχήμα 2: : Το δίκτυο επίγειων υδρομετεωρολογικών σταθμών με δεδομένα βροχόπτωσης (ΕΑΑ) και με δεδομένα ομβρίων καμπυλών (IDF)

Μεθοδολογικό Πλαίσιο

Το μεθοδολογικό πλαίσιο που αναπτύχθηκε και εφαρμόστηκε στη παρούσα αΔ.Δ. παρουσιάζεται στο Σχήμα 3. Αποτελείται από πέντε κύρια υποσυστήματα, 1) τη διαχείριση και διόρθωση των μετεωρολογικών δεδομένων, 2) τη βαθμονόμηση της σχέσης Z-R, 3) το μοντέλο βροχής-απορροής, 4) το σύστημα GFFG και 5) τον αλγόριθμο παρακολούθησης καταιγιδοφόρων νεφών. Τα δύο πρώτα συστήματα απαρτίζουν την πρώτη ενότητα της Δ.Δ., δηλαδή αυτής που επικεντρώνεται στη συλλογή, επεξεργασία και ανάλυση των δεδομένων του μετεωρολογικού ραντάρ. Τα υπόλοιπα τρία συστήματα επικεντρώνονται στην εκτίμηση του πλημμυρικού κινδύνου στο πλαίσιο εφαρμογής ενός ΣΕΠΠ.
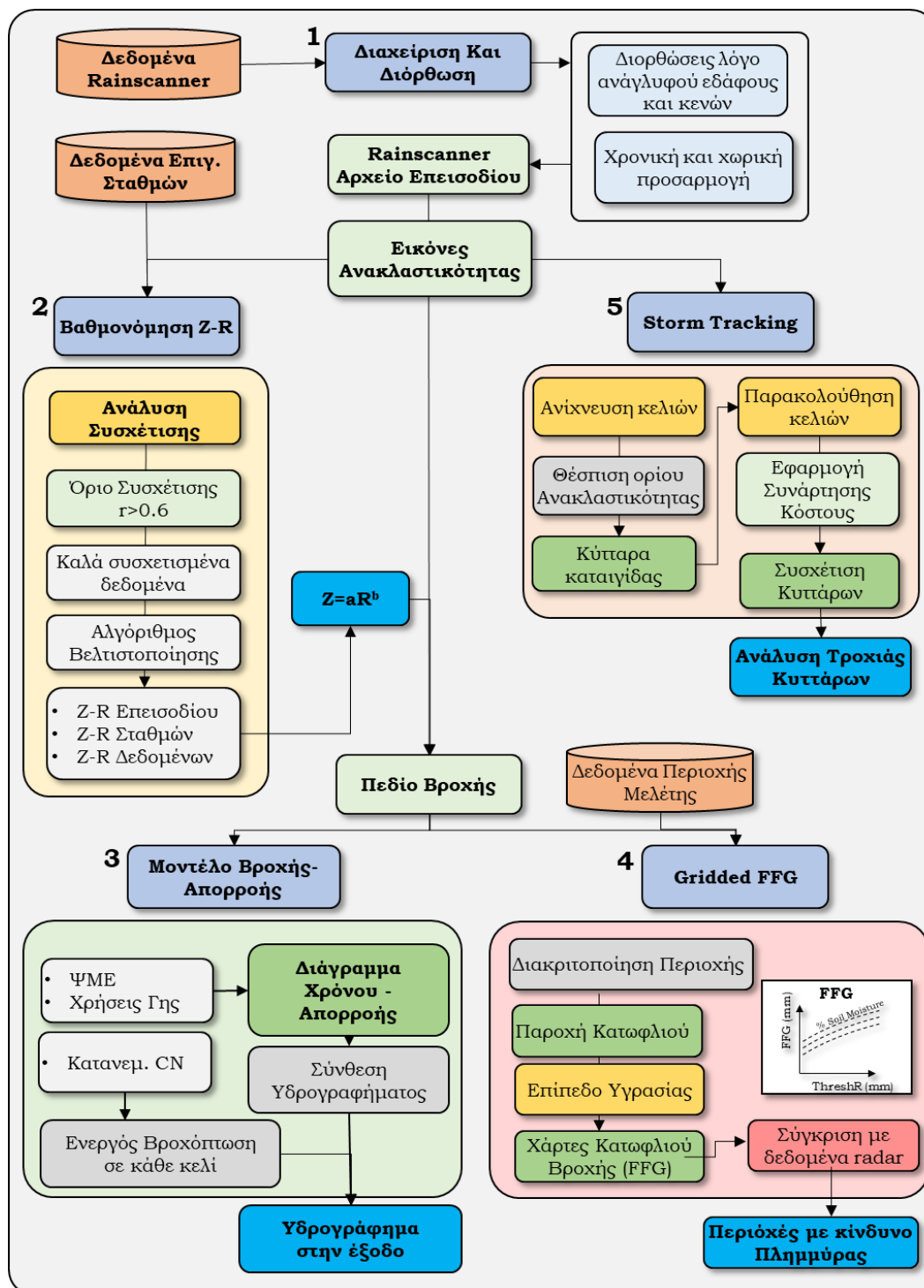
Σχήμα 3: Το μεθοδολογικό πλαίσιο

Παρακάτω παρουσιάζονται οι επιμέρους διαδικασίες κάθε υποσυστήματος.

1.   Η Διαχείριση και διόρθωση των μετεωρολογικών δεδομένων σχετίζεται τον έλεγχο ποιότητας, δηλαδή τις διορθώσεις στα ανεπεξέργαστα δεδομένα του ραντάρ για να αντιμετωπιστούν κυρίως τα προβλήματα που προκαλούνται στο σήμα από τις ανακλάσεις του ανάγλυφου του εδάφους και της διόρθωσης της εικόνας ραντάρ από κενά δεδομένων. Τα σφάλματα λόγω ανάγλυφου αναφέρονται σε ανεπιθύμητα

σήματα από αντικείμενα που δεν είναι βροχή, ενώ τα κενά μπορούν να εμφανιστούν από σημειακές αποκλίσεις τους σήματος ραντάρ λόγω στατικών και μη στατικών στόχων. Αυτές οι διορθώσεις περιλαμβάνουν αρχικά τον εντοπισμό των προβληματικών περιοχών, χρησιμοποιώντας παρατηρήσεις σε συνθήκες αίθριου καιρού, ενώ η διόρθωση των κενών πραγματοποιείται με την εφαρμογή κριτηρίων συμπλήρωσης, σύμφωνα με τις τιμές γειτονικών κελιών. Στη συνέχεια, εφαρμόζονται οι κατάλληλες χωρικές και χρονικές προσαρμογές για να εξασφαλιστούν οι επιθυμητές αναλύσεις. Τα επεξεργασμένα δεδομένα, αποθηκεύονται σε συγκεκριμένες μορφές αρχείων, ASCII, και ονομάζονται με βάση τη χρονική σήμανσή τους. Τέλος, στο στάδιο της μετά-επεξεργασίας πραγματοποιούνται περαιτέρω έλεγχοι για την αντιμετώπιση ακραίων τιμών καθώς και τη χρονική συνέπεια στο σύνολο των δεδομένων.

2. Η διαδικασία βαθμονόμησης της σχέσης Z-R σχετίζεται με την παραγωγή της σχέσης $Z=aR^b$, η οποία χρησιμοποιείται για τη μετατροπή της ανακλαστικότητας του ραντάρ (Z) σε ένταση βροχής (R) με χρήση των παραμέτρων *a* και *b*. Η βαθμονόμηση βασίζεται στη συσχέτιση των δεδομένων ραντάρ με τα δεδομένα επίγειων, μετά την ευθυγράμμιση της χωρικής και χρονικής ανάλυσης των δεδομένων σε αυτή των επίγειων βροχογράφων, καθώς αυτές λήφθηκαν ως "το πραγματικό ύψος βροχόπτωσης". Η ανάλυση της συσχέτισης γίνεται με τον υπολογισμό του συντελεστή συσχέτισης ρ, που χρησιμοποιείται για τον καθορισμό των καλά συσχετισμένων δεδομένων, δηλαδή αυτών με συντελεστή ρ άνω του 0.60, που χρησιμοποιούνται μετέπειτα στις διαδικασίες βαθμονόμησης. Έπειτα η βαθμονόμηση στοχεύει στον υπολογισμό και σχολιασμό των τιμών των παραμέτρων της Z-R, *α* και *b*, μέσω της ελαχιστοποίησης του τετραγωνικού σφάλματος (RMSE). Τρεις ομάδες βαθμονόμησης επικεντρώνονται στην παραγωγή σχέσεων βάσει σταθμών, συμβάντων και ολόκληρου συνόλου δεδομένων. Τα αποτελέσματα συγκρίνονται με καθιερωμένες εξισώσεις Z-R, αποκαλύπτοντας την χωροχρονική μεταβλητότητα και ενισχύοντας την κατανόηση των χαρακτηριστικών της βροχής.

3. Η διαδικασία του μοντέλου βροχής-απορροής σχετίζεται με την ανάπτυξη και εφαρμογής ενός κατανεμημένου μοντέλου βροχής-απορροής που θα κάνει χρήση των δεδομένων ραντάρ. Το μοντέλο βασίζεται στην τεχνική διαγράμματος χρόνου-απορροής, βασισμένη στο μοναδιαίο υδρογράφημα κατά Clark. Οι παράμετροι του μοντέλου υπολογίζονται μέσω του ΨΜΕ της περιοχής μελέτης και τεχνικών GIS. Η ενεργός βροχόπτωση υπολογίζεται χρησιμοποιώντας τη μέθοδο NRCS-Curve Number (CN), ενώ η απορροή διοδεύεται μέσω ενός συστήματος γραμμικού ταμιευτήρα. Για τον υπολογισμό των τιμών CN με βάση τις τρέχουσες συνθήκες υγρασίας του εδάφους χρησιμοποιείται μια γραμμική σχέση μεταξύ των ξηρών, μέσων και υγρών συνθηκών υγρασίας και του ποσοστού υγρασίας σε κάθε χρονική στιγμή. Το μοντέλο

εφαρμόστηκε στη ΛΑΠ Σαρανταπόταμου όπου επιλέχθηκε μια σειρά σχέσεων Z-R για να διερευνηθεί η επίδρασή τους στα χαρακτηριστικά του πλημμυρογραφήματος όπως ο χρόνος αιχμής, σε μια σειρά επεισοδίων βροχής.

4. Το σύστημα GFFG είναι ένα σύστημα προειδοποίησης έναντι αιφνίδιων πλημμυρών βασισμένο σε υπολογισμένα σε πραγματικό χρόνο όρια ύψους βροχής, δεδομένης διάρκειας, την τιμή FFG, η οποία υπό τις συγκεκριμένες υδρολογικές συνθήκες θα προκαλέσει μικρής έκτασης πλημμύρα. Το σύστημα συνδυάζει υδρολογικές και μετεωρολογικές διεργασίες για τον εντοπισμό περιοχών με κίνδυνο πλημμύρας για χρονικές προειδοποιήσεις έως 6 ώρες, και χρησιμοποιεί τρεις παραμέτρους: α) την παροχή κατωφλιού (threshold runoff), β) την κατάσταση υγρασίας του εδάφους (soil moisture condition) και γ) την αθροιστική βροχόπτωση δεδομένης διάρκειας. Η πρώτη παράμετρος, θεωρείται στατική και εξαρτάται από τα χαρακτηριστικά της λεκάνης απορροής ή στην συγκεκριμένη περίπτωση του Grid. Για τον υπολογισμό χρησιμοποιείται ένα μοντέλο βροχής απορροής με εφαρμογή βροχής ίσης με αυτής που προκύπτει για περίοδο επαναφοράς 5-ετών. Η δεύτερη είναι μια δυναμική μεταβλητή που επηρεάζει τις απώλειες βροχόπτωσης και εκτιμάται, είτε από εφαρμογή υδρολογικού μοντέλου, είτε από το ύψος βροχόπτωσης των τελευταίων ημερών. Τέλος, η τιμή FFG υπολογίζεται μέσω αντίστροφης διαδικασίας βροχής-απορροής, για μια δεδομένη απορροή κατωφλιού και συνθήκες υγρασίας του εδάφους. Έπειτα η τιμή αυτή συγκρίνεται με την τιμή της πρόγνωσης. Σε αυτήν την εφαρμογή, το GFFG εφαρμόζεται σε κατανεμημένη μορφή κλίμακας 500μ x 500μ, παράγοντας χάρτες FFG για τρεις τυπικές συνθήκες υγρασίας του εδάφους και διάρκειας βροχόπτωσης. Τέλος, το σύστημα εφαρμόζεται σε μια σειρά επεισοδίων χρησιμοποιώντας τα δεδομένα του Rainscanner, εντοπίζοντας τις περιοχές που είναι επιρρεπείς σε πλημμύρες.

5. Ο αλγόριθμος Storm tracking περιλαμβάνει δύο διαδικασίες, α) τον εντοπισμό των καταιγιδοφόρων κυττάρων και β) την παρακολούθηση των κυττάρων αυτών. Στη διαδικασία εντοπισμού των κυττάρων, χρησιμοποιούνται κατώφλια ανακλαστικότητας για τον καθορισμό των περιοχών που περιβάλουν το κύτταρο καθώς και τις συντεταγμένες του κέντρου του. Συγκεκριμένα, εξετάζονται κατώφλια από 25 dBZ έως 35 dBZ, για τον εντοπισμό κυττάρων με ελάχιστο εμβαδό 4 km². Επιπλέον χρησιμοποιείται εκτός του πολυγώνου και η εφαρμογή μιας έλλειψης, η οποία ως μαθηματικό μοντέλο εφαρμόζεται καλύτερα στις διαδικασίες παρακολούθησης. Η διαδικασία παρακολούθησης των κυττάρων χρησιμοποιεί διαδοχικές εικόνες και εφαρμόζει ένα μοντέλο σύναψης σχέσεων μεταξύ των κυττάρων. Συγκεκριμένα πραγματοποιείται μία διαδικασία βελτιστοποίησης του γραμμικού προβλήματος αντιστοίχισης κυττάρων του παρελθόντος με τωρινά κύτταρα, βάσει συγκεκριμένων χαρακτηριστικών τους, όπως το σχήμα, το εμβαδόν, και κυρίως την μεταξύ τους

ευκλείδεια απόσταση. Επιπλέον, λαμβάνονται υπόψη και οι διαδικασίες συγχώνευσης και διαίρεσης των κυττάρων. Ο αλγόριθμος εφαρμόζεται σε μια σειρά επεισοδίων βροχής για να καθοριστεί η δυνατότητά του να ανιχνεύει και να καταγράφει κύτταρα σε διάφορες χρονικές κλίμακες, όπως η παρακολούθηση πεδίων ανακλαστικότητας 10-λεπτών. Τέλος, ο αλγόριθμος εφαρμόζεται και για κύτταρα υψηλής ανακλαστικότητας, άνω των 35 dBZ, σε πολλαπλά επεισόδια βροχής και διερευνώνται τα χαρακτηριστικά των καταιγιδοφόρων νεφών στην Αττική.

Αποτελέσματα και Συζήτηση

Βαθμονόμηση Z-R

Σε αυτήν την ενότητα πραγματοποιείται μια σφαιρική ανάλυση και βαθμονόμησης της σχέσης Z-R για τη βελτίωση της ακρίβειας της εκτίμησης της βροχής μέσω ραντάρ. Η διαδικασία αποτελείται από δύο κύρια στάδια, την ανάλυση συσχέτισης των δεδομένων και τη διαδικασία βαθμονόμησης της σχέσης Z-R. Στόχος είναι μέσω της συσχέτισης των δεδομένων των επίγειων σταθμών και του μετεωρολογικού ραντάρ, να προκύψουν πολλαπλές σχέσεις Z-R και να αναλυθούν τα χαρακτηριστικά τους για κάθε περίπτωση.

Η ανάλυση της συσχέτισης βασίζεται στον υπολογισμό του συντελεστή συσχέτισης Pearson ρ. Οι υπολογισμοί αρχικά πραγματοποιούνται σε επίπεδο σταθμού, δηλαδή υπολογίζεται ένας συντελεστής συσχέτισης για κάθε σταθμό ανά συμβάν. Στο Σχήμα 4 παρουσιάζεται ο αριθμός των συμβάντων ανά σταθμό, από τα 13 επεισόδια που χρησιμοποιήθηκαν, όπου ο συντελεστής συσχέτισης ήταν άνω του ορίου, ενώ στο Σχήμα 5 εμφανίζεται η μέση τιμή συσχέτισης ανά σταθμό, πρώτον όταν χρησιμοποιούνται όλα τα συμβάντα και δεύτερον όταν χρησιμοποιούνται μόνο τα καλά συσχετισμένα δεδομένα, δηλαδή συσχέτιση άνω του 0.6.

 Η ανάλυση των σταθμών με κακή συσχέτιση σε σχέση με τη θέση τους στην περιοχή της μελέτης αποκαλύπτει αρκετά μοτίβα. Οι σταθμοί που βρίσκονται κοντά ή εντός περιοχών με θόρυβο, ειδικά στα βορειοανατολικά του Rainscanner, εμφανίζουν συνεχώς χαμηλές συσχετίσεις, κάτω από 0.6, και περιορισμένο αριθμό συμβάντων με καλή συσχέτιση.
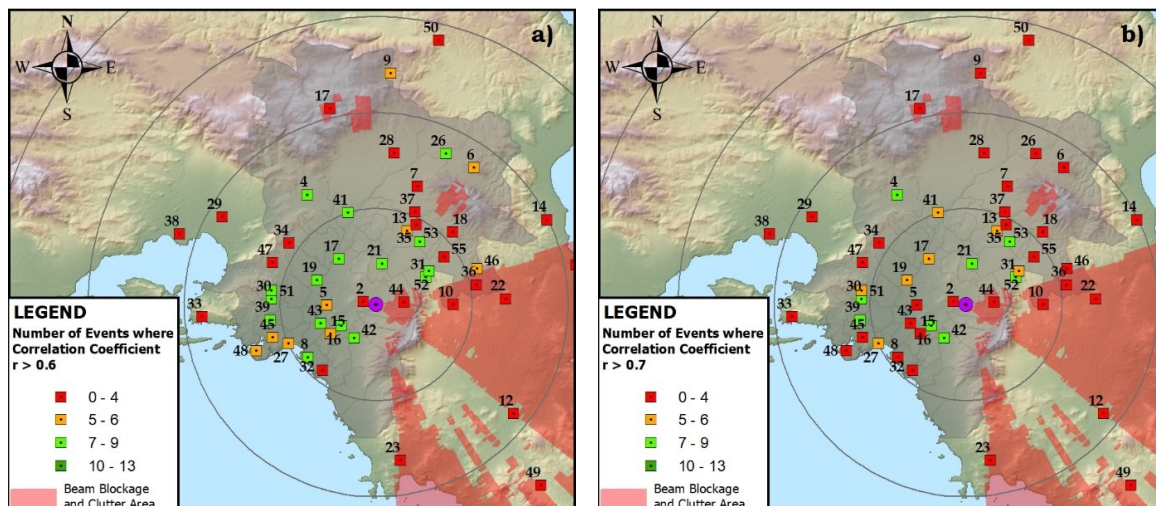
Σχήμα 4: Ο αριθμός των συμβάντων με συντελεστή συσχέτισης μεταξύ του Rainscanner και των επίγειων σταθμών να είναι υψηλότερος από (α) 0,6 και (β) 0,7. Πηγή: (Bournas και Baltas 2022α)
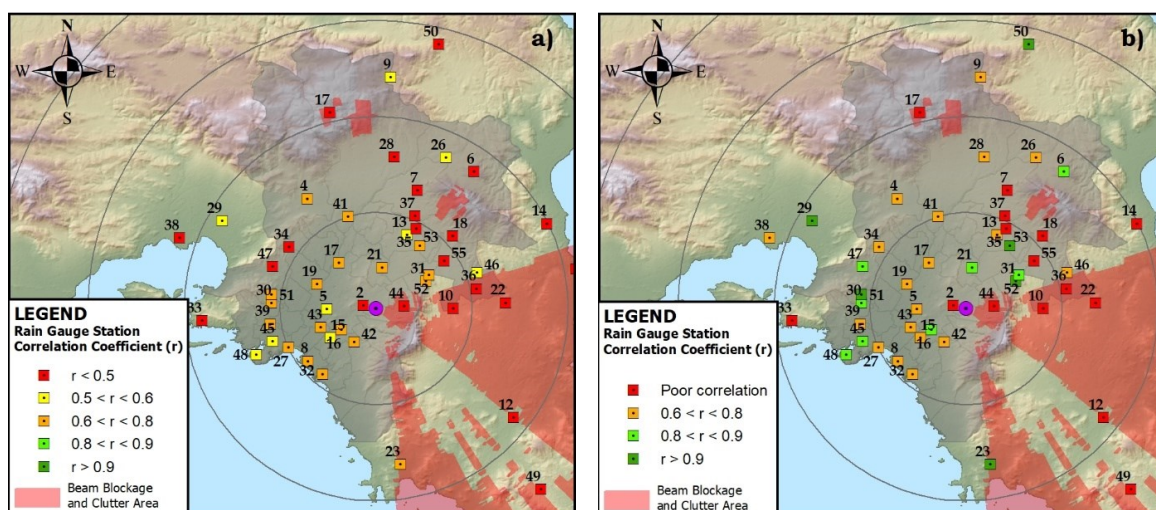
Σχήμα 5: Ο μέσος συντελεστής συσχέτισης μεταξύ του Rainscanner και των επίγειων σταθμών για (α) όλα τα διαθέσιμα συμβάντα και (β) χρησιμοποιώντας τα συμβάντα που εμφάνισαν συσχέτιση άνω του 0.6 σε κάθε σταθμό. Πηγή: (Bournas και Baltas 2022α)

Οι σταθμοί εντός ακτίνας 10 km από το Rainscanner εμφανίζουν γενικά πολλά συμβάντα με καλή συσχέτιση, εκτός από τον σταθμό Αμπελόκηποι (ID 2), ο οποίος αποτελεί εξαίρεση. Οι σταθμοί που βρίσκονται στο παραλιακό μέτωπο παρουσιάζουν μείωση στα καλώς συσχετισμένα συμβάντα όταν εφαρμόζεται ένα υψηλότερο κατώφλι. Για παράδειγμα, ο σταθμός Φάληρο (ID 8) από επτά καλά συσχετισμένα συμβάντα με κατώφλι 0.6, έχει καλή συσχέτιση σε μόλις τέσσερα όταν το κατώφλι είναι 0.7. Αυτή η τάση δεν είναι αποκλειστική μόνο για της παράκτιες περιοχές, καθώς και ο σταθμός Διονύσου (ID 6) στη βορειοανατολική περιοχή εμφανίζει παρόμοια

συμπεριφορά. Μετά τον έλεγχο διαφόρων κατωφλίων, το κατώφλι 0.6 θεωρήθηκε βέλτιστο καθώς φιλτράρει αρκετά καλά τις κακές συσχετίσεις, ενώ διατηρεί επαρκή δεδομένα για τη βαθμονόμηση. Τέλος, είναι σημαντικό να σημειωθεί ότι ορισμένοι σταθμοί παρουσιάζουν υψηλές συσχετίσεις μόνο σε ένα περιορισμένο αριθμό συμβάντων. Αυτή η συμπεριφορά συσχετίζεται με τα χαρακτηριστικά τις καταιγίδας όπως το ύψος βροχής, την έντασή της. Επιπλέον, οι χαμηλές συσχετίσεις μπορεί να μην οφείλονται μόνο σε σφάλματα του Rainscanner, αλλά μπορούν να υποδηλώνουν συστηματικά σφάλματα σε συγκεκριμένους σταθμούς ραντάρ. Τέτοιες διερευνήσεις απαιτούν επιπλέον δεδομένα και ήταν εκτός πεδίου ανάλυσης της εν λόγω Δ.Δ..

Μετά την ανάλυση συσχέτισης, πραγματοποιείται το στάδιο της βαθμονόμηση της σχέσης Z-R. Χρησιμοποιούνται τρεις ομάδες βαθμονόμησης, αυτή που αφορά στα επεισόδια βροχής, αυτή που αφορά στους σταθμούς και αυτή που αφορά στο σύνολο των δεδομένων. Ο σχολιασμός των αποτελεσμάτων γίνεται στη βάση των τιμών των παραμέτρων *a* και *b*. Συγκεκριμένα βάσει βιβλιογραφίας, τιμές της παραμέτρου *a* που κυμαίνονται από 50 έως 250 εφαρμόζονται για στρατόμορφα συστήματα (stratiform) ενώ τιμές από 300 έως 500 είναι κατάλληλες για μεταγωγικού τύπου (convective-based) επεισόδια βροχής. Οι convective τύπου βροχές χαρακτηρίζονται από μεγάλης έντασης βροχόπτωση και μικρή χωρική κλίμακα, σε αντίθεση με τα stratiform συστήματα που αφορούν νέφη με μεγάλη χωρική κλίμακα και ήπια χαρακτηριστικά βροχής. Οι convective τύπου καταιγίδες συμβαίνουν κυρίως το καλοκαίρι, καθώς οφείλονται στη βίαιη ανύψωση νερού λόγω θερμοκρασιακής διαφοράς, ενώ οι stratiform είναι τυπικά συστήματα των χειμερινών μηνών. Τέλος τιμές της παραμέτρου *a* μεγαλύτερες του 1000 συναντώνται σε επεισόδια χιονιού.

Τα αποτελέσματα από τη βαθμονόμηση της σχέσης Z-R για κάθε ομάδα εμφανίζονται παρακάτω:

Βαθμονόμηση σε επίπεδο επεισοδίου βροχής

Η βαθμονόμηση σε επίπεδο επεισοδίου βροχής αποσκοπεί στο να αναδείξει τη μεταβλητότητα της σχέσης Z-R μεταξύ διαφορετικών επεισοδίων βροχής. Οι παράμετροι που προκύπτουν μπορούν να χρησιμοποιηθούν για να αξιολογηθεί η κατάταξη της κάθε καταιγίδας σύμφωνα με τα ως άνω αναφερθέντα. Διεξήχθησαν δύο βελτιστοποιήσεις, μία όπου και οι δύο παράμετροι βελτιστοποιούνται και μία όπου η παράμετρος b ορίζεται σταθερή στην τιμή 1.60 και βελτιστοποιείται μόνο η παράμετρος α. Και οι δύο βελτιστοποιήσεις οδήγησαν σε υψηλή μεταβλητότητα των τιμών των παραμέτρων σε κάθε περίπτωση. Σε τρεις περιπτώσεις, η παράμετρος α υπολογίστηκε σε τιμές άνω του 1000, οι οποίες συνδέονται με επεισόδια χιονόπτωσης. Ελέγχοντας τα τρία αυτά επεισόδια με πληροφορίες καιρού, επιβεβαιώθηκε πως αποτελούσαν επεισόδια χιονόπτωσης και άρα αναδεικνύεται η αξία της βαθμονόμησης σε επίπεδο

επεισοδίων βροχής. Συγκεκριμένα, επειδή τα επεισόδια χιονιού απαρτίζονται από διαφορετικά χαρακτηριστικά από ότι αυτά της βροχόπτωσης, επηρεάζονται αρνητικά οι παράμετροι της σχέσης Z-R και άρα επιβάλλεται η αφαίρεση των επεισοδίων αυτών από μετέπειτα βαθμονομήσεις, π.χ. βαθμονομήσεις σε επίπεδο σταθμών.

Βαθμονόμηση σε επίπεδο επίγειου σταθμού

Σε αυτήν την προσέγγιση, οι σχέσεις Z-R βαθμονομούνται για κάθε μεμονωμένο σταθμό, χρησιμοποιώντας πολλαπλά επεισόδια, μετά την αφαίρεση των επεισοδίων χιονιού. Τα αποτελέσματα παρουσιάζονται στο Σχήμα 6, όπου δεξιά και αριστερά παρουσιάζεται η χωρική μεταβλητότητα των τιμών των παραμέτρων *a* και *b* αντίστοιχα. Επιπλέον, στο Σχήμα 7, παρουσιάζεται η χωρική μεταβλητότητα της παραμέτρου *a* όταν η παράμετρος *b* ορίζεται σε μια σταθερή τιμή.
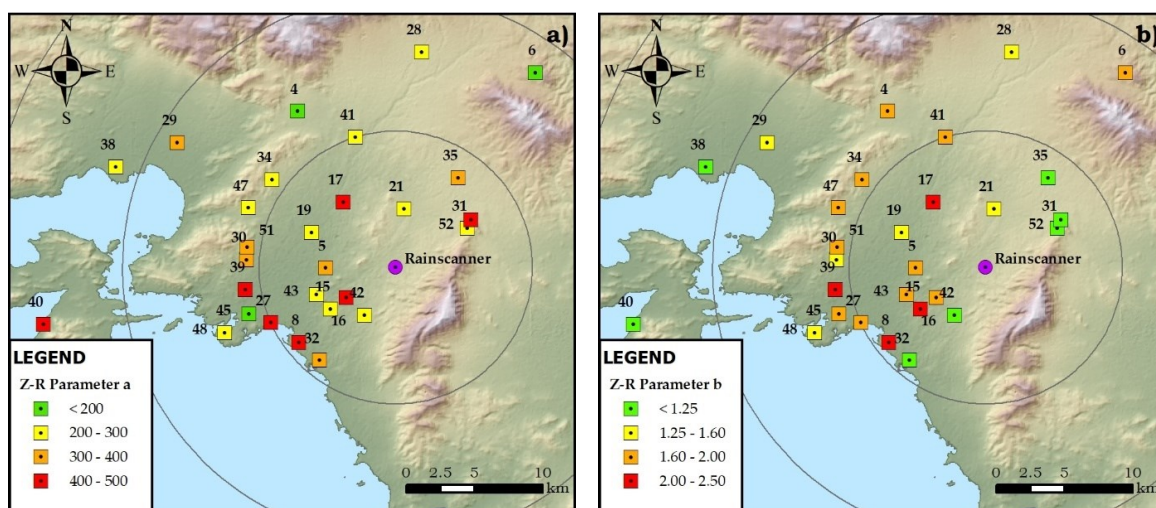
Σχήμα 6: Χωρική συσχέτιση των παραμέτρων Z-R, a) παράμετρος a, b) παράμετρος b,
Πηγή: (Bournas and Baltas 2022a)

Όπως φαίνεται στο πάνελ a του Σχήματος 6, οι υψηλές τιμές της παραμέτρου *a* εντοπίζονται στο νοτιοδυτικό μέρος, στο παράλιο μέτωπο της Αθήνας, ενώ οι χαμηλότερες τιμές στο βόρειο τμήμα. Όπως αναφέρθηκε, υψηλή τιμή της παραμέτρου *a* και αντίστοιχα χαμηλή τιμή της παραμέτρου b εμφανίζονται σε σχέσεις Z-R που είναι πιο κατάλληλες για convective επεισόδια. Δεδομένου ότι το δείγμα περιλαμβάνει τόσο convective όσο και stratiform επεισόδια, αυτό το αποτέλεσμα υποδεικνύει ότι η υψηλότερη ανακλαστικότητα συναντάται στο παράλιο μέτωπο και λιγότερο στο βορειοανατολικό τμήμα της περιοχής μελέτης. Η διαφοροποίηση αυτή μπορεί να σχετίζεται και με την τυπική τροχιά των καταιγίδων στην Αθήνα, καθώς οι καταιγίδες στην Αθήνα τείνουν να έχουν διεύθυνση από τα δυτικά προς ανατολικά. Συγκεκριμένα το κέντρο των καταιγίδων περνάει πάνω από τον κόλπο της Σαλαμίνας όπου

l

τροφοδοτείται από το νερό της θάλασσας, και οδηγείται προς το όρος Αιγάλεω και την περιοχή του Πειραιά. Η εκφόρτωση της μεγαλύτερης ποσότητας νερού, δηλαδή η βροχόπτωση, συμβαίνει απότομα πρώτα στις παράκτιες περιοχές, μιμούμενη τα χαρακτηριστικά convective καταιγίδων. Έπειτα, η καταιγίδα συνεχίζει να εκφορτώνεται με κατεύθυνση προς τα ανατολικά μέχρι να φτάσει στο κέντρο της Αθήνας. Εκεί τελικά κατευθύνεται προς τα βορειοανατολικά ή στα ανατολικά λόγω της παρουσίας του όρους Υμηττός. Όταν φτάνει σε τοποθεσίες με υψηλό υψόμετρο, η ένταση της βροχόπτωσης έχει μειωθεί, και έτσι στις περιοχές αυτές παρατηρούνται βροχοπτώσεις με χαρακτηριστικά stratiform, δηλαδή μέτριας έντασης μεγάλης διάρκειας.
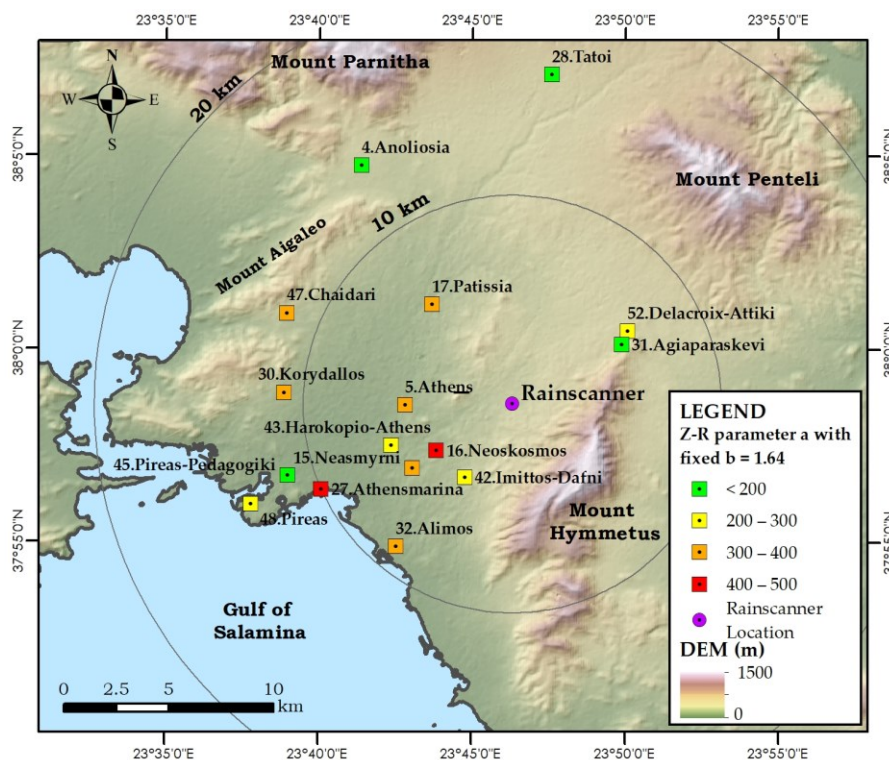
Σχήμα 7: Χωρική συσχέτιση της παραμέτρου a της σχέσης Z-R όταν η παράμετρος b είναι σταθερή Πηγή: (Bournas and Baltas 2022a)

Βαθμονόμηση ενιαίας σχέσης Z-R

Σε αυτή τη βαθμονόμηση, σκοπός είναι η ανάδειξη μίας ενοποιημένης σχέσης Z-R χρησιμοποιώντας το σύνολο των συσχετισμένων δεδομένων. Εξετάζονται δύο προσεγγίσεις: μία χρησιμοποιώντας όλα τα διαθέσιμα δεδομένα και μια άλλη χρησιμοποιώντας ένα σχήμα βελτιστοποίησης/επαλήθευσης. Στην πρώτη περίπτωση η σχέση που εξάγεται είναι η $Z=300R^{1.69}$, ενώ στην δεύτερη η $Z=321R^{1.53}$. Η επαλήθευση της δεύτερης σχέσης σε σταθμούς που δεν συμμετείχαν στην βαθμονόμηση δείχνει μικρές αποκλίσεις τόσο στο συντελεστή συσχέτισης όσο και στο σφάλμα RMSE σε

επίπεδο σταθμού, και άρα θεωρείται και πιο αξιόπιστη σε σχέση με την πρώτη προσέγγιση.

Οι παραγόμενες σχέσεις Z-R συγκρίνονται στη συνέχεια με βιβλιογραφικές σχέσεις. Αρχικά, η σύγκριση γίνεται με βάση τις χρονοσειρές βροχόπτωσης και αθροιστικής βροχόπτωσης ανά σταθμό. Στο Σχήμα 8 παρουσιάζεται ένα παράδειγμα για τον σταθμό, Ψυχικό, και το επεισόδιο Ε6. Οι μπλε μπάρες υποδεικνύουν τις μετρήσεις του βροχόμετρου, ενώ οι μετρήσεις του Rainscanner παρουσιάζονται με γραμμές σε διάφορα χρώματα, με βάση τη σχέση Z-R που χρησιμοποιήθηκε. Συγκεκριμένα, με πράσινο χρώμα, η εξίσωση Marshal και Palmar, $Z=200R^{1.6}$, με κόκκινο χρώμα η εξίσωση βαθμονόμησης όλων των δεδομένων, $Z=321R^{1.53}$, με μωβ χρώμα η εξίσωση Z-R βασισμένη στο επεισόδιο βροχής, με μαύρο χρώμα η εξίσωση που υπολογίσθηκε για τον σταθμό και με μπλε χρώμα η βελτιστοποιημένη σχέση (optimum), όταν χρησιμοποιείται το σύνολο δεδομένων του σταθμού μόνο για το συγκεκριμένο επεισόδιο βροχής. Το αποτέλεσμα που ταιριάζει καλύτερα σε κάθε γράφημα είναι η τελευταία επιλογή από τις παραπάνω, αφού οι παράμετροι Z-R βελτιστοποιούνται για να ταιριάζουν με τα συγκεκριμένα δεδομένα.

Σε όλα τα σχήματα, η εξίσωση Marshal και Palmer δείχνει τις μεγαλύτερες αποκλίσεις. Συγκεκριμένα, η σχέση οδηγεί σε υπερεκτίμηση της βροχόπτωσης σε σύγκριση με τα δεδομένα του βροχογράφου. Η εξίσωση που είναι πιο κοντά στη βελτιστοποιημένη σχέση είναι αυτή που βασίζεται στον σταθμό, και ακολουθούν οι εξισώσεις που βασίζονται στο σύνολο των δεδομένων και για το συγκεκριμένο επεισόδιο. Στο Σχήμα 8, παρατηρείται ότι ενώ η βελτιστοποιημένη σχέση (optimized) φαίνεται να δείχνει την καλύτερη προσαρμογή σε κάθε 10λεπτο ύψος βροχόπτωσης, η τιμή της αθροιστική βροχόπτωσης δεν παρουσιάζει το καλύτερο αποτέλεσμα σε σύγκριση με τις άλλες σχέσεις. Αυτό οφείλεται στην έλλειψη δεδομένων του Rainscanner στις 02:00, όπου δεν καταγράφονται δεδομένα, διαταράσσοντας το γράφημα αθροιστικής βροχόπτωσης.

Τέλος, στα διαγράμματα του σχήματος 9, παρουσιάζονται οι δείκτες RMSE, BIAS, Normalized Mean Absolute Error (NMAE) και Normalized Mean Bias (NMB) μεταξύ των μετρήσεων του βροχογράφων και των υψών βροχόπτωσης που εκτιμήθηκαν μέσω κάθε σχέσης Z-R.

Όπως φαίνεται στο Σχήμα 9, τα καλύτερα αποτελέσματα σε όλους τους δείκτες τα παρουσιάζει το σύνολο των δεδομένων που απαρτίζουν τις βέλτιστες λύσεις (optimum), δηλαδή τις Z-R που προκύπτουν για κάθε σταθμό ανά γεγονός. Όλοι οι δείκτες έχουν ως βέλτιστη τιμή την μηδενική τιμή, ενώ οι δείκτες BIAS και NMAE έχουν και αρνητικές τιμές, αναδεικνύοντας την υποεκτίμηση ή υπερεκτίμηση της βροχής από το Rainscanner. Επιπλέον, εκτός από τις τιμές των δεικτών, και συγκεκριμένα την τιμή της διαμέσου, που απεικονίζεται με την κόκκινη γραμμή και πρέπει να προσεγγίζει την

μηδενική τιμή, εξετάζεται επίσης και η διασπορά του δείγματος, όπου η μικρότερη διασπορά είναι και η βέλτιστη.
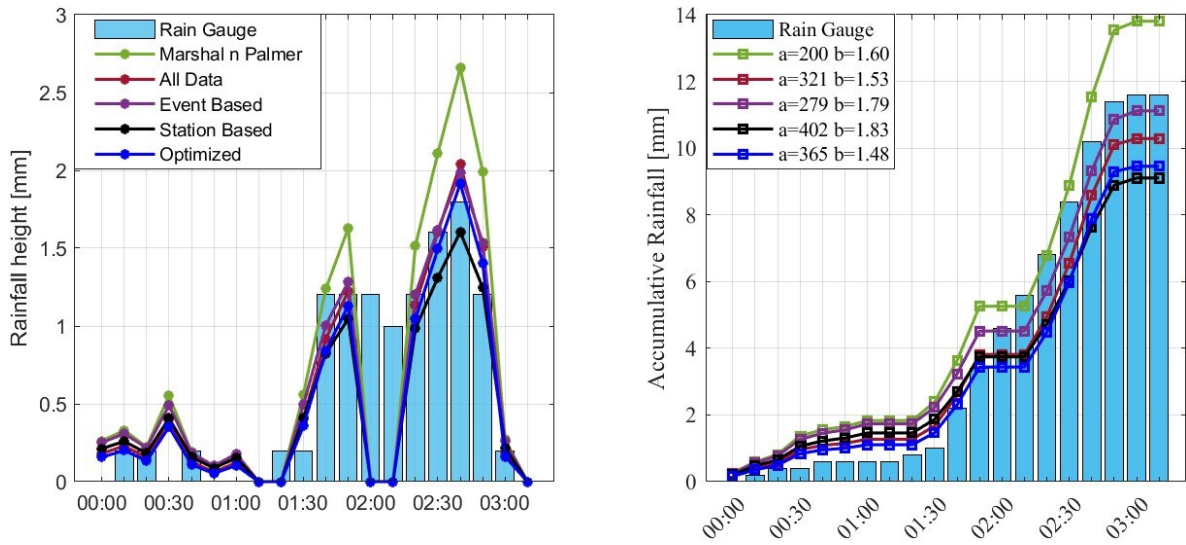
Σχήμα 8: Ύψος βροχής (αριστερά) και αθροιστική βροχόπτωση (δεξιά) για τον σταθμό Ψυχικό, στο επεισόδιο Ε6.
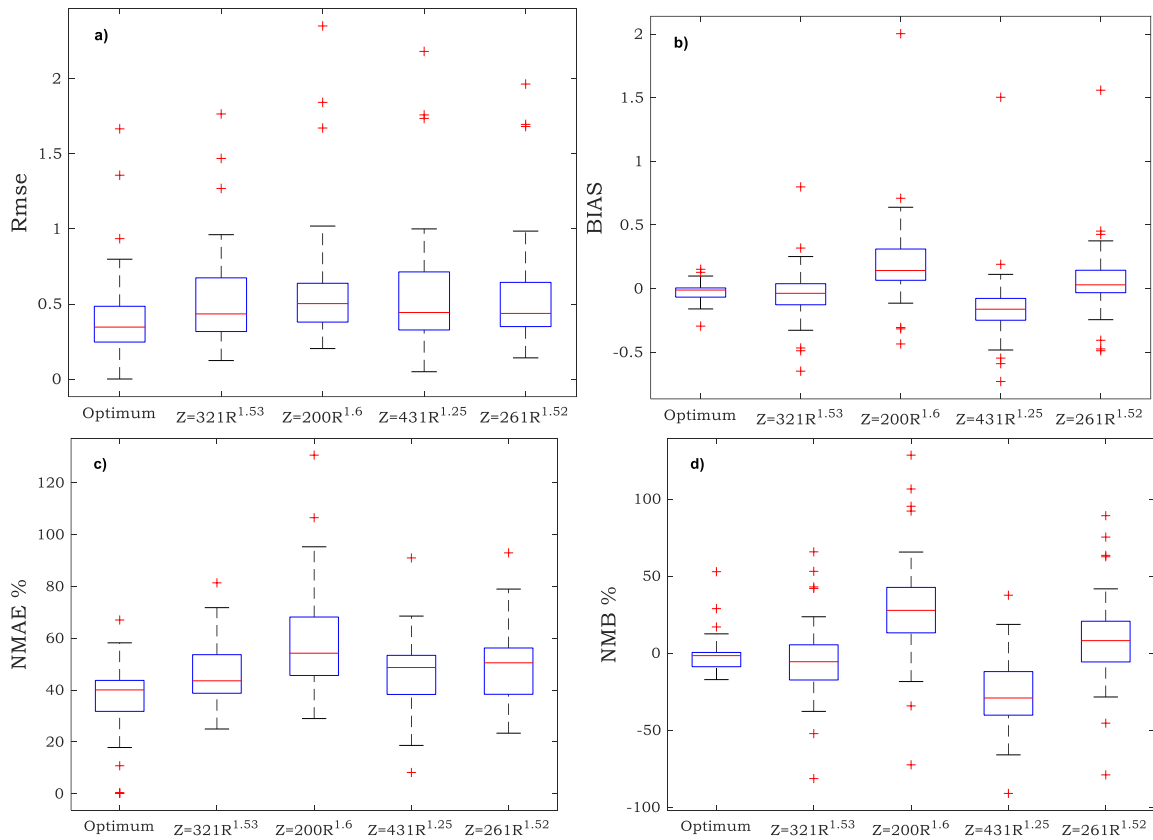
Σχήμα 9: Boxplots των a) RMSE, b) Bias, c) NMAE, and d) NMB για κάθε σχέση Z-R

Ανάμεσα στις αξιολογημένες σχέσεις Z-R, αυτή που βασίζεται σε όλα τα δεδομένα, $Z=321R^{1.53}$, είναι η καλύτερη, ακολουθούμενη από τις $Z=261R^{1.52}$ και $Z=431R^{1.25}$, ενώ η $Z=200R^{1.6}$ της Marshal και Palmer δίνει τα χειρότερα αποτελέσματα σε όλες τις μετρικές. Η σχέση Marshal και Palmer λόγω της μεγάλης απόκλισης της διαμέσου, από αυτή της βέλτιστης, καθώς και τη μεγάλη τυπική απόκλιση, όπως αναδεικνύεται από το μεγάλο εύρος μεταξύ του άνω και κάτω τεταρτημόριου, φαίνεται πως δεν ενδείκνυται για το σύνολο των σταθμών. Παρόλο που η $Z=431R^{1.25}$ παρουσιάζει θετικά αποτελέσματα, η αρνητική τιμή NMB υποδεικνύει υποεκτίμηση της βροχόπτωσης, και άρα κρίνεται, κατάλληλη κυρίως μόνο για επεισόδια υψηλής ανακλαστικότητας.

Μοντέλο Βροχής - Απορροής

Το μοντέλο βροχής-απορροής αναπτύχθηκε και εφαρμόζεται στο μη αστικό τμήμα της ΛΑΠ Σαρανταπόταμου, με έξοδο το σημείο διασταύρωσης του ποταμού με τον αυτοκινητόδρομο της Αττικής Οδού συνολικής έκτασης 231,50 km². Το διάγραμμα χρόνου-απορροής προκύπτει στο εφαρμογή ΣΓΠ, χρησιμοποιώντας μέγεθος κελιού 500 μ x 500 μ με βάση το μέγεθος της λεκάνης απορροής. Η κατανεμημένη αυτή μορφή οδηγεί σε συνολικά 1021 κελιά. Στο Σχήμα 10 παρουσιάζονται οι κλίσεις των κελιών και οι τιμές CN AMC-II, ενώ στο Σχήμα 11 παρουσιάζεται το διάγραμμα χρόνου-επιφάνειας της ΛΑΠ Σαρανταπόταμου. Το μοντέλο βροχής-απορροής εφαρμόζεται στη συνέχεια σε έξι επεισόδια βροχής, που παρουσιάζονται στον πίνακα 2. Ο πίνακας 2 επιπλέον περιλαμβάνει τη διάρκεια του γεγονότος, καθώς και την αθροιστική βροχόπτωση των προηγούμενων πέντε ημερών, προκειμένου να αξιολογηθούν οι συνθήκες υγρασίας του εδάφους την ημέρα του γεγονότος.

Πίνακας 2: Προσομοιωμένα επεισόδια και κύρια χαρακτηριστικά.
Πηγή: (Bournas and Baltas 2022b)

Επεισόδιο	Αρχή Ημερομηνία	Τέλος Ημερομηνία	Διάρκεια (h)	5-Day API (mm)	Μέση επιφανειακή βροχόπτωση (mm)
6	17-12-2018 23:40	18-12-2018 13:50	14.2	13.8	25.8
21	24-11-2019 21:40	25-11-2019 08:30	10.8	37.0	30.4
31	01-06-2020 14:00	01-06-2020 20:00	6.0	0.0	20.5
48	09-06-2021 18:00	10-06-2021 02:44	8.7	0.2	25.0
50	12-06-2021 11:50	12-06-2021 19:00	7.2	32.0	26.0
61	23-11-2021 17:30	24-11-2021 07:40	14.2	2.6	26.4

Σχήμα 10: Κατανεμημένα δεδομένα; a) Κλίσεις %, b) Curve Number για AMC-II συνθήκες
Πηγή: (Bournas and Baltas 2022b)
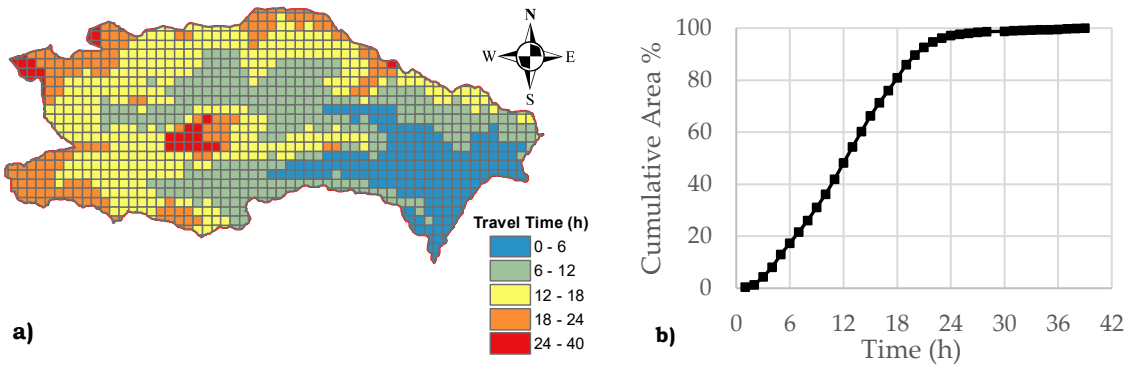
Σχήμα 11: Διάγραμμα χρόνου-επιφάνειας: a) Χρόνος απορροής; b) Ποσοστό αθροιστικής
απορροής ανά ώρα έως στην έξοδο της λεκάνης. Πηγή: (Bournas and Baltas 2022b)

Από τα προσομοιωμένα επεισόδια βροχής, τα επεισόδια 31, 48 και 50 είχαν χαρακτηριστικά που βασίζονταν σε convective βροχόπτωση, δηλαδή σε αυξημένης έντασης βροχή με μικρή χωρική κλίμακα. Ενώ στα επεισόδια με stratiform βροχόπτωση η επιλογή της σχέσης Z-R έδειξε μικρές διαφορές, στα επεισόδια convective, μια σχέση Z-R, Z=275$^{1.05}$, η οποία υπολογίστηκε για τον σταθμό Ελευσίνα, οδήγησε σε μη λογικές τιμές βροχόπτωσης, όπως φαίνεται από το γεγονός ότι η περίοδος επαναφοράς της βροχής σε αυτές τις περιπτώσεις υπολογίστηκε σε πάνω από 100 χρόνια, ενώ οι υπόλοιπες σχέσεις Z-R εκτίμησαν περίοδο επαναφοράς 10-20 χρόνια. Αυτό το αποτέλεσμα δείχνει ότι πρέπει να χρησιμοποιείται με προσοχή η σχέση Z-R, και ειδικά σε επεισόδια βροχής με μεγάλες τιμές ανακλαστικότητας και έντασης. Επιπλέον, μεταξύ των χρησιμοποιημένων σχέσεων, φαίνεται ότι η σχέση Marshal και Palmer οδηγεί στη μεγαλύτερη παροχή αιχμής. Αντίθετα, οι σχέσεις Z-R που βασίζονται σε convective επεισόδια εμφανίζουν την μικρότερη αιχμή στα stratiform επεισόδια βροχόπτωσης και τη μεγαλύτερη στα convective επεισόδια. Αυτό το αποτέλεσμα δείχνει

ότι μια σχέση που βασίζεται σε convective επεισόδια είναι προτιμότερη για χρήση αποκλειστικά σε τέτοιου τύπου επεισόδια, δηλαδή σε επεισόδια όπου παρατηρείται υψηλή ένταση βροχής, καθώς σε stratiform επεισόδια, και σε μέτριας έντασης βροχής, η υποεκτίμηση της παροχής είναι δεδομένη.
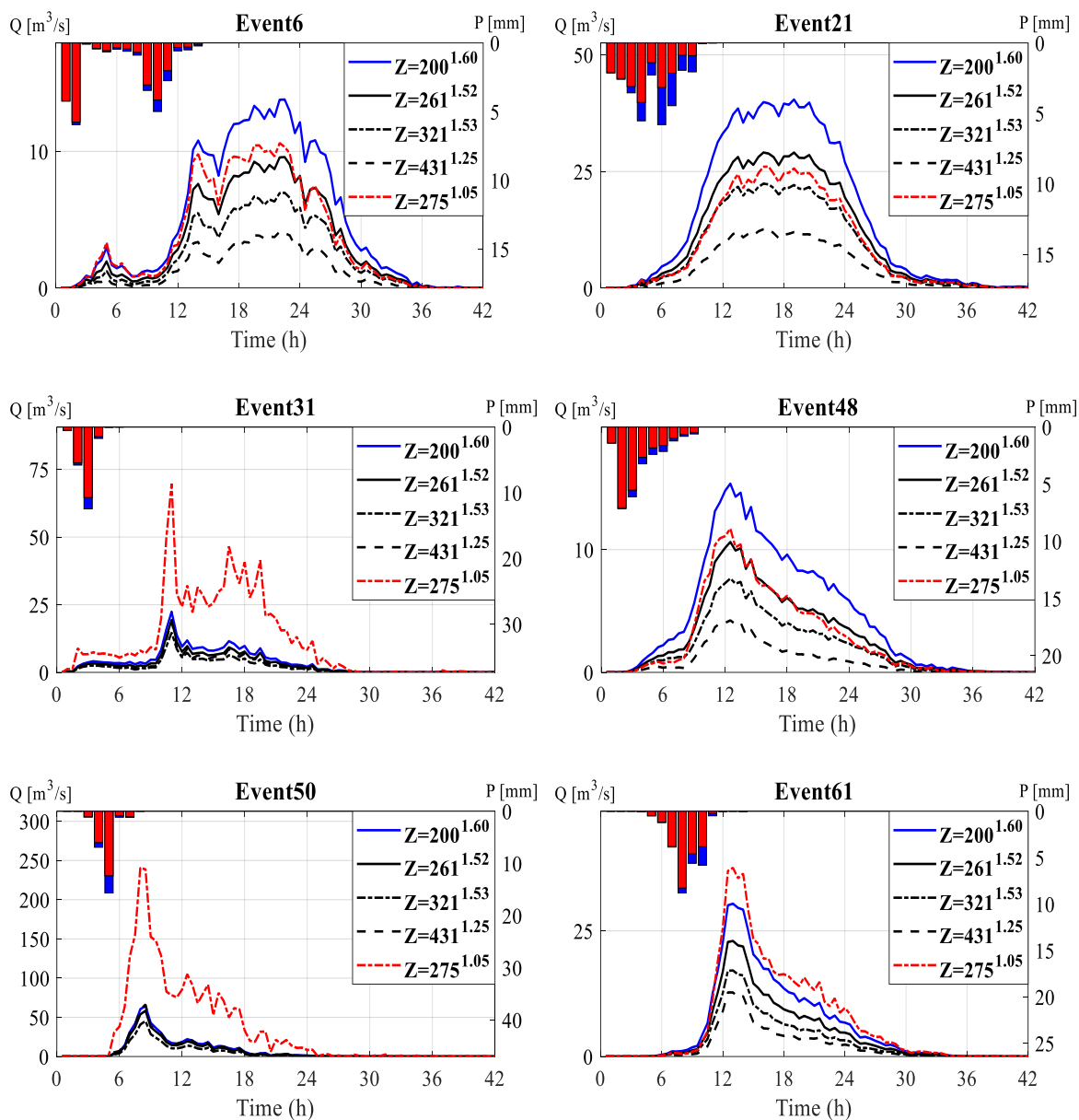
Σχήμα 12: Υδρογραφήματα για διαφορετικές σχέσεις Z-R ανά επεισόδιο βροχής. Οι μπλε και κόκκινοι ράβδοι υποδηλώνουν τη μέση επιφανειακή βροχόπτωση και τις απώλειες, αντίστοιχα. Πηγή:(Bournas and Baltas 2022b)

Gridded Flash Flood Guidance

Το GFFG εφαρμόζεται σε δύο περιοχές, στη ΛΑΠ Σαρανταπόταμου και στο σύνολο της περιφέρειας Αττικής. Αρχικά, παρουσιάζονται οι χάρτες που αποτυπώνουν το κατώφλι βροχής και αναλύονται τα αποτελέσματα. Στη συνέχεια, το σύστημα εφαρμόζεται σε μια σειρά επεισοδίων βροχής, προκειμένου να εξαχθεί ο δυνητικός κίνδυνος πλημμύρας σε κάθε περίπτωση.

Στο Σχήμα 13 παρουσιάζονται οι χάρτες που απεικονίζουν το κατώφλι βροχής για τα τρία χρονικά διαστήματα αθροιστικής βροχόπτωσης, 1, 3 και 6 ώρες, για μέτριες συνθήκες υγρασίας του εδάφους, ενώ στο Σχήμα 14 παρουσιάζεται το κατώφλι για δύο διαφορετικές συνθήκες υγρασίας του εδάφους, μέτριες και κορεσμένες συνθήκες. Σε κάθε περίπτωση, εάν οι πραγματικές τιμές της υγρασίας του εδάφους ταιριάζουν με τις προαναφερθείσες τιμές, τότε το κατώφλι αποτελεί την τιμή FFG που χρησιμοποιείται για σύγκριση με τους προγνωστικούς χάρτες βροχόπτωσης.
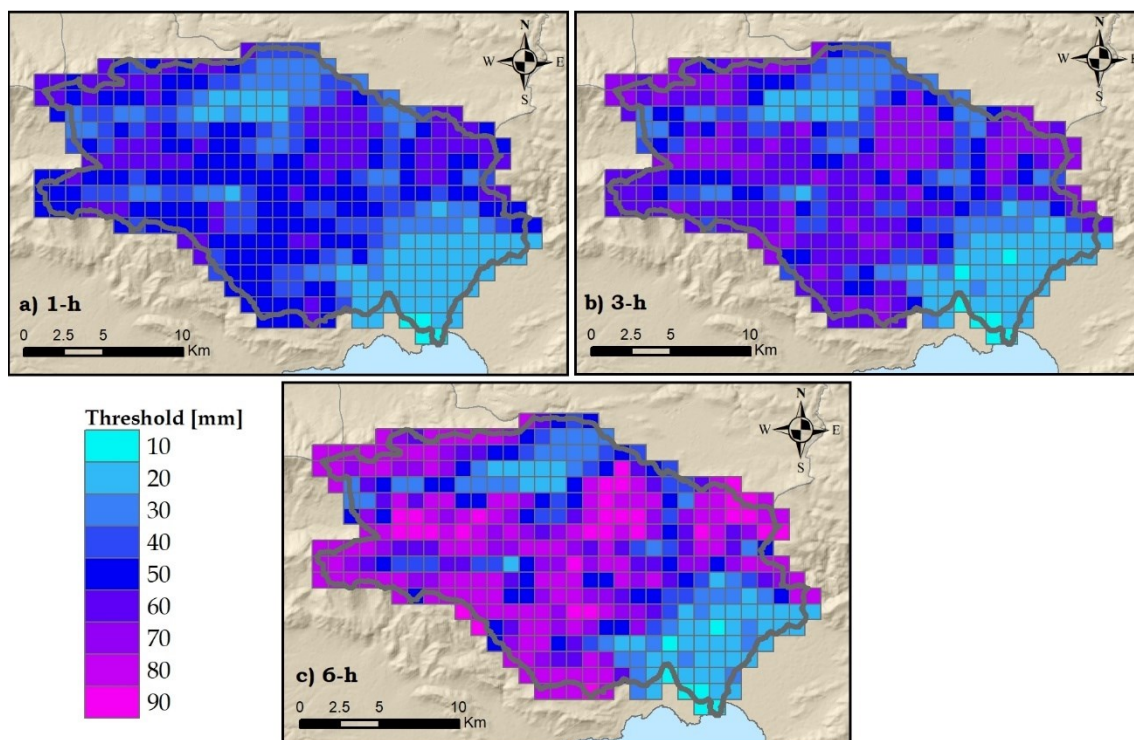
Σχήμα 13: Κατώφλι βροχής για μέσες τιμές υγρασίας και για τρείς διαφορετικής διάρκειας αθροιστική βροχόπτωση a) μίας ώρας b) 3-ωρών και c) 6-ωρών Πηγή (Bournas and Baltas 2022c)

Εφαρμόζοντας την παραπάνω μεθοδολογία, προκύπτουν οι χάρτες FFG για τρεις διάρκειες αθροιστικής βροχόπτωσης, των 1-, 3- και 6- ωρών. Οι χάρτες αυτοί συγκρίνονται με δεδομένα πρόγνωσης αντίστοιχης διάρκειας, εξασφαλίζοντας μία ισορροπία μεταξύ του διαθέσιμου χρόνου προειδοποίησης και της αυξανόμενης αβεβαιότητας. Συγκεκριμένα, το σύστημα δεν απαντά σχετικά με την ακριβή στιγμή

που συμβαίνει η πλημμύρα, αλλά εάν θα προκληθεί πλημμύρα στην εν λόγω διάρκεια. Έτσι, ενώ η χρήση μεγαλύτερης διάρκειας βροχής επιτρέπει μεγαλύτερο χρόνο αντίδρασης, είναι άγνωστο η ακριβής στιγμή πότε θα συμβεί η πλημμύρα εντός της διάρκειας αυτής.
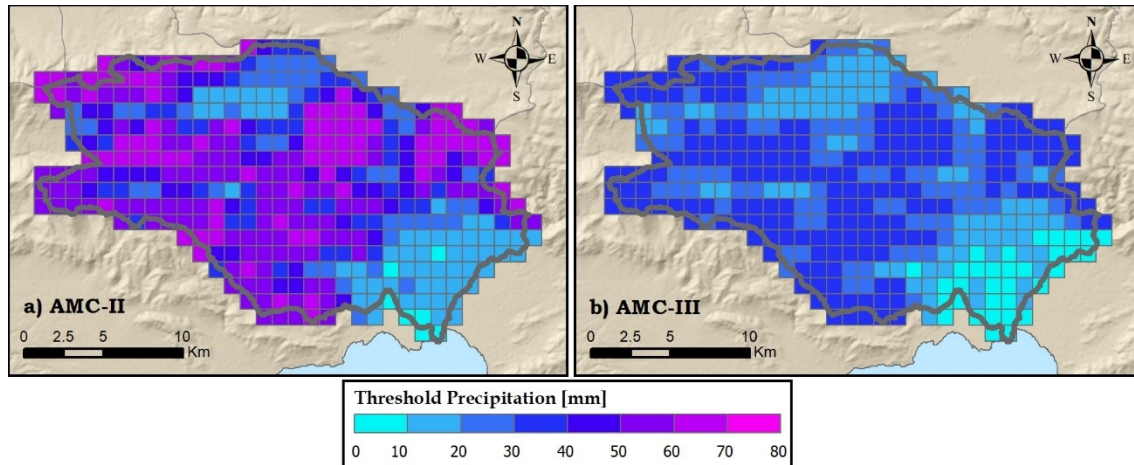
Σχήμα 14: Κατώφλι βροχής για 3-ωρη διάρκειας αθροιστική βροχόπτωση και για συνθήκες υγρασίας a) ACM-II (μέσες) και b) AMC-III (υγρές); Πηγή (Bournas and Baltas 2022c)

Η επίδραση της υγρασίας του εδάφους στους παραγόμενους χάρτες είναι σημαντική, όπως φαίνεται στο Σχήμα 14, όπου απεικονίζεται το κατώφλι βροχής για δύο συνθήκες υγρασίας, μέτριες και υγρές συνθήκες. Στη δεύτερη περίπτωση οι τιμές που έχει το κατώφλι είναι μικρότερες, που υποδηλώνει ότι απαιτείται μικρότερο ύψος βροχής για να εκδηλωθεί πλημμύρα. Τονίζεται ότι ο αντίκτυπος της υγρασίας του εδάφους είναι μέγιστος σε περιοχές με διαπερατά εδάφη, διότι η τιμή του CN σε αυτά τα εδάφη μεταβάλλεται σημαντικά όταν επικρατούν ξηρές ή υγρές συνθήκες. Αντίθετα, περιοχές που είναι σχετικά αδιαπέρατες, όπως ο αστικός ιστός, δείχνουν λιγότερη εξάρτηση από τις συνθήκες υγρασίας του εδάφους, καθώς η δυνατότητα απορροής είναι ήδη υψηλή.

Στη συνέχεια, παρουσιάζεται η εφαρμογή του συστήματος GFFG στη ΛΑΠ Σαρανταπόταμου καθώς και σε όλη την έκταση της περιφέρειας Αττικής για μια σειρά επεισοδίων βροχής. Σε αυτήν την περίληψη, παρουσιάζεται το Επεισόδιο βροχής Ε50, που συνέβη στις 12-06-2021. Οι χάρτες βροχόπτωσης και τα κελιά όπου εκτιμάται ο κίνδυνος πλημμύρας για δεδομένα αθροιστικής βροχόπτωσης 3 ωρών, παρουσιάζονται στο Σχήμα 15. Όπως φαίνεται στο σχήμα, οι περιοχές στις οποίες εμφανίζεται κίνδυνος πλημμύρας είναι συνδεδεμένες με τις περιοχές όπου παρατηρήθηκε υψηλή βροχόπτωση. Στο Σχήμα 16 παρουσιάζονται οι περιοχές όπου το σύστημα εμφάνισε κίνδυνο έναντι πλημμύρας, σε κάποια χρονική στιγμή, τόσο για τη ΛΑΠ Σαρανταπόταμου όσο και για την περιοχή της Αττικής.
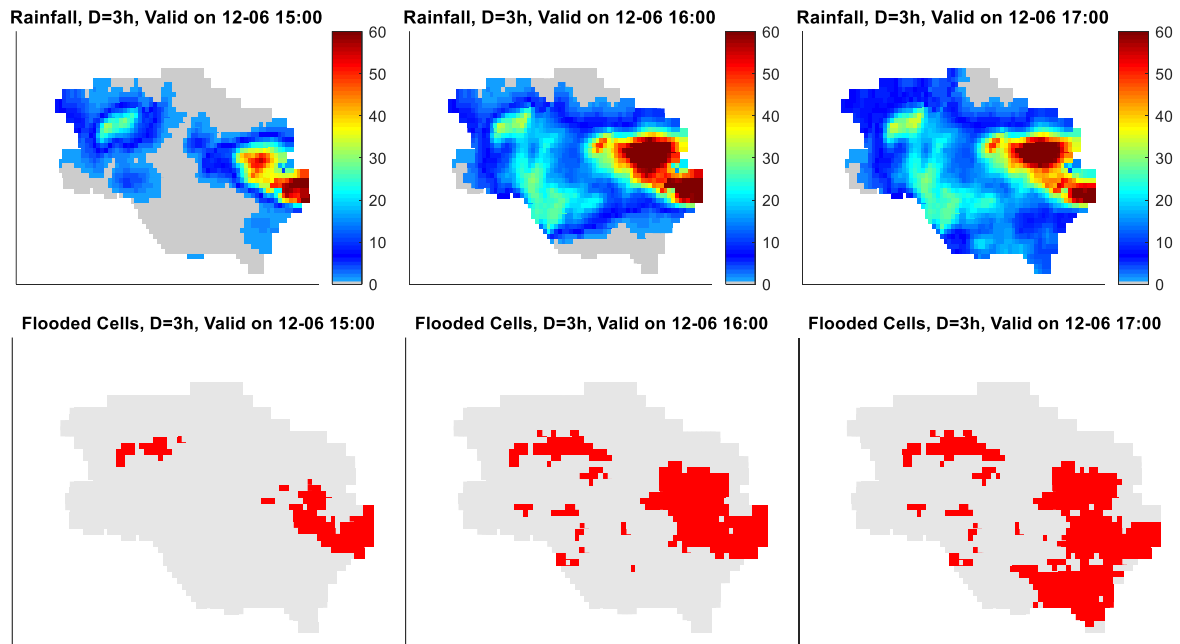
Σχήμα 15: 3-ωρη Κατανεμημένη μορφή βροχή και κελιά με κίνδυνο πλημμύρας για τρεις χρονικές στιγμές κατά τη διάρκεια του Επεισόδιου E50 στη ΛΑΠ Σαρανταπόταμου
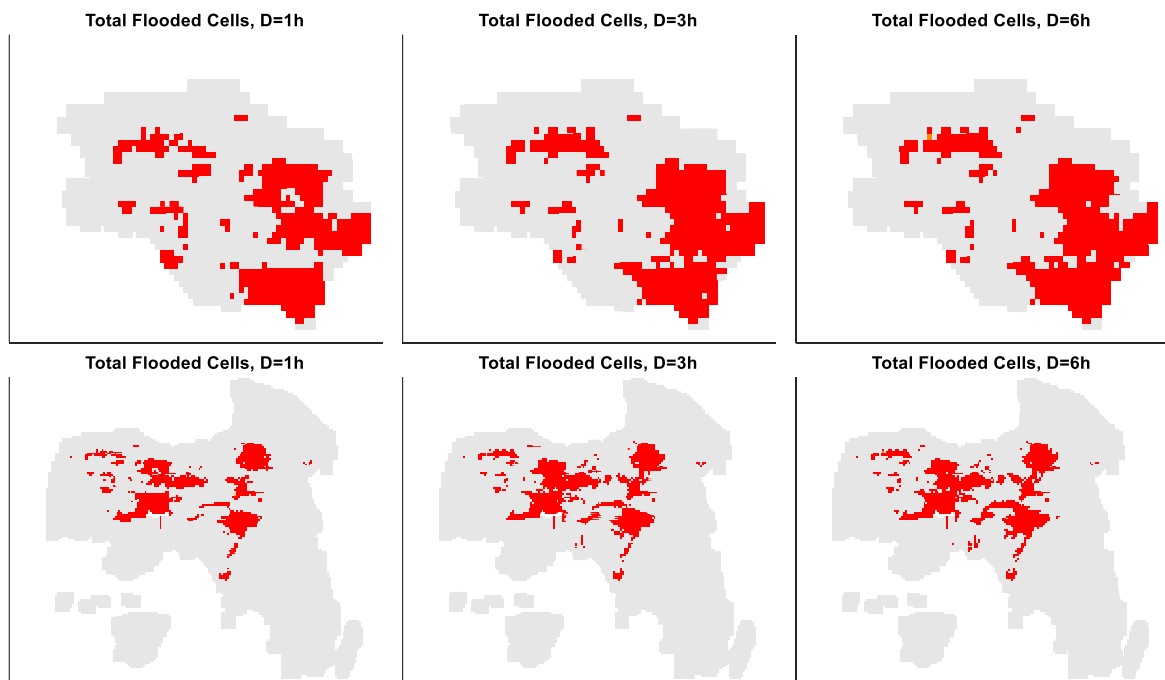
Σχήμα 16: Περιοχές για τις οποίες το σύστημα ανέφερε κίνδυνο πλημμύρας, για το επεισόδιο E50, χρησιμοποιώντας διαφορετικής διάρκειας αθροιστική βροχόπτωση.

Όπως φαίνεται, το τελικό αποτέλεσμα είναι το ίδιο, ανεξαρτήτως της αθροιστικής διάρκειας που χρησιμοποιείται (1- ,3- ή 6-ωρών). Η διαφορά μεταξύ των αποτελεσμάτων των βροχοπτώσεων διαφορετικής διάρκειας όπως αναφέρθηκε έγκειται στον χρόνο προειδοποίησης με την 6-ώρη να έχει τον μεγαλύτερο. Αντίθετα, με τη χρήση της FFG διάρκειας μίας ώρας είναι εφικτός ο προσδιορισμός της χρονικής πλημμύρας, όπου στην περίπτωση αυτή είναι μεταξύ των ωρών 15:00 και 16:00, ανατολικά της λεκάνης ενώ μεταξύ 16:00 με 17:00 εμφανίζονται οι μέγιστες τιμές. Το πλεονέκτημα του μετεωρολογικού ραντάρ έγκειται στο γεγονός ότι οι προβλέψεις αυτές μπορούν να ανανεώνονται σε λεπτές χρονικές κλίμακες (π.χ. 10λέπτα) και άρα μπορεί να συνεισφέρει στην παραγωγή άμεσων προγνώσεων (Nowcasts).

Τέλος, πραγματοποιείται μια ανάλυση ευαισθησίας, όπου οι κύριες παράμετροι του συστήματος μεταβάλλονται και εκτιμάται η επίδραση τους στο αποτέλεσμα. Οι κύριες παράμετροι του συστήματος είναι α) η περίοδος επαναφοράς της βροχόπτωσης που χρησιμοποιείται για τον υπολογισμό της παροχής κατωφλιού, β) οι συνθήκες υγρασίας του εδάφους και γ) η σχέση Z-R που χρησιμοποιείται για τον μετασχηματισμό της ανακλαστικότητας σε βροχόπτωση. Στο Σχήμα 17, στη πρώτη γραμμή απεικονίζεται το στιγμιότυπο του συστήματος για μια δεδομένη χρονική στιγμή (12-06, 16:00, τρίωρη βροχόπτωση), όπως υπολογίζεται βάσει των αρχικών παραμέτρων του συστήματος. Στην δεύτερη γραμμή, η αριστερή εικόνα απεικονίζει την επίδραση της περιόδου επαναφοράς της βροχόπτωσης στον υπολογισμό του κατωφλίου απορροής, με τη μεταβολή της από T=5 έτη σε T=10 έτη, η μεσαία εικόνα απεικονίζει την επίδραση του ποσοστού υγρασίας του εδάφους, με την μεταβολή του από 70% σε 100%, και η δεξιά εικόνα απεικονίζει την επίδραση της σχέσης Z-R, με τη μεταβολή της σχέσης από $Z=321R^{1.53}$ σε $Z=200R^{1.60}$. Σε σύγκριση με το αρχικό στιγμιότυπο, η επίδραση της περιόδου επαναφοράς είναι ελάχιστη, ενώ η επίδραση των συνθηκών υγρασίας του εδάφους είναι η πιο μεγάλη. Η αλλαγή στη σχέση Z-R αυξάνει τον αριθμό των κελιών που πλημμυρίζουν, αφού η εφαρμογή της οδηγεί σε υψηλότερες τιμές έντασης βροχής, αλλά όχι στον ίδιο βαθμό με την επίδραση του ποσοστού υγρασίας.

Τα αποτελέσματα δείχνουν πως οι διαφορές στην περίπτωση μεταβολής της σχέσης Z-R είναι συνήθως μικρές, αφού το ύψος της βροχής δεν μεταβάλλεται σημαντικά, με αποτέλεσμα να επηρεάζονται κυρίως τα κελιά των οποίων το ύψος της αθροιστικής βροχόπτωσης ήταν κοντά στην τιμή της υπολογιζόμενης FFG.
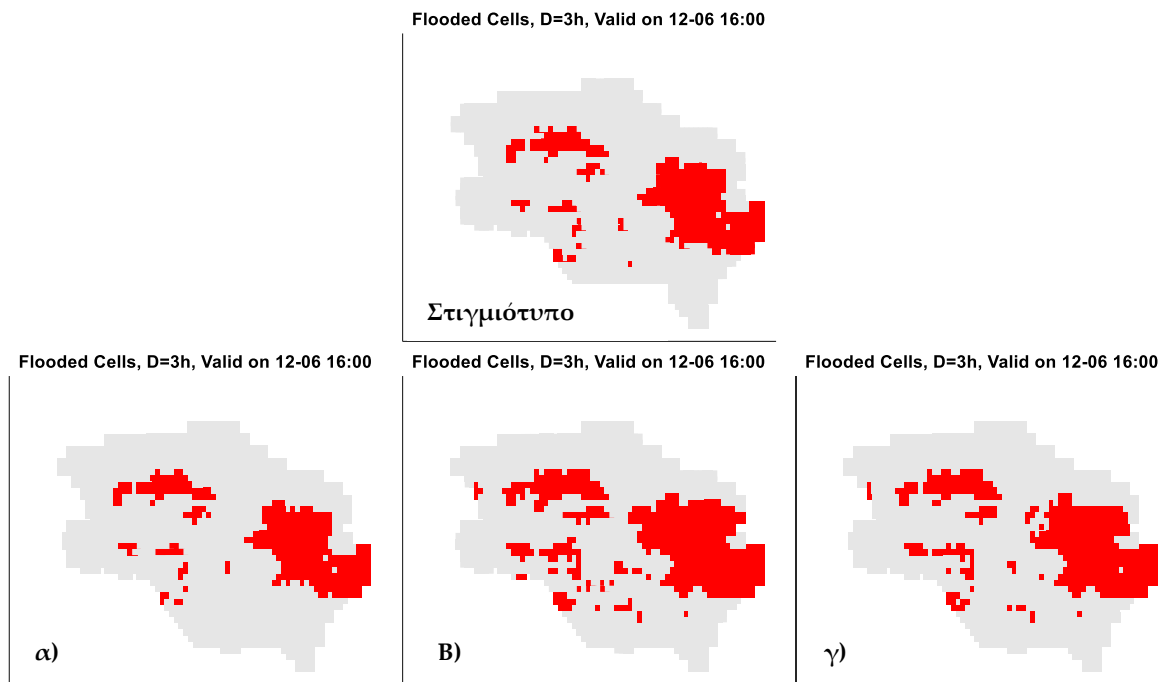
Σχήμα 17: Ανάλυση ευαισθησίας ενός στιγμιότυπου (πρώτη γραμμή) με αλλαγή: α) της περιόδου επαναφοράς από T=5 έτη σε T=10 έτη, β) τις συνθήκες υγρασίας από 70% σε 100% και γ) τη σχέση Z-R από Z=321R$^{1.53}$ σε Z=200R$^{1.60}$.

Αλγόριθμος παρακολούθησης καταιγιδοφόρων νεφών

Ο αλγόριθμος παρακολούθησης νεφών αποτελείται από τις διαδικασίες ανίχνευσης των κυττάρων και της παρακολούθησης της πορείας τους. Στην πρώτη περίπτωση, παρουσιάζεται η ικανότητα του αλγορίθμου να ανιχνεύει τα σύννεφα με βάση το όριο ανακλαστικότητας. Στο Σχήμα 18 παρουσιάζεται η διαφορά μεταξύ της χρήσης διαφορετικού κατωτάτου ορίου ανακλαστικότητας, 25 και 30 dBZ, καθώς και η χρήση του αυστηρού πολύγωνου ή της προσαρμογής μίας έλλειψης (fitting ellipse) για την αναπαράσταση των περιοχών των κυττάρων. Όπως φαίνεται, το όριο 25 dBZ λειτουργεί καλά όταν χρησιμοποιείται για την αναγνώριση των πολυγώνων, αλλά όχι όταν χρησιμοποιείται με ένα προσαρμοσμένο ελλειψοειδές. Επιπλέον χρησιμοποιώντας ως ελάχιστο εμβαδόν ενός καταιγιδοφόρου νέφους τα 4 km², προσδιορίζονται συνολικά 11 κύτταρα. Στην περίπτωση των 30 dBZ, το προσαρμοσμένο ελλειψοειδές παρουσιάζει καλά αποτελέσματα, σχετικά με την προσαρμογή του στα αντίστοιχα πολύγωνα, την εκκεντρότητα του και την κλίση του. Επομένως, δεδομένης της έμφασης σε συστήματα έντονης βροχόπτωσης, χρησιμοποιείται το 30 dBZ με την προσαρμοσμένη έλλειψη για τον προσδιορισμό των κέντρων των κυττάρων. Τέλος, επιλέγεται και το όριο των 35 dBZ για την επισήμανση περιοχών στις οποίες επικράτησαν ισχυρής έντασης βροχές, κατάλληλες για την εφαρμογή του αλγόριθμου παρακολούθησης σε επίπεδο επεισοδίου βροχής.
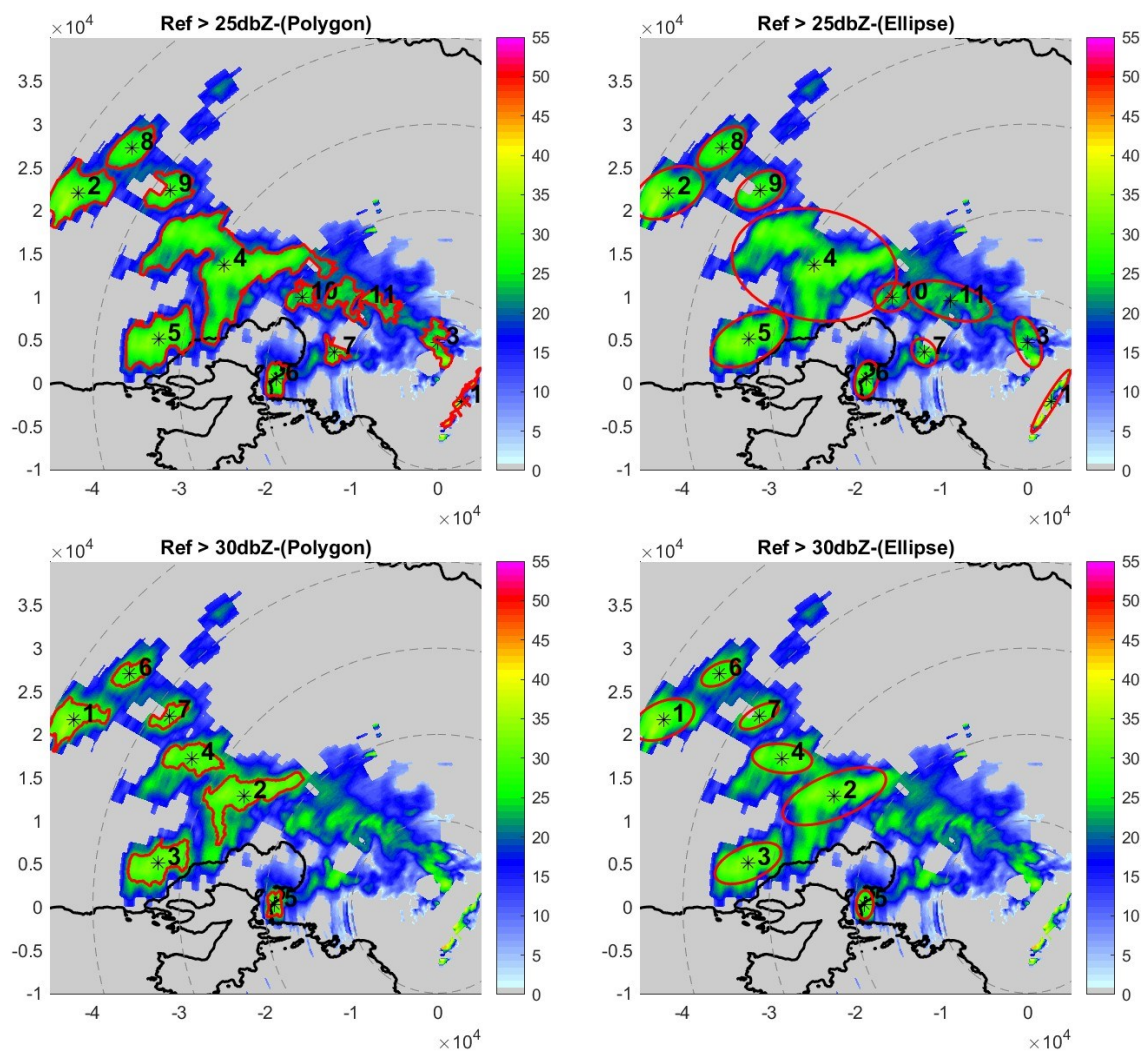
Σχήμα 18: Αποτελέσματα του αλγορίθμου ανίχνευσης όταν χρησιμοποιείται διαφορετικό κατώφλι ανακλαστικότητας και σχήμα προσαρμογής.

Σχετικά με τη διαδικασία παρακολούθησης σε διαδοχικές εικόνες, ο αλγόριθμος επιλύει το πρόβλημα της αντιστοίχισης κάθε ιστορικού κυττάρου με τα κύτταρα που απεικονίζονται στη νέα εικόνα. Ένα κύτταρο δύναται, είτε να εντοπιστεί σε μία νέα, ανεξάρτητη θέση, είτε να συγχωνευτεί με ένα άλλο κύτταρο σε μία νέα θέση (merge), είτε να εξαφανιστεί. Τέλος νέα κύτταρα δύνανται να δημιουργηθούν χωρίς να έχει υπάρχει κάποια σύνδεση τους με ένα ιστορικό κύτταρο, εφόσον δεν τηρείται ο κανόνας του διαμερισμού (split) που βασίζεται κυρίως στην απόσταση, το μέγεθος και σχήμα των δύο κυττάρων. Στο Σχήμα 19, ο αλγόριθμος παρακολούθησης εφαρμόζεται χρησιμοποιώντας 10-λεπτες εικόνες ανακλαστικότητας ανά 10-λεπτο χρονικό διάστημα. Συγκεκριμένα, πέντε εικόνες ανακλαστικότητας, διάρκειας 2 λεπτών, που είναι η χρονική ανάλυση του ραντάρ, συγχωνεύονται για να οριστεί το πεδίο αντανάκλασης διάρκειας 10 λεπτών. Στο σχήμα με κόκκινα πολύγωνα παρουσιάζονται τα κύτταρα της τρέχουσας χρονικής στιγμής, ενώ με διακεκομμένη μαύρη γραμμή τα

κύτταρα της προηγούμενης χρονικής στιγμής για τα οποία γίνεται η αντιστοίχιση. Από τα αποτελέσματα φαίνεται πως ο αλγόριθμος λειτουργεί ικανοποιητικά, εφαρμόζοντας τους κανόνες συγχώνευσης και διαμερισμού όπου απαιτείται.
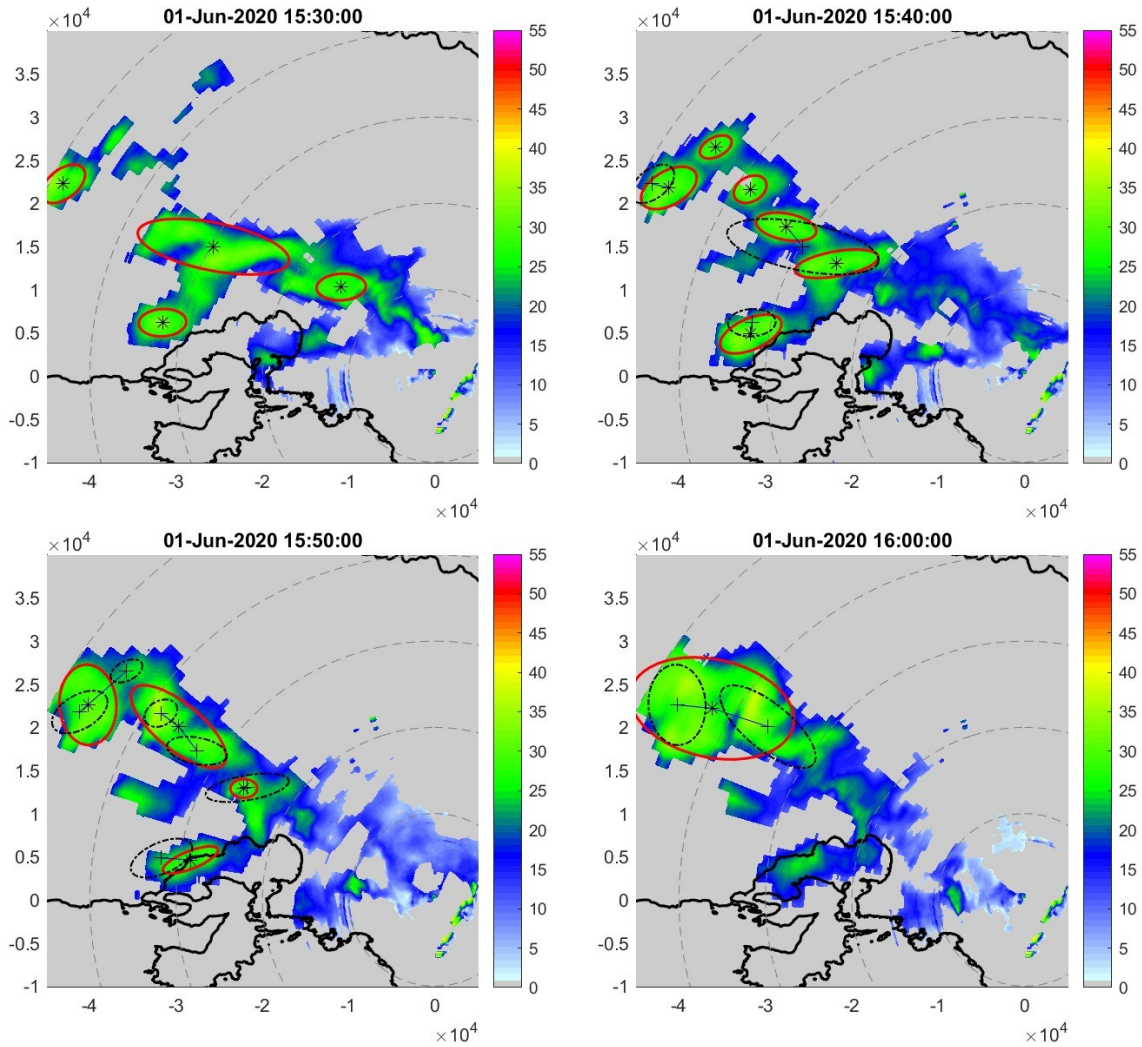
Σχήμα 19: Εφαρμογή του αλγόριθμου παρακολούθησης μεταξύ 4 εικόνων με χρονικό βήμα 10-λεπτών

Τέλος, ο αλγόριθμος παρακολούθησης εφαρμόζεται σε όλα τα επεισόδια βροχής που συλλέχθηκαν από το Rainscanner (Appendix A). Στο Σχήμα 20, παρουσιάζεται η παρακολούθηση για τα επεισόδια Ε31 και Ε50. Συγκεκριμένα, με μπλε γραμμή παρουσιάζεται το όριο κάθε κυττάρου (σε πολύγωνο) το οποίο σε κάποια χρονική στιγμή ήταν πάνω από το κατώφλι ανακλαστικότητας, 35 dBZ στην πρώτη γραμμή και 40 dBZ στην δεύτερη γραμμή. Επιπλέον, με κόκκινο χρώμα απεικονίζονται τα κέντρα των κυττάρων ενώ με διακεκομμένες μαύρες γραμμές η συνεχής παρακολούθηση τους. Τα αποτελέσματα για τα 40 dBZ είναι πιο ευκρινή λόγω του μικρότερου αριθμού των αναγνωρισμένων κυττάρων. Τα αποτελέσματα για όλα τα επεισόδια βροχής

απεικονίζονται στο Παράρτημα B (Appendix B), όπου γίνεται ο εντοπισμός των περιοχών στις οποίες παρατηρήθηκαν μεγάλες τιμές ανακλαστικότητας, και άρα όσο περισσότερη έκταση καταλαμβάνουν αυτές στην περιοχή μελέτης, τόσο περισσότερες περιοχές επηρεάζονται αρνητικά από το συγκεκριμένο επεισόδιο βροχής. Δηλαδή, γίνεται μια εκτίμηση της σφοδρότητας μεταξύ των επεισοδίων βροχής.
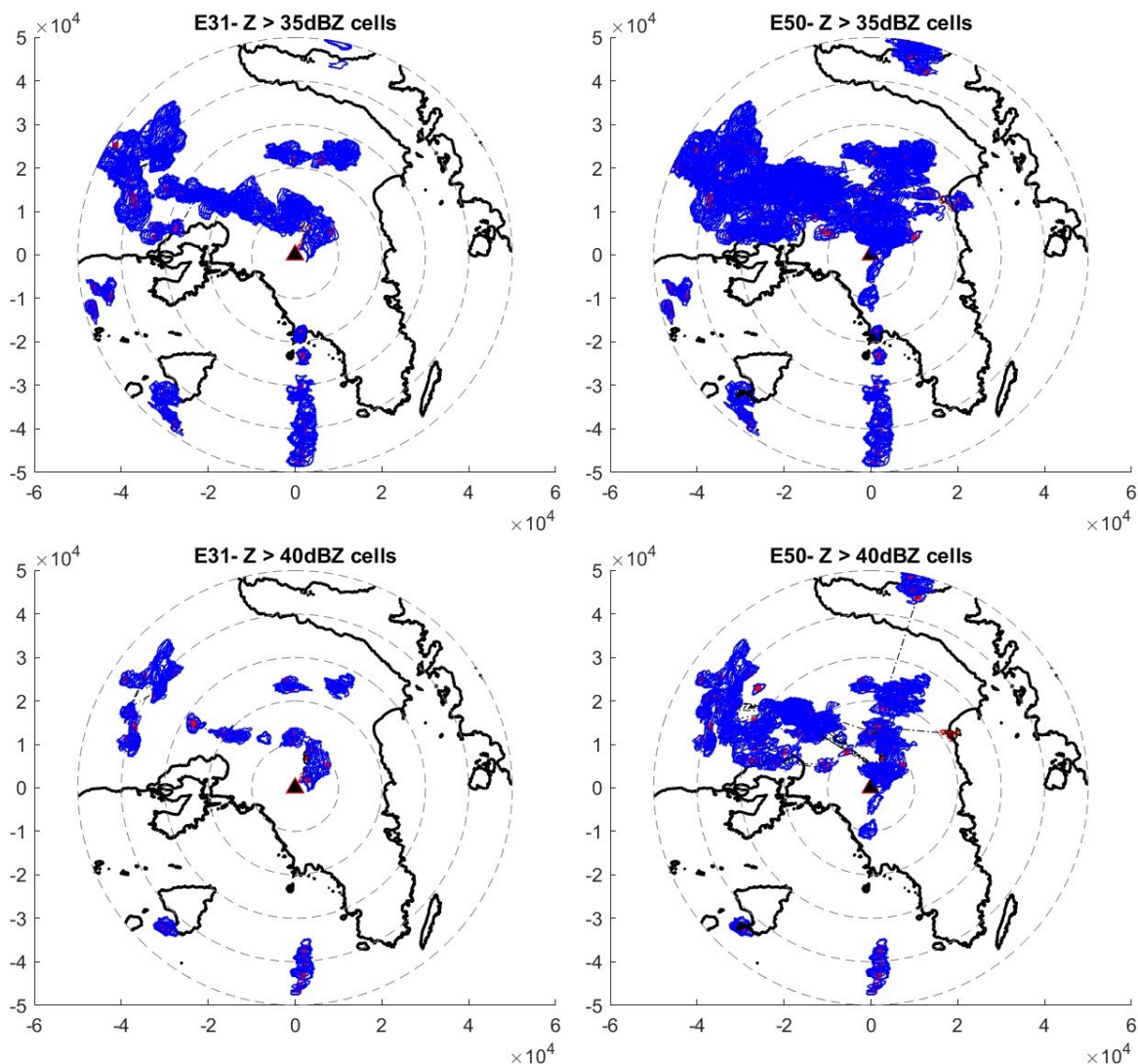
Σχήμα 20: Περιοχές με υψηλές τιμές ανακλαστικότητα, άνω των 35 dBZ (πρώτη γραμμή) και κάτω των 40 dBZ (δεύτερη γραμμή), για τα επεισόδια βροχής 31 και 50

Στο Σχήμα 21, για τα επεισόδια 31 και 50, παρουσιάζονται τα κέντρα των κυττάρων για κατώφλι 35 dBZ, όπου απεικονίζεται με βελτιωμένη σαφήνεια η θέση των κυττάρων και κυρίως η διεύθυνση των νεφών. Τα αντίστοιχα αποτελέσματα για όλα τα επεισόδια βροχής παρουσιάζονται στο Παράρτημα C (Appendix C). Η εφαρμογή αυτή οδηγεί στο Σχήμα 22 όπου απεικονίζονται οι κύριες διευθύνσεις των καταιγιδοφόρων νεφών στην Αττική.
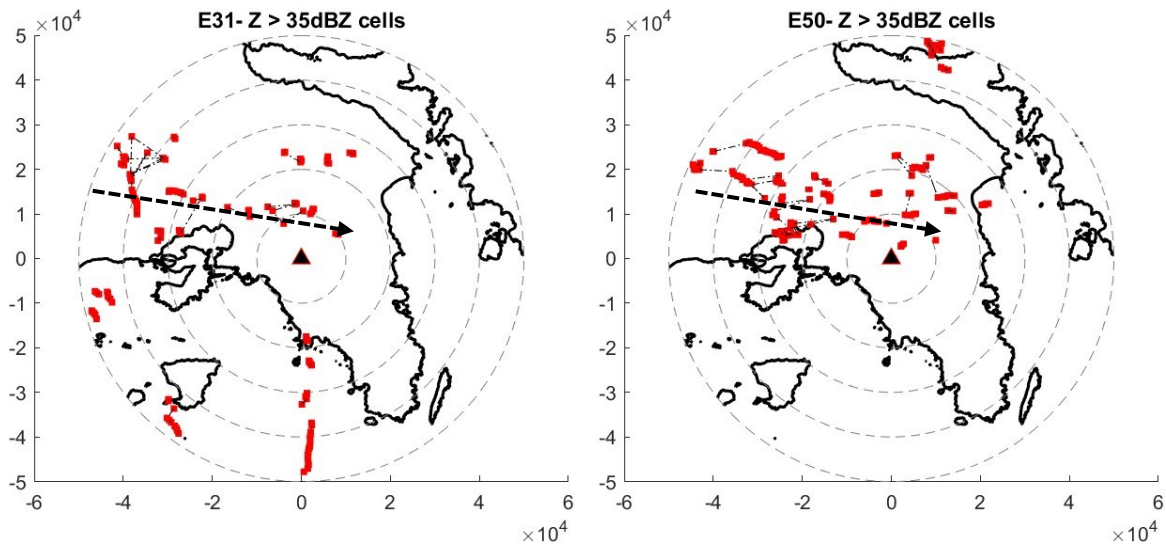
Σχήμα 21: Αποτύπωση των κέντρων των καταιγιδοφόρων νεφών με ανακλαστικότητα πάνω από 35 dBZ και εντοπισμός της κύριας διεύθυνσης
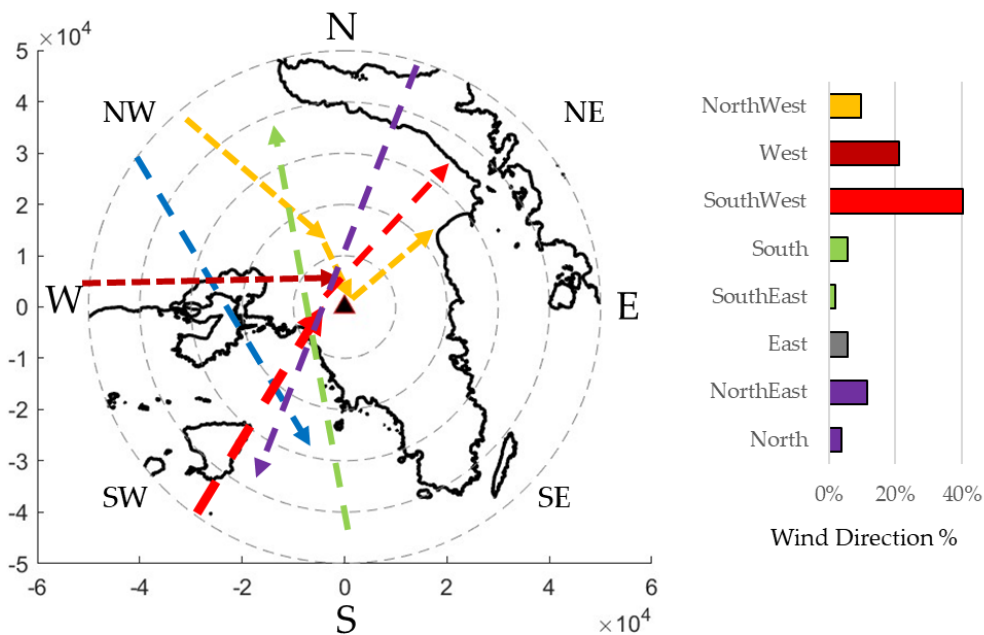
Σχήμα 22: Κύριες Διευθύνσεις καταιγιδοφόρων νεφών στην περιοχή της Αττικής. Με κόκκινες γραμμές οι πιο συχνές, και εν συνέχεια οι μπλε, οι κίτρινες και οι μοβ, με ποσοστά σύμφωνα και με το διάγραμμα.

Η πλειονότητα των καταιγίδων, το 40% των επεισοδίων βροχής που μελετήθηκαν, έχει κατεύθυνση από νοτιοανατολικά προς βορειοδυτικά, περνώντας πάνω από την Αθήνα. Ακολούθως, παρουσιάζονται κατευθύνσεις από δυτικά προς ανατολικά και από βορειοδυτικά προς ανατολικά, καθώς και μερικές περιπτώσεις με κατεύθυνση από νότο προς βορρά. Τέλος, αποκλειστικά σε περιπτώσεις χειμερινών επεισοδίων, εντοπίζονται

και διευθύνσεις από βορρά προς νότο. Σε αυτές τις περιπτώσεις, τα νέφη χαρακτηρίζονται από χαμηλή ταχύτητα και χαμηλές έως μέτριες τιμές ανακλαστικότητας, που απαντώνται σε stratiform νέφη. Εν γένει, η πλειονότητα των επεισοδίων βροχής με convective χαρακτηριστικά, δηλαδή υψηλές τιμές ανακλαστικότητας και ταχύτητας είχαν διεύθυνση δυτικά / νότιο δυτικά προς ανατολικά, όπως αυτές απεικονίζονται στο Σχήμα 21 για τα επεισόδια Ε31 και Ε50.

Συμπεράσματα και Μελλοντική Έρευνα

Η παρούσα Δ.Δ. παρέχει ένα ολοκληρωμένο πλαίσιο για τη χρήση δεδομένων μετεωρολογικού ραντάρ με σκοπό την εκτίμηση του πλημμυρικού κινδύνου και την έγκαιρη προειδοποίηση πλημμυρών. Η έρευνα προσφέρει απαντήσεις σε βασικά ερωτήματα σχετικά με τη χρήση δεδομένων μετεωρολογικού ραντάρ, αποκαλύπτοντας ότι, ενώ τα δεδομένα μετεωρολογικού ραντάρ μπορεί να έχουν ευρεία εφαρμογή, η αβεβαιότητα ως αποτέλεσμα των σφαλμάτων και μη ύπαρξης ποιοτικού ελέγχου μπορεί να περιορίσει την πρακτικότητά τους.

Η έρευνα αποτελείται από δύο κύριες ενότητες. Η πρώτη ενότητα εξετάζει τις διάφορες πτυχές της τεχνολογίας των μετεωρολογικών ραντάρ, συμπεριλαμβανομένων των τύπων, των πηγών σφαλμάτων και των διαδικασιών ελέγχου ποιότητας. Επιπλέον, επικεντρώνεται στη σχέση Z-R και στη μεταβλητότητά της στο χρόνο και στο χώρο. Συγκεκριμένα, μέσω της συσχέτισης με επίγειους βροχογράφους, αναδεικνύεται η συσχέτιση των παραμέτρων της σχέσης Z-R με τοπογραφικά χαρακτηριστικά, όπως η εγγύτητα στην ακτογραμμή και στα υψηλά υψόμετρα. Παράγοντες όπως ο τύπος του ραντάρ, η τοποθεσία, η βαθμονόμηση και η διόρθωση του σήματος είναι κρίσιμοι και επηρεάζουν την ποιότητα των παραγόμενων δεδομένων.

Η δεύτερη ενότητα επικεντρώνεται στην εφαρμογή ενός ΣΕΠΠ που εστιάζει σε επεισόδια αιφνίδιων πλημμυρών, τα οποία χαρακτηρίζονται από μεγάλης έντασης βροχής, μικρής διάρκειας και μικρής χωρικής κλίμακας. Συγκεκριμένα, αναπτύσσεται ένα ολοκληρωμένο πλαίσιο εφαρμογής ενός ΣΕΠΠ, εστιάζοντας στην ενσωμάτωση υδρολογικών διαδικασιών για την εκτίμηση του πλημμυρικού κινδύνου. Αυτή η προσέγγιση λαμβάνει υπόψη μεταβαλλόμενους παράγοντες σε πραγματικό χρόνο, όπως οι συνθήκες υγρασίας του εδάφους και η υδρομετεωρολογική κατάσταση που επικρατεί στην περιοχή εφαρμογής. Ειδικότερα, αναπτύσσεται και εφαρμόζεται ένα υδρολογικό κατανεμημένο μοντέλο βροχής-απορροής το οποίο υποβοηθάει το σύστημα GFFG για την αξιολόγηση του κινδύνου πλημμύρας σε επίπεδο κελιού (500x500 m²). Τα αποτελέσματα της Δ.Δ. διερευνούν και αναδεικνύουν την επίδραση των τιμών των παραμέτρων στα χρησιμοποιούμενα μοντέλα, και επισημαίνουν ότι, παρά την ύπαρξη αβεβαιότητας, η πιο κρίσιμη παράμετρος για την βελτίωση της αξιοπιστίας ενός ΣΕΠΠ

είναι η αξιοπιστία των δεδομένων εισόδου του και κυρίως αυτά της βροχόπτωσης και του επιπέδου υγρασίας του εδάφους.

Τέλος, αναπτύσσεται και εφαρμόζεται ένας αλγόριθμος ανίχνευσης και παρακολούθησης των καταιγιδοφόρων νεφών, μέσω του οποίου μελετώνται οι κύριες διευθύνσεις των νεφών. Η εφαρμογή του αλγορίθμου αναδεικνύει τα πολλαπλά οφέλη της χρήσης ενός μετεωρολογικού ραντάρ υψηλής χωροχρονικής ανάλυσης, σε συστήματα υδρομετεωρολογικής πρόγνωσης.

Συνοψίζοντας, η Δ.Δ. θέτει τις βάσεις για την ανάπτυξη και εφαρμογή ενός ολοκληρωμένου ΣΕΠΠ, το οποίο θα παρέχει σε επιχειρησιακό επίπεδο μετεωρολογική πρόγνωση, εκτίμηση πλημμυρικού κινδύνου και εξαγωγή μηνυμάτων προειδοποίησης σε πραγματικό χρόνο. Η μελλοντική έρευνα επικεντρώνεται στην επέκταση των ευρημάτων της εν λόγω διατριβής και σε άλλες περιοχές με διαφορετικά χαρακτηριστικά, ενώ προτείνεται η διαφοροποίηση και ανάλογη συγκριτική αξιολόγηση επιμέρους σημείων της έρευνας, χρησιμοποιώντας επιπλέον δεδομένα όπως μετρήσεις παροχών, δορυφορικά δεδομένα, δεδομένα από ντιστρόμετρα και άλλα μετεωρολογικά ραντάρ. Τέλος, εξετάζεται η εφαρμογή στοχαστικών μεθόδων με σκοπό την ποσοτικοποίηση και μείωση της αβεβαιότητας των επιμέρους συστημάτων.

1. Introduction

1.1 Natural Hazards and Disasters

Natural hazards are severe and extreme weather and climate events that can potentially cause excessive negative impacts on human life, society, the economy, and the environment. In this case, a natural hazard is renamed as a natural disaster. The United Nations Office for Disaster Risk Reduction (UNDRR) defines a disaster as a "serious disruption of the functioning of a community or a society at any scale due to hazardous events interacting with conditions of exposure, vulnerability, and capacity, leading to one or more of the following: human, material, economic and environmental losses and impacts" (UNDRR 2017).

Although a natural hazard is usually the result of natural processes, how humans interact with the environment contributes to their potential to cause natural disasters. Therefore, the root causes of disaster risk and disasters stem from structural conditions of a particular mode of development and growth (Oliver-Smith et al. 2017).

Natural hazards can be categorized with various conditions. The classification of natural hazards is usually done based on the source of the natural cause. These can either be a) Geophysical, e.g., earthquakes and volcanos, b) climate-related (hydrometeorological), e.g., floods, wet mass movement, storms, extreme temperature, drought, and wildfire, and c) biological, e.g., epidemic, insect infections (Leaning and Guha-Sapir 2013).

Globally, natural hazards, e.g., tropical cyclones (wind and storm surge), earthquakes, tsunamis, and floods, are anticipated to cause an average annual loss of US$314 billion to the built environment. This issue seriously threatens the global agenda of sustainable development. Large, high-income, hazard-exposed economies make up most of the worldwide average annual loss in absolute terms. The most significant risk concentrations are found in many low- and middle-income countries, particularly small-island developing states, as compared to yearly capital investment or social expenditure. In Figure 1-1 the annual economic damages from disasters as a share of GDP for the years between 2010-2020 is shown, indicating a considerable amount in the North and South America, as well as in Asia, Australia and southeast area of Africa.

Regarding Europe, the most economic damages are found in the easter part of Europe, namely Italy, and the Balkans. In Figure 1-2, Figure 1-3 and Figure 1-4 the number of events, the number of people affected and the economic losses per each natural disaster, floods, extreme temperature, wildfires, storms and winds, droughts and mass movement are illustrated, respectively (CRED 2022). As shown, the majority of events occurring are flood events followed by storms and winds, which are usually interrelated. Moreover, floods affect the majority of people and cause the second most economic damages per year. Furthermore, the graphs show that year-by-year the percentage in each case is not decreasing, signifying that more measures are needed to decrease these numbers.

No data 0% 0.01% 0.05% 0.1% 0.5% 1% 10% 50%
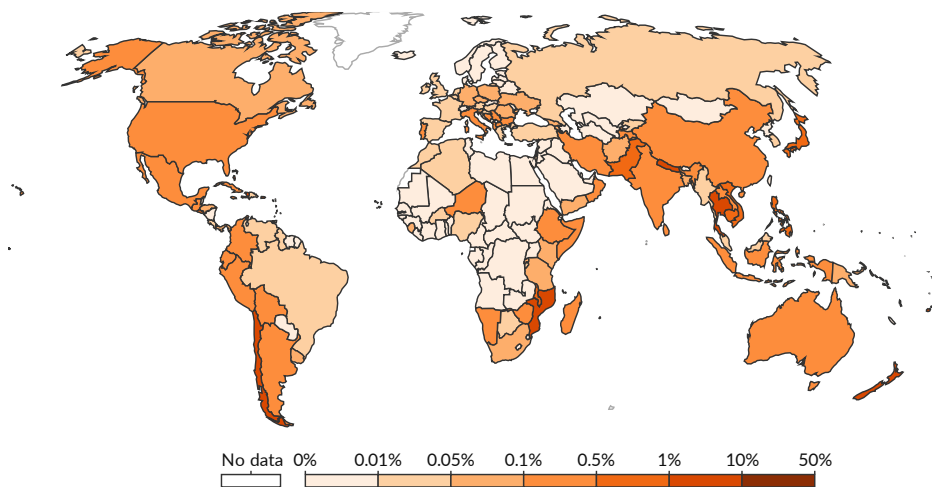
Source: Our World in Data based on EM-DAT, CRED / UCLouvain, Brussels, Belgium – www.emdat.be (D. Guha-Sapir)
Note: Decadal figures are measured as the annual average over the subsequent ten-year period. This means figures for '1900' represent the average from 1900 to 1909; '1910' is the average from 1910 to 1919 etc.
OurWorldInData.org/natural-disasters • CC BY

Figure 1-1: Annual economic damages from disasters as a share of GDP, 2010-2020. Source: Our World in Data, (stated within figure)
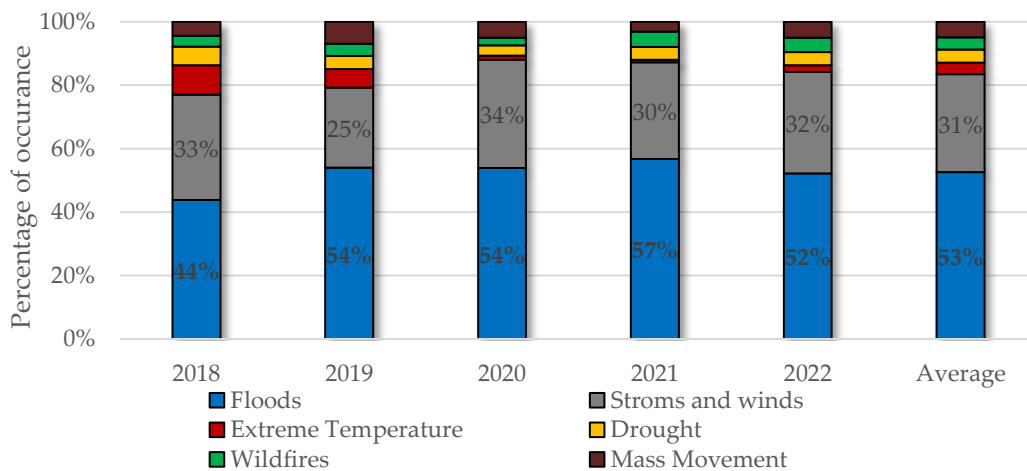
Figure 1-2: Number of Natural Hazards worldwide per year

2
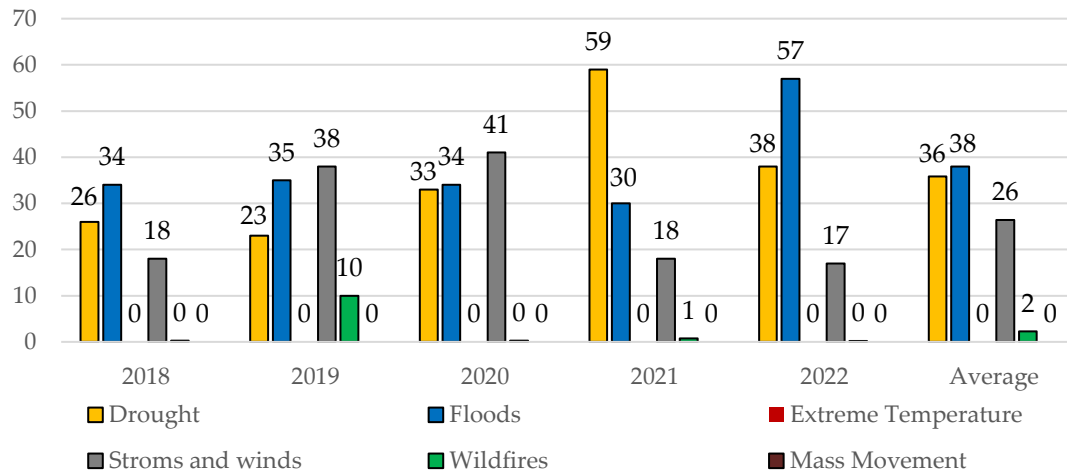
Figure 1-3: Number of people in millions affected by Natural Hazards worldwide per year
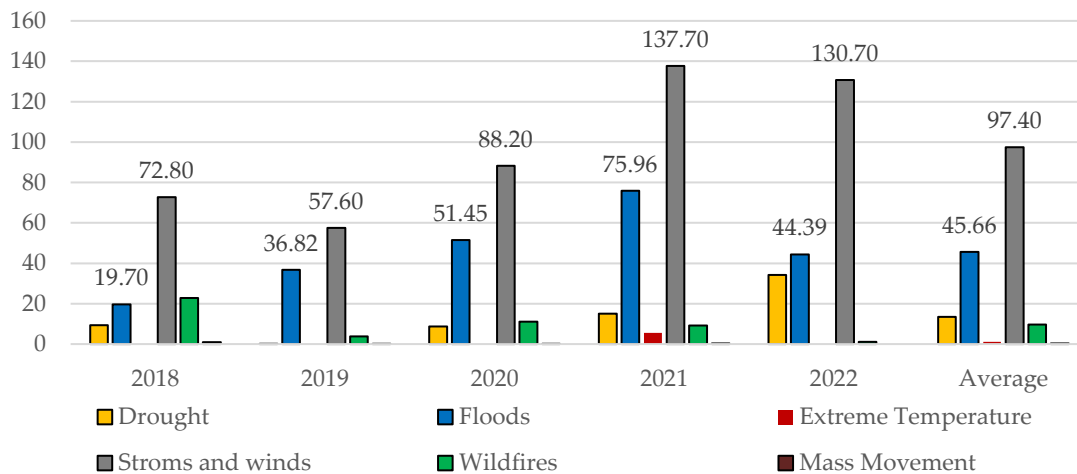
Figure 1-4: Economic losses in billion € caused by Natural Hazards worldwide per year

1.2   Floods

Floods affect more people globally than any other natural hazard. They can cause widespread devastation that can displace people, damage property and critical public infrastructure, and ultimately result in loss of life. Moreover, as the planet continues to warm up due to climate change, the intensity and frequency of flooding will likely increase. The EU 2007/60 directive defines a flood as "the temporary cover of the soil by water which is not normally covered by it, which includes floods from rivers, mountain torrents, Mediterranean ephemeral water courses, and floods from the sea in coastal areas, and may exclude floods from sewerage systems" (European Union 2007). There are three common flood types: fluvial floods, also known as river or stream floods, pluvial or flash floods, and coastal floods, which are often called storm surges. Each type of flood occurs and is forecast in different ways. The impacts of each type of flood are also different, as are the models and

actions needed to avoid or minimize flooding damage. More detail for each type of flood is as follows:

Fluvial (Riverside)

A fluvial, or river flood, occurs when the water level in a river, lake, or stream rises and overflows onto the neighboring land. The water level rise of the river could be due to excessive rain or snowmelt. This is the most common type of flooding found in typical river systems. The damage from a river flood can be widespread as the overflow affects smaller rivers downstream, which can cause dams and dikes to break and swamp nearby areas.

The severity of a river flood is determined by the terrain profile and the duration and intensity of rainfall in the river's catchment area. Other factors include soil water saturation and climate change effects on rainfall duration and intensity. In flat areas, floodwater tends to rise slowly and be shallower, but it can often remain for days. In hilly or mountainous areas, floods can occur within minutes after heavy rain, drain very quickly, and cause damage due to debris flow.

Pluvial (Flash Floods)

A pluvial flood occurs when extreme rainfall creates a flood independent of an overflowing water body. Pluvial flooding can occur in any location, urban or rural, even in areas with no nearby bodies of water. There are two common types of pluvial flooding: surface and flash floods. The first occurs when an urban drainage system is overwhelmed and water flows into streets and nearby structures. In such a case, flooding occurs gradually, so there is adequate lead time to address the problem with low risk. The water level is usually shallow and creates no immediate threat to lives but may cause significant economic damage.

The second case is Flash Floods, which are sudden and rapidly developing floods characterized by their swift onset and high intensity. Flash floods typically occur in areas with steep terrain, urban environments with poor drainage systems, arid regions where the ground cannot absorb water quickly, and places prone to intense rainfall. They can be triggered by various factors, mainly heavy rain but also rapid snowmelt, dam or levee failures, and sudden water releases from reservoirs. Other factors that contribute are the geomorphological and geological characteristics of the basin, such as the basin size and slope, the poor infiltration capacity of soils, and the soil moisture conditions at the start of the event (Merz and Blöschl 2003; Houze Jr. et al. 2015; Velásquez et al. 2020). Flash floods are usually local-scaled events, as they are highly related to convective-type storms, and thus, the spatial coverage of the affected areas is reduced (Houze Jr. et al. 2015). Sometimes, flash floods can also be caused by landslide debris flows (Posner and Georgakakos 2015).

Uncontrolled urbanization and deforestation are among the first causes behind flash flooding, while climate change effects, such as the increasing occurrence and rain intensity

of storm events, have altered the periodicity of these events (Alfieri et al. 2012; Gaur and Simonovic 2015; Rogger et al. 2017; Caloiero et al. 2017). All the above factors have made flash flooding an evolving threat since areas that once did not flood are now prone to flooding (Bournas and Baltas 2021a).

Flash floods occur within a concise timeframe, often within a few hours or even minutes of heavy rainfall. A flood occurring in less than six hours is usually classified as a Flash Flood. Their unpredictability and ability to catch people off guard due to their rapid formation often lead to devastating impacts on human communities and the natural environment, making flood floods among the deadliest weather-related hazards worldwide. In the Mediterranean, flash floods have recently caused substantial economic damages and the cost of human lives (Diakakis et al. 2012, 2019; Pereira et al. 2017; Feloni 2019; Varlas et al. 2019; Spyrou et al. 2020).

Coastal floods

Coastal flooding is the inundation of land areas along the coast by seawater. Common causes of coastal flooding are intense windstorm events occurring at the same time as high tide (storm surge), and tsunamis. Storm surge is created when high winds from a windstorm force water onshore – this is the leading cause of coastal flooding and often the most significant threat associated with a hurricane or typhoon. The effects increase depending on the tide – windstorms during high tide can result in devastating storm surge floods. In this type of flood, water overwhelms low-lying land and often causes devastating loss of life and property. Several other factors, including the windstorm's strength, size, speed, and direction, determine the severity of a coastal flood. The onshore and offshore topography also plays an important role. Due to rising sea levels and climate change, more coastal cities and communities tend to become more vulnerable to coastal flooding.

1.2.1 Flooding Mitigating Measures

A combination of measures can be adopted to mitigate the risk and the consequences of flooding. The standard approach categorizes the mitigating measures as prevention, protection, and preparedness. Prevention measures are usually non-structural measures aiming at flood-mitigating regulation and policy, while protection measures are usually structural measures that aim to reduce the likelihood or the severity of flood events or both. Finally, preparedness measures are proactive plans and strategies that prepare individuals, communities, and infrastructure for potential flood events, such as Early Warning Systems (EWS). A list of measures can be found below.

Prevention Measures

- Sustainable planning and development management:
- Land-use and Floodplain planning: Integrating flood risk considerations into land-use planning to avoid or implement regulations to control development in flood-prone areas and preserve natural flood storage areas.
- Sustainable drainage systems: Promotion of techniques to manage surface water runoff and reduce the risk of local flooding.
- Sustainable agriculture practices: Encouragement of agricultural practices that minimize soil erosion and promote natural water retention.
- Climate Change Adaptation: Considering the potential impacts of climate change on flood patterns, incorporating climate change projections into planning processes can help design more resilient infrastructure and flood management strategies.

Protection Measures

- Flood defense infrastructure: Construction or improvement of flood defenses, such as levees, flood walls, and embankments, to protect communities and critical infrastructure.
- Flood reservoirs: Construction of reservoirs to retain excess water during heavy rainfall and release it gradually to mitigate downstream flood risks.
- Coastal defenses: Installation or enhancement of coastal protection measures, such as seawalls, dikes, or beach nourishment, to mitigate coastal flooding and erosion.
- Floodplain restoration: Restoration of floodplains and wetlands enhance natural flood storage capacity and promotes ecosystem-based flood risk reduction.
- Retrofitting: Implement measures to retrofit existing buildings and infrastructure to withstand or minimize flood damage, such as installing flood barriers or raising foundations.

Preparedness Measures:

- Early warning systems: Developing and implementing robust early warning systems to provide timely alerts and evacuation instructions to at-risk communities.
- Emergency response plans: Creation of comprehensive emergency response plans, including evacuation procedures, coordination mechanisms, and communication strategies.
- Flood forecasting and monitoring: Establishment of systems for monitoring rainfall, water levels, and river flows to improve flood forecasting accuracy and response capabilities.

- Public awareness and education: Implement public awareness campaigns, educational programs, and community engagement initiatives to enhance understanding of flood risks and encourage proactive preparedness actions.
- Insurance and financial mechanisms: Promotion of insurance schemes and financial instruments to support individuals, businesses, and communities in managing and recovering from flood-related losses.

1.2.2   The 2007/60/EC Flood Directive

The European Union (EU) has established a framework for flood risk management and mapping through Directive 2007/60/EC (European Union 2007). Apart from the definition of flooding, the directive introduces the "Flood risk" term, defined as the combination of the probability of a flood event and the potential adverse consequences for human health, the environment, cultural heritage, and economic activity associated with a flood event (European Union 2007). The definition of Flood Risk follows the flood hazard, exposure, and vulnerability framework. Flood hazard refers to the probability of occurrence of a flood event and its characteristics, such as the magnitude, frequency, and duration of flooding. In contrast, flood exposure and vulnerability refer to the degree of susceptibility of a system to the impacts of a flood hazard. The combination of the above results in the flood risk, representing the probability of a flood event occurring and the potential negative consequences or impacts resulting from that event.

Under the 2007/60/EC Directive, each EU member state is required to proceed with the following reports:

- Preliminary Flood Risk Assessment (PFRA). The assessment focuses on identifying areas at potential risk, assessing historical flood events, and evaluating the potential adverse consequences of future floods for humans, the environment, cultural heritage, and economic activity.
- Flood Hazard and Risk Maps (FHRM). Flood hazard maps contain the potential extent, depth, and flow velocity for different probability scenarios, e.g., returning periods of 50, 100, and 1000 years, while risk maps also include the potential adverse consequences associated with the flood scenarios.
- Flood Risk Management Plan (FRMP): These plans aim to reduce flood risk through prevention, protection, and preparedness measures, considering environmental, social, and economic factors.

Furthermore, the Flood Directive recognizes the influence of climate change on flood risk. Therefore, the above reports are not only required to be reviewed every six years but the impact of climate change on the probability of flood occurrence is also stated to be addressed by considering climate change projections in the flood risk assessments and management

plans, which highlights the need for adaptive strategies to address changing flood patterns and potential impacts.

The directive follows the general principles laid by the 2000/60/EC directive, which focuses on water management. Specifically, the river basin approach is promoted, encouraging coordination and cooperation among member states sharing river basins or coastal areas, which leads to holistic and integrated management of flood risks, considering the interconnected nature of water systems. Moreover, the directive also emphasizes the importance of involving the public, stakeholders, and relevant authorities in flood risk management by encouraging member states to promote information sharing, public consultation, and cooperation at different levels to ensure effective flood risk management. Concerning the implementation of the Directive, the first implementation cycle was from 2010- 2015, while the second cycle covered the period from 2016-2021. The Commission assessed the second cycle's Preliminary Flood Risk Assessments as prepared by the Member States at the end of 2021 in the 6th Implementation Report in December 2021 (European Union 2021). The third cycle is ongoing and covers the years between 2022-2027. All states have completed the FRMPs of the first cycle, while the FRMPs of the second cycle have been sent to the commission by most Member states. Specifically, out of the 27 EU states, eight have not yet sent their second cycle FRMP to the commission, with the public consolation process either ongoing or just concluded as of March 2023. Greece features the most prolonged delays, where the second cycle FRMP has not yet reached the public consolation process (European Union 2021), although the second cycle PFRA has been sent (Directorate-General for Environment (European Commission) 2021).

1.3   Flood Early Warning Systems (FEWS)

1.3.1   Introduction

A Flood Early Warning System (FEWS) is a non-structural flood preparedness measure that does not focus on mitigating the impact of the hydrological characteristics of a flood. Instead, it focuses on providing the needed information to take timely actions to reduce the disaster risk. The United Nations Office for Disaster Risk Reduction (UNDRR) defines an EWS as "*an integrated system of hazard monitoring, forecasting, and prediction, disaster risk assessment, communication and preparedness activities systems and processes that enable individuals, communities, governments, businesses, and others to take timely actions to reduce disaster risks in advance of hazardous events*" (UNISDR 2017), while the World Meteorological Organization (WMO), defines a flood forecasting and warning system as "*the linkage between the basic structures*" that "*include provision of specific forecasts with magnitude and timing of*

rainfall, establishment of a network of hydrometric stations, operation of real-time flood forecasting model software and issuance of early flood warnings" (WMO 2013a).

Although not a direct flood mitigation measure, FEWS's ability to reduce the flood risk is widely acknowledged (UNDRR 2003; WMO 2013a; Pappenberger et al. 2015; Thielen-del Pozo et al. 2015), but there are not widely implemented in the required level worldwide. Specifically, a report made by the UNDRR (Perera et al. 2019) found that 43% featured an advanced EWS system, while 38% and 19% featured intermediate and basic systems, respectively. In a basic system, simple methods are used to observe and predict floods, such as manual collection and data transfer of stream level and rainfall, and do not feature a dedicated Flood Forecasting Center (FFC). The intermediate level uses more resources, such as real-time monitoring, but warnings are not issued after a model-based flood forecasting system but instead on the decision-making of flood forecasting professionals based on past experiences. Finally, advanced systems include all the available requirements for a proper FEWS implementation, such as a) telemetric data collection and transfer, b) model-based flood forecast, and c) continuous monitoring and updates. From the above, it is understandable that only advanced systems are model-based FEWS implementations, while the basic and intermediate levels mainly focus on observation and thresholds set manually, mainly by experience.

The WMO and UNODFF have begun an initiative to provide worldwide coverage of EWS, the "*Early Warnings of All*" initiative which is built around four key pillars, a) The disaster risk knowledge and management, b) Detection, observation, monitoring, analysis, and forecasting, c) Warning dissemination and communication and d) preparedness and response capabilities. The UN Secretary-General formally launched the initiative in November 2022 at the COP27 meeting in Sharm El-Sheikh to provide a worldwide EWS by the end of 2027.

1.3.2   FEWS Components

A FEWS consists of various components such as a) disaster risk knowledge, b) detection and monitoring analysis, c) forecasting and thresholds of hazards, d) warning dissemination and communication, e) preparedness to respond, and f) response capabilities (Perera et al. 2019). The first three components form the technical components, while the latter are non-technical. One of the most critical parameters of a FEWS is the forecasting lead time provided. However, attention should be given to the forecasted lead time by a FEWS since the actual lead time required in real-time may differ from the forecasted lead time. Actual lead time is subject to time delays due to data processing, model simulation, and even the time it takes to decide to issue the warning until the warning reaches its target. In Figure 1-5, an illustration of EWS time delays times in non-relative magnitudes is presented (Sene

2008). For instance, if the catchment response time is less than the forecast lead time, the EWS should rely on rainfall-based forecasts rather than rainfall-runoff simulation forecasts.
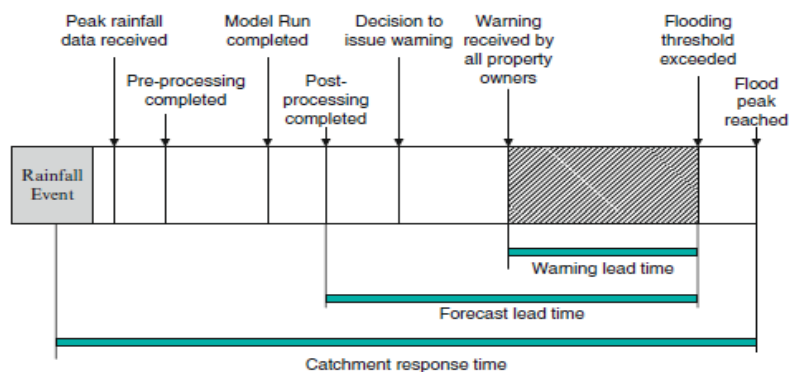
Figure 1-5: Illustration of time delays in issuing a warning for a single rainfall-runoff model
Source: (Sene 2008)

Therefore, although the technical components are decisive in providing sound flood risk estimations, they may be ineffective if the intended recipient does not receive the warnings, does not understand it, or cannot take action promptly (Perera et al. 2020). Below, the components of a FEWS are explained in more detail:

1. The disaster risk Knowledge component involves the knowledge of historical flood records in the area. Moreover, it involves risk mapping and vulnerability assessment to identify areas at higher risk of flooding and the potential impact on communities and infrastructure under continuous land use change conditions. This information helps in targeting warnings to specific areas and implementing mitigation measures.

2. The detection and monitoring component involves observing and forecasting the meteorological, river, and tidal conditions. Challenges in this component lie in the collection, quality control, and assimilation of real-time datasets concerning rainfall, river water levels, soil moisture, and other relevant hydrological parameters in sufficient temporal and spatial scales. A sufficient number of gauge stations and the implementation of quality controlled remote-sensed datasets such as weather radars and satellites are required to achieve high-quality datasets.

The Forecasting and Modeling component is the core of a FEWS implementation, as it uses forecasting and hydrological models to predict potential flood events. These models analyze current data and simulate future scenarios, providing forecasts of river flows and flood extents and allowing for timely warnings. Finally, the required thresholds, which are used to either issue or not a warning, are also derived in this component. Alternative words for thresholds include triggers, criteria, warning levels, critical conditions, alert levels, and alarms, which all denote the hydrometeorological conditions, allowing an acceptable lead time before the flooding threshold is reached. A decision should be reached to issue a flood

warning (Sene 2008). The hydrological variables used to define the thresholds may vary, such as rainfall accumulation or stage heights, and define the complexity of the FEWS and the models required. Challenges in the forecasting component mainly lie in producing high-resolution results in an increased lead time.

3.   The warning dissemination and communication component involves how the flood warning is disseminated to the public, local authorities, and emergency responders. Defined procedures should be established concerning which, to whom, and how information is transmitted. Typical channels may include text messages, sirens, mobile apps, social media, and other means to ensure broad and timely dissemination of information. The challenges lie in reaching the right stakeholders in a suitable format at the right time. For instance, simple text messages can be transmitted to the public in an adequate lead time, but more detailed information and hazard maps to the emergency response agencies in near real-time to form flood mitigation strategies.

The preparedness to respond and response capabilities components consist of the procedures followed after receiving a warning message or in case of a system failure. The preparedness mainly lies in the awareness of FEWS operators and developing a healthy understanding of detailed response plans. These plans should include information about which organizations and agencies, e.g., the civil protection, the police, and the social and health services, among others, should be involved to what an extent in responding to a flood event. Some key points of these plans should include (Sene 2008), a) clear chain of command for better coordination and information communicating to the public and the media, b) key contacts which are used for regular communication between the agencies, c) resilience of the system in case of a component failure, d) special arrangements concerning vulnerable groups, e.g., people with disabilities, elderly people and children and transient populations, i.e., the population that is temporary residents such as tourists and travelers, e) health and safety considerations apart from flooding, such as waterborne diseases, hazardous materials, and electrocution from exposed cables, f) community engagement for tailored response plans and g) continuous improvement of the system. Early warning systems work best when communities know the risks, understand the warnings, and know how to respond (Perera et al. 2020). Community engagement and awareness programs are crucial in ensuring people understand the importance of heeding flood warnings and know what actions to take. Training emergency responders and the public on how to respond to flood warnings also improves the community's overall preparedness. Finally, a FEWS system should undergo regular testing and exercises to ensure its functionality and effectiveness. Critical components of the system should have redundancies to minimize the risk of failure during critical situations by being reliable, resilient, and capable of functioning during adverse weather conditions.

These first three components, the technical components, define the system's complexity. A FEWS's primary purpose is first to identify areas that are vulnerable to flooding and secondly to be able to identify and monitor weather systems that produce flood events in a reasonable lead time (Spyrou et al. 2020). The first can be performed in non-real-time by studying historical events and multi-criteria analysis (Feloni et al. 2020) implemented into the FEWS. The second should be performed in near real-time, considering the requirement of high-resolution and quality results in adequate lead time. These two parameters are usually in direct contrast since a) high-resolution results may require more information and model processing time, leading to reduced lead times, and b) longer lead times require more extended forecasts, which are subject to higher uncertainty.

FEWS classification

When designing a FEWS, several considerations should be made, such as a) the forecasting requirement, b) the real-time data availability, c) the forecasting system on which the model will operate, d) the required model performance, and e) the time, budget, and skills available for the model implementation (Sene 2008). The forecasting requirement is usually formed by the end user needs but restrained by the real-time data availability and the budget. Typical forecasting requirements are presented in Table 1-1 in a general descending order considering model complexity.

Table 1-1: Typical applications of flood forecasting Source: (Sene 2008)

Requirements	Typical Applications
To provide additional warning lead time	Providing the emergency services and public with advanced warning of the likely times for the onset of flooding or the peak of the flood event
To estimate peak levels or flows.	As above, also providing estimates for peak values, perhaps also linking to maps of likely flooding extent based on off-line simulation modeling or past experience
To estimate flooding duration.	As above, also considering when to issue the message that the flood risk has reduced or passed
To model flooding depths, extent, and possibly, velocities.	As above, but providing real-time updates to the likely spatial extent of flooding, together with depths and velocities at general or specific locations (districts, roads, houses, etc.)
To provide information to assist with the operation of control structures	Optimizing response to mitigate flooding (e.g., at dams, river control structures, tidal barriers etc.) and possibly to reduce penalty payments and opportunity losses
To provide information to assist with event-specific factors	Providing advice on the implications of various problems arising during an event; for example, failure of flood defense, blockages by debris, pumps failing etc. Also, exploring different options for response (e.g., controlled diversion of flows)

For instance, when only additional warning lead time is required, the FEWS can be designed to monitor only rainfall intensities and compare them to pre-defined thresholds. However, if peak flows or event depths and velocities are required, then hydrological and hydrodynamic modeling is required. These requirements define the needed processes that the FEWS should be simulating. The overall model complexity is determined by the model parameters and resolution, i.e., the spatial and temporal resolution of the used datasets and provided results, as well as the use of sophisticated models for the hydrological, hydrodynamic, and forecasting processes. Apart from requirements for specific control structure operations, i.e., dams and barriers, most FEWS usually meet the first two requirements, i.e., the additional warning lead time and the estimation of peak levels and flows.

FEWS design is based on various parameters such as a) the provided lead times, b) the models and processes used, and c) the scale. In Table 1-2, such a classification is shown, along with their characteristics. For instance, a FEWS designed for flash flood events would focus on short-term forecasting, while a FEWS designed for river basin monitoring may focus on medium-term forecasts. The difference in scale often defines the models and hydrological processes used since strictly meteorological forecasts are often used with long-term weather assessment or with short-term flash flood systems, where the provided forecast times are not allowed to provide adequate forecasting times. The FEWS implementation scale also defines the results' spatial resolution. When nationwide or large regions are studied, increasing the spatial resolution may lead to significant computing times, which do not usually add to the purpose of an EWS, such as providing simple warning lead times in large areas. In contrast, in local applications such as the protection of urban areas and sensitive facilities, the cost of flooding is higher, and therefore integrated hydrological and hydrodynamic models are preferred due to their high-resolution products.

Table 1-2: FEWS Classification based on several characteristics

Characteristics	#1	#2	#3
Based on Lead Times (Forecast time)	Short-term 1 - 6 hours	Medium-term Hours - days	Long-term Weeks - months
Based on the Models used (Thresholds)	Meteorological Rainfall Thresholds	Hydrological Flow/Stage Thresholds	Integrated Flood depth Flood extent
Based on Scale (Spatial Resolution)	National Level Small	Regional Medium	Local High

Most FEWS applications usually focus on short-term and medium-term forecasts based on either rainfall or flow and stage flow thresholds. Medium-term systems are used when flood

warnings are required for medium and large river basins with extensive concentration time. In these cases, flooding occurs several hours after a rainfall event. Therefore, flow-based systems that use single or multipoint stage-water observations provide better, more detailed information. In such cases, using medium-range forecasts is advantageous since they provide increased lead time, while the continuous monitoring of the event provides less uncertainty regarding the hydrological processes involved. Short-term systems, usually referred to as nowcasts, aim to provide warnings for fast-paced rainfall events such as flash floods. Flash floods usually occur due to convection and are characterized by their high-intensity rainfall rates and local footprint. In these events, a FEWS is usually designed to use rainfall thresholds since there is no time to monitor the river's stage and flow conditions.

The main difference between rainfall-based and flow-based FEWS implementations lies in the hydrological variables each system uses as the threshold. A rainfall-based system will use a rainfall-derived product as the flood threshold, such as rainfall intensity and accumulation, while a flow-based system relies on flow-derived products, such as peak discharge, flood volume, and stage. Flow-based systems usually derive more information but require more data to calibrate and operate. A rainfall-based system compares current and forecasted weather conditions, but in most cases, a rainfall-runoff modeling process is intergraded to assess the hydrological causes of flooding. Compared with a flow-based system, the main issue with a rainfall-based system is that they cannot predict the exact time and place where flooding may occur. However, they are more cost-effective and can be easier applied and maintained (Suhardi et al. 2020).

Moreover, the majority of any uncertainty involved in any system is caused by the quality of the rainfall forecasts made. In flash floods with fine time scales, a rainfall-based system can be as reliable as the flow-based system in flash floods at high rainfall return periods (Corral et al. 2019). The key to maximizing the performance of a rainfall-based system is the quality of high-resolution rainfall forecasts. To that end, the use of well-calibrated weather radar QPE with increased spatial and temporal scales, such as the ones provided by new X-Band weather radar systems, is a crucial component for accurate and effective FEWS (Anagnostou et al. 2010, 2018; Borga et al. 2011; Picciotti et al. 2013).

1.3.3 FEWS Implementations

MeteoAlarm

MeteoAlarm is a rainfall threshold-based EWS implemented in 37 European countries through their National Meteorological and Hydrological Services (NMHSs). Although not a Flood EWS, since MeteoAlarm is easier to be implemented, it is often used as a rainfall-based FEWS when more advanced systems are not in place (Staudinger et al. 2009).

The system aims to streamline the dissemination of weather warnings and ensure that timely and accurate information reaches the public to improve preparedness and response to adverse weather conditions. The system observes up to 12 weather parameters, such as temperature and rainfall rate, and uses a color-coded system to represent different levels of weather warnings based on the following:

- Green: No warnings - no particular awareness of the weather is required.
- Yellow: Be aware - the weather situation is potentially dangerous; people should be attentive to changes in weather conditions.
- Orange: Be prepared - there is a high likelihood of severe weather, and people should take action to protect themselves and their property.
- Red: Take action - severe weather is expected, and people must take immediate action to stay safe.

The system lacks any modeling processes and uses deterministic thresholds for each hydrometeorological parameter derived from each NMHS. The spatial resolution of the warnings is usually at an administrative prefecture scale. Nevertheless, the system is still operational since it acts as a one-stop-shop service where data can easily be implemented into cell phone weather applications (Kaltenberger 2022).

European Flood Awareness System (EFAS)

The EFAS system is a FEWS implementation to improve the preparedness for floods within Europe. It was the first service of the Copernicus Emergency Management Service (CEMS), launched in 2013 and, since 2012, is fully operational. The System is designed to provide early flood warnings and forecasts, particularly in large trans-national river basins, even up to five days in advance. The CEMS Meteorological and Hydrological Data Collection Centers (MDCC and HDCC, respectively) collect and analyze the datasets. The EFAS products are available in real-time only for the national agencies, while archived products older than one month are available under specific terms and conditions. The generated products are:

- Flash-flood indicators: indication of flood risk from flash floods up to 5 days,
- Medium-range flood forecasts: Upcoming flood events up to 10 days,
- Seasonal hydrological outlooks: Hydrological situation over the next eight weeks
- Flood impact forecasts: Regions where flood impacts are expected in the next ten days.

The system first targeted the medium-range flood forecasts aimed at large river systems often found in central Europe. To that end, the generated products are points within the river network. EFAS hydrological forecasting chain is designed to follow three key

elements, a) the meteorological forcing and land surface data, b) the hydrological models, and c) the EFAS forecasts and products.

The meteorological forcing and land surface data are divided into three groups, a) the historical hydro-meteorological time series records and land surface data, b) the real-time hydro-meteorological observations, and c) the meteorological forecasts. The historical data are the data that are collected and used to calibrate and validate the models, while the real-time datasets are collected through numerous sources, such as national agencies, and quality checked by the MDCC and HDCC. Finally, the meteorological forecasts are forecasts in either a single realization or an ensemble (multiple realizations) from a single Numerical Weather Prediction System (NWPS), using the real-time datasets as the forecast's starting point.

The EFAS system makes use of the LISFLOOD hydrological model. The model is a spatially distributed conceptual and physical-based rainfall-runoff model explicitly designed for large river basins (Thielen et al. 2009). The model simulates canopy and surface processes, soil and groundwater flow, and river channel flow. It incorporates precipitation, temperature, potential evaporation, and evaporation rates for open water and bare soil using two soil layers, Topsoil and Subsoil. More information and a complete description of the LISFLOOD model can be found in (Van Der Knijff et al. 2010). The model datasets required are easily accessible since they are in line with European-wide available datasets. The model is used in 6-hour and daily time steps using five km grid cells of the EFAS domain. The runoff generated in each grid is then routed downstream using the kinematic wave approach.

Finally, the EFAS meteorological forecasts are forced into the LISFLOOD model to produce a series of forecasting products. The model is used in a deterministic simulation, i.e., single forecast, or ensemble forcing, i.e., multiple realizations. The simulations are performed in 6-h and daily steps. The results for each cell are then compared with flood thresholds derived after statistical analysis. Specifically, threshold classes are derived based on the associated hazard class as low (L), medium (M), high (H), and severe (S). Low and medium classes report high water levels but no flood expected, while high and severe denote flooding, with high reporting near bank-full conditions. The classification is based on a quantile approach, where a selected time-return period, e.g., 5- 10- and 20- years, is defined as the threshold.

Considering Flash Flood indicators, the EFAS system uses two approaches. The first is the ERIC system (Alfieri and Thielen 2015; Raynaud et al. 2015), where forecasts are performed using numerical weather prediction datasets and the LISFLOOD model to provide surface runoff in a 1 km x 1 km spatial scale. Following this, the accumulated flow in pre-specified points, the ERIC reporting points for 6, 12, and 24-hour periods, is compared with thresholds derived from the mean annual maximum from 20-year climatology datasets. The products

derived are the probability of flash flooding in the reporting points for a provided lead time of fewer than 48 hours and the ERIC affected area, i.e., the river network contributing to each ERIC reporting point, indicating the areas at risk from flash flooding.

The second approach is the EPICHA system (Park et al. 2017, 2019), based on radar precipitation monitoring and nowcasting. In this approach, the European OPERA radar composite provides nowcasts, using the Lagrangian persistent up to 6 hours ahead, for rainfall accumulation of 1-, 3-, 6-, 12- and 24-hour periods. The forecasted rainfall accumulation is then compared with regional intensity duration thresholds derived from the regional climatic characteristics and river basin upstream area, as published by the MeteoAlarm consortium. The EPICHA flash flood indicators are generated every 15 minutes, in a 1 km x 1km grid scale and up to 6 hours lead time. The benefit of this approach lies in providing products outside the river network on a high-resolution temporal scale aimed at very localized events that are difficult to predict with NWPSs. The downside is the provided lead time, i.e., less than 6 hours, which is much less than what is provided by the ERIC system.

The Flash Flood Guidance System (FFG)

The Flash Flood Guidance (FFG) system was designed and developed by the Hydrological Research Center (HRC) for the US National Weather Service (NWS), which currently still uses operationally in the USA for protection against flash floods. The system was developed in the 1980s to combine meteorological and hydrological processes in real-time to produce operational flash flood predictions. The system relies on estimating two hydrological parameters, a) the threshold runoff and b) the Flash Flood Guidance (FFG) value. The threshold runoff is defined as "*the volume of effective rainfall of given duration that is generated over a given catchment area, and that is just enough to cause bankfull flow at the outlet of the draining stream,*" while the FFG value is defined as "*the volume of actual rainfall of a given duration, that generates the said threshold runoff*" (Georgakakos 2006). The first is equal to the surface runoff that produces bankfull conditions and therefore is related to the basin's characteristics, such as the basin's area, slope, land use, and cross-section dimensions. The second one, the FFG value, is the output of the system and denotes the amount of rainfall of a given duration that is required to generate the threshold runoff conditions (Georgakakos 1986, 2006; Norbiato et al. 2008; Hapuarachchi et al. 2011; Douinot et al. 2016). When the rainfall losses and runoff are known, the FFG value can be calculated using reverse rainfall-runoff modeling. Since the threshold runoff is static, the FFG value varies based on soil moisture conditions that act as rainfall loss interpretation. In saturated soil moisture conditions, a lower value of FFG is expected, denoting that less rainfall is required to reach the runoff threshold. The FFG value is then used as a rainfall-based threshold above which minor flooding will occur.

The system is used as a decision support system, meaning it does not produce robust deterministic flood warnings but through its multiple products.

The system is divided into three components; the threshold runoff component, the hydrological model, and the FFG computations. The first is a pre-process of the system, which aims to derivate the threshold runoff value. The second involves the continuous hydrological simulation of the study area, used to obtain the current and future soil moisture conditions before the storm. Finally, the FFG computations involve the FFG value's real-time computations and the comparisons made with forecasted values.

Since the NRCS has used the system for operational usage, there have been numerous studies concerning the various components of the system. While research on the estimation of the threshold runoff value is deemed crucial (Carpenter et al. 1999; Reed et al. 2002; Kim and Bae 2006), the majority of the research concern the Hydrological model used (Finnerty et al. 1997; Gupta et al. 1998; Carpenter et al. 1999; Anderson 2002; Norbiato et al. 2008, 2009). Specifically, the Sacramento Soil Moisture Accounting (SAC-SMA) hydrological model is being used in the operational system, which features two soil layers, upper and lower zones, while 16 parameters govern all the hydrological processes. Therefore, the primary part research focused on the SAC-SMA model, specifically the optimization algorithm and procedure of its parameters (Gupta et al. 1998; Hogue et al. 2000; Koren et al. 2000; Boyle et al. 2001; Anderson 2002; Norbiato et al. 2008, 2009; Zhang et al. 2011; Wu et al. 2012). Moreover, although the model was designed to be a deterministic, lumped-based model for daily simulations, it has been used as a semi-distributed model (Boyle et al. 2001) and in distributed form (Smith et al. 2004; Reed et al. 2007) as well, while it is the temporal scale has also been explored (Finnerty et al. 1997; Bournas and Baltas 2021a). Overall, the SAC-SMA model has proven to be robust, with the advantage of applying a-priori estimation of its parameters, based on soil characteristics (Koren et al. 2000, 2003; Anderson et al. 2006), making it applicable in ungauged basins where FFG values are estimated. Nonetheless, other hydrological models and implementations of the FFG system have been used with promising results, such as the ones concerning different spatial resolutions, leading to the lumped FFG (LFFG) (Sweeney 1992), the Flash Potential Index (FFPI), (Smith 2003), the Gridded Flash Flood Guidance (GFFG) (Schmidt et al. 2007) and the Distributed Flash Flood Guidance (DFFG), (Clark et al. 2014). Finally, various studies focused on the success rate of the flood warning estimations on historical events, which led to the conclusion that although the system performed well, improvements are possible through more precise calibration and simulation of the system using and high-resolution datasets (Seo and Breidenbach 2002; Norbiato et al. 2009; Patsinghasanee et al. 2017).

The FFG concept has also been applied for Global coverage by the WMO, utilizing satellite-derived soil and weather datasets. Implementations have been established in South and

West Africa, Southeast Europe, Turkey, India, South and Central Asia, and Central America (Georgakakos et al. 2022). The FFG concept does not require high-temporal and tuned hydrological modeling, is easy to understand and implement, and therefore, is considered practical and easy to operate FFWS (Hapuarachchi et al. 2011; Zeng et al. 2016; Georgakakos et al. 2022). The FFG systems are continuously evolving, favoring a) the training of local forecasters to improve the quality of forecasts and decision-making, b) the use of better quality datasets, c) implementations of urban flash flood forecasting, landslide assessment, and riverine routing, and d) continuous development of ancillary system products for agriculture (Georgakakos et al. 2022). The FFG long process of a Research to Operation (R2O) FFWS has shown that such systems should be continuously evolving through the collaboration of nation-based forecasts and system configurators to tailor the system to the individual country needs (Georgakakos et al. 2022).

FEWS in Greece

A dedicated flood or flash flood alert system does not exist in Greece. As a member of the EU, Greece benefits from products with European coverage. To that end, Greece uses the Copernicus emergency programs, specifically for floods, the EFAS system. As beforementioned, the EFAS system focuses mainly on medium-term forecasts for medium and large river systems. Such systems are rarely found in Greece since Greece features an extensive coastline and thus is subjectable mainly to flash floods and floods of small ephemeral rivers. Flash flood products such as ERIC and EPICHA are deemed more valuable for application in Greece. However, the EPICHA product, which is capable to provide up to 6-hour nowcasts, is unavailable due to the non-coverage of the OPERA weather radar composite in Greece. At the same time, the ERIC system focuses on specific rivers which require continuous monitoring and are usually not the case of recent flooding events in Greece.

Greece's only EWS application is the MeteoAlert system, a meteorological warning system that uses pre-determined rainfall thresholds based on historical events and experience. The National Hellenic Meteorological Service (NMMS) provides such forecasts and warnings in daily reports, but they usually lack the needed temporal-spatial information to deal with flash flood events. In the wake of catastrophic floods (Diakakis et al. 2019, 2022; Feloni et al. 2020; Varlas et al. 2021), as well as other natural disasters, mainly wildfires, a warning transmission system, the "112" system is being used to transmit warning messages about natural disasters is being implemented. The message includes information about the areas where natural disasters occur or may occur, along with evacuation directions. Although the system has not been validated yet, it is deemed to have increased the awareness of people to the risks of natural disasters (Diakakis et al. 2022). Overall, the system works best when the events occur, while forecasted warnings are mainly based on MeteoAlarm products. In

general, FEWS focuses on flash floods and relies their products on the use of weather radar nowcasts, in contrast to NWP forecasts which are the only source of forecasts provided in Greece. Greece's weather radars are currently not used to warn against floods, a widely discussed problem (Kolydas 2023).

1.4   Means of Precipitation Measurement

The measurement and estimation of the precipitation field remains a challenging task in both meteorology and hydrology. The instruments used to measure precipitations can be categorized into two groups: ones that detect and quantify rainfall at the surface, such as rain gauges and disdrometers, and the remote-sensed instruments that measure rainfall well above the ground (Michaelides et al. 2009). Both instrument categories tend to measure the flux of the DSD using different methods, which do not always correlate with each other. Remote-sensed instruments can provide estimates of the entire rainfall field instantly, while on-surface instruments require a designated network and the application of interpolation algorithms.

Rainfall gauge stations provide point measurements of precipitation using various technologies such as an accumulation mechanism, a tipping bucket, a weighting type, and optical technology. In each case, the measurement mechanism differs, improving the quality of the measurement or the temporal resolution. The oldest method is the accumulation mechanism, which uses a simple cylinder to record precipitation on a rolling paper. However, problems with digitization and temporal distribution resulted in preferring a tipping bucket technology, which is the most cost-effective and used type of rain gauge. The weighting type gauge uses a high sensitivity weight mechanism to measure the input precipitation, which offers advantages over the tipping bucket, both in quality since it does not underestimate high rainfall rates and applications since it can measure hail and snow. Optical rain gauges are similar to disdrometers, using a light beam source and a detector to identify and measure falling hydrometers. The weight-type and optical rain gauges provide significant quality improvements but are more expensive and require more maintenance, making the tipping bucket the most typical technology in existing rainfall gauge networks. In either case, the datasets are stored in a digital recorder within the rain gauge station, and their extraction is made by either an in-situ visit to the station or by transmitting them through a wired or wireless network connection, e.g., GPRS, should an internet connection is available to the location.

The main advantage of rain gauges over remote-sensed instruments is the quality of precipitation measurement at the station level, which is often referred to as the "true rainfall" since rainfall, in hydrological applications, is the amount of water that reaches and

is measured in the ground level instead in the upper level's atmosphere. The main disadvantage, however, is that they are point measurements of rainfall height and, therefore, cannot represent the spatial variability of a rainfall field. Instead, a rain gauge network must first be established, and an area interpolation algorithm, e.g., Inverse Distance Weighting (IDW) method or geostatic methods (Kriging), should be applied. This interpolation tends to correlate the quality of a generated rainfall field with the density of the station network. A dense network will most likely recreate the rainfall field with acceptable accuracy, but a sparse network's generated rainfall field will most likely have quality issues regardless of the interpolation algorithm used. The desired density of a rain gauge network depends on the application.

In most cases, rainfall datasets are required for weather monitoring or hydrological applications; thus, the density is designed to fit in specific administrative borders or onto a specific basin. The World Meteorological Organization (WMO 2008) provides general guidelines for implementing such networks, but practical reasons, such installation issues, e.g., power and internet connections, as well as practical reasons, e.g., inaccessibility of designated locations and equipment safety, among others, has often led to the formation of heterogenous rain gauge networks, with inappropriate density for basin scale applications. For instance, in Attica, Greece, most rain gauge stations tend to be located within or near cities, while high-elevation areas are non-represented according to the guidelines (Theochari et al. 2021). Moreover, the demand for high-resolution data in real-time has raised the cost of each station, making the maintenance of the entire network challenging. An un-maintained rain gauge can accumulate many problems due to weather exposure, reducing the measured data quality (La Barbera et al. 2002).

For these reasons, more efficient ways involving remote-sensed precipitation measurements, i.e., weather radars and satellites, have increased attention (Berenguer et al. 2005). Weather radars have a long history of implementation. They are considered the best data source for rainfall-runoff modeling and storm-tracking applications (Price et al. 2014), while satellite data are recent implementations gaining ground due to their accessibility of datasets with extensive coverage (Gilewski and Nawalany 2018).

Weather radars use radio waves to detect and measure the reflectivity of objects, which is later transformed into rainfall intensity, whereas satellites measure the radiation emitted or reflected by clouds and precipitation. The instrument's main differences lie in the generated product's spatial and temporal resolution. Weather radars provide better resolution and quality datasets than satellite measurements but are restricted to a pre-specified range. Satellites instead tend to cover broader views, such as continental and even global views, with reasonable accuracy. Satellite datasets are preferred for meteorological applications, such as monitoring cloud movement and formation in the cynoptic, and less on mesoscale

systems, while weather radars are preferred for mesoscale and microscale storm tracking and rainfall-runoff applications. Table 1-3 features the characteristics, advantages, and disadvantages of the above means of precipitation field estimation.

The most reoccurring debate in rainfall-runoff applications is about the advantages and disadvantages of rain gauges to weather radar. Rain gauge measurements require a network with a proper density to represent the rainfall field but tend to feature the best quality regarding the actual rainfall measurements. On the other hand, a weather radar tends to feature a better spatial representation of rainfall but is subject to quantitate errors due to its remote-sensed nature. Weather radar datasets require proper quality control and calibration of the radar system to reduce errors derived by signal errors, attenuation, noise, and transformation to rainfall rate (Villarini and Krajewski 2010; Pathak et al. 2013).

Table 1-3: Most frequently used means of precipitation field estimation

Recording Device	Spatial Resolution/ Weather Scale	Temporal Resolution	Advantages	Disadvantages
Rain Gauge Network	Interpolation of Point Measurements Microscale/ Mesoscale	1 min - 1 h	High-quality measurements on points location	Low Spatial Resolution Difficult maintenance
Weather Radar Network	0.5 - 2.0 km Mesoscale	5-15 min	High spatial resolution	Numerous measurement Errors
Meteorological Satellites	4 - 6 km Cynoptic Scale	5-15 min	High area coverage High data availability Good reproduction of clouds location	Numerous measurement Errors Low-Quality QPE Low Spatial Resolution

The preference between the use of the two products is usually related to the required application for the actual datasets to be used. Since weather radars provide better spatial and temporal resolution compared to rain gauges, their use has seen increased interest in numerous applications such as hydrological modeling and simulation and storm tracking and forecasting (K. Ajami et al. 2004; Nanding et al. 2015; Anagnostou et al. 2018; Grek and Zhuravlev 2020; Schleiss et al. 2020; Sokol et al. 2021). The gridded nature of the radar datasets is intergraded better when fully distributed models are used, semi-distributed and lumped models can also be used through the aggregation of the datasets in either coarser scales or in sub-basin and basin scales by calculating the Mean Areal Precipitation (MAP).

A critical factor in all studies is the scale of the analysis. While the spatial scale can be easily configured through modeling, the temporal resolution between radar and rain gauges must be identified and analyzed accordingly (Paschalis et al. 2013; Price et al. 2014; Schleiss et al. 2020). Another factor involving the desired rainfall field representation resolution is the size of the basin examined. Specifically, in small basins, such as urban basins, the required

resolution is much higher than in larger basins. In the work of Berne et al. (2004), two equations that relate the basin size and the required spatial and temporal resolutions are as follows:

$$\Delta t = 0.75A^{0.3} \tag{1.1}$$

$$\Delta x = 1.5\Delta t \tag{1.2}$$

where Δt [s] is the required temporal resolution, A[km²] is the basin area, and Δx[m] is the desired spatial resolution. By solving the above equations, Figure 1-6 forms, where it is easily observed that for basins below 10 km², the desired temporal resolution of the rainfall field should be less than six minutes, and its spatial resolution should be less than 4 km x 4 km. This finding indicates that in small catchments, the limitation of the required rainfall fields lies more on their temporal resolution rather than their respective spatial resolution. Above 100 km², the spatial resolution limitation becomes more critical than temporal resolution.
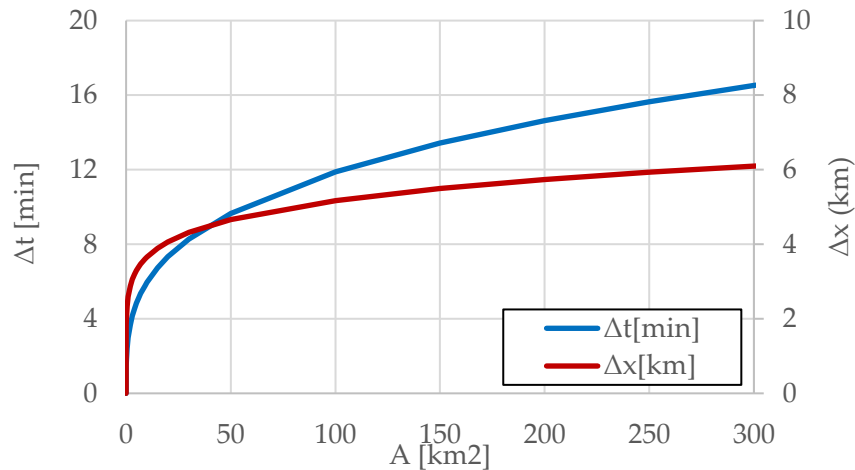
Figure 1-6: Relationship between temporal and spatial resolution of precipitation to the basin area based on Eq. 1.1 and 1.2 by Berne et. al (2004)

In any case, it is vital to notice that while radars feature higher spatial and temporal resolution, their application in rainfall-runoff modeling does not always translate into more accurate estimations (Cunha et al. 2015; Seo et al. 2015a). The problem is mainly the significant processes and quality control needed to obtain good QPE from the radar system. Moreover, while calibrating a weather radar system secures the correction of systematic errors, weather-related errors are difficult to correct using a single weather radar image. To that end, weather radar rainfall estimates are best used after being corrected using rain gauge measurements. This practice yields better accuracy than raw unadjusted radar estimates (Borga 2002; Zhang and Srinivasan 2010). Overall, advances in radar and computer technology have increased the number of high-quality QPE applications (Collier 1996; Sokol et al. 2021).

1.5   Weather Radar

1.5.1   Introduction

Weather Radars ought their development to the radar technology which was developed and used for military use before, during, and after World War II. A Radar, an acronym of Radio Detection and Ranging, is an instrument that generates, transmits, and receives electromagnetic waves to detect objects at a maximum distance and minimum size restricted by the power of the transmitted signal and wavelength, respectively. The original scope of radar systems was to locate enemy ships and aircraft. However, scientists during and after the war noticed echoes and noise in the scans where rainfall occurred. Although this was first considered an annoyance instead of a significant interest (Probert-Jones 1990), scientists began closely examining the correlation between precipitation and the generated echoes. The basis of weather radar meteorology was established first with the work of Ryde (1946) on the attenuation and radar echoes produced by various meteorological phenomena at the centimeter wavelengths, followed by the work of Marshal and Palmer (1948), which were first to show and establish a relationship between the radar reflectivity (Z) and rainfall intensity (R), based on measurements of rainfall Drop Size Distribution (DSD), the so-called Z-R relationship.

1.5.2   Types of Weather Radars

Weather radars can be classified based on several characteristics. The most common classification is based on the wavelength they use, which is related to the wave frequency and the speed of light as follows:

$$c = f * \lambda \tag{1.3}$$

where c is the speed of light [cm/s], f is the frequency [1/s], and λ the wavelength [cm]. Since the speed of light is constant, the other variable is determined by setting a desired frequency or wavelength, making the choice of a higher wave frequency into the production of a smaller wavelength. In Table 1-4, the most typical weather radar types are shown based on the selection of frequency or wavelength. As the table suggests, the most typical weather radar types for precipitation monitoring are the S-Band, C-Band, and X-Band radar systems, which operate in wavelengths of 3, 5, and 10 cm, respectively. Although the frequency value defines the wavelength, the wavelength value is critical since a longer wavelength has better penetration capabilities, i.e., is less subject to signal attenuation and can measure in long ranges. A typical S-Band can operate at more than 300 km, while a C-Band up to 200 km and an X-Band at 100 km, although precise QPE is obtained for up to 200 km, 100-150 km, and 50 km for each radar type, respectively. On the other hand, a smaller wavelength makes it possible to detect smaller targets, thus, featuring the best spatial resolution.

Table 1-4: Common Weather Radar Types used in weather radar monitoring

Type	Frequency	Wave Length	Application
S-Band	2.9 GHz	10 cm	Precipitation
C-Band	5.6 GHz	5.4 cm	Precipitation
X-Band	10 GHz	3 cm	Precipitation
K-Band	25 GHz	1.2 cm	Clouds
W-Band	95 GHz	3 mm	Clouds

S-Band radars are much more prominent in size than the respected C-Band and X-Band radars, making them more expensive in their purchase and deployment, as well as their maintenance, while X-Band radars are versatile, much smaller in size, e.g., they can be mounted even in a vehicle, and much more cost-effective (Berenguer et al. 2012), making them better for applications in a local scale.

The choice of a weather radar type depends on several factors, such as a) the desired coverage area, b) the desired purpose and applications to be used, c) the desired spatial and temporal resolution, and d) the available budget and resources. The score of each radar in the respected characteristics is featured in Table 1-5. An S-Band radar features small spatial resolution but low signal attenuation and, thus, the most extensive coverage. An X-Band is the least expensive and features high spatial resolution but small coverage. C-Band radars combine the above benefits and problems, but their usage and size are more typical to the respected S-Band systems than the X-Band systems, which are strictly local solutions.

Table 1-5: Radar Types Scores on selected characteristics

Characteristic	S-Band	C-Band	X-Band
Frequency	2.7 – 2.9 GHz	5.6-5.65 GHz	9.3 – 9.5 GHz
Wave Length	11 cm	5.4 cm	3 cm
Quality QPE Range	200 km	100-150 km	50 km
Spatial Resolution	+	++	+++
Ability to detect small particles	+	++	+++
Signal Attenuation	+	++	+++
Cost	+++	++	+
Coverage	+++	++	+
Applications	National Coverage in Flat Terrains	National Coverage in Orography	Local Coverage

In practice, the national meteorological services use S-Band and C-Band systems for their respective national weather monitoring services. S-Bands are best deployed when the

observation areas are usually flat, and no issues are generated from the orography, beam height, or other sources of clutter and beam blockage, while C-Band radars are preferred when such issues appear.

X-Band systems are only recently being utilized because their small coverage did not fit nationwide weather monitoring. However, currently, they are preferred to be used to fill gaps in already integrated weather radar networks, especially in complex mountainous regions and urban areas, where high beam blockage and vertical profile variability is present (Anagnostou et al. 2010, 2018; Sokol et al. 2021). Moreover, X-Band systems are also used to increase the spatial and temporal resolution of weather radar monitoring for specialized applications such as early warning applications for outdoor sports events, local media, military, research, and development. The increased spatial and temporal detail allows for better analysis of the subtle interplay between the spatial and temporal rainfall variability and the sensor-controlled spatial and temporal resolution (Uijlenhoet et al. 1999).

Apart from the spatial resolution of a weather radar system governed by the selected wavelength, another critical factor regarding object identification is the temporal resolution of the radar system, which is determined by the selected Pulse Length and Pulse Repetition Frequency (PRF). Since the weather radar signals are not transmitted continuously but in pulses, the pulse length refers to the duration of each transmitted radar pulse and determines the temporal resolution of the radar system, while PRF refers to the rate at which the radar transmits pulses. The pulse length is an essential factor of a weather radar since it controls its ability to distinguish between targets close together in range. A longer pulse length will detect weaker and more distant targets since more power per pulse is transmitted, resulting in fewer second-trip echoes, while a short pulse provides better resolution and can detect small-scaled features. However, short pulse lengths can be subject to signal attenuation due to heavy precipitation since they are more likely to be absorbed or scattered by large raindrops. The PRF value is chosen in relationship to the pulse length. Higher PRF values increase the maximum range but reduce the range resolution. Moreover, by choosing an appropriate PRF, the radar can minimize the overlap between the clutter spectrum and the desired Doppler spectrum of the weather targets, which helps better identify and separate moving weather features.

Optimizing the pulse length and PRF in a weather radar system involves considering trade-offs between range resolution and coverage. A short pulse length usually uses a high PRF and the opposite.

1.5.3   Historical use of Weather Radars

Weather Radars in the USA

Most research regarding weather radar usage was performed in the United States (US). The first operational Weather Radar System, the WSR-57, was introduced in 1957 by the US Weather Bureau. The first radar system was installed in Miami in 1959 and the last in Charleston, US, in 1996 (Whiton et al. 1998). The system operated on the 10-centimeter wavelength (S-Band), which allowed a maximum range of approximately 350 km. The system provided enough information, which led to essential updates, mainly regarding the spatial and temporal resolution of the precipitation fields. In 1974, the system was updated to the WSR-74, which provided information regarding the intensity, location, and movement of precipitation compared to the WSR-57, which only allowed the visualization of echoes as patterns of varying intensity. The final upgrade to the US weather monitoring program came in 1988, with the WSR-88D system, also known as the NEXRAD (Next Generation Weather Radar), developed by the National Weather Service (NWS) and the Federal Aviation Administration (FAA). The system introduced the Doppler technology to weather surveillance, where the Doppler effect was being utilized to provide measurements of the precipitation particle's velocity, allowing the detection of wind patterns within the storms necessary for the observation of phenomena such as tornadoes, thunderstorms, and mesoscale weather systems. The NEXRAD system now features 160 S-Band radars, with varying spatial accuracy depending on data type and scan angle, with an initial level III resolution of 1 km x 1 km, updated in all systems in 2008 to the level II resolution of 250 m x 250 m. Although the system still operates, several enchantments in selected radars or networks have been applied and planned. These include main advances in weather radar monitoring, such as dual polarization, advanced signal processing, increased resolutions, and phased array technology.

Weather Radars in Europe

In Europe, the first weather radars were deployed in the 1970s in the United Kingdom (UK) and France, leading to the development of the UK's Met Office Nimrod and the Meteo-France ARAMIS systems. Due to the low exchange of datasets during that time, a bottom-up approach was used to develop a European network, where a radar network is sought to be developed on existing individual radar systems. Each country's meteorological service independently developed its national-wide operational network radar, and only by 1990, through the European Meteorological Services Network (EUMETNET) initiative, did data exchange start to occur. This has led to numerous issues regarding the development of a single weather radar network for the entire of Europe since high heterogeneity exists regarding a) the technology and age of the radar systems, b) the scanning strategies, c) the

signal processing, and d) the product generation (Huuskonen et al. 2014). The median height of the radar antennas in the European network is 256 m above the mean sea, with the highest being 2824 m located in Valluga (Austria; Alps Mountains) and the lowest is only 14.5m, located in Røst (an island in the Norwegian Sea) (Huuskonen et al. 2014). Currently, there are approximately 205 weather radars, of which the majority are of 5 cm wavelength (C-Band), as shown in Figure 1-7. Although many challenges have been overcome, heterogeneity exists since the national services operate and maintain the radar networks. The radar data exchange initiative is coordinated by the Operational Program for Exchange of Weather Radar Information (OPERA), established in 1999. The program is also called the equivalent of "Europe's NEXTRAD, " which generates a European Radar Mosaic through the OPERA Radar Data Center ODYSSEY. The ODYSSEY data center initially used 134 radar sites from 21 countries to provide, in real-time, three continental-scale mosaic products, i.e., the 15-min surface rain rate and maximum reflectivity and 1-hour rainfall accumulation (Mattheus et al. 2012). Currently, the center incorporates 163 sites from 25 countries (Saltikoff et al. 2019b), as seen in Figure 1-7, where the locations of the weather radars and their type are shown in the left panel, while in the right, the composite of the annual precipitation for the year 2018 is shown. The right panel of Figure 2-1 shows that the system does not include datasets from Italy or Greece, as no data is shown in these areas.
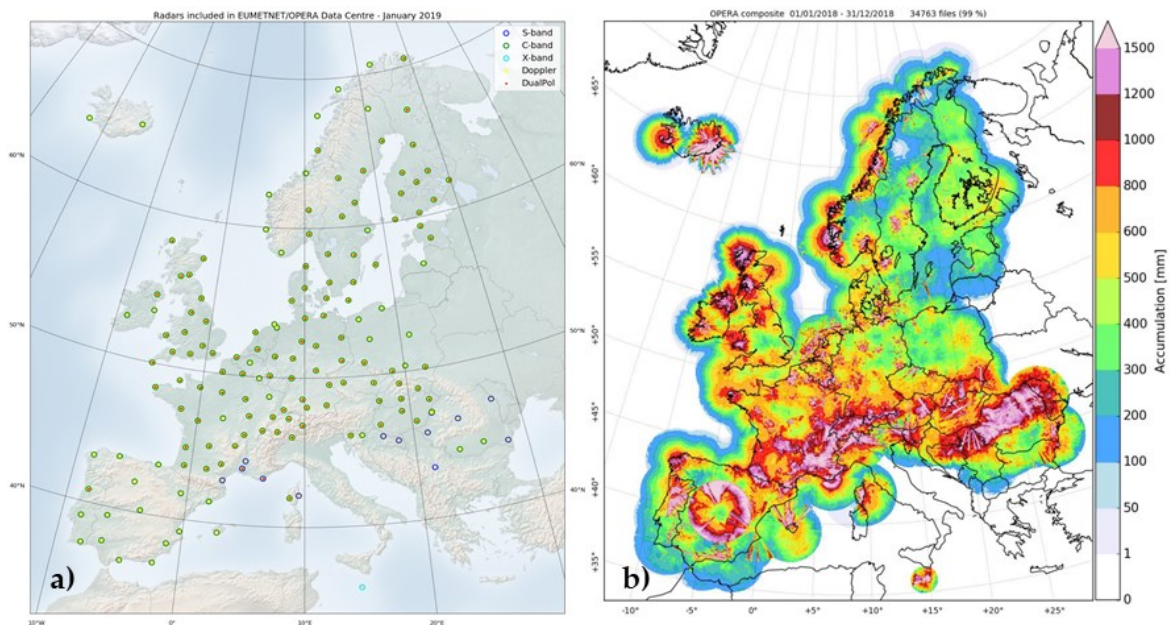
Figure 1-7: Map of the European radar network OPERA; a) radar locations, b) annual precipitation of the year 2018; Source: (Saltikoff et al. 2019b)

Weather Radars Worldwide

Worldwide, based on WMO Radar Database (WMO 2023), there are currently over 1200 radars deployed. The majority, 220, are found in the US, followed by 216 in China (WMO 2013b), 94 in Japan, 56 in Australia, and 53 in Russia. Most European countries list 10-15 radars each, with France reporting 30 radars, Italy 22, and Greece eight. In Figure 1-8, a worldwide map features the location of weather radars with their coverage shown as illumination of a 200 km radius (Saltikoff et al. 2019a). The map shows that most weather radars have been installed in developed countries, namely the entire continent of the US, Europe, and the eastern part of China, while areas with high population density are found, such as the coastal areas of Australia, the Philippines, and South America. Africa does not feature any coverage apart from the state of South Africa and Morocco. This distribution is namely to the fact that weather radars require a significant amount of cost for their deployment and maintenance, and their primary purpose is for weather monitoring and flood forecasting applications, which are used mainly in developed countries.
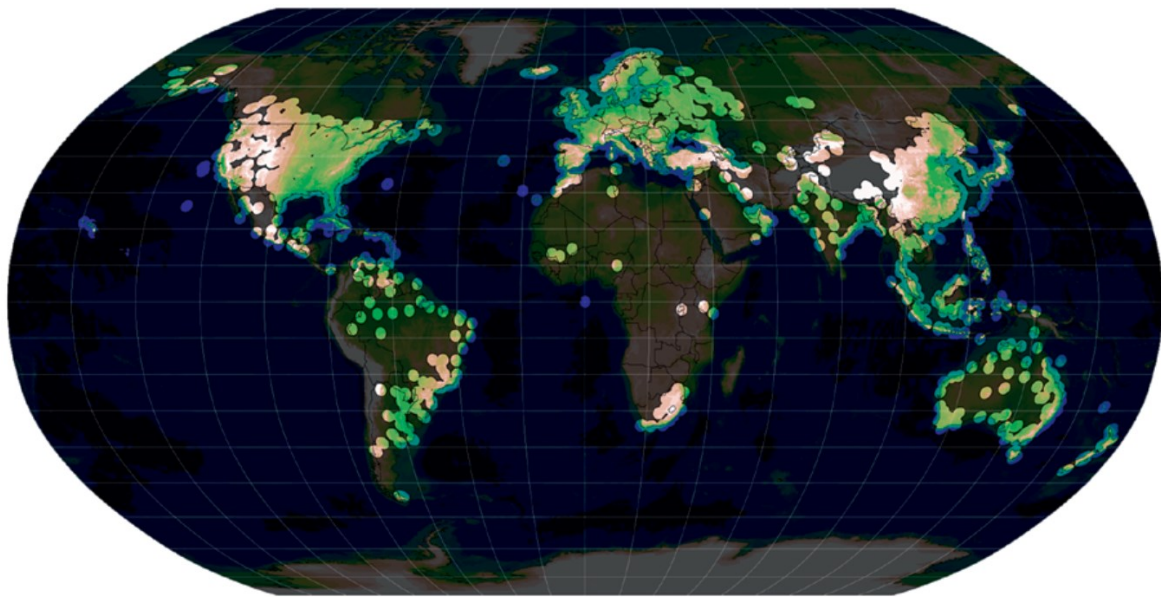
Figure 1-8: Map of weather radar coverage in the world (in Robison projection); Illumination shows a 200 km radius from the radar location; Source: (Saltikoff et al. 2019a)

Weather Radars in Greece

In Greece, the first weather radars were deployed in 1980. The first four are WSR-74 weather radars installed by the HNMS service, mainly for weather monitoring. Two S-Band radars were installed in Thessaloniki and Larissa, while two C-Band were installed in Athens, at Mount Hymettus, and in Andravida, near Patra city. Apart from weather monitoring, the weather radars were heavily used for anti-hail programs performed by the Hellenic Agricultural Insurance Organization (ELGA).

A significant upgrade of the system occurred due to the hosting of the ATHENS 2004 Olympic games. Specifically, a C-Band radar was installed at Aegina Island to support the games with weather forecasts. The site was selected after an optimization analysis, which sought to maximize the coverage area with as low as possible observation height due to the orography diversity of the region (Baltas and Mimikou 2002a). The selected site covers almost the entire mainland of Attica, with an observation range of 250 km.

Following this, the HNMS performed upgrades of its existing radars, with plans for further installations to set up a network of radars with centralized control (Kollias et al. 2007). These were performed under the program "Development of a Network of Weather Radars," and three new radars were installed in Preveza, Kavala, and Astypalaia, while two more radars were scheduled to be, but were not installed in Skyros and Souda. The current state of the Greek weather Radar network, as reported to the WMO Radar Database (WMO 2023), consists of eight radars, shown in Figure 1-9, along with their respected 200 km range. The radars cover the entire Greek territory, apart from the west part of Crete and the Islands of Lesvos and Chios in the east. However, due to orography and the technology of the weather radars, i.e., not all radars operate at 200 km range, the actual radar composite is less, with gaps within the mountains.
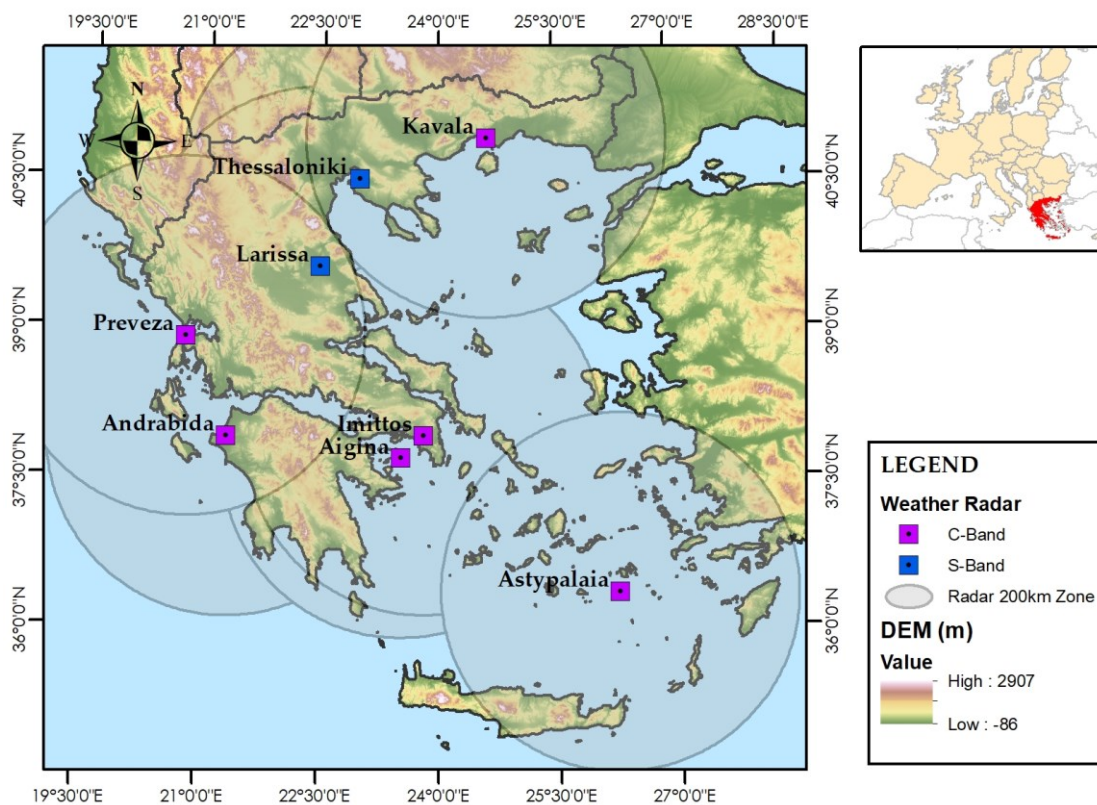
Figure 1-9: The Greek Weather Radar Network

Currently, the use of these radars has been attained, with some of them not being functional due to presumably pending repairs and upgrades. In Athens, none of the two radars is used operationally for providing weather warnings, as noted after the recent flood event in Mandra (Kolydas 2023).

Non-operational radars include the National Observatory of Athens (NOA), X-POL radar (Kalogiros et al. 2013), and the National Technical University of Athens (NTUA) Rainscanner system (Bournas and Baltas 2020, 2022a), which are used for scientific and research purposes. These radars are X-Band type (2-3 cm), which feature increased spatial and temporal resolution but limited range, less than 100 km. Both radars are installed in Attiki, the first in Penteli, at the facilities of the NOA, while the second at the NTUA facilities in Zografou.

1.5.4   Formulation and Equations

Radar Equation

Weather radar works by sending and receiving multiple electromagnetic waves in a horizontal plane, which assist in a) locating the object's distance and angle compared to the radar location and b) measuring the reflectivity of the object, i.e., the amount of energy that is transmitted back from the object. The first is easily calculated since waves travel with the speed of light. Therefore, the distance between the object and the radar can be calculated through the time it takes for the signal to reach the object and return. The second is more challenging and can be estimated by measuring the difference between the transmitted, P_t, and received energy P_r. The general equation of the reflected power P_σ of the target and the received power to the radar P_r to the weather radar system are described as follows:

$$P_\sigma = \frac{P_t g A_\sigma}{4\pi r^2} \tag{1.4}$$

$$P_r = \frac{P_t g^2 \lambda^2 A_\sigma}{64\pi^3 r^4} \tag{1.5}$$

where, g is the antenna gain, A_σ the target area, λ the wavelength, and r is the distance between the radar and the target. Since a weather radar targets the hydrometeors, the A_σ area can be easily identified since these are considered to be spherical. The value of A_σ is then replaced with parameter σ, the area of a sphere. For small spheres, the area A_σ is related to the sixth power of its diameter D, and therefore σ is calculated as:

$$\sigma = \frac{\pi^5 |K|^2 D^6}{\lambda^4} \tag{1.6}$$

where $|K|^2$ is a coefficient related to the physical properties of the target, mainly its electrical conductivity, i.e., the ability to conduct an electric current. The most typical value of the coefficient $|K|^2$ is 0.93 for liquid water and 0.197 for ice crystals for typical temperatures.

Since the returning power is the sum of multiple objects, i.e., the hydrometeors, which feature different diameters, the sum of target areas σ_i, $\Sigma\sigma_i$, should be used instead in the equations. Replacing the above into equation 1.5 and assuming that the distribution of radar lobes follows a Gaussian distribution, the returning power is then found to be:

$$P_r = \frac{\pi^3}{1024ln2} \frac{P_t g^2 \theta\varphi h |K|^2 \Sigma D_i^6}{\lambda^2 r^2} \tag{1.7}$$

where θ and φ are the horizontal and vertical angle beam width, and h is the radar pulse length. Finally, since the issue lies with the calculation of factor ΣD_i^6, it is replaced with a new parameter, Z, called the reflectivity factor. The result is the following equation used as the general weather radar equation:

$$P_r = \frac{\pi^3}{1024ln2} \frac{P_t g^2 \theta\varphi h}{\lambda^2} \frac{|K|^2}{r^2} Z \tag{1.8}$$

Where, P_r is the received power, P_t is the transmitted power, g is the antenna gain, θ is the half-power beam horizontal width, φ is the half-power beam vertical width, h is the radar pulse length, λ is the radar wavelength, $|K|^2$ is the complex index of refraction, and Z is the reflectivity factor. A list of the above variables is presented in Table 1-6, along with their units and typical value ranges, while Figure 1-10 illustrates some of the parameters.

The equation is written in three factors, the first being the geometrical constants, the second including the weather radar coefficients, and the third the variables related to the target, i.e., the hydrometeor. Since the two first are constant in a single weather radar scan, equation (1.8) is usually simplified, as shown in equation (1.9), by replacing the two first factors with a parameter, C1, called the "weather radar parameter." In many cases, the water liquid value of $|K|^2$ is also added into the constant, resulting in parameter C2 as follows:

$$P_r = C_1 \frac{|K|^2}{r^2} Z = C_2 \frac{Z}{r^2} \tag{1.9}$$

Table 1-6: Weather Radar General Equation Variables

Variable	description	unit	Remarks / Typical values
g	Antenna gain	-	20000 (~43dB)
Pr	Received power	mW	$1-10^{-11}$ (0 - 110 dBm)
Pt	Transmitted power	mW	$250*10^6$ (250 kW)
Z	Reflectivity factor	mm^6/m^3	0.001 to $50*10^6$ (-30-75 dBZ)
h	Radar pulse length	m	600 (2 μs)
$|K|^2$	Complex index of refraction	-	0.93 (water) / 0.197 (ice)
r	Target range	m	$100*10^3$
λ	Radar wavelength	m	0.03 to 0.10 (3-10 cm)
θ	Half power beam width (horizontal)	rad	0.017 (~1 degree)
φ	Half power beam width (vertical)	rad	0.017 (~1 degree)
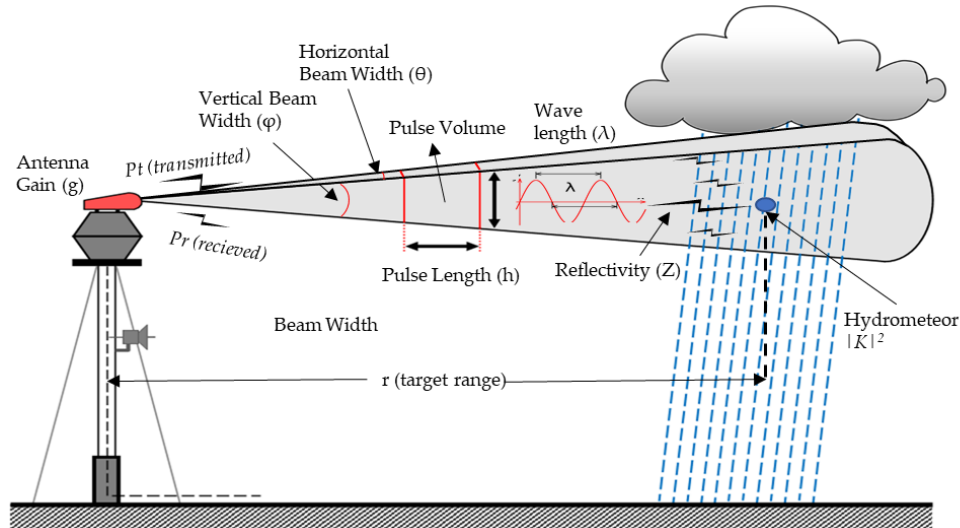
Figure 1-10: Weather Radar Beam Characteristics

This simplification is shown in eq. (1.9) highlights that the returning power is proportional to the reflectivity factor and inverse proportionally to the second power of the distance between the radar and the target. The output of a radar is the reflectivity factor; thus, by simple reordering, the reflectivity factor is calculated as:

$$Z = \frac{1}{C_2} P_r r^2 \tag{1.10}$$

The reflectivity factor, Z, is measured in mm^{6}m^{-3} units, ranging from 0.001 to 50 million mm^{6}m^{-3}. Since this is a relatively large range, a unit conversion is preferred to be made, which produces a smaller range of values as follows:

$$Z[dBZ] = 10 \log_{10}(Z[mm^6 m^{-3}]) \tag{1.11}$$

This logarithmic change transforms reflectivity values in dBZ, limiting the range between 30 and 75 dBZ. Light rainfall is observed for reflectivity values above 15 dBZ, while values above 30-35 dBZ showcase strong rainfall intensity fields. Values above 45 dBZ showcase extreme rainfall intensity, while values over 55 dBZ can be considered to be hail instead. The magnitude of reflectivity depends upon the hydrometeor's characteristics, mainly its size, i.e., diameter, and its physical state, i.e., whether they are in liquid water, ice crystals (hail), or snow. Other factors such as shape and density also contribute but not in the same degree.

The Z-R Relationship

The hydrometeor's diameter ranges from 0.2 mm to 5 mm in liquid form. If the distribution of the hydrometeors size is known, then the reflectivity factor and the rainfall intensity can be estimated as follows:

$$Z = \int_0^\infty N(D)D^6 dD \tag{1.12}$$

$$R = \pi/6 \int_0^\infty N(D)D^3 V(D) dD \tag{1.13}$$

where *N(D)* is the total number of hydrometeors with a diameter between (*D)* and (*D+dD)*, and *V(D)* is a function that describes the velocity of the hydrometeors based on their diameter. The velocity of a hydrometeor is usually a power law equation proportionally to its diameter in the form of:

$$V(D) = kD^m \tag{1.14}$$

where *V(D)* [m/s] is the velocity, *D* [mm] is the diameter, and *k, m* coefficients. In the work of Atlas and Ulbrich (1977), the values of coefficients *k* and *m* were determined to be either 17.67 and 0.67 or 14.2 and 0.5, respectively. In a case study conducted by Feloni et. al (2017) using disdrometer datasets in Athens, Greece, it was found that the Gossard equation (Gossard et al. 1992), featured below, provided the best correlation in most cases.

$$V(D) = 9.65(1 - e^{0.53D}) \tag{1.15}$$

Comparing equations (1.12) and (1.13), it is visible that while reflectivity is proportional to the sixth power of the hydrometeor's diameter, rainfall intensity is approximately on its fourth power (by assuming a typical velocity function). This difference results in a non-linear relationship between the reflectivity and rainfall intensity. To overcome this problem, Marshal and Palmer (1948), after analyzing the hydrometeors DSD of various events measured with a disdrometer, found that an empirical exponential relationship, the Z-R relationship, can fit the data well as follows:

$$Z = aR^b \tag{1.16}$$

where, *Z* [mm⁶m⁻³] is the reflectivity value, *R* [mm/h] is the rainfall intensity, and *a* and *b* parameters. The hydrometeors DSD, *N(D)*, determines the values of parameters a and b, which range from 30 to 2000 for parameter *a* and one up to three for parameter *b*. It becomes evident that when the hydrometeor's size distribution changes, so do the values of parameters *a* and b. This results in a continuous problem for weather radar data since the DSD changes in space, i.e., in different geographical locations and time, i.e., between different rainfall events. Marshal and Palmer (1948) calculated the value 200 for parameter a and 1.6 for parameter b on their sample of multiple stratiform events. Research has shown

that the Z-R relationship is related to the storm's characteristics, such as it being stratiform or convective-based. In Figure 1-11, three Z-R relationships are applied to reflectivity values ranging from 5 to 60 dBZ. Each value's coloring matches the standard color of reflectivity used by many weather radar systems, while the rainfall description is derived by the actual rainfall intensity calculated. The used relationships are the ones mentioned. The relationships used feature a constant parameter b value of 1.5, while parameter a varies between 100, 250, and 500, which is preferably applied for drizzle, widespread, and thunderstorm weather systems as suggested by the work of Joss et al. (1970), which investigated a series of Z-R relationships published up to that day.

Z (dBz)	R (mm/h) $Z = 100R^{1.5}$	R (mm/h) $Z = 250R^{1.5}$	R (mm/h) $Z = 500R^{1.5}$	Rainfall Description
5	0.08	0.05	0.03	
10	0.17	0.12	0.07	
15	0.37	0.25	0.16	Weak
20	0.80	0.54	0.34	
25	1.72	1.17	0.74	
30	3.71	2.52	1.59	Moderate
35	7.99	5.43	3.42	
40	17.22	11.70	7.37	Strong
45	37.09	25.20	15.87	Very Strong
50	79.91	54.29	34.20	intensive
55	172.15	116.96	73.68	Extreme
60	370.89	251.98	158.74	Hail
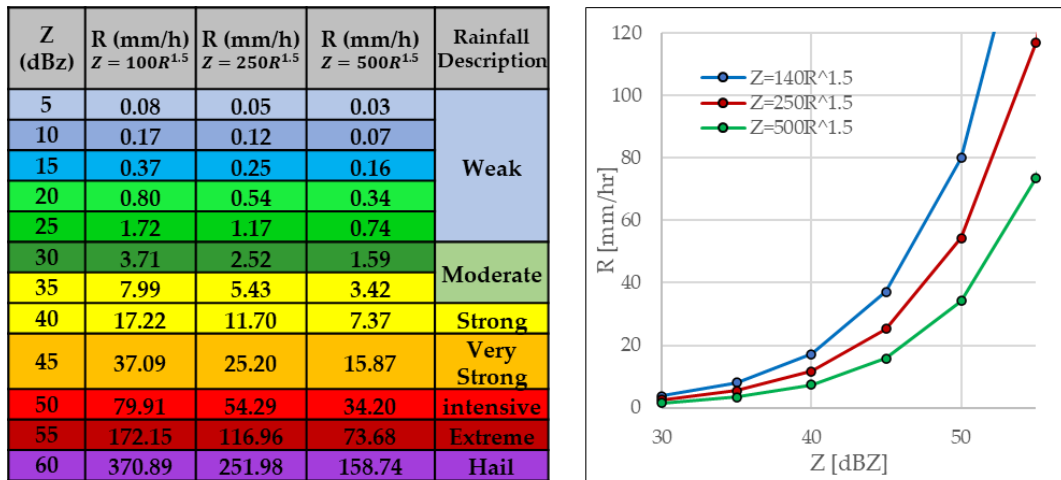
Figure 1-11: Reflectivity to Rainfall Intensity relationship for various the Z-R used

Figure 2-6 shows the difference between the used relationships highlighted in the higher reflectivity values. Specifically, the difference is minimal at 30 dBZ, but above 40, the difference is noticeable, and by 50 dBZ, the difference becomes extreme. Overall, a Z-R relationship with a high parameter a value results in less rainfall rate for the same amount of reflectivity. Values above 50 dBZ, in either case, result in extreme rainfall rates as they lead well above 30 mm/h. Above 60 dBZ reflectivity, hail presence is suggested; thus, specific hail-based Z-R relationships should be used instead.

Z-R Calibration

The estimation of the Z-R relationship parameters is crucial for providing quality QPE. As previously mentioned, parameters a and b range between 1 to 2000 and 1 to 3, respectively, although parameter a will most likely feature values within the 50 to 500 range for typical rainfall events when snowfall and hail events are excluded. The most common values used in weather radars are 200 and 1.6 for parameters a and b, respectively, derived by the work of Marshal and Palmer (1948). However, it is well documented that these parameters show high variability (Joss et al. 1970; Austin 1987; Feloni et al. 2017; Bournas and Baltas 2020, 2021b; Pappa et al. 2021). Factors that affect the parameter values are mainly the

classification of the rainfall events, i.e., that being a stratiform, a convective, a haze, or a snowfall event, the spatial and temporal resolution of the analysis, and even the radar hardware properties (Joss and Waldvogel 1970; Austin 1987; Krajewski and Smith 2002).

The estimation of the parameters can be performed using two primary methodologies. One is the direct method, involving the solving of equations (1.12) and (1.13), and the second, the indirect method, by performing optimization on the Z-R parameters based on the best-fit between the estimated rainfall height and "true rainfall" measured by another instrument such as rain gauges.

In the first case, the knowledge of the hydrometeors DSD, $N(D)$, is required, which can be measured when a disdrometer device is used (Todini 2001; Goudenhoofdt and Delobbe 2009; Zhang and Srinivasan 2010; Colli et al. 2013). A disdrometer is a device that can measure the size of the hydrometeors in a given period, therefore providing measurements of the required $N(D)$ parameter. A velocity function such as equation (1.15) is then applied to determine rainfall intensity and derive the Z-R parameters for a specific event. Although the method is straightforward to apply, the problem lies with the availability of the disdrometer datasets. Specifically, disdrometer instruments are rarely available since they are hardware-sensitive devices and do not usually belong to the standard instruments of a typical hydrometeorological station. Therefore, only a few instruments would be available for a given study area, which results in inadequate spatial coverage of the weather radar scanning area. For instance, in Attica, two disdrometer devices are known to be used, one by the NTUA (Baltas and Mimikou 2002b; Baltas et al. 2015; Feloni et al. 2017) and one by the NOA, both used for research purposes. Only with one or two disdrometer devices the DSD variability in space within the weather radar field cannot be adequately interpreted.

The second methodology relies on the correlation between radar and rain gauge measurements (Hasan et al. 2016; Gilewski and Nawalany 2018, p.; Sahlaoui and Mordane 2019; Qiu et al. 2020; Bournas and Baltas 2022a), assuming the measurements are the ground truth (Colli et al. 2013). This method is usually preferred since, as mentioned, disdrometer data are scarce and do not offer a complete area coverage, whereas rain gauge networks are already established, providing not only calibration datasets but continuous validation data as well. When incorporating rain gauge datasets, two strategies can be followed. The first is by performing the corrections provided by the rain gauges directly onto the QPE estimates after applying a "default" Z-R equation, while the latter involves the calibration of the Z-R equation first. In the first case, a bias-driven statistical analysis is performed at either the station level (Ciach and Krajewski 1999; Legates 2000) or on the area level, using geostatistical interpolation algorithms such as inverse distance or co-kriging (Todini 2001; Goudenhoofdt and Delobbe 2009; Zhang and Srinivasan 2010). This strategy does not rely on the Z-R relationship quality itself but on the quality of available datasets, i.e., the rain

gauges, weather radar, and datasets, to provide a merging algorithm to calculate and minimize any bias applicable to the QPE generated from the radar. This strategy can be applied using geostatistics, but the application of machine learning techniques and Artificial Neural Networks (ANN), which tend to skip the intermediate part, have shown promising results (Alqudah et al. 2013; Orellana-Alvear et al. 2019). However, as shown in both studies, using a locally derived Z-R relationship provided the best correlation and QPE in most cases. Therefore, although direct correction of QPE tends to improve the weather data results, they can be time-consuming and provide little benefit compared with more straightforward methods, such as using a calibrated Z-R relationship. Nevertheless, the combination of both methods is highly advised.

The strategy for optimizing the Z-R parameters lies in deriving the optimum set of parameters a and b that fit the historical or even real-time datasets. In the historical case, multiple radar-rain gauge data pairs are used through calibration and validation schemes. Before any data is used, quality control and thresholds are usually applied, such as the removal of zero or low values of either reflectivity, e.g., less than 15 dBZ reflectivity, and rainfall intensity, depending on the scope and temporal resolution of the analysis (Ciach and Krajewski 1999; Legates 2000; Germann et al. 2006; Gires et al. 2014). Following this, the optimization procedure is applied by fitting the parameters a and b using an objective function, such as minimizing the error between the weather radar QPE and the rain gauge stations datasets. During the optimization process, different approaches can be made. First, it involves the method of optimization, either that being a) linear optimization of a single parameter, usually parameter a, with parameter b kept as a constant, b) nonlinear calibration and optimizing both parameters (Bruen and O'Loughlin 2014), or even c) nonlinear calibration of more parameters added to the equation such as the rain gauge-radar distance (Anagnostou and Krajewski 1999; Borga et al. 2000; Legates 2000). Secondly, it depends on the goal and resolution of the optimization, i.e., the used dataset in each case. Apart from providing a single Z-R relationship, numerous Z-R relationships can be derived at the station level, thus exploring the spatial characteristics of the Z-R relationship (Bournas and Baltas 2022a), while the temporal evolution of the relationship can also be explored by adopting seasonal or rainfall-based characteristics multiple rainfall events (Gabella and Amitai 2000; Park et al. 2005). Finally, dynamic approaches with continuously updated Z-R parameters based on current or short-term measurements have shown promising results, useful for real-time monitoring (Alfieri et al. 2010; Wang et al. 2012; Libertino et al. 2015).

The above procedures show that the solution to the Z-R optimization problem can be reached after considering various conditions. However, the solution depends on the available dataset's quantity, quality, and scale. Storm event characteristics are dynamic and related to the season and the topography of a given study area (Auipong and Trivej 2018).

Moreover, the scale of the data used, such as different temporal resolutions, e.g., 10 min to 1 h, and spatial resolutions, larger or smaller pixel sizes, tend to lead to different Z-R formulations. Therefore, the results of a Z-R optimization procedure should be used in the same scale and study area, and a direct comparison of Z-R relationships should be made after such considerations are taken into account.

1.5.5   Weather Radar Sources of Errors

While weather radar measurements feature many advantages over rain gauges, they are prone to non-negligible and sometimes significant errors from different sources (Robbins and Collier 2005; Collier 2009; Sokol et al. 2021). The majority of errors are the result of the nature of the measurement, that being the transmission of microwave radiation pulses and their reception when they are reflected after hitting rain hydrometeors and other meteorological objects (Collier 1996; Doviak and Zrnić 1993; Sene 2008). A review of the different sources of uncertainty in weather radar is mentioned in the work of Villarini and Krajewski (2010). These errors are categorized into four groups, a) hardware-related errors, b) errors related to the radar beam geometry and scanning strategy, c) errors related to noise and echoes d) errors related to the transformation of reflectivity into rainfall products.

The first group consists of systematic errors related to radar electronics, antenna accuracy, and signal processing quality (Gekat et al. 2004). Most errors are derived by the proper calibration of the constant parameters of the radar general equation, shown in eq. (1.9). These errors are usually related to the hardware of a single weather radar and can be eradicated or minimized with proper system calibration. However, proper and regular maintenance of the system is deemed necessary.

The second group of errors is related to the radar beam geometry and scanning strategy. These are errors such as generated uncertainty due to the increasing distance from the radar site, the radar beam width, and the vertical angle of the radar beam. For instance, with increasing distance, due to the Earth's curvature, radar beams tend to monitor away from the ground surface, often leading to misinterpreting the actual rainfall values over a specified area. This problem is also found when the radar beam angle is such that overshooting or undershooting of a storm cloud occurs, which results in not identifying the storm cloud ore and, thus, rainfall, leading to false measurements. Other such errors are anomalous propagation that occurs when radar signals are refracted or ducted within layers of the atmosphere, leading to the detection of false echoes on the radar display. Such errors are subrefraction and superrefraction. Subrefraction is an atmospheric phenomenon that occurs when the radar beam emitted by a weather radar system bends downward due to an increase in the atmospheric refractive index with height. This bending causes the radar beam to deviate from its expected straight-line path and follow a curve closer to the Earth's surface. In extreme cases, trapping may occur where the radar beam will bounce far beyond

the operation range, increasing clutter and the likelihood of second-trip echoes. Superrefraction is the opposite of subrefraction and occurs when the radar beam bends upward due to a decrease in the atmospheric refractive index with height. Both phenomena lead to false measurements, where subrefraction will lead to underestimation, while superrefraction to overestimation of rainfall height, and therefore, in such cases, it is advised to reduce the radar operational range. Finally, the Bright-Band effect might interact with measurements, also known as the melting layer or bright band, which occurs when precipitation particles, usually snowflakes, transition from frozen to liquid as they fall through a layer of warmer air aloft. This frozen layer causes the radar echoes to appear stronger and more reflective than they would if they were purely frozen snowflakes.

The third error group is generated when noise is added to the measurements. These noises can either be ground clutter and second-trip noises, i.e., reflectivity echoes transmitted by non-rainfall objects, such as the terrain, static radio or cell network transmissions (Saltikoff et al. 2016), and even biological objects such as birds and insects (Gauthreaux and Diehl 2020). These errors generate the majority of the uncertainty of weather radar images since they are not systematic and may evolve. A proper clutter filter can detect and eliminate the characteristics of such errors and should be applied in line with proper quality control of the radar datasets. Dual-polarization radars can distinguish such errors better than single-pol radars, but still, ground clutter remains a challenge for weather radar systems, particularly in areas with complex topography or a high density of structures.

The opposite of adding noise is the underestimation of reflectivity, and consequentially precipitation heigh when the strength or intensity of radar signals as they pass through precipitation, such as rain, snow, or other forms of moisture in the atmosphere, are reduced. This effect is referred to as radar attenuation, which is natural and unavoidable. However, in some cases, the impact of radar attenuation may severely affect measurements. When a high rainfall intensity storm is measured with a low wavelength radar, radar attenuation is rapidly increasing with distance, and therefore reduction of the operational range of the radar is advised. X-Band radars are more prone to signal attenuation due to their small wavelength and the strength of the generated signal. Therefore, limiting their operation distance is advised for providing good-quality datasets. However, other techniques can be used for reduction attenuation, such as dual-polarization radars, attenuation correction algorithms that consider the radar system's energy loss, and cross-reference corrections with datasets provided from other sources of measurements.

Finally, the last group of errors is related to transforming weather radar measurements into rainfall products. Specifically, this is related to the selected Z-R relationship, or in the case of dual-polarization radars, to the algorithm using differential reflectivity (Z_{DR}) and specific differential phase (K_{DP}). The main issue with the Z-R relationship is that it is a static

relationship used to translate a non-static variable. A Z-R relationship assumes that the DSD distribution is consistent in time and space, which is not in line with an actual storm event occurring. Calibration of the Z-R relationships through the derivation of parameters a and b, the methods discussed in 2.2.3, should be performed, but with care concerning the seasonal and regional variability and the convective and stratiform storm classification. Dual-polarization radars offer more information regarding the shape of hydrometeors and thus their distribution but still Z-R relationships, which include differential products, are still required to be determined, and spatial corrections may be required to be applied to meet the accuracy of rain gauges (You et al. 2022).

The majority of errors can be mitigated or eradicated with proper radar calibration. This process includes calibrating the electronic parts of the weather radar to determine its constants, optimum beam elevation angle, and overall good operation and developing the required algorithms for correcting the generated radar images. Maintenance of a weather radar system should be performed regularly to avoid errors generated by hardware and validate the quality-control algorithms. It is usually inevitable that weather radars are prone to errors and uncertainty generated by the corrections methods applied (Villarini and Krajewski 2010). This is usually the cost for increased spatial and temporal resolution for rainfall fields. Therefore, it is suggested to quality control the obtained datasets with other sources of datasets, namely ground rain gauge stations or even radar images that cover the same area.

1.5.6   Weather radar applications

Weather radar usage is focused on three main application categories; a) the observation and analysis of microphysics during precipitation events, b) rainfall-runoff modeling, and c) storm tracking and nowcasting applications. While the first is usually research-orientated to improve the generated QPE, the latter are typical hydrological applications that are improved with better high-resolution datasets. However, weather radar data for hydrological applications was not as fast realized as their potential (Kammer 1991a; Seo et al. 2015b). Even though their potential was and is still well documented, the use of weather radar in modelling and application usually lacked quantity. Weather radar rainfall fields benefit rainfall-runoff simulations when a distributed model is used compared to lumped or semi-distributed models since the higher spatial resolution provides a better description of a study area (K. Ajami et al. 2004; Grek and Zhuravlev 2020). A distributed model is expected to have better results if the required datasets are provided (Borga 2002), but because hydrologists are skilled and comfortable using rain gauge datasets and lumped models, this assumption is debatable. There have been numerous studies where the results derived from distributed models, which are often complex and data-demanding, do not always reach better or equal results with respected lumped models. Berne and Krajewski

(2013) discuss various aspects of the challenges and unfulfilled promise of using weather radars, concluding that although weather radar provides high-resolution datasets, their limitations have hampered their usage.

Nevertheless, the same review acknowledges that rainfall is the driving force of all hydrological-related processes. Since technological advancements have made more complex calculations easier to perform, better and more precise rainfall datasets will inevitably be required. In strictly hydrological models, i.e., rainfall-runoff modeling for water management projects, weather radars are not widely used. Although much has improved since the beginning of radar usage, weather radar requires significant understanding and know-how, which makes novice users, such as consulting engineers in small firms, a challenging task to adopt. To address this situation, Berne and Krajewski (2013) suggest developing tools and resources that would not be difficult to calibrate and understand products but easy to access and process data for specific drainage basins. This leads to the need for easier to calibrate and use models.

Recently, through the advance of radar technology, radar errors such as signal attenuation in X-Band radars have been mitigated, making them more popular since they cost less and provide increased spatial and temporal resolution products. This resolution is deemed not only essential but also as a pre-required for the study of local events and areas (Cristiano et al. 2017; Paz et al. 2019), such as urban basins, which are considerably small in size (Einfalt et al. 2004; Thorndahl et al. 2017). Therefore, the use of weather radars in hydrological modeling has seen new sights, with the focus on flash flood events and small-scaled basins where the high resolution provided by weather radars increases the added value of the distributed nature of the rainfall fields (Sayama et al. 2020; Ghimire et al. 2022).

Flash floods are the deadliest types of flooding, and the increased resolution offered by weather radars is suitable for rainfall-runoff modeling, storm tracking, and nowcasting applications. Most FEWS rely on weather radar datasets to provide warnings based on rainfall thresholds (Norbiato et al. 2009; Liu et al. 2018; Georgakakos et al. 2021; Cheng et al. 2022). Although satellite datasets are assimilated in forecasting systems (Varlas et al. 2019; Spyrou et al. 2020), increased uncertainty is still involved, and complex analyses have not prepared such applications for operational usage. In contrast, weather radars have been used for nowcasting and forecasting since their establishment as a means for precipitation measurement. The benefit here lies in that the weather radar datasets can be used before the transformation to rainfall height by simply analyzing the reflectivity fields (Dixon and Wiener 1993; Li et al. 2015) and removing the uncertainty generated by the reflectivity to rainfall transformation. FEWS is usually as good as the input they are provided with; therefore, the higher temporal and spatial resolution input of weather radar data, compared with those from rain gauge networks, satellites, or lightning networks, is considered vital to

the nowcasting algorithms (Kohn et al. 2011; Karagiannidis et al. 2016). Therefore, weather radar measurements are usually the cornerstones of modern FEWS implementations.

1.6   Research Aim

According to the introduction above, it can be summarized that floods constitute one of the most significant types of natural hazards globally, affecting many people. Floods are typically caused by intense rainfall, with their consequences being felt either immediately in the form of human life loss and substantial economic damages to infrastructure, agricultural, and industrial activities, or in time by impacting the environment in general and deterioration of land cover by the transport of substantial debris and pollutants transportation pollutants. Among the types of floods, the most common and destructive for humans are flash floods, which are characterized by intense rainfall over a short period of 3 to 6 hours. Flash floods account for 85% of recorded flood events and feature the highest mortality rate, i.e., the number of deaths relative to the number of affected individuals.

Most research on flood management is focused on understanding the hydrometeorological processes that influence the extreme weather conditions leading to flood events. To that end, one of the main non-structural methods for mitigating flood and flash flood problems is the development and use of FEWS. An integrated FEWS consists of various subsystems, including hydrological and meteorological data collection and processing, quality control, mathematical simulation of the rainfall-runoff process, and storm predictions. Although the methods used to simulate the hydrometeorological processes are essential, the main problem lies in the chaotic nature of the atmosphere and the lack of sufficient resolution and quality data. In a recent study (Marchi et al. 2010), an investigation of 25 major storms that caused floods in Europe over the past 20 years revealed that only about half of the cases were adequately documented with conventional field measurements.

Similarly, even in cases with a good level of data, there may be high uncertainty in modeling a watershed system, which could lead to incorrectly estimated discharges compared to observed values (Di Baldassarre and Montanari 2009). The same issue applies to rainfall estimates and to the accuracy of hydrological forecasts since the desired spatial and temporal scale to monitor rainfall events such as flash floods is higher than the respected resolution offered by traditional rain gauges networks of rain gauges (Anagnostou et al. 2017). These characteristics generally limit the ability for timely warnings (Mimikou and Baltas 1996), while in cases where measurements are nearly absent, unreliable, or non-good spatially available, such as in Greece, the problem is exacerbated.

In conclusion, the expected benefits of further deepening the development and organization of EWS against flood risk include a) higher quality predictions, b) increased response time,

and c) more information regarding flooded areas to strategically design and implement flood protection measures. Therefore, the main areas where a FEWS can advance are a) new technologies concerning data collection and mining and b) more precise and more effortless to apply methods that would reach more and better-quality decision-making information. The first can be achieved by incorporating new technologies such as high-resolution weather radars or satellites and implementing a data assimilation process. In contrast, the second can be achieved by developing and calibrating rainfall-runoff models suitable for leveraging the new data in ungauged basins and improved data analysis and nowcasting techniques.

The development of a FEWS is expected to lead to significant reductions in the mortality rate but in the economic impact of the flood-affected areas. In Greece, where such systems are absent, the expected benefit after applying a FEWS is multiplied in contrast to most Western European countries. In this dissertation, the Attica region was selected as the case study since it is where the new NTUA weather radar system was installed and able to monitor. Furthermore, the Attica region features varying land use in the form of a) heavily urbanized areas consisting of the city of Athens, where approximately 50% of the population resides, b) peri-urban areas on the outskirts of Athens, where towns and industry are located, and c) rural areas found on the foothills of surrounding mountains. Overall, the Attica region combines high and low-elevation areas, while at the same time, its extensive coastline leads to a high number of small ephemeral streams, which have been overlooked during the city expansion plans and the residential areas in general, leading them being vulnerable to flash flooding.

The main goal of the Ph.D. dissertation is the development of a suitable methodology for processing weather radar datasets of high spatial and temporal resolutions. A newly installed weather radar system, the NTUA X-Band Rainscanner system, is calibrated and evaluated through a series of rainfall events against datasets provided by ground-based measurements from meteorological stations. Using the correlation of the abovementioned datasets, the properties of the reflectivity (Z) to rainfall rate (R), and Z-R relationships are analyzed both in time and space. Following the calibration of the weather radar system, a rainfall-runoff model is designed to a) incorporate the weather radar datasets and b) be readily applicable in ungauged basins, which is used for providing the hydrological status of a given study area. A distributed flash FEWS based on the FFG theory is then devised to provide flash flood indicators in historical and real-time events. Finally, the derivation and application of a storm-tracking algorithm are performed using the available weather radar datasets and image analysis tools to identify and track cell cores, providing storm-tracking capabilities. The tool is intended to provide future rainfall forecasts that will feed the devised gridded FEWS.

This research was conducted in urban and non-urban areas of the Attica Region, which fall within the coverage of the meteorological radar of the School of Civil Engineering at the National Technical University of Athens (NTUA).

1.7   Scientific Significance, Questions, and Originality

The critical point of this research is the collection, analysis, and extraction of products related to the newly installed weather radar. A weather radar is not a typical device, and therefore proper handling of the raw generated datasets is essential to avoid systematic. On the other hand, weather radar datasets are an improvement over traditional ways of rainfall measurements. Although weather radar's history is over 50 years, they are still considered a cutting-edge technology through technological upgrades regarding its hardware and software components. X-Band weather radars are becoming more and more attractive due to their small size and cost while providing high-resolution products. Exciting and new early warning system applications are estimated to be favored by using multiple X-Band radars to provide higher-than-ever resolution products to be integrated into sophisticated hydrological and hydrodynamic models.

This thesis's significance lies in analyzing and understanding the weather radar components. Unfortunately, research on weather radars is only performed when such datasets are available, making future applications in Greece lacking information. Based on research on the latest Ph.D. thesis conducted in Greece regarding floods, focus on areas that aim to identify flood-prone areas and the hydrodynamic representation of historical floods. Relevant scientific research focuses on using satellite datasets for early warning systems, but due to their complexity and data availability, research to operation practice is not expected in the near future. Moreover, satellite datasets cannot still match the resolution and quality of weather radars but are only favored in research due to their high availability. The leading research on weather radar application in Greece has been performed by Prof. Baltas, the supervisor of this thesis, with his Ph.D. thesis back in 1996, where an S-Band radar system was used. Following this, considerable research was performed by the National Observatory of Athens with the X-POL, X-Band weather radar. Still, the focus lies in the processes to provide quality QPE and less in early warning applications.

The need for adequate early warnings for floods in Greece multiplied after a series of flash flood events that ended in the cost of human lives and economic damages that people feel should not occur in developed EU countries. All the points mentioned above make this research on flood early warning systems, and weather radars a valuable contribution. This research highlights the benefits of using weather radar systems and provides a complete framework and tools for early warning applications in a data-scarce area.

The research questions this dissertation aims to answer, are divided into two sections, the first concerning the use of weather datasets:

1. *"What are the major factors to consider when utilizing weather radar datasets? Do weather radar datasets provide with any benefit compared to rain gauge networks or are they governed by uncertainty?"*

The following question derives two more questions regarding the Z-R relationship as follows:

- *"How does the Z-R relationship variate in time and space? What are the factors that influence the Z-R relationship and how do they affect it in the case of the Attica Region?".*
- *"Is the derivation of a single Z-R relationship feasible for operational usage, and which Z-R relationship should be used for Athens?"*

The second question concerns the implementation of a FEWS:

2. *What are the necessary components of an integrated flood early warning system (FEWS) based on weather radar datasets? Can such a system be efficient at an operational level and how can it be implemented?*

Furthermore, in response to the above question, the following questions are also raised:

- *"How does each component parameters influence the FEWS results?*
- *"What FEWS products are available? How can one interpret the results of such a system?*

The above questions, Finally, the originality of this research is highlighted by actions performed in this thesis and presented in a list as follows:

- An in-detail review and methodology are presented regarding the process of raw weather radar datasets and the required quality control procedures.
- The measurement and analysis of rainfall fields through the and analysis of raw weather radar datasets. Most rainfall events in Attica from 2018 to 2023 are recorded within the span of this Ph.D. thesis.
- The use of statistical analysis for a) exploring the properties of the Z-R relationship and weather radar in space and time and b) calibrating a Z-R relationship for further use.
- The correlation analysis between rain gauge – Rainscanner datasets to improve the QPE.
- The development and application of a gridded rainfall-runoff model can easily be calibrated in ungauged basins and areas with data scarcity.

- The development of a FEWS aimed at flash floods and its application in historical events.
- The development and application of a simple storm-tracking algorithm can analyze the weather radar datasets, identify possible storm cells and track their location in multiple consecutive images.

1.8 Limitations

The main limitations of this thesis lie in the weather radar type. Specifically, the weather radar used is a single-phased X-Band weather radar system, contrary to more advanced systems that use dual-polarization systems that offer advantages concerning quality control of QPE. Moreover, due to its technical characteristics, the observation range is limited for providing adequate lead times, and therefore, adequate "space" for providing long-range forecasts based on cloud movement is not performed. Furthermore, a limitation concerning the rain gauge datasets exists since these datasets were available for the periods of 2018 up to 2020.

1.9 Thesis Structure

This research work is divided into five chapters.

Chapter 1: Introduction

In this chapter, an introduction to the thesis is made. Specifically, a literature review is performed regarding the means for flood mitigation, such as the flood early warning systems and the use of weather radars. The general aim and the research questions formed are presented, as well as the novelty of the thesis.

Chapter 2: Study Area and Data Used

This chapter includes information regarding the study area, the Attica Prefecture, and the data used in this research. Specifically, focus is given to the characteristics that lead to flooding, such as the geomorphological characteristics and the hydrometeorological conditions. Finally, a description of the datasets collected and used in this study is performed.

Chapter 3: Methodological Framework

This chapter comprises the entire methodological framework devised and applied in this research. Specifically, this chapter is divided into five main subchapters, which consist of the methods used, a) for the analysis of the weather radar raw datasets, b) for the analysis, optimization, and derivation of the reflectivity to rainfall intensity (Z-R) relationships through correlation with ground stations, c) for setting and calibrating a gridded rainfall-runoff, d) for the application of an early warning system, the gridded flash flood guidance

and e) the methods used for the storm tracking and trajectory analysis based on the weather radar datasets. Each subchapter consists of an integral part of the entire methodological framework.

Chapter 4: Results and Discussion

This chapter features the results of applying the above methods to the study area. The results are discussed, and the significant findings are highlighted.

Chapter 5: Conclusions and Future Research

In this chapter, the main findings of this Ph.D. thesis are presented. These consist of all the individual findings for each subprocess, followed by the findings of the research questions raised. Finally, recommendations for future work are also presented in this chapter.

Finally, three Appendixes, A, B and C, support the abovementioned chapters. The first is a list of all the events measured by the Rainscanner system from 10/2018 up to 12/2022, while the second and third present the results maps of the storm tracking algorithm in multiple events.

2. Study Area and Data Used

2.1 The Attica Region

The study area is the Attica region, and specifically, the area defined by the area coverage of the Rainscanner system Figure 2-1. The Rainscanner is located in Athens, Greece, and features a 50 km range. The extent of the Rainscanner, as seen in Figure 2-1., includes the majority of the Attica Prefecture, apart from a small area on the west, beyond Mount Gerania, as well as a small section of the Central Greece prefecture north of Mount Parthitha, a part of the Asopos river basin.
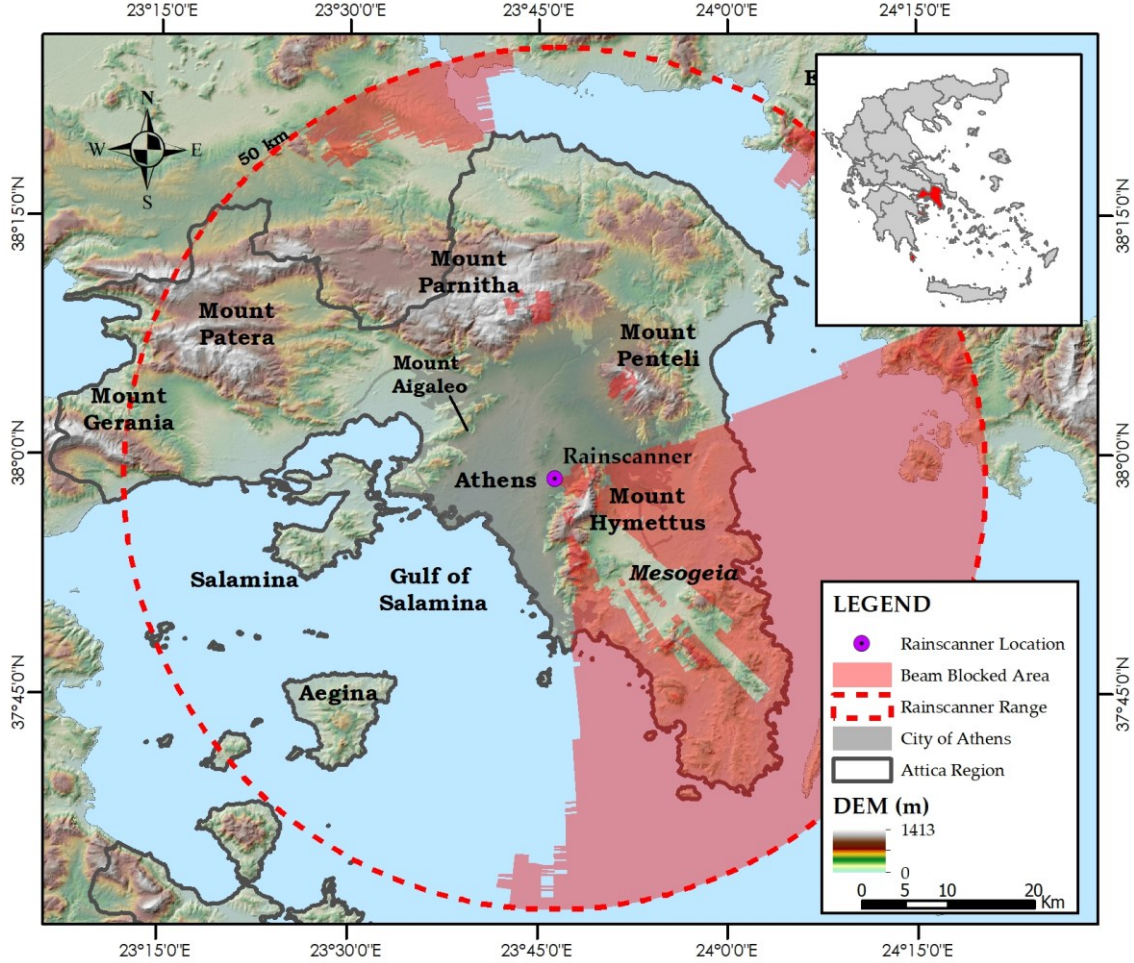

Figure 2-1: The Study area, the Attica Region, including the Rainscanner range

The Rainscanner is installed at the Zographou district, at the foot of Hymettus Mountain, within the premises of the NTUA campus, and specifically on the roof of the Santorini building, where the facilities of the Department of Hydrological Engineering of the School of Civil Engineers lie. The elevation of the installation is 200 m and oversees the east side of Athens. The covered area includes the entire Athens metropolitan area, surrounded by Mounts Aigaleo on the west, Penteli and Parnitha on the north, and Hymettus on the east. Due to the presence of Hymettus Mountain, the entire southwest area is obstructed and cannot be measured. Unfortunately, the entire "Mesogeia" region, including the Athens "Eleftherios Venizelos" airport, is out of reach. However, the Rainscanner location is favored for observing precipitation systems with a west-to-east and north-to-southwest direction which are the majority of systems in the area, making it a viable option for observing and providing nowcasts and forecasts for the city of Athens and its vicinity.

2.1.1 Attica Districts

The Attica Prefecture is divided into eight regional units, five consisting of the Athens metropolitan area; Central Athens, North Athens, West Athens, South Athens, and Piraeus, while the rest, West Attica and East Attica, are larger and complete the mainland area of the prefecture. Finally, the Island region includes the islands within the Argo-Saronic Gulf, such as Salamina and Aigina, and the island of Cythera in the south.

Attica is the most populated area in Greece, where a total of 3.8 million out of 10.4 million people reside, i.e., 36% of the total population. Within the Athens metropolitan area, which consists of the administrative prefecture divisions of Central, West, South, and North Athens, as well as the Piraeus, a total of 3 million reside, i.e., 30% of the total population and 80% of Attica population, while in west Attica and east Attica, 1.6% and 5% of the total population reside, and 4.35 and 12.5% of the Attica population, respectively.

Moreover, based on the Hellenic Statistical Authority report (ELSTAT 2023), the region's Gross Domestic Product (GDP) for 2020 was 78.99 billion €, accounting for 47.7% of the Greek economic output, the highest GDP per capita in Greece. Of this percentage, 35% of GDP is generated in Central Athens, 18% in North Athens, 12% for each in South Athens, Peiraeus, and East Attica, 6% in West Athens, and only 5% in West Attica. GDP per capita lies at 20% for each region. However, the West Attica region houses high industrial activity, namely in the municipality of Aspropirgos and the Thriasion Plain between Aspropirgos and Elefsis. Specifically, industrial plants that produce chemicals, metals, and plastics are found, and the Aspropirgos refinery is the largest in Greece.
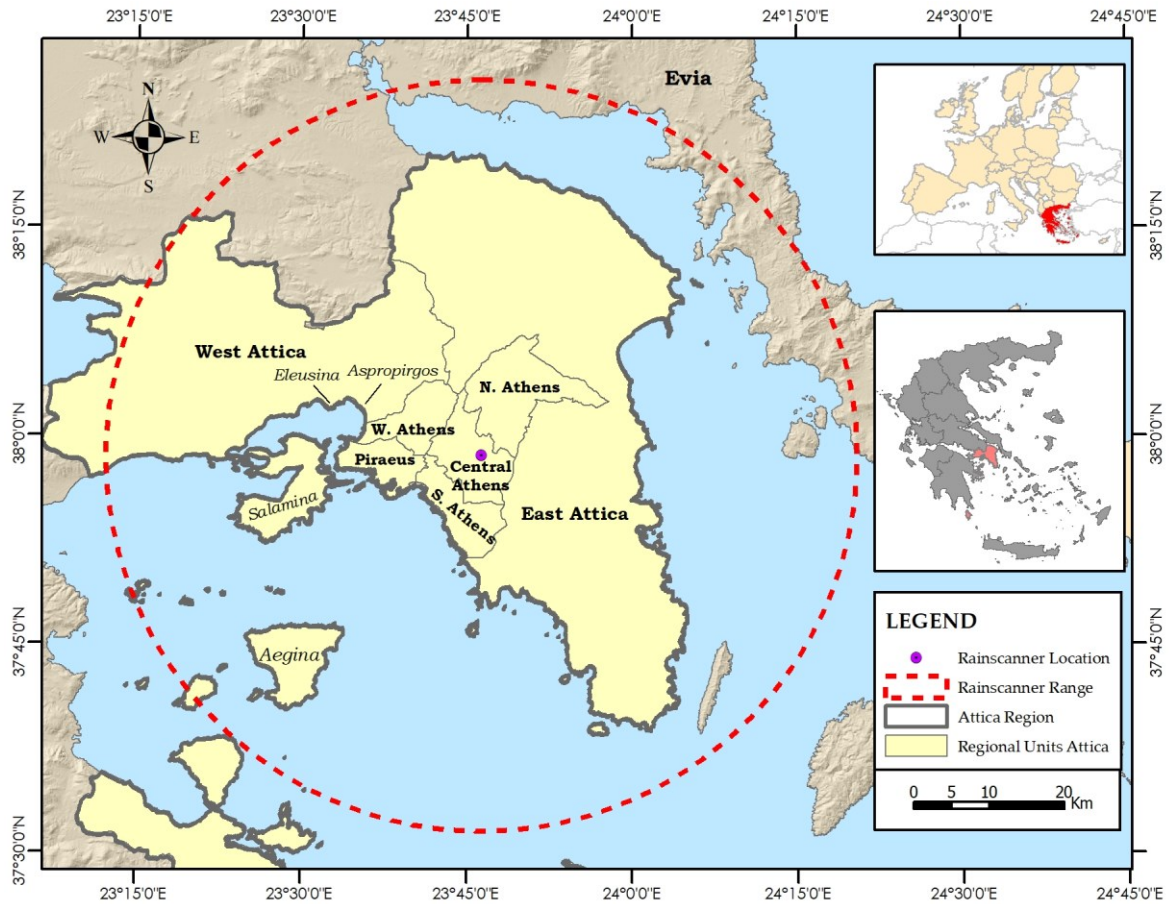
Figure 2-2: The Attica Regions Prefecture and its regional units

2.1.2 Land Use

High urban and semi-urban areas characterize the Attica region. In Figure 2-3, the Corine Land Cover (CLC) for 2018 is shown. Overall, 27% of the region is of artificial type, while the rest, 73%, is agricultural and forest type. However, as seen by two figures, the density of urban, i.e., impervious areas, is not even within the entire region. Three distinctive areas are identified: the high continuous urban fabric areas found in Athens, the semi-urban, i.e., discontinuous urban fabric areas found in west Attica, e.g., Aspropirgos and Eleusis as well as in the Mesogeia region, and the rural areas in east Attica. When analyzing the land use in these areas, the mean percentage of artificial surfaces is about 66%, 19%, and 10%, respectively, and the corresponding percentages of natural land (crops, grassland, and forests) are 33.9% in Athens, 89.4% in Western Attica and 80.1% in Eastern and Northern Attica (Feloni 2019). These percentages are expected to change, especially in the West and East areas, since in Greece, legislation that allows out-of-city planning construction is still in place, and city-expanding plans are underway. These areas are favored for both primary residence and holiday housing since they lie close to the Athens metropolitan area and the sea coast, adding real estate value.

The above fact has led to continuous urbanization of the region since the 1960s, which has altered the natural stream's waypaths. In Athens, several streams have been covered to form road networks, with the most notable cases being the Kifissos, Alexandras, and Kalliroi avenues. In peri-urban areas, uncontrolled urbanization has led to the obstruction of the natural stream's pathways by obstructing their natural path, which is only revealed after intense rainfall leads to flooding.
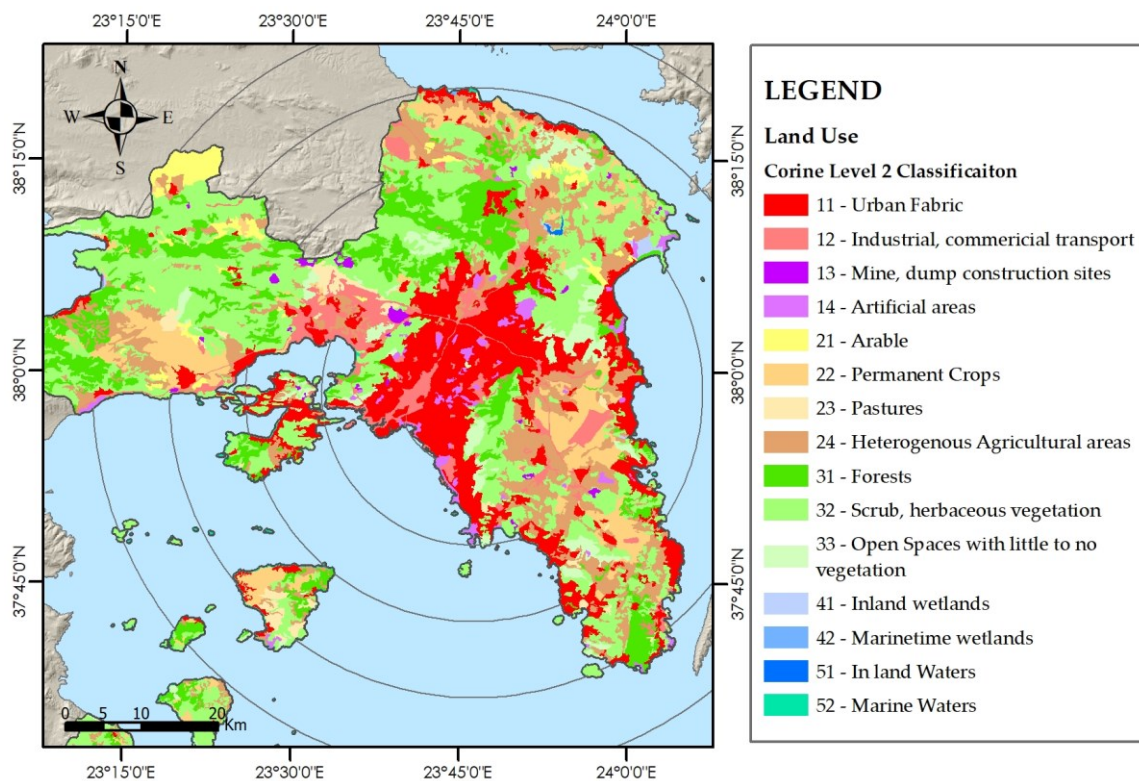

Figure 2-3: Land cover and use in Attica Region: Data Source: CORINE Land Cover 2018

As the featured land use map shows, most of the region is described by an urban environment. Rural areas can be found in west Attica, in the foothills of Mounts Partnitha in the North, and in the Mesogia region in the southeast.

2.1.3   Hydrological Scheme - Climate

Athens has a Mediterranean climate, with mild, rainy winters and hot, dry summers. The city typically receives most of its precipitation between November and March, with relatively little rainfall during the summer months. According to Koppen (1884) the climate of Attica is characterized as Hot-Summer Mediterranean (Csa), except for high altitudes, where it is characterized as Humid continental (Dsb and Dfb). The average temperature during the summer months is 30° C, while in the winter months, the average is 10° C. Although summer months are characterized by high temperatures, which has led to the European temperature record of 48° C measured in Eleusina and Tatoi in 1977, the climate

throughout the year is highly influenced by the area's proximity to the sea, which contributes to providing relief as well as providing more rainfall during winter.

Concerning rainfall, the average annual rainfall highest is 400mm but ranges between 350 mm and 1000 mm in the lowlands and mountainous parts, respectively (Baltas 2008).

The rainfall regime is Attica is characterized by Convective and Stratiform events. Stratiform events occur during the winter months, mainly in November and February, while convective events are typical in the summer, especially in June. From the above, the convective events feature the highest rainfall intensities, which often result in flooding even if a dry period was observed previously.

In Figure 2-4, the main subbasin formed within the Attica Region boundaries are displayed. The largest basin is the Kifissos river basin, with an area of approximately 341 km^2, which consists the entire Athens metropolitan area. The basin is highly urbanized, with its main stream, kifisos stream, being turned into an open and covered channel stream.

Figure 2-4: Main basins formed in Attica Region with their respected area. With blue, the basins with an area over 100 km^2

The majority of subbasins are characterized by their proximity to the sea, and the high percentage of urban use. The largest rural or peri-urban basins are Sarantapotamos and Megara River basins in the West, and Marathon, Erasinos and Rafina basin on the east. Due

to the Rainscanner beam blockage to the east of Hymettus areas, the main focus in this research is focused in the west and specifically the Sarantapotamos river basin. This basin, features a total area of 341 km² of which the majority, i.e., 231 km² features rural characteristics. One main characteristic of the subbasins formed in the Attica region is the large number of small basins due to the lengthy coastline. The majority of these areas are highly urbanized in the areas closest to the sea, making them vulnerable to flash floods events.

2.1.4   Historical Flood Events

Records of historical flood events are available on the website of YPEKA (http://floods.ypeka.gr), which were collected to implement the 2007/60 EC Flood Directive and submitted to the European Dataset "EIONET." In the Ph.D. dissertation of Dr. Feloni (Feloni 2019), a complete list from 1987 up to 2017 is presented using the YPEKA dataset and other sources and scientific articles. From the listing, also shown in Figure 2-5, it is evident that although the number of rainfall events has remained the same or even increased, the fatality rate has decreased except for the November 2017 Mandra event, which led to the fatality of 24 human lives. Overall, most flood events have occurred in the winter months, with October and November being the highest.

In the last decade, the most notable events were February 2013, October 2014, October 2014, and November 2017. The geographical distribution of floods reveals that most flood areas occur mainly in the western areas of Athens and Attica, respectively. A few areas in the north are also affected, mainly after flash flood events in summer months, generated through the high rainfall height due to orography.
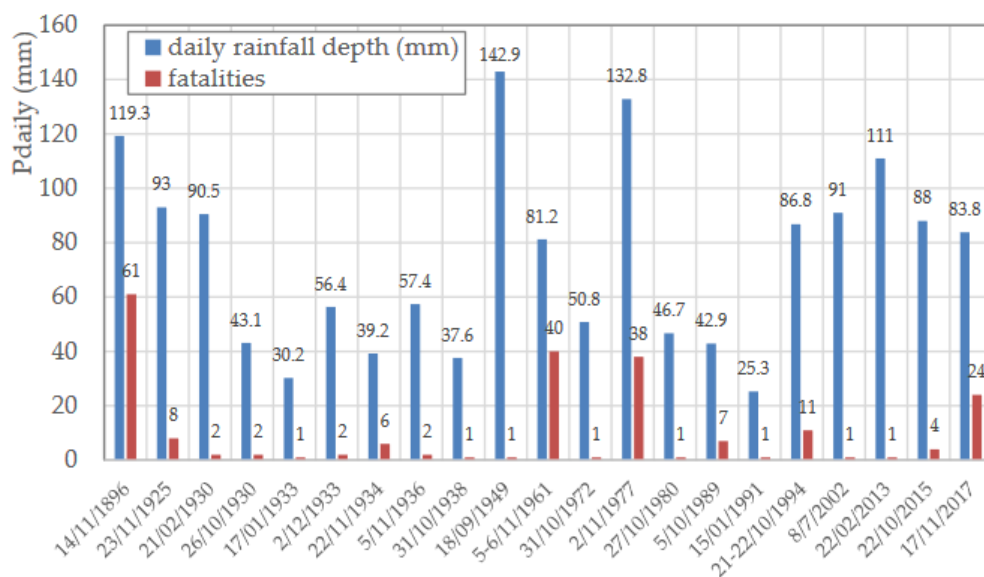

Figure 2-5: The most sever flood events for the period 1896-2017

Source: (Feloni 2019)

Regarding the duration of the storm events, it is observed that almost all flood events featured a rainfall event with a duration of less than a day; most times, the duration can be less than six hours. Summer events resulting from convective events often lead to flash floods. These floods are usually locally based events, where a high volume of rainfall affects a single basin. Although the number of fatalities might be low, the severity of the events in conjunction with the unawareness has historically led to near misses of fatalities.

In most cases, flooding occurs within the urban fiber of Athens, leading to roads being converted into streams resulting in infrastructure damages, the flooding of basement properties, and the dysfunction of economic activity. One aspect that contributes to this fault is the high urbanization of the city, in conjunction with the old and poorly maintained storm sewer system. Especially in the center of Athens, the system is still combined, i.e., storm and wastewater, which has a higher chance of being inadequate in higher return periods of rainfall events. The problem is usually located in the relatively low maintenance and cleaning of roads. Specifically, debris and waste usually block the sewer system's drain holes during the first minutes of a rainfall event.

Finally, it is worth mentioning that in the last three years, the region of Attica suffered from high volumes of snowfall, at least one event per year since 2021, that has led to substantial socioeconomic damages. Overall extreme weather events have increased in frequency and intensity in many parts of the world, including Greece, with this trend being linked to climate change and urbanization.

2.1.5 Early Warning Systems in Greece

In Greece, the authority responsible for flood protection is the Civil Protection Agency (CPA), which works under the Ministry of Environment, Energy and Climate Change (YPEN). However, most predictions and forecasts are provided by the Hellenic National Meteorological Service (HNMS), which operates as part of the Greek Armed Forces and the Ministry of National Defence. The HNMS is responsible for providing meteorological forecasts for aviation and navigation and, as such, has been heavily affiliated with weather forecasting against natural phenomena. The HMNS works as the gateway of European-based alert systems such as the MeteoAlarm and the EFAS. The first is mainly used for providing alerts of all events, such as high rainfall, winds, and heat, using four levels of alert, green, yellow, orange, and red for no action, get informed, prepare, and get preventive measures alert levels, respectively. The state of alert is configured for each meteorological parameter based on groups of fixed limit values. The forecasted accumulated rainfall height of either 12 or 24 hours is examined, depending on the location, as shown in Table 2-1, in which the values in bold concern the rainfall thresholds used for Attica. This system only provides alerts depending on rainfall height, and does not consist of an actual FEWS.

The EFAS system is EU-wide system which offers valuable products. However, as mentioned in the introduction, the system effectiveness is limited in Greece due to the formation of numerous small river basins are vulnerable to flash flooding, while the system is designed to support decision-making, emphasizing large trans-national river basins and large river basin systems.

Table 2-1: The MeteoAlarm Thresholds that are used in Greece

Variable	Location	No Warning	Be Aware	Be prepared	Take Action
Wind [km/h]		W < 60	60 ≤ W < 80	80 ≤ W < 100	W ≥ 100
Wind Gusts [km/h]		G < 80	80 ≤ G < 110	110 ≤ G < 130	G ≥ 130
Rainfall Height (24 hour) P[mm]	West Greece, NE Aegean and Dodecanese	P < 20	20 ≤ P < 60	60 ≤ P < 100	P ≥ 100
	N. Greece, East Sterea Ellada, Thessaly, Peloponisos, Cyclades & Crete	**P < 15**	**15 ≤ P < 40**	**40 ≤ P < 75**	**P ≥ 75**
Rainfall Height (12 hour) P[mm]	West Greece, NE Aegean and Dodecanese	P < 15	15 ≤ P < 50	50 ≤ P < 80	P ≥ 80
	N Greece, East Sterea Ellada, Thessaly, Peloponisos, Cyclades & Crete	**P < 10**	**15 ≤ P < 30**	**30 ≤ P < 60**	**P ≥ 80**
Max Temperatures T[°C]	North Greece, Ipeiros	T < 35	35 ≤ T < 39	39 ≤ T < 42	T ≥ 42
	Central and South Greece	T < 37	37 ≤ T < 41	41 ≤ T < 44	T ≥ 44
	Islands	T < 33	33 ≤ T < 37	37 ≤ T < 40	T ≥ 40
Min Temperatures T[°C]	North Greece, Ipeiros	T < -5	-5 ≤ T < -8	-8 ≤ T < -15	T ≤ -15
	Central and South Greece	T < -1	-1 ≤ T < -4	-4 ≤ T < -8	T ≤ -8
	Islands	T < 0	0 ≤ T < -2	-2 ≤ T < -5	T ≤ -5
Snow [cm]		Not Specified	Urban: ≤ 2 Rural: ≤ 5	Urban: ≤ 10 Rural: ≤ 25	Urban: ≥10 Rural: ≥ 25
Storm		Not Specified	Wind Gust: ≤ 40 kns Hail: ≤ 1cm	Wind Gust: 40 ≤ G < 60 kns Hail: 1 ≤ D < 2	Wind Gust: ≥ 60 kns Hail: D ≤2
Fog (Visibility) [m]		≥ 500 m	100 ≤ V<500	V < 100	V < 50 m

The CPA has recently been utilizing the "112" EU emergency number as a warning system. Specifically, after catastrophic fire events that caused the loss of multiple human lives, the CPA has also enhanced the "112" system with sending information. Initially, the "112" number was a free-of-charge number used in Europe to contact any emergency services, such as an ambulance, the fire brigade, or the police, of the EU state one is located. The "112" system is now updated to send prespecified warning messages to smartphones using Cell

Broadcast technology or, in lack of a smartphone, simple SMS messages after registration in both Greek and English. The system started to be utilized by sending messages about the COVID-19 pandemic. Since May 2021, the system is used mainly as an evacuation tool since most messages were related to wildfire events, while the first message transmitted for a rainfall event was on December 2021. From March 2020 until February 2023, out of the 217 messages transmitted, 40 were related to extreme rainfall and four for floods. The flood events for which alerts were issued were three and occurred on the 14th of October 2021, the 26th of January 2023 flood in Athens, and the 09th of December 2021 in Central Macedonia prefecture.

The system is only recently being used, so validation is not performed. Regarding rainfall and flood alerts, the HNMS service and the fire brigade in some cases inform the CPA. In a study regarding people's perception of EWS, the most reliable source is the HNMS reports followed by other authorities, namely the CPA, by either SMS messages or door-to-door warnings (Diakakis et al. 2022). Radio, internet, and television were considered as less but still relatively reliable. Although this adds credibility to the system, regarding flood alerts, the lack of detailed precipitation forecast and nowcast products and the lack of rainfall-runoff modelling on river basin scale cannot deem the system as genuinely reliable. Although warnings are essential, when regular miss-hits occur, the credibility of such systems can be easily lost.

Apart from the official agencies, several agencies and institutes that perform meteorological forecasts issue newsletters through their websites or social media that can also be conceived as warnings. The most watched institute is the NOA which features the densest rain gauge network. The NOA's METEO research team has developed a methodology to rank rain storms by calculating the Regional Precipitation Index (RPI) (Lagouvardos et al. 2022). The index considers the daily accumulated precipitation and its exceedance of specific percentile thresholds, such as the total area where the exceedance occurs and the population where these exceedances occur, leading to a five-group classification from low to extreme risk.

All the above systems operate using mainly precipitation indexes without any rainfall-runoff modeling. Since flood occurrence probability is highly correlated now only by the rainfall amount but also by the basin characteristics and the soil moisture condition before the event, none of the above systems can be classified as a dedicated flood EWS. Moreover, the generated forecasts are usually in an inadequate space and time scale for the necessary rainfall-runoff computations.

2.2   Data Used

2.2.1   Weather Radar Datasets

The weather radar used, referred to as the Rainscanner system, is an X-Band weather radar system provided by Selex ES GmbH company. Currently the system is installed in the NTUA campus, at the roof of the laboratory of hydrology and water resources management of the school of civil engineers Figure 2-6 .

Figure 2-6: The installed Rainscanner® unit, Antenna and Head unit

The technical specifications of the featured model, RS90, are displayed in Table 2-2. The system consists of the following units: the antenna, the head unit, the interface unit, the signal processor, and the user workstation which interact with each other as shown Figure 2-7. The antenna is installed above the head unit and inside a radar dome, while the interface unit supplies power to the head unit and triggers the generation of electromagnetic pulses. The signal processor runs in a Linux environment and performs the overall unit control, the analog to digital signal transformations, clutter filter corrections, and the generation of slices. These processes can be set up and triggered by the end-user using the RainView® Analyzer software, which through a user interface, the operator can manage and set up any pre-process required to the raw datasets, such as the application of clutter corrections, the definition of the spatial resolution of the final product, the temporal aggregation and the file format of the generated datasets. Overall, the system is a small and robust installation, that can be fitted in any location.
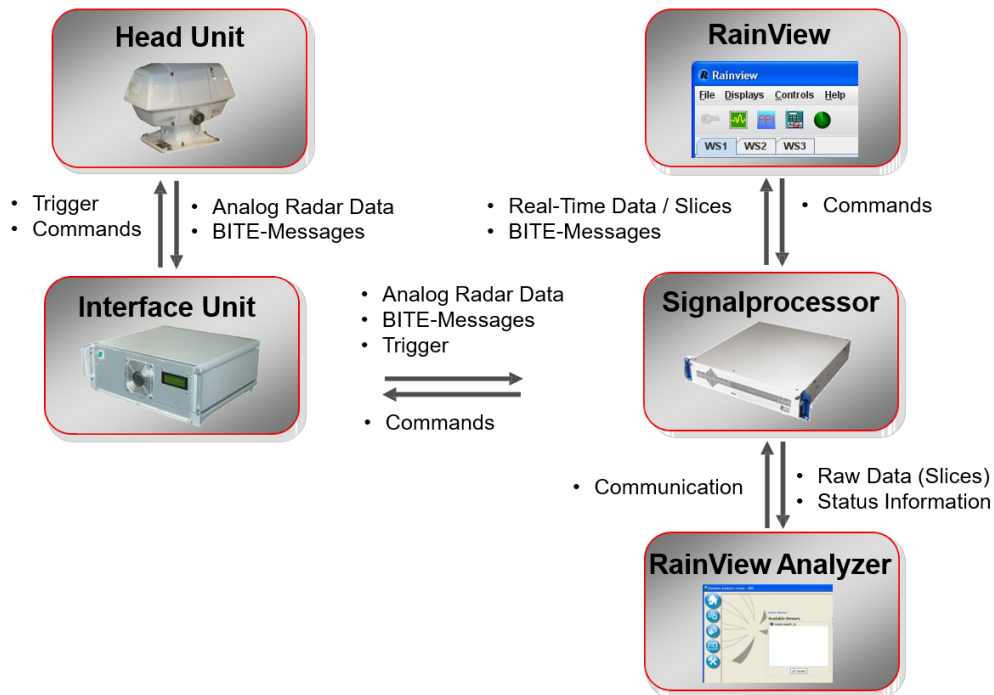
Figure 2-7: Rainscanner main components and functions. Source (Selex ES 2014)

Table 2-2: Technical Specifications of the NTUA Rainscanner weather radar system

Parameter	Value
Peak Power	25 kW
Wave Length	X- Band 3.2 cm
Frequency	9410 (± 30 MHz)
PRF	833 – 1500 Hz
Pulse Duration	1200 – 500 ns
Rotation Rate	12 rpm
Azimuth & Elevation Beamwidth	2.5o
Azimuth Accuracy	± 0.5°
Scanning Range	50 km
Maximum Spatial Resolution	100 m x 100 m

The generated files are provided into "Arc/Info ASCII Grid" file format, using an Azimuthal Equidistant projection, with the Rainscanner as its center, which includes an ASCII file format containing a 1000 x 1000 dimensions reflectivity matrix. Since 2023, a NetCDF type 4 file format is also generated, with the scope of replacing the Arc/Info ASCII Grid format. The new file format reduces the file size significantly, from approximately 6 MB for each 2-minute measurement to less than 1 Mb. The generated files receive a name based mainly on the timestamp in Universal Time Coding (UTC) and information regarding the generated file. More information regarding the specific processes that are performed on the raw weather radar datasets is discussed in Chapter 3.2.

A complete list of all the events measured by the Rainscanner system in shown in Appendix A. Specifically, the events starting and end datetimes, along with their duration is shown. Not all events featured considerable amount of rainfall, as shown by their small durations, therefore only a sublist of these were utilized in this research.

2.2.2 Rain Gauge Datasets

The precipitation measurements used in this research were provided by the National Observatory of Athens Automatic Network (NOANN) station, operated by the Institute for Environmental Research and Sustainable Development of the National Observatory of Athens. The network is continuously expanding nationwide with multiple hydrometeorological measurements, including rainfall, wind direction, speed, ambient air temperature, atmospheric pressure, relative humidity, and solar and UV radiation (Lagouvardos et al. 2017). Most of the stations feature a "Davis Vantage Pro 2" model and can provide real-time measurements with a 10min temporal resolution. The data collected are quality controlled in two stages. First, a procedure performed twice daily results in flagging questionably quality data such as null values of wind for many hours. Secondly, all flagged datasets are re-examined concerning spatial and temporal inconsistencies with neighboring stations. This procedure is performed before incorporating the new data into the database. In this research, 53 stations are used, as shown in Figure 2-8, with a date span between 2018 and 2020. The data were provided after the quality-controlled processes and therefore considered the ground truth.
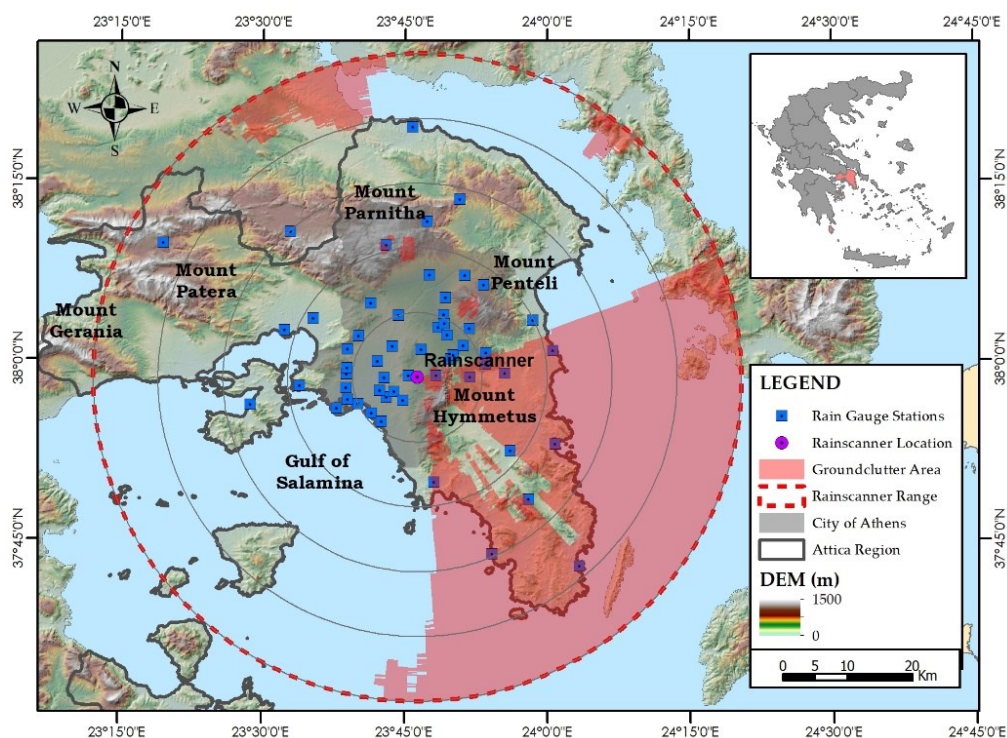

Figure 2-8. The Rainscanner coverage along with the rain gauge stations.

Finally, the Intensity Duration Curves (IDF) derived in the course of the Flood Risk Management Plans for Greece by the Ministry of Environment, Energy and Climate Change (SSW-MEECC 2017) were also incorporated in this study. The IDF was evaluated at the station level, using a Log Pearson GEV 5 parameter. Table 3-2 presents the list of the stations with their respective parameters and the calculated accumulative rainfall height for three rainfall durations and five years return period. In Figure 2-9, the location of each station is featured, using the ID number featured in Table 2-3 as a reference. As in the case of the NOAs stations, the majority lie within the Athens metropolitan area, while only two stations, Eleusina, ID #286 and Mandra, ID #292, lie in the west Attica where the Sarantapotamos subbasin is located. Two stations in the north are also shown in Figure 2-9 but were not used since not only there are they stationed away from the study area, but they are located on the other side of the central mountain peak, Mount Penteli, resulting in different rainfall characteristics that are not suitable for use with any interpolation algorithm.
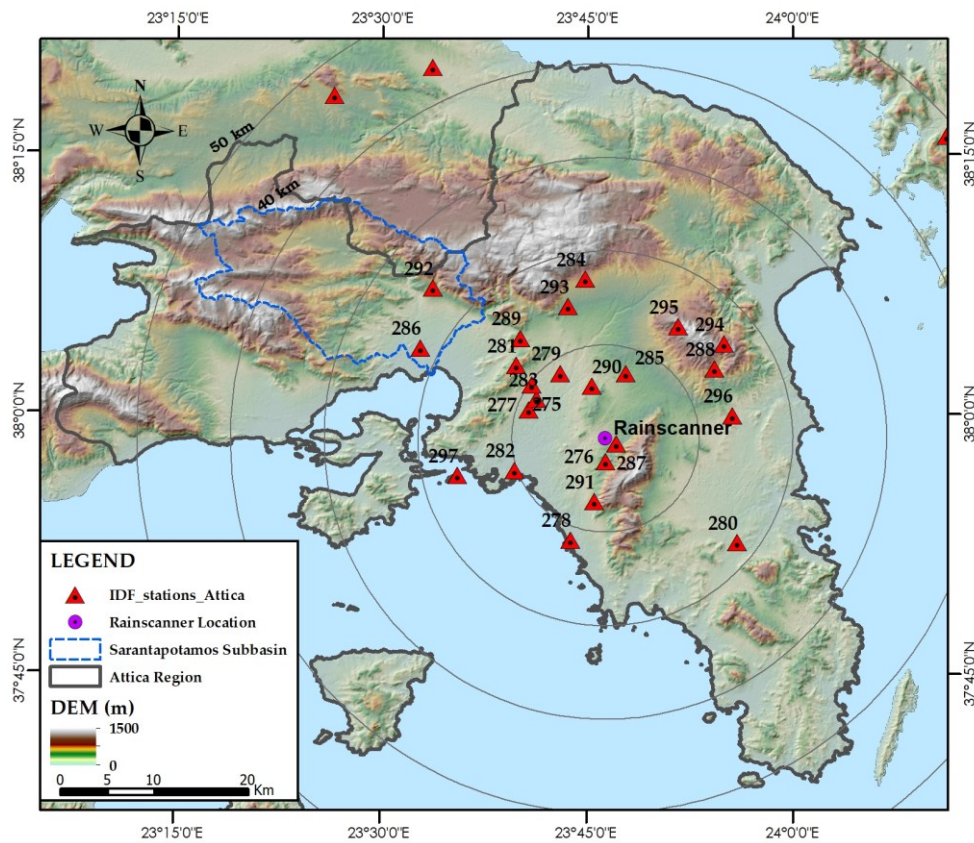

Figure 2-9: IDF Stations in Attica Region; Stations marked with their respected ID, referenced in Table 2-3.

Table 2-3: List of Stations with their IDF parameters and calculated rainfall accumulation

Station	ID	Elevation	IDF Parameters					Accumulate Rainfall (mm) T=5 years		
			η	κ	λ	ψ	θ	1-h	3-h	6-h
Eleusina	286	31	0.622	0.125	171.4	0.695	0.124	23.0	36.5	48.0
Mandra	292	258	0.622	0.125	213.4	0.641	0.124	31.5	50.1	65.9
Psytaleia	297	20	0.622	0.125	160	0.759	0.124	18.8	29.9	39.4
Nea Philadelphia	281	136	0.622	0.125	195.5	0.72	0.124	25.0	39.6	52.2
Ano Liosia	289	184	0.622	0.125	229.8	0.678	0.124	31.8	50.5	66.4
Nikaia	277	67.2	0.622	0.125	101.1	0.55	0.124	17.3	27.4	36.1
Peristeri	283	75.4	0.622	0.125	124.8	0.694	0.124	16.8	26.6	35.0
Lomfos Nymfon	279	107	0.622	0.125	163	0.698	0.124	21.7	34.5	45.4
Menidi	293	248	0.622	0.097	334.6	0.771	0.124	33.8	53.7	70.6
Helliniko	278	10	0.622	0.125	216.9	0.735	0.124	26.9	42.7	56.1
Tatoi	284	0	0.622	0.097	289.7	0.792	0.124	27.7	44.0	57.9
Galatsi	290	176	0.622	0.125	142.4	0.57	0.124	23.6	37.5	49.3
Vyronas	291	206	0.622	0.07	365.3	0.881	0.124	22.1	35.1	46.2
Zographou	276	226.4	0.622	0.07	282.1	0.828	0.124	20.9	33.1	43.6
Chalandri	287	219	0.622	0.125	266.7	0.699	0.124	35.5	56.3	74.1
Penteli	285	189.3	0.622	0.125	135.7	0.63	0.124	20.4	32.4	42.7
Ag. Nikolaos	295	729	0.622	0.097	375.4	0.809	0.124	34.3	54.5	71.7
Penteli D.B.	288	383	0.622	0.097	300.2	0.758	0.124	31.3	49.7	65.5
Pikermi	294	630	0.622	0.097	360.7	0.739	0.124	39.4	62.5	82.3
Markopoulo	296	133	0.622	0.097	236	0.727	0.124	26.5	42.1	55.3
Peiraias	280	85	0.622	0.07	275.8	0.805	0.124	22.0	34.9	46.0
Ag. Ierotheos	282	2	0.622	0.125	99.1	0.534	0.124	17.3	27.5	36.2

2.2.3 GIS Datasets

Apart from the hydrological measurements, other datasets that were used in this research include the following:

- A Digital Elevation Model (DEM) is provided by the National Cadastre & Mapping Agency S.A. (Copyright © 2012, National Cadastre & Mapping Agency S.A.). The DEM features a 5 m x 5 m spatial resolution elevation grid with a geometric accuracy of RMSEz ≤ 2.00 m and an absolute accuracy of less than 3.92 m for a 95% confidence level. The format of the files is in ERDAS Imaging (IMG), projected into the Hellenic Geodetic Reference System 1987, also known as Greek Grid, GGRS87, or EPSG:2100.

- The CORINE Land Cover (CLC, 2018) dataset was used, which features an inventory of land cover in 44 European classes. The CLC dataset was first established in 1990 and, since 2000, has been updated every six years, with the latest product being in 2018. The minimum mapping unit (MMU) is 25 hectares (ha) for areal objects and 100m m for linear elements. Because of the coarse resolution, it is suggested that a

more detailed land cover map should be used instead for various uses. The 2018 version made use of the Sentinel-2 and Landsat-8 satellite datasets, for a period between 2017-2018. The geometric accuracy of the datasets was less than 10 m due to the high Sentinel-2 resolution images, which results to a better than 100m of the final product.

- The URBAN Atlas 2018 land use dataset is also used. The Urban Atlas focuses on "hot spots," i.e., in urbanized areas, where a dense variability between land uses is found. The dataset was first introduced in 2016, with 2012 and 2018 the following products. The dataset is based on image classification of very high-resolution satellite imagery, the multispectral SPOT 5 & 6, and Formosta-2 pan-sharpened featuring a 2 to 2.5 m spatial resolution. Finally, the dataset is enriched with local information, such as city maps and online services, to increase its accuracy. The 2018 dataset features an inventory of 27 classes with an MMU of 10m and positional accuracy of 5 m. The 2018 version is not validated yet, but the 2012 installment featured an 85% accuracy for artificial classes and an 80% for all classes.

- GIS-based datasets provided by open access sources such as the geodata.gov.gr website, where the boundaries of the administrative regions were provided, and datasets, e.g., road network, provided by the OpenStreetMap initiative.

A list of the available IDF stations and their respected fitted parameters derived in the course of the Flood Risk Management Plans for Greece by the Ministry of Environment, Energy and Climate Change (SSW-MEECC 2017), in a .shp format.

3. Methodological Framework

3.1   Introduction

In this chapter, the methodological framework followed in this dissertation is explored. This framework's main objective is to aid in developing a FEWS that implements weather radar datasets. As described in the previous chapters, weather radar is extremely useful for FEWS implementations but requires proper calibration and user expertise to achieve reliable measurements and forecasts. The methodological framework covers the steps needed to reach hydrological products for FEWS applications. The entire framework is illustrated in Figure 3-1. The main components are illustrated with different colors, as referred to in the attached legend. There are four components: the input data, the processes, the algorithms, and the output. The input and output files refer to the raw datasets collected in this study, and the output files are either intermediate core files or actual hydrological products. The processes are the main components of this dissertation. Each component solves a different problem required for the entire process. The main processes are:

The first process is the file management and data corrections process, which is essential for further processing the raw Rainscanner datasets. There are two specific actions, one that is referred to as pre-process and one referred to as post-process. The pre-process is user-calibrated beforehand and is performed on the fly for each measurement within the Rainscanner software. The post-process provides an additional layer of quality control by addressing temporal inconsistencies and other raw data errors.

The second process is the Z-R calibration, where a methodology is described and applied for deriving a Z-R relationship based on Rainscanner – rain gauge correlation analysis of past events. This process is crucial for transforming reflectivity into rainfall height, thus obtaining reliable gridded rainfall maps for further analysis.

The third process involves the design and application of a gridded Rainfall-Runoff (RR) model suitable for implementing the Rainscanner-derived rainfall maps. The RR model uses GIS tools to calculate its parameters based on the basin's characteristics, making it easily applicable in areas with little data to calibrate.

The fourth process is a Flash Flood Guidance (FFG) implementation, the Gridded Flash Flood Guidance (GFFG). The implementation incorporates the proposed RR model to produce gridded rainfall thresholds, upon which a FEWS relies.

Finally, the fourth process is a Storm tracking algorithm. The algorithm first identifies rainfall cells based on reflectivity thresholds and generates each cell track after analysis of numerous instances. Then, the algorithm is used to examine the trajectory of rainfall events in the study area while providing the first step for generating nowcasting products.

Each process leads to an "Output" product, which, apart from its usage in this dissertation application, can also be used in other products.
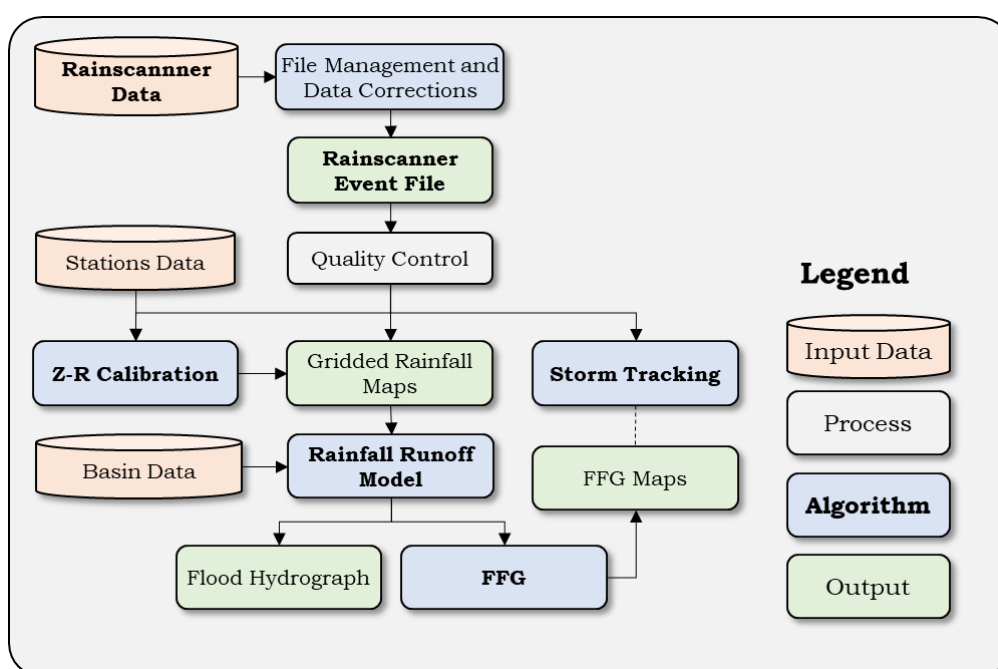

Figure 3-1 The Methodological Framework

3.2   Radar File Management and Quality Control

The weather radar conducts three-dimensional time and space observations. A total of 24 instances are utilized to create a single 2-minute duration volume scan. This volume scan is projected into 2-D, generating the Plan Point Indicator (PPI) and the Azimuth-Distance scans. The PPI scan shows the measurements projected into a 2-D surface in radial coordinates, with the radar system at its center. The Azimuth-Distance scan projects the measurements onto a 2D chart, with the x-axis representing the radar-to-target distance and the y-axis representing each point's azimuth.

Each volume scan is first subjected to quality control algorithms and later to spatial and temporal aggregations to match the desired scales. Finally, the resulting scans are georeferenced to the desired coordinate system and saved to the appropriate file type for further analysis. These actions consist of the " pre-process " performed by the Rainscanner software RainView® after user calibration and include the following:

- Ground Clutter and Occultation Corrections
- Temporal and spatial aggregation
- Georeferencing and File management

The preprocess flowchart is depicted in Figure 3-2, along with the settings established for the featured Rainscanner system.
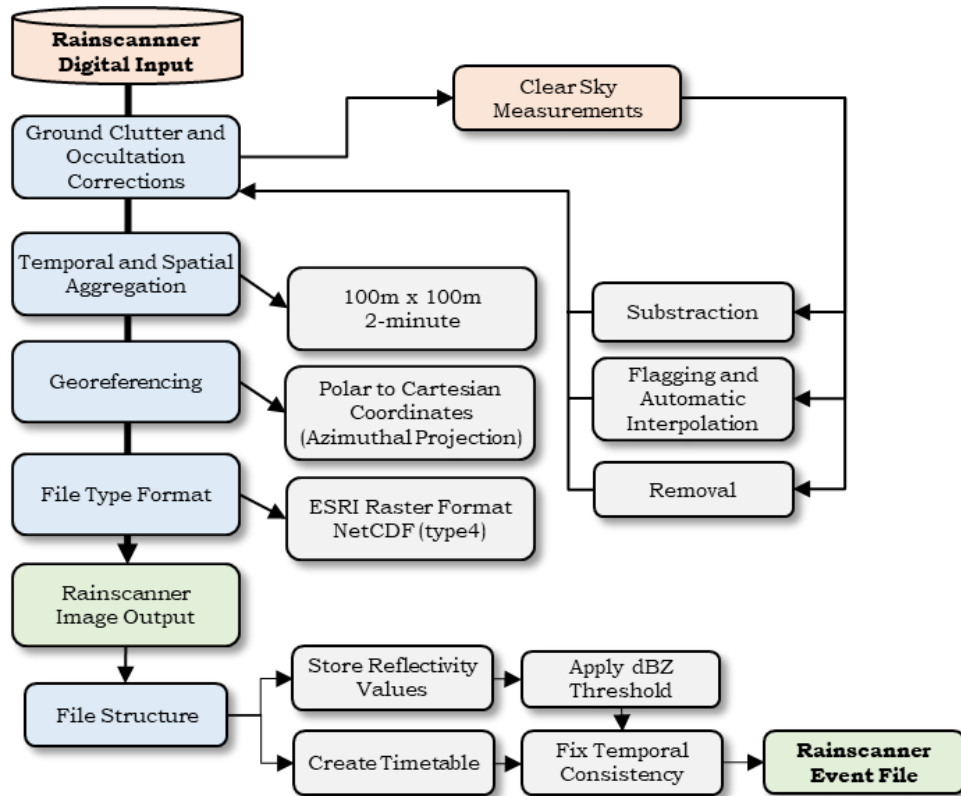

Figure 3-2 Data process flow chart

3.2.1   Pre-Process Quality Control

Ground Clutter and Occultation corrections

Ground clutter refers to reflectivity echoes transmitted by non-rainfall objects, such as the terrain, or stable signal-transmitting objects, such as radio or cell network transmissions, while occultation refers to areas of no data due to the obstruction of the radar's line of sight. The aim of these corrections is first to identify the regions where signal noise is generated

or signal is lost and, secondly, to correct it. The identification of these regions is accomplished by analyzing observations of clear sky. Observations of a clear sky measure non-rainfall objects' reflectivity values. As a result, these areas can be highlighted and further analyzed appropriately. In order to maximize the identification process, numerous scans of the clear sky are performed and mosaiced into a single image, the clear sky map.

The Occultation correction is performed first. This correction is made to cure areas where obstacles partially block the antenna beam. The data gaps are shown as no-data cones created beyond the signal-blocking obstacles in a PPI view. Instead of omitting these areas, an interpolation algorithm is applied to fill these gaps. The neighboring non-occulted points in the azimuthal direction are discovered and used to fill the *NoData* points using linear interpolation. If one of the neighboring points is a *NoData* point, the value is determined by the distance between the neighboring non-occulted points and the point to be filled. If the "no data" point is closer than the "has data," then the point gets a *NoData* value. Following this procedure, the occultation map is created, which indicates the position of the affected pixels and the interpolation parameters to be performed in real-time measurements.

The Ground clutter corrections follow a similar procedure. The clear sky map is used to identify areas to be flagged for corrections, but real-time gap-filling interpolation can also be performed. The clutter-affected or missing data gaps can be treated based on one of the following procedures:

- Removal of the cluttered area
- Clutter Subtraction.
- Flagging and Automatic interpolation

In the first case, any clutter-detected areas are manually marked as *NoData* areas and are ignored from future scans. This treatment is performed if large clutter areas are detected and no further action is preferred. Moreover, replacing the value with *NoData* makes the file smaller and easier to configure.

The second and third cases are correction algorithms. The clutter subtraction is relatively simple since it treats the clear sky reflectivity values as data to be subtracted from the real-time scans. Although this correction may work for low-reflectivity noise, it is impractical for use with high-reflectivity noise since a considerable amount of reflectivity is substracted, rendering the treated area as low as zero reflectivity targets on real-time scans, where actual rainfall should be observed instead.

Finally, the flagging and automatic interpolation algorithm is usually the preferred choice. In this case, an interpolation algorithm (Kammer 1991b) is applied to the clutter-affected areas using nearby clutter-free areas. The algorithm can be performed in either user-defined

areas or automatically to the entire scan, which is also the default. In this case, the algorithm is performed conditionally, based each time on real-time measurements.

When performed automatically, the clutter-affected areas are identified first for each can. In order to avoid interpolation from points that are seemingly non-clutter data but are found within clutter zones, a radial segmentation is performed in each case. A segmentation interval is chosen, and the number of flagged areas is calculated for each radial area. If more than half of an interval's areas are highlighted, the interval's radial areas are also highlighted. The size of the segmentation interval is calculated as follows:

$$N = 4 \frac{1}{\sqrt{\Delta_r}} \frac{1}{\sqrt{RS}} \qquad (3.1)$$

, where N is the segmentation interval, Δ_r the range area resolution (in km), and RS is the range sampling (range averaging).

The *NoData* gaps are polygon-shaped areas interpreted as an ellipse. The corrections applied, i.e., the gap-filling interpolation algorithm is performed into two axes: the azimuthal direction, i.e., left and right of the missing data, and the radial axis, i.e., the axis defined by the line between the target and the Rainscanner. For each area, the following parameters are stored, as illustrated in Figure 3-3:

- The maximum distance in the radial direction, D_r
- The maximum distance in the azimuthal direction, D_a
- The radial direction bounding points location, R_0 and R_1
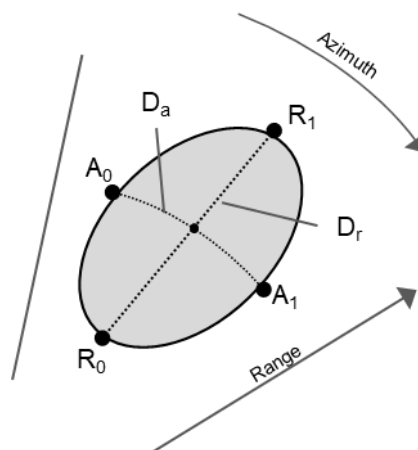- The azimuthal direction bounding points location, A_0 and A_1

Figure 3-3: Clutter-affected area calculated parameters

The nearest data from clutter-free points are searched for interpolation for each area. If the distance of these points is less than a pre-defined maximum radial, $D_{a,max}$, and azimuthal direction, $D_{r,max}$, then the interpolation can be applied in both directions. However, if the radial or azimuthal distance exceeds their pre-defined maximums, the interpolation is

performed only in the direction where the maximum is not exceeded. Finally, no interpolation is performed if the distance exceeds the maximums in both directions. These cases are illustrated in Figure 3-4, where panel a shows interpolation in both directions, panel b shows interpolation only in one direction, the azimuthal, and panel c shows the case of no interpolation.
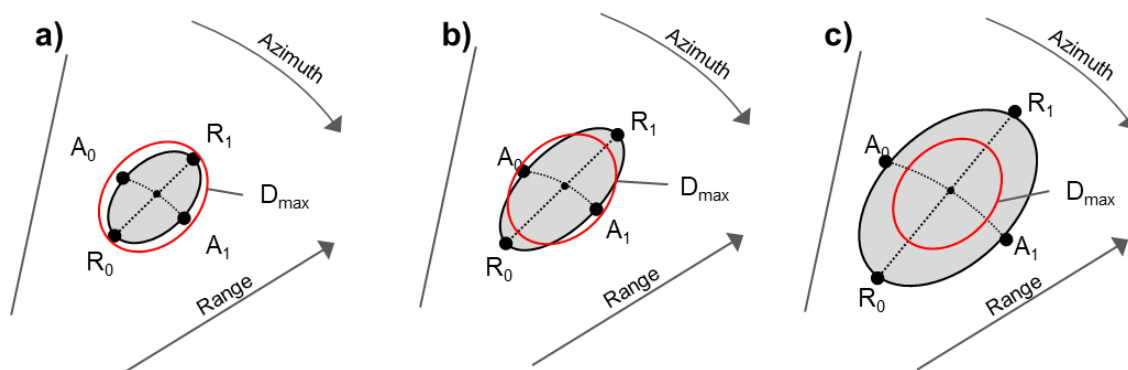

Figure 3-4: Clutter-affected area interpolation cases based on pre-defined maximum distances, a) both directions, b) one direction, c) no interpolation

If the missing data area has a complex shape, as shown in Figure 3-5, multiple bounding points are calculated, and interpolating each direction is performed based on the distances calculated for each bounding point group. Specifically, each Rainscanner ray has a 0.5-degree fixed step in the azimuthal direction, and therefore, for each ray, a R_0 start and R_1 end bounding point are defined.
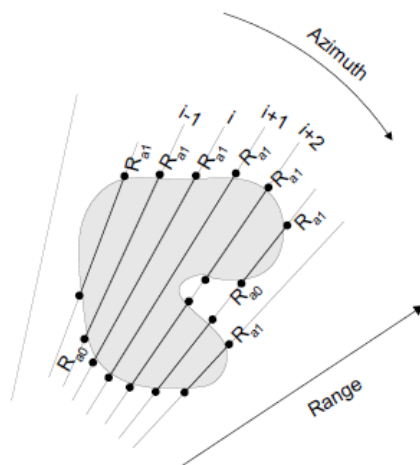

Figure 3-5: Ground clutter identification and flagging algorithm in a complex shape

The interpolation performed is linear, with the user setting the maximum distance D_{max} in each direction. In this Rainscanner, the limit is ten cells, i.e., 1000 m. If both-direction interpolation is feasible, then the calculated value is the mean value of the interpolated

values of each direction. If any neighbor cell is of *NoData*, then the next neighbor is used for interpolating up to the maximum distance previously set.

Finally, if automatic and user-defined areas overlap, then the "OR" rule is applied, where the interpolation is applied by the most restrictive rules set in each case. For instance, if only radial interpolation is pre-selected for a user-defined area, the automatic interpolation will not perform two-directional interpolation, even if feasible. Moreover, the *MAX* rule is also applied, which dictates that the maximum reflectivity value is selected if two interpolations are performed for the same point.

Spatial and Temporal aggregation

This procedure is performed automatically to define the desired spatial and temporal resolutions. The Rainscanner system, by default, creates a 1000 x 1000 pixels raster. The spatial resolution of the scans is then related to the scanning range. When large scanning ranges are selected, the system degrades the resolution to fit the data into the 1000x1000 pixels raster. Therefore, although a 100 km range is feasible by the system, a smaller 50 km range will lead to a better spatial resolution scan. Moreover, the smaller range is a more reliable choice since X-Band radars suffer from signal attenuation, thus making long-range scans through storms unreliable. Therefore, for a 50 km range selected, a 100 m x 100 m pixel size is calculated.

Concerning the temporal resolution, the minimum 2-minute temporal resolution is selected. The temporal aggregation of reflectivity values can be easily performed by calculating the average values of the selected 2-minute intervals within the desired time interval. Although the aggregation may be conducted on the precipitation data, executing the aggregation on the reflectivity values is preferable to prevent errors that can be amplified when applying a power-law equation, such as the Z-R relationship used first.

Data projection and File Type

This step deals with the necessary projection transformations, i.e., the conversion from polar to Cartesian grid coordinates. The conversion is applied using interpolation between the nearest points of the polar grid to the nearest point of the predefined cartesian projection. The selected projection for the generated datasets is the Azimuthal Equidistant projection, with the Rainscanner as its center. Finally, the dataset is stored in an "Arc/Info ASCII Grid" file format. The files generated are of ASCII file format containing a 1000 x 1000 dimensions matrix, with the reflectivity measurements in dBZ values, and ASCII files containing the georeferencing information. Since 2023, a NetCDF type 4 file format has also been generated, with the scope of replacing the Arc/Info ASCII Grid format. The new file format reduces the file size significantly, from approximately 6 MB for each 2-minute measurement to less than 1 Mb.

The generated files receive a name based mainly on the timestamp in Universal Time Coding (UTC) and information regarding the generated file. The following file name coding is used:

<YYYYMMDDhhmmss><NN><data-type>.<product-type>

The first part is the timestamp, where YYYY, MM, DD, hh, and ss denote year, month, date, hour, minutes, and seconds. The <NN> is an increasing counter to distinguish file names of the exact date and time stamp, while the <data-type> and <product-type> refer to the data type, such as whether it refers to reflectivity or other measurements, and the Rainscanner type of product, e.g., PPI, CAPPI, max or others. More information about the two latter can be found in the Rainscanner manual (Selex ES GmbH 2014; Selex ES 2014). The typical reflectivity scans used in this study follow the following example:

2020060111020000dBuZ.ppi_top.asc

The previous files refer to a 2-minute reflectivity image with a timestamp of 2020/06/01, 11:02:00 (UTC). The following two numbers are the <NN>, which are 00, typical for images with unique timestamps. The data type is "dBuZ," a reference to dBZ, which are reflectivity units. The u letter in the dBuZ extension denotes that the product is a ground clutter-corrected dataset. Finally, the product type is a "ppi_top," which refers to a PPI image, and its extension, .asc, refers to the ASCII file format. When the Arc/Info ASCII Grid file format is used, additional files, such as a projection file and other GIS-related files, are also generated. All files are stored within an automatically generated folder named after the date of their creation. Therefore, all measurements of the same date are stored within the same folder, regardless of whether the system went offline briefly.

3.2.2 Post-Process Quality Control

The post-process quality control consists of quality controlling any unreliable high reflectivity values missed during on-the-fly corrections and temporal inconsistencies of the generated data. After creating the necessary data structure, the process is performed within the MATLAB programming environment.

First, the event folder is constructed. As stated earlier, the Rainscanner generated folders based on the date they were created. Therefore, an overnight event might be stored in two different folders, or a single date might consist of two events, one in the morning hour and one in the evening. Such gaps might exist due to a) power failures that result in turning the system offline for several hours or b) limiting the radar usage when rainfall is not observed. The latter is performed to reduce the cost of maintaining a radar system. The maintenance is related to its usage. For example, it is referenced that the magnetron of a weather radar

should be changed after 3500 hours of usage. In this study, a single event is considered complete when the dataset features a continuous timeline without gaps of over 30 minutes. However, smaller temporal gaps, e.g., 10 - 20 minutes, can still be considered significant data loss, especially when examining small basins as in the study area. Nevertheless, the Rainscanner datasets used, apart from gaps due to power failure, did not include such gaps. Each event is given a serial number, and further management is performed within the MATLAB environment. A data struct is created, containing the entire reflectivity images of the event in 1000 x 1000 and the date time timeseries. In this stage, the Greek time zone is used to sync the data to the timezone of other used datasets, such as rain gauge datasets. Care is taken for transforming to winter (UTC+2) or summer time (UTC+3), based on the event date.

Two quality control actions are performed in these raw datasets, as shown in Figure 3-2. First, a dBZ threshold is applied to limit any extreme values missed during the ground clutter corrections. This limit is set to 55 dBZ, meaning values above 55 dBZ are reduced to 55 dBZ. This threshold is set since values over 55 dBZ can be either hail, which is not common in Attica unless noticed otherwise, or the effects of the bright-band effect. This threshold limits the latter's impact on the data since it is impossible to detect it without vertical scanning. The second correction is optional and consists of a secondary "clear sky" correction. This correction might be necessary if the ground clutter corrections are outdated and constant noise is observed at various points of the image.

The second action is fixing the temporal consistency and aggregating the final product. While each image has a 2-minute timestep, most analysis is performed in a 10-minute temporal scale. This scale was selected since the rain gauge datasets are also at a 10-minute resolution, which is suitable for analyzing storm systems in the area. The data aggregation is performed by calculating the average value of the datasets within a 10-minute interval. If some time instances are missing, then the value is calculated by the remaining files. If an entire 10-minute is missing, this is set to *NoData*.

Following these quality controls, the main processes are undertaken, as shown in Figure 3-1, i.e., the Z-R calibration, the R-R model, the GFFG model, and the storm tracking algorithm.

3.3   Z-R Calibration Framework

The Z-R relationship is a critical aspect of weather radar monitoring. The relationship transforms measured radar reflectivity (Z) into rainfall intensity (R). As previously described in Chapter 1.5, the parameters of the Z-R relationship are related to the rainfall droplet size distribution. This distribution is not static but varies in time and space. In order

to reach valuable conclusions, a complete framework is devised using the rain gauge-Rainscanner correlation method. The framework is displayed in Figure 3-6.

In the correlation method, first, the spatial and temporal resolution of the two datasets is matched. The rain gauge datasets are point measurements, whereas the Rainscanner is of a gridded format. However, the rain gauge datasets are considered as the "true rainfall," i.e., the actual rainfall discarding any errors or uncertainty, and therefore, any conversion made is performed to the Rainscanner datasets. These conversions refer to matching the 100 m x 100 m raster files into "point" measurements and converting from 2-minute scans into 10-minute resolutions.
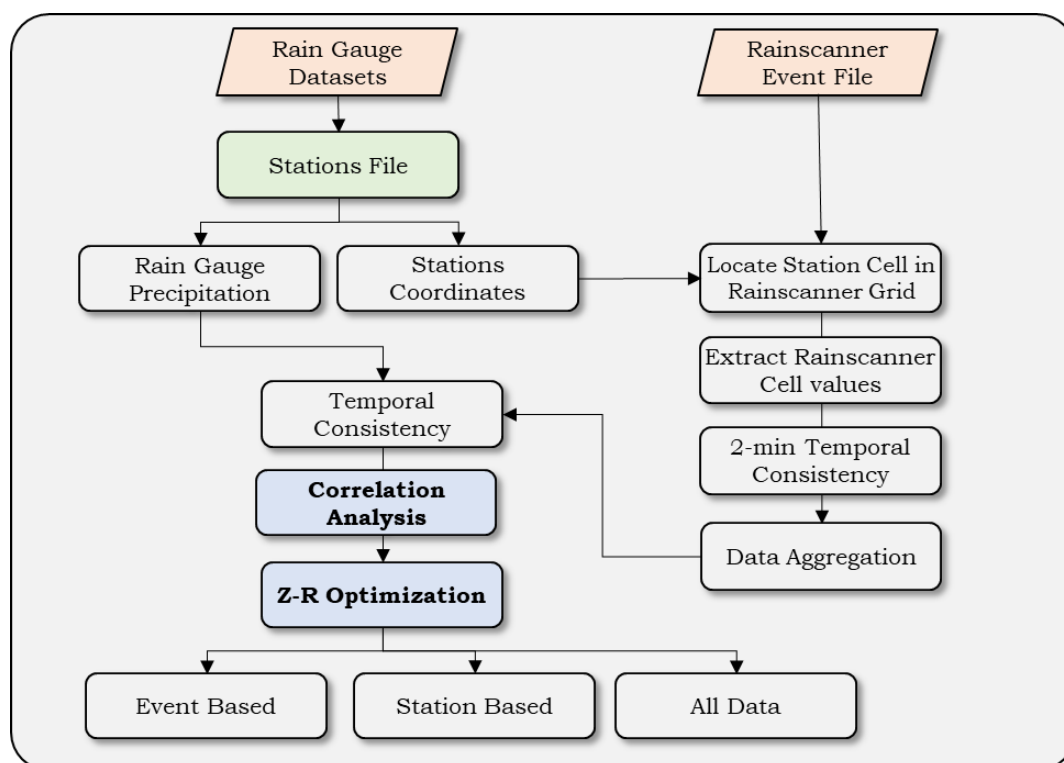
Figure 3-6. Correlation analysis and Z-R optimization flow chart

3.3.1 Data conversion

First, the spatial conversion is performed by finding the designated pixel of the Rainscanner grid that matches a targeted station (Pappa et al. 2021; Bournas and Baltas 2022a). The Rainscanner cell has a 100 m x 100 m resolution, deemed more than adequate to match the rainfall height of a point to a cell since rainfall will not adjust significantly within 100 m. In Figure 3-7, the procedure to find the designated cell for each station is shown. The process is a nearest neighbor proximity search between the station coordinates and the Rainscanner cell's centroid coordinates. Although the Rainscanner generates data for a circular region with a 50 km radius, the generated datasets, i.e., the ASCII files, consist of a square region of 1000x1000 cells (Figure 3-7a). The ASCII file geoinformation defines two parameters: the

coordinates of the bottom right corner (angular point) and the cell dimensions dx and dy. Through this information, all cells can be identified. It is essential to notice that although a 100m x 100m cell dimension is often mentioned, the actual dimension varies slightly due to the polar to cartesian coordinates transformation performed, as mentioned in section 4.2. From the angular point, the bottom left centroid coordinates are found first, and then the rest of the cell's centroids are discovered by adding dx and dy accordingly. The Euclidean distance between the station and the Rainscanner cell centroids is then calculated. The matching cell is the one in which Euclidean distance is the smallest, i.e., closest to the station. This process is performed for each station, and the matching cell's matrix indices are stored for later usage. This operation is performed only once since the Rainscanner dataset coordinates or sample size are not expected to change.
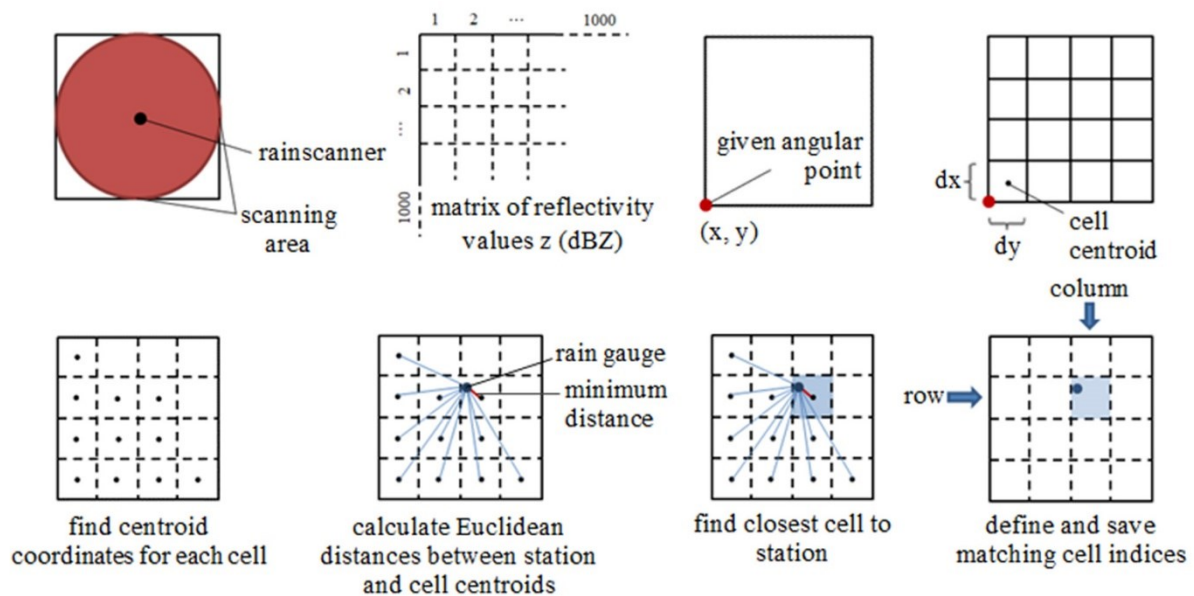

Figure 3-7. The procedure of locating the rain gauge location inside the radar raster dataset.
Source: (Pappa et al. 2021)

The temporal scale adjudgment is shown in Figure 3-8. The Rainscanner datasets account for two-minute reflectivity measurements, whereas the rain gauge measurements are on a 10-minute temporal scale. For each station, the temporal adjustment is performed on the reflectivity values, specifically the reflectivity timeseries extracted from the Rainscanner dataset. Reflectivity is a non-accumulative measurement; thus, the aggregation to 10-minute values is performed by calculating the average value of the five two-minute instances within the same 10-minute time interval of the rain gauge. The aggregation follows the rules as mentioned in section 4.2.2. If a timestep is missing, the aggregated value is calculated as the average of the remaining four instances. Moreover, when a single two-minute value has values unrelated to the other instances, such as NaN, zero, or extreme values, these values

are excluded from the aggregation. Finally, if a complete 10 min interval is missing, the no data value is set, although this never occurred. Measurements that featured significant time gaps due to power failures of the Rainscanner system were not included in the Z-R calibration. However, such gaps were rarely found, albeit in some situations where some instances were lost when the system had to create a new date folder to store the files.
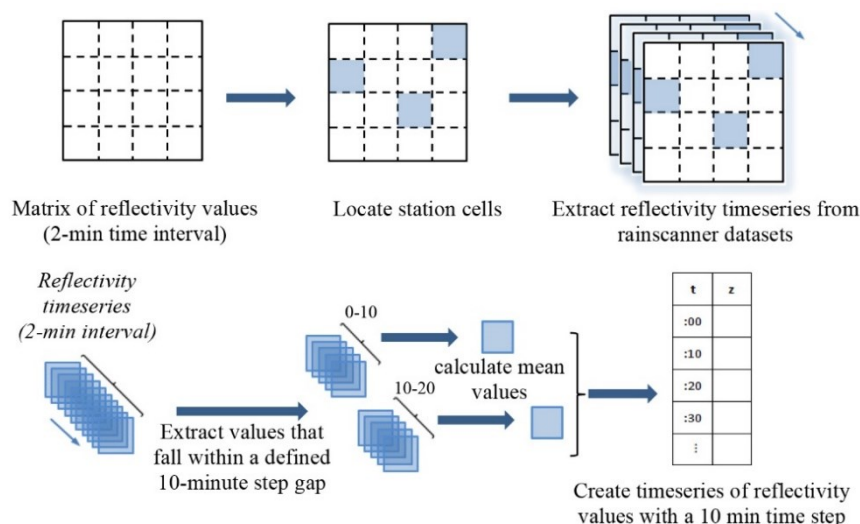

Figure 3-8. Raster to 10min timeseries procedure
Source: (Pappa et al. 2021)

3.3.2 Correlation Analysis

The Z-R optimization process is divided into two sub-processes: a) the optimization process and b) the correlation analysis. The first is the actual optimization process, where the parameters of the Z-R relationship are determined, while the correlation analysis, which is performed first, consists of a quality control procedure. The entire process is displayed in Figure 3-9.

It is acknowledged that the Z-R parameters, parameter *a* and parameter *b*, vary in time and space (Hasan et al. 2016; Gilewski and Nawalany 2018; Sahlaoui and Mordane 2019; Qiu et al. 2020). Therefore, it is expected that the Z-R parameters will not only vary between different events but also in space, i.e., within the scanning range. In order to detect these variabilities, various optimizations are performed. These optimizations are categorized into three groups: a) Station-based optimizations, b) Event-based optimizations, and c) Entire dataset optimization.
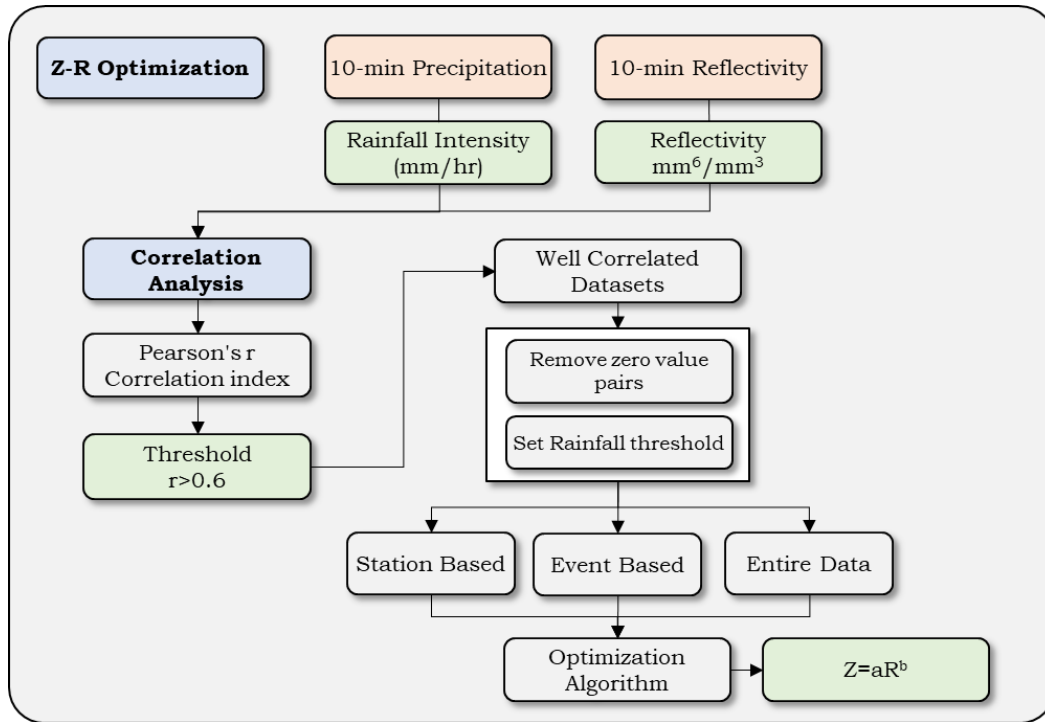
Figure 3-9: The Z-R Optimization Process

The correlation analysis consists of a quality control procedure. Pearson's *r* correlation coefficient index is calculated to distinguish the raingauge–Rainscanner datasets. The Pearson correlation coefficient between two datasets evaluates whether the two datasets are related. When used between radar and rain gauge timeseries, the coefficient evaluates whether the two timeseries follow the same pattern, i.e., the same increase and decrease are found between the two datasets. A high correlation between the Rainscanner and rain gauge datasets is evidence that the datasets are recording the same phenomenon, while a low correlation shows that the datasets are unrelated and, thus, unsuitable for optimization. Low correlation can be attributed to a variety of factors. The more frequent is a systematic error in either instrument. For instance, low correlation is observed when one instrument, e.g., the Rainscanner, features rainfall values while the other does not. In this case, three conditions may be occurring. The first is due to the Rainscanner readings suffering from signal noise, e.g., ground clutter, that has not been dealt with in pre-process, and therefore it observes false readings. The second is due to possible errors with the rain gauge measurements. Although the rain gauges are usually considered as the actual rainfall readings, this does not forfeit the fact that errors might still be in place. Finally, low correlation can also be attributed to other factors that lead to temporal inconsistencies, e.g., lag, between the two datasets. For example, an increase in precipitation in the Rainscanner is recorded in the next or several timesteps of the rain gauge recorder. This lag can occur in areas near the edge of the Rainscanner scanning range, where the observation height is high, e.g., 2 km, thus the time it takes for a rain droplet to reach the ground, or in this case, the

77

rain gauge basket, leads to being measured in a different time step. Another error is due to Rainscanner spatial resolution, where rainfall measured by the Rainscanner may not be measured by the rain gauge because it is driven away from strong winds.

Various approaches are taken in this study to account for all these errors. First, the effect of the Rainscanner sample size is tested. Secondly, the correlation coefficient, second order, is also used to detect any temporal inconsistencies. Lastly, various threshold levels are applied each time, and the number of omitted stations is examined. When setting a threshold level, one must account for the fact that fewer station datasets are eligible for optimization by setting a higher threshold. While this leads to better performance in the optimization, it significantly limits the sample size, e.g., the Rainscanner – rain gauge data pairs, thus obtaining an overfitted relationship. By lowering the threshold, more unrelated data pairs are included in the mix, but the more significant sample allows for more sturdy results. Moreover, it is significant to note that in previous research, this kind of optimization was usually performed at a 1-hour temporal resolution, whereas in this study, the 10-minute resolution was maintained. In high temporal scales, datasets show higher variability between each time step; thus, the error in each time step can be considerably higher than in coarser scales, e.g., 1-hour, where the data variability is mitigated through the aggregation process (Bournas and Baltas 2021a). A threshold of 0.6 is used, although various limits are also examined.

The correlation threshold is set to remove stations that feature unrelated datasets. This threshold is used for each event independently. For instance, one station might feature unrelated datasets in one event, but in a different event, the data are related. In this case, only the well-correlated events of the specific station are used for the station's Z-R relationship. In the event-based optimization, only the stations that feature above the threshold are used, and in the all-dataset optimization, all of the well-correlated stations of each event are used. Finally, especially in the all-dataset optimization, a calibration validation grouping of the stations is chosen. In this case, some of the station's datasets are used in calibration, while the latter is for validating the derived Z-R relationship. The selection of each group is made according to their location to have good coverage of the study area in each group.

3.3.3 Z-R Optimization algorithm

The Z-R optimization is based on the correlation of the Rainscanner and rain gauge datasets. Therefore, it focuses on deriving the values of parameters *a* and *b* of the Z-R relationship by minimizing an objective function. The parameters have specific boundaries, 0 to 2000 for parameter *a* and 1 to 3 for parameter *b*.

The optimizations are performed in three groups. For the station-based optimization, the target is to reach station-specific Z-R relationships. This result also allows for a better

understanding of the spatial variability of the Z-R relationship. For event-based optimization, the target is to reach event-based relationships and compare them to the individual stations derived relationships. Finally, the entire-dataset optimization aims to provide a single Z-R for general purposes and to be compared with the results of the previous optimization. In this optimization, the procedure is performed in two stages: a) using the entire dataset and b) separating the stations into calibration and validation groups. The selection of calibration stations relies on their correlation coefficient, meaning that stations exhibiting higher correlation values are chosen for calibration. This selection is made while also ensuring an evenly distributed presence of calibration and validation stations across the study area.

The optimization is performed within the MATLAB environment. The objective function is the minimization of the Root Mean Square Error (RMSE) of the selected Rainscanner – rain gauge pairs, as defined below in the equation (4.1):

$$RMSE = \sqrt{\frac{\sum_{i=1}^{n}(R_i - G_i)^2}{n}} \qquad (3.2)$$

where *Ri* and *Gi* are the Rainscanner and rain gauge 10-minute rainfall heights, respectively, and *n* is the number of pairs. Furthermore, other indexes are calculated as well, such as the Mean Bias Error (MBE), the Normalized Mean Bias (NMB), and the Normalized Mean Absolute Error (NMAE), formulated as seen in equations 4.2, 4.3, and 4.4. The NMAE highlights the actual percentage error, while the NMB and MBE highlight whether an overestimation or underestimation of rainfall is performed by the Rainscanner (Pappa et al. 2021).

$$MBE = \frac{\sum_{i=1}^{n} R_i - G_i}{n}. \qquad (3.3)$$

$$NMB = \frac{\sum_{i=1}^{n}(R_i - G_i)}{\sum_{i=1}^{n} G_i} \times 100\% \qquad (3.4)$$

$$NMAE = \frac{\sum_{i=1}^{n}|R_i - G_i|}{\sum_{i=1}^{n} G_i} \times 100\% \qquad (3.5)$$

Finally, all results are compared with Z-R relationships derived in previous research: a) the well-known Marshal and Palmer equation Z=200R[1.60] (Marshall and Palmer 1948), b) a convective-based Z=431R[1.25] (Baltas and Mimikou 2002b) and c) Z=261R[1.53], a Z-R consisting of datasets from both stratiform and convective events (Baltas et al. 2015). All relationships have been derived from distrometer measurements, while the last two have been derived from measurements within Athens.

3.4   Rainfall-Runoff Model

3.4.1   Introduction

The Rainfall-Runoff (RR) model is used to transform rainfall into runoff. A typical RR model accepts rainfall as input and generates runoff as the output. Numerous hydrological models are available, so the common problem is selecting the most appropriate model to perform this transformation. The RR models can be categorized based on numerous factors. The most common ones are a) based on the mathematical approach, b) the temporal analysis, c) the spatial discretization, and d) the handling of uncertainty.

In forecasting applications, the main factors that need to be considered are (Sene 2008):

- Forecasting requirement: the intended use of the forecasts;
- Data availability
- Forecasting System: the system on which the model will operate
- Performance requirements: run time, accuracy, provided lead time
- Type of model

The Forecasting requirement is the actual aim of the forecast. The aim can be to assist with issuing flood warnings, controlling river control structures, or monitoring river station levels. Moreover, the model selection may also rely on potential users, such as local authorities, emergency services, or the public. In EWS, event-based models are used to simulate the evolution of a flood event, while continuous simulation models determine the initial conditions or variables that change slowly in time, e.g., the prior event soil moisture conditions.

The Data availability factor is usually the crucial factor. Data availability refers not only to current available and monitoring datasets but historical datasets as well. The quantity and quality of historical datasets are required for proper model calibration. Therefore, the data availability also dictates the model type to be used.

Process or physically-based models are the most data-demanding models since they use partial or ordinary differential equations or conceptual relationships to represent the physical processor overland flow, soil infiltration, groundwater flow, and other factors. These models are well suited to spatially distributed inputs, making them favorable for EWS applications since they make the most out of gridded datasets such as weather radar or satellite datasets. Conceptual models represent the physical processes in a simplified way, while the model's parameters are usually associated with basin characteristics, making them easy to calibrate. These models are usually used within a lumped or event semi-distributed format. Finally, data-based models, called Black Box models, use system analysis concepts

where their variables and parameters are unrelated to any physical process. A black-box model does not care about the values of its parameters as long as it produces the correct amount of runoff for a given rainfall input. Typical black box models are transfer functions and Artificial Neural Network (ANN) models.

The Forecasting system and the performance requirements are operational factors. Specifically, the forecasting system dictates the variable upon which action should be made. For instance, in the FFG system, the primary variable is the accumulative rainfall over a designated duration; thus, more focus is given to deriving rainfall thresholds rather than streamflow thresholds. Concerning performance, there is a give and take between model simulation running time and provided lead time. Sophisticated or stochastic models may provide more information, but the simulation time limits the provided lead time. In small basins, where the concentration time is small, this can be deemed a crucial loss of time.

Specifically, for EWS applications incorporating weather radar datasets, a distributed format is favorable. When the datasets required for calibration are available, the distributed format is advantageous against the lumped or semi-distributed formats and is expected to provide better results (Borga 2002). In addition, the higher spatial resolution of the basin characteristics, such as the slope, soil type, and land use, provides a better description of a study area (K. Ajami et al. 2004; Grek and Zhuravlev 2020), and simulated streamflow is enhanced (Aouissi et al. 2018). Moreover, recent research concluded that higher resolutions are necessary when examining small-scaled basins, e.g., urban basins (Cristiano et al. 2017; Paz et al. 2019).

Distributed models are usually data demanding, making using them often an avoiding factor for EWS implementations (Sitterson et al. 2018). However, it is deemed feasible to implement simple conceptual or data-based methods, such as the UH, into a distributed format. For instance, the Clark UH method has been the subject of multiple such implementations (Kull and Feldman 1998; Sadeghi et al. 2015; Cho et al. 2018) with good performance.

Methods that rely on data that can be assessed through Geographical Information Systems (GIS) tools have increased in popularity. GIS has proved to be a massive tool for hydrological modeling (Dieulin et al. 2006), especially in ungauged basins. These implementations, referred to as gridded models, require few datasets to be calibrated and thus are advantageous for large-scale EWS applications and flash flood EWS, where most affected basins are small ungauged basins.

3.4.2 Gridded Model

The rainfall-runoff devised in this dissertation is a gridded model based on the time-area diagram method (Bournas and Baltas 2022b). The method is partially used in the Clarks unit hydrograph model, and its gridded implementation is the modified Clark (ModClark) UH.

The main difference between the models and the proposed model is the cell's travel time implementation method. In the Clark model, the two parameters derived are the time of concertation, t_c, and the storage coefficient R. Since the Clark model is applied in a lumped format, a basin t_c is only required, while the time-area relationship is derived based on that value. In the ModClark model, the travel times of each cell are calculated as a factor of the time of concentration of the basin based on the distance of each cell from the outlet. Specifically, equation 4.5 is solved to configure the cell time.

$$t_{cell} = t_c \frac{d_{cell}}{d_{max}}$$

(3.6)

Where t_{cell} is the time each cell takes to reach the outlet, t_c is the time concentration of the basin, d_{cell} is the travel distance of the cell to the outlet, and d_{max} is the travel distance of the most distant cell to the outlet.

In either case, the excess rainfall is first calculated through a loss method, e.g., the SCS CN method, and the basin or cells outflows, for the Clark and ModClark models, respectively, are routed through a linear reservoir, yielding the outflow hydrograph. Finally, in the ModClark model, a convolution is performed to determine the runoff at the basin outflow. Compared with the ModClark method, the distributed version of Clarks UH, in the proposed model, instead of estimating the cell's time travel as a friction of the basin time of concentration, a unique time travel is calculated based on the time-area diagram. This change leads to a better approximation of the cell's travel time since each cell's travel path's characteristics are considered. Following this, a rainfall event can be simulated by applying a loss method to calculate the excess rainfall in each cell, while the hydrograph at the outlet is calculated through a time-area convolution:

$$Q_n = \sum_{m=1}^{n<M} P_m U_{n-m+1}$$

(3.7)

where Q_n is the outlet discharge ordinate at time n, P_m is the excess rainfall depth in time interval m, M is the total number of discrete rainfall pulses, and $U_{(n-m+1)}$ is the U, the cell's hydrograph ordinate at the time (n-m+1).

The specific model aims to be used for flash flood forecasting in small to medium-sized basins found within the study area. The rainfall input is the Rainscanner datasets, aggregated to a more desired grid resolution output, i.e., 500m x 500m. Concerning the loss method, the National Resources Conservation Service (NRCS Curve Number (CN) method is selected mainly due to its easy implementation with ungauged basins. The model is used to provide two products, the Flood Hydrograph and the FFG calculations, as shown in Figure 3-1. The first, shown in Figure 3-10, is applied to derive the flood hydrograph in pre-specified critical locations of the basin. The second is implemented into the FFG calculations

performed at a grid level, further discussed in Chapter 3.5. The model's ease of use lies in its capability to be employed on any temporal and spatial scale, while the only parameters that need to be determined are the time-area diagram and the gridded CN map.
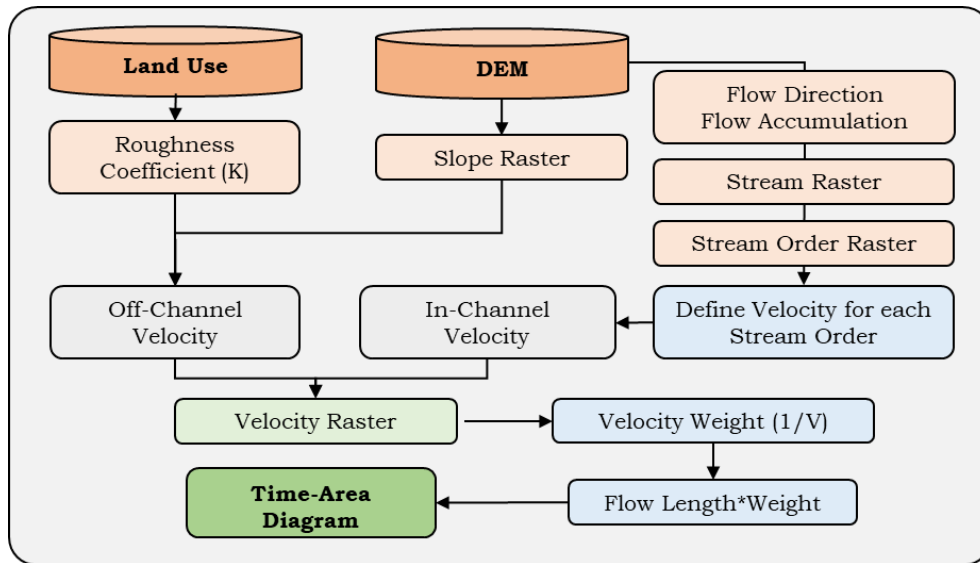

Figure 3-10. The Rainfall-Runoff Model schematic

3.4.3   Time-Area Diagram

The time-area diagram is a relationship between travel time and a percentage of the basin area. The time-area diagram, also called Isochrone curves, is produced when the travel times of all cells are calculated within the basin. Then, by dividing the basin into specific time intervals, the Isochrone curves are created. The area between two isochrone curves is the percentage of the basin that discharges at the time set by the higher isochrone curve. When the selected time interval approaches zero, the time-area diagram is a continuous line that usually represents a UH shape. In order to calculate the time-area diagram, a DEM and a Land Use file are required. The procedure is performed in GIS software, as shown in Figure 3-11.

The GIS procedure derives the Flow direction and Flow accumulation rasters through a hydrologically corrected DEM. The flow direction raster is a nine-integer values raster, where each value represents the desired runoff direction. The direction is calculated based on the maximum slope between the cell's center and the eight neighboring cells. The main idea is that each grid follows a specific route to reach the outlet, and thus, the main objective is to calculate the time it takes for water to complete this route. The flow accumulation raster represents the number of cells that flow to a designated cell. The higher the value its cell has, the more cells flow to that cell. Therefore, it is easily understandable that high-value cells in the flow accumulation raster represent the stream network. By setting a cell

threshold, the flow accumulation raster is divided into cells that represent streams and cells that do not. The threshold set is crucial since it defines the stream network density.
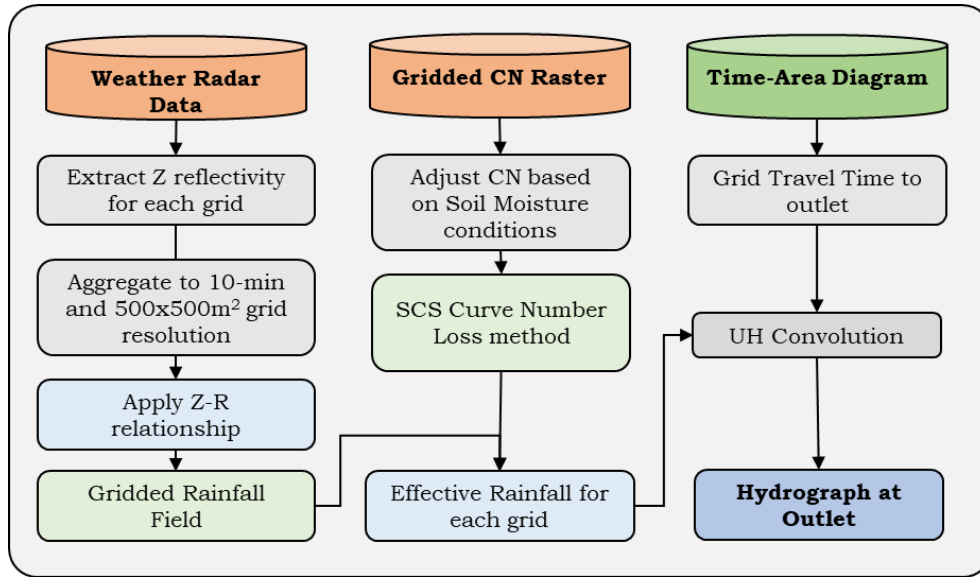

Figure 3-11. Time-Area Diagram derivation procedure

The grid route to the outlet is calculated by applying the Flow Length tool. However, since what is desired is the actual travel time, the designated route length is needed first to be divided by the velocity raster, which represents the water velocity at each cell. Within a basin, the velocity raster can be defined by two flow velocities: the off-channel and the in-channel velocity. Off-channel are areas where sheet flow occurs, i.e., areas outside the stream channels, while in-channel refers to areas within streams.

First, the off-channel or overland velocity is calculated. In this application, the calculations are performed at the grid level, providing a gridded velocity raster instead of a single off-channel velocity value, as in most studies. The governing parameters are the grid slope (S) and roughness coefficient (k). Grid slope can be easily calculated through the DEM, while the roughness coefficient can be derived through land use maps. Next, the off-channel velocity is calculated through the following equation:

$$V = kS^{0.5} \tag{3.8}$$

where k is a parameter related to land use and the roughness coefficient for shallow flow, while S is the grid slope. The values of parameter k can be found in various textbooks, such as in the Part 630 Hydrology National Engineering Handbook (NRSC USDA 2009).

In-channel velocity is estimated through open-channel equations, i.e., the Manning equation. The cross-sectional data can be derived through the DEM, with water depth assumed to be equal to the bankful conditions. In contrast to the off-channel velocity, the in-channel velocity is calculated in the stream order level. Specifically, it is assumed that cells

of the same stream order have equal velocities. The higher the stream order, the higher the cell's velocity since the higher order streams feature more width for equal slope.

The off-channel and in-channel velocity rasters are finally merged into a unified raster, representing the velocity raster of the entire basin. The Flow Length tool is then used to calculate the travel time of each cell. The tool is designed to calculate the downstream distance (L) along the flow path for each grid. Since the desired output is time rather than length, the inverted velocity raster (1/V) is used as a weight raster. This results in a weighted "distance" raster (L×1/V) representing travel time. Therefore, instead of featuring the total distance of each grid to the basin outlet, the flow length raster calculates the grid's travel time to the outlet. This product is the actual time-area diagram for zero-time intervals. When a pre-specified time interval is set, e.g., 10-min or 30-min, adding the number of cells that fall within a time interval and multiplying by the cell's area, the time-area diagram is constructed. The time interval chosen is related to the basin size and should be equal to or finer than the rainfall input. Since the Rainscanner datasets are designed to be simulated at the 10-min interval, this value is also chosen for the time-area resolution.

3.4.4   Loss Method

Apart from the time-area diagram, the effective rainfall must also be calculated. As previously mentioned, the method used is the NRCS-CN method (US Department of Agriculture 1986). The NRCS-CN method is an easy-to-apply and widely used method for estimating precipitation losses, especially in ungauged basins. The equation used for calculating the excess rainfall is the following:

$$P_e = \frac{(P - I_a)^2}{P - I_a + S} \tag{3.9}$$

where, Pe [mm] is the accumulated precipitation excess, P [mm] is the accumulated rainfall depth, Ia [mm] is the initial abstraction, and S [mm] is the potential maximum retention defined by equation 4.8 (in SI units):

$$S = 254 \left(\frac{100}{CN} - 1 \right) \tag{3.10}$$

Two parameters need to be estimated: the CN value and the initial abstraction depth Ia. The first can be estimated through the geomorphological characteristics of the basin, namely the land cover, e.g., the CORINE land Cover, and the Hydrological Soil Group (HSG) classification. The initial abstraction depth is usually set as a fraction of the maximum potential retention *S*, calculated through eq. 3-10. The NRCS suggested value is 20% of the maximum potential, i.e., 0.2S. However, the 0.1 value is used instead, based on the research in a nearby basin (Baltas et al. 2007).

Finally, the CN values are related to the rainfall conditions of the previous days. The CN number is derived first for Antecedent Soil Moisture (AMC) medium conditions (AMC-II). In the case of antecedent dry or saturated conditions, i.e., AMC-I and AMC-III, the generated runoff is expected to change significantly. For example, in dry conditions, rainfall losses are high, making the CN take a lower value, and therefore runoff is decreased, while in saturated conditions, the opposite occurs. To account for this aspect, the NRCS suggests the use of modified CN numbers based on the antecedent conditions, as defined by the following two equations:

$$CN_I = \frac{0.42CN_{II}}{1 - 0.0058CNII} \qquad (3.11)$$

$$CN_{III} = \frac{2.3 \cdot CN_{II}}{1 + 0.013 \cdot CN_{II}} \qquad (3.12)$$

The AMC conditions can be determined by calculating the 5-day antecedent accumulated rainfall. Specifically, the AMC class is determined by the values featured in Table 3-1.

Table 3-1: AMC classification based on 5-day accumulated rainfall

AMC Class	Total 5-day antecedent accumulate rainfall (mm)	
	Dormant season	Growing Season
I	< 13	< 36
II	13 - 28	36 - 53
III	> 28	> 53

More recently, the NRCS has abandoned this hypothesis by favoring the opinion that the CN value does not change based on the "Antecedent Soil Moisture conditions" but instead on the "Antecedent Runoff Conditions" (ARC). This change highlights that not only soil moisture conditions are dictating the amount of runoff, but other factors as well. Nevertheless, the mechanism remains the same, which dictates that previous rainfall events significantly affect the CN value and the generated runoff. The antecedent precipitation index (API) is also used, as formulated by Kohler and Linsley (1951):

$$API_i = P_i + (API_{i-1} + K_i) \qquad (3.13)$$

where API_i and P_i are the API value and precipitation for day i, and K is an empirical decay factor less than one with values usually between 0.85 and 0.98. Cordery (1970) recommended an average value of 0.92, with a value of 0.98 for winter and 0.86 for summer, while Hill et al. (2014) recommended a value of 0.95 annually.

In order to overcome the problem of selecting three specific CN numbers, a linear relationship is applied between each state based on a given percentage of soil moisture conditions (Bournas and Baltas 2022c). Specifically, an assumption is made to relate the

presumable soil moisture percentage conditions to the CN value. The aim is to dictate the CN value based on a given soil moisture percentage, which can be derived from a soil moisture model or satellite data. To incorporate the soil moisture conditions impact into the CN value, it is assumed that AMC-II conditions refer to 50% soil moisture, while AMC-I and AMC-III correspond to 0% and 100% soil moisture. A linear relationship is then used between the different soil moisture states to define the adjusted CN value.

An example is shown in Figure 3-12 to understand this adjustment better**.** In the example, a CN_{II} value of 50 for 50% soil moisture leads to an adjusted value CNm of 50, while for 0% and 100%, the value is calculated at 30 and 70 based on equations 4.7 and 4.8, accordingly. This interpolation makes evaluating other values, e.g., 70% soil moisture, possible. Therefore, the value will be linearly interpolated between 50% and 100%. Figure 3-12 shows that the change between the different soil moisture conditions is at its maximum when the CN value is 50 and lower when it is 100 or 0. This change is logical since high numbers of CN represent near impervious areas, thus generating high runoff. The runoff potential in these areas does not change with soil moisture since the runoff potential is already high.
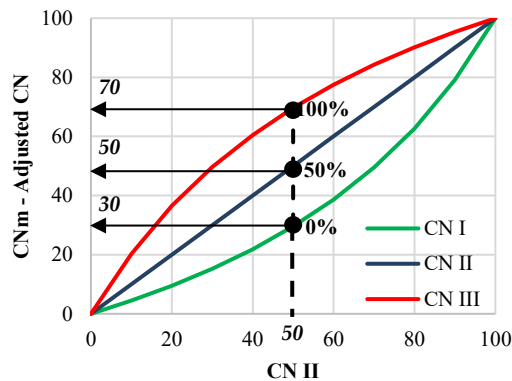

Figure 3-12. CN adjustment based on soil moisture conditions (%)

3.5   Gridded Flash Flood Guidance

Flash Flood Guidance (FFG) is the accumulated rainfall depth of a given period, which will cause minor flooding over a specified area (Georgakakos 2006). The FFG value is a rainfall depth threshold above which a flood is expected. The FFG system relies on deriving the value of this threshold and comparing it with forecasted values. Figure 3-13 illustrates a simplified version of the FFG EWS flowchart.

The FFG value depends on two main parameters: the threshold runoff and the soil moisture conditions. The first is static and depends on the study area's spatial characteristics, specifically the cross-section where the FFG value is estimated. The threshold runoff is the necessary amount that can be safely routed downstream, while any excess will lead to minor flooding. The second parameter, i.e., the soil moisture conditions, is dynamic and is used to

calculate rainfall losses. The estimation of FFG relies on inverted rainfall-runoff computations, where the runoff and the rainfall losses are the known variables, and the total rainfall is the unknown. When the amount of runoff is equal to the threshold runoff, the inverted rainfall-runoff calculations estimate the FFG value.
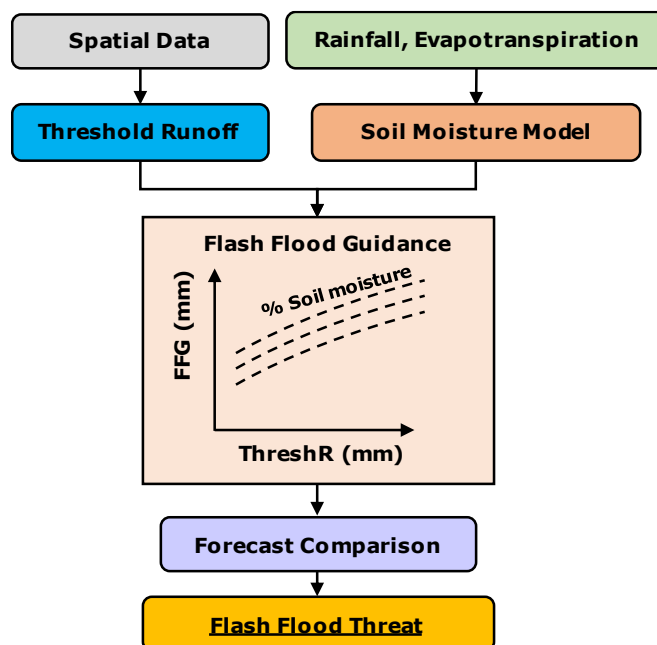

Figure 3-13: Simplified FFG System Flow Chart

This dissertation examines a gridded implementation of the FFG system, the Gridded Flash Flood Guidance (GFFG), first introduced by Schmidt et al. (2007). The difference lies in the spatial resolution of the calculations. In the original FFG, all calculations are performed first on a subbasin level, and the results are then interpolated in grids that match the spatial resolution of the incoming rainfall forecasts, e.g., weather radar forecasts. In the GFFG implementations, all calculations, including the rainfall-runoff computations, are performed at the grid level, which has the advantage of setting the desired result scale without the need for interpolation. Moreover, it is easier to understand, employ and maintain. The flow chart of the GFFG method is shown in Figure 3-14. The flow chart includes all the needed steps to reach GFFG values.

The GFFG process is divided into two subprocesses; the pre-process and the real-time monitoring. In the pre-process, the model's parameters are devised and calibrated, while in real-time monitoring, the system uses current data to provide the FFG values. The pre-process includes the study area delineation, the threshold runoff calculation, the hydrological model, and the runoff threshold to rainfall threshold, i.e., the FFG value calculations. The real-time monitoring uses the pre-process models to extract the FFG value for the current soil moisture percentage derived from the hydrological model and compare

this value with the forecasting products of equal spatial and temporal scales to provide warning issuing estimations. Although the current implementation is deterministic, the decision to issue a warning or not should be taken after various FFG products, i.e., different rainfall accumulated periods, are examined in conjunction with the study area characteristics or other knowledge.
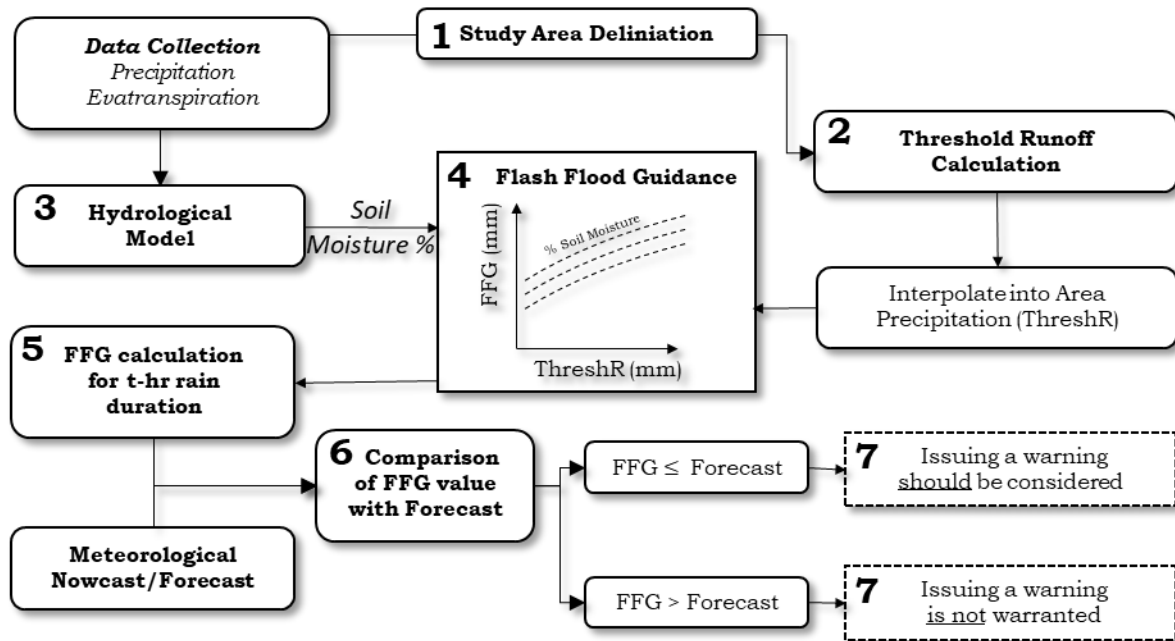

Figure 3-14. Flash Flood Guidance Components

3.5.1 Threshold Runoff Component

The threshold runoff component is a pre-process of the system, which involves the geomorphological analysis of the study area and its delineation into smaller units (Bournas and Baltas 2022c). First, the delineation of the area is performed by setting the grid dimensions and coordinate system. In the original FFG implementation, the area is delineated into subbasins varying in size from 200 – 2000 km². However, the delineation size, apart from the forecasted rainfall grid which will be used, is also related to the topography of the study area. The original FFG implementation was applied in the USA, where the subbasin sizes are large, while in Greece, the majority of basins are small to medium sizes, i.e., 20 to 500 km², making the desired analysis of finer detail. In the GFFG implementation, a grid size matching the forecasting analysis is desired. Typical operational meteorological and atmospheric forecasting models feature from four to eight km² resolution, while some research efforts to increase the spatial resolution to two km² (Bournas and Baltas 2022c). Finer spatial resolution can be achieved using downscale processes (Spyrou et al. 2020) or by nowcasting products such as weather radar or satellite measurements. Grid sizes used in previous FFG research vary from 1 km² to 4 km², matching

the grid size of the forecasting field (Seo et al. 2013; Zeng et al. 2016; Wasko et al. 2021). In this study, a 1 km² grid size is set considering all of the above limitations, e.g., the subbasins size and available rainfall forecasting products in Greece (Papadopoulos et al. 2002; Lagouvardos et al. 2003; Mariani et al. 2015; Varlas et al. 2020, 2021).

The threshold runoff is then estimated for each grid. The threshold runoff is equal to the bankfull conditions runoff, as illustrated in Figure 3-15. Any excess runoff will cover the floodplain area, resulting in minor flooding.
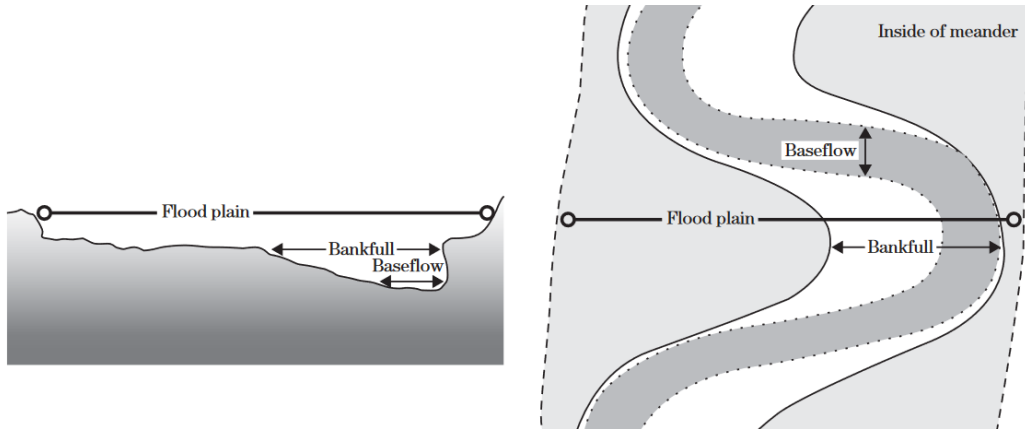
Figure 3-15. Bankfull conditions illustration: Source (NRSC USDA 2009)

The threshold runoff can be estimated using two methods; a) derivation and use of regional relationships concerning the bankfull cross-section properties and b) historical flow analysis. In the first case, the bankfull runoff is calculated using the cross-section data, and a regional relationship that relates the cross-section data to the basin data is set. In the second case, the bankfull runoff is considered equal to the 2-year Average Recurrence Interval (ARI), i.e., the 50% Annual Exceedance Probability (AEP) of the section's actual runoff. However, historical flow records are needed to extract the 2-year runoff ARI, or regional relationships should be established (Carpenter et al. 1999; Reed et al. 2002). In the current implementation, the desired 2-year runoff can be calculated indirectly using a rainfall ARI instead, in conduction with a rainfall-runoff model, to overcome this issue. Rainfall ARIs are much easier to obtain from IDF curves based on historical rainfall data. The 2-year discharge ARI is highly related to the 5-year ARI of rainfall (Schmidt et al. 2007; Erlingis et al. 2013; Bournas and Baltas 2022c). However, this is an approximation, and the actual ARI depends on several factors, such as the definition of flooding and the flood vulnerability of the study area. The rainfall-runoff model used is the same one used for the FFG calculations. It is based on the SCS triangular UH and the SCS CN method.

The calculations are performed for each grid and pre-determined accumulation periods of 1-, 3-, and 6 hours. The rainfall-runoff model is based on the SCS triangular model following

these steps: First, the lag time of each cell is calculated using the Mochus lag time equation (Mockus 1961):

$$t_L = \frac{l^{0.8}(S+1)^{0.7}}{1900y^{0.5}}$$

(3.14)

Where t_L [h] is the lag time, l [ft] is the cell's flow length, S [in] is the maximum potential retention of the CN method, and y [%] is the cell's slope. This equation is favorable since it utilizes two aspects easily calculated through GIS, the slope of the cell and the retention S, which is calculated based on the CN value according to eq. (3.10) after unit conversion. Following this, the time of concentration and time to peak is calculated as follows:

$$t_L = 0.6t_c => t_c = t_l/0.6$$

(3.15)

$$T_R = \frac{D}{2} + t_p$$

(3.16)

Where tc [h] is the time of concentration, T_R [h] is the time to peak, and D [h] is the rainfall duration. Finally, the peak discharge is calculated through the NRCS triangular UH method as follows

$$Q = 2.08Ah/T_R$$

(3.17)

Where Q [m³/s] is the peak runoff, A [km²] is the cell's area, and h [mm] is the effective rainfall.

Given that FFG calculations are performed for predetermined rainfall durations, three runoff thresholds are derived for 1-, 3- and 6-hour duration by changing the value D in eq. 3.16. In each case, the value of abstraction value S, in eq. 3.14 is also changed to account for the variability within an event (Schmidt et al. 2007). Specifically, 10mm of rainfall in one hour will produce more runoff than 10mm in six hours. Therefore, the CN value is modified for each accumulation period to address this issue. Specifically, for the 1-hour duration, the average CN value between ARC-II and ARC-III is used, while for the 6-hour duration, the average CN value between ARC-I and ARC-II. The 3-hour duration uses the ARC-II conditions.

3.5.2 Hydrological Model

The second component involves a hydrological model to estimate the soil moisture conditions for each time interval. The model runs continuously since soil moisture conditions do not change as fast in time as rainfall input (Bournas and Baltas 2022c). The temporal resolution depends on the data availability, with a desired sub-6-hour temporal resolution. The soil moisture conditions dictate the amount of rainfall retained, thus the potential of generating either high or low runoff. In the FFG calculations, since inverse rainfall runoff is performed, the amount of soil moisture dictates the amount of rainfall

needed to cause flooding. A high soil moisture percentage means high runoff potential; therefore, less rainfall is required.

The hydrological model is designed to use precipitation and evapotranspiration as inputs, conduct any necessary precipitation division to rainfall and snowfall, and provide a soil moisture percentage. The soil moisture percentage can either be a direct product of the model or a value derived by the value of its state variables, as in the case of the original FFG implementation where the Sacramento Soil Moisture Accounting Model (SAC-SMA) (Burnash et al. 1973; Burnash 1995) is used.

Without such a model, the soil moisture percentage can also be estimated based on the 5-day antecedent precipitation index, API. The index is then used to estimate each cell's soil moisture percentage. This percentage is finally used to determine the adjusted CN value used in the FFG implementations, as explained in Chapter 3.4.4.

3.5.3 FFG Computations

The third and final component is the FFG computations. As stated earlier, the computations are based on inverse rainfall-runoff modeling, where the desired runoff and rainfall losses are known, and the accumulated rainfall is sought. The CN equation is shown in eq. (3.9), can be used to calculate the runoff. By assuming initial losses *Ia* equal to 10% and solving eq. (3.9) for P, the following equation results

$$P = FFG_x = \frac{0.1 S_{sm} + Q_x \pm \sqrt{2 Q_x S_{sm} + Q_x^2}}{2} \qquad (3.18)$$

where *P* [mm] is precipitation, *FFGx* [mm] is the Flash Flood Guidance for duration *x*, *Q* [m³/s] is the threshold runoff for duration *x*, and *Ssm* [mm] is the initial storage calculated from eq. (3.10), after the CN adjustment is performed based on the current soil moisture conditions. The Equation (3.18) highlights that the FFG value is a nonlinear relationship between the threshold runoff and the soil moisture conditions.

Figure 4-17 illustrates an example where the FFG value of a single cell is calculated for three different soil moisture conditions. For each soil moisture condition, by using increasing runoff threshold values and applying the equation (3.18), the colored lines are drawn. Each line is a guide to performing fast calculations in real-time monitoring. For instance, when a cell's threshold runoff is calculated as 20 m³/s, the FFG value changes dramatically for each soil moisture condition. For saturated conditions, i.e., 90% soil moisture, the FFG value is 18 mm in three hours, while for less saturated at 80% is 20 mm, and for normal conditions, the value is 26 mm rainfall in three hours. These results show that the higher the soil moisture percentage, the lower the FFG value, which is logical since highly saturated conditions result in high runoff potential, requiring less rainfall to reach the desired runoff amount.
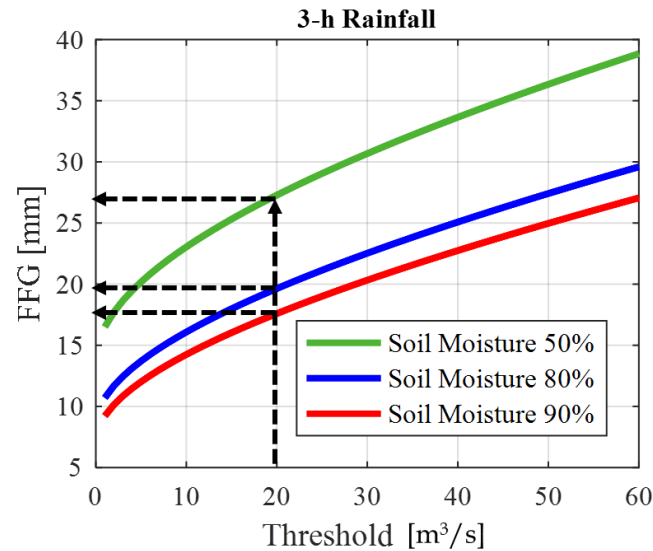
Figure 3-16. Relationship between FFG and Threshold rainfall values for different soil moisture conditions

After calculating the FFG values for each of the three durations, a comparison is made with the respective forecasted values. If the forecasted rainfall exceeds the FFG value, flooding is expected over the specified cell, and a warning should be issued. Moreover, the threat level can be approximated by calculating the difference between the forecasted and the FFG value. Given the deterministic nature of the system result, any cell that features a forecasted rainfall above the FFG value, either that being some millimeters or by a large margin, will be flagged for flooding, while other cells can be flagged as non-flood cells, even when the value of the forecast is just below the threshold. To overcome this uncertainty problem, all accumulated periods should be examined before decision-making. Low accumulation periods, e.g., 1-hour, are used for comparing with 1-hour forecasts, which tend to have the least uncertainty involved, compared to the 3- and 6-hour forecasts, but provide the lesser lead times. It should be noted that the system relies on accumulated rainfall thresholds; thus, the exact time when the flood will occur cannot be determined when the longer accumulation periods are used.

Finally, a secondary decision-making strategy can also be applied before issuing a warning regarding the total area flagged for flooding. In the GFFG implementation, cell sizes are relatively small, making warnings for single-cell flooding not ideal. Therefore, a strategy may be applied to decide on different flood-preventing measures based on the number of cells flagged for flooding or each cell's potential flood hazard level. For instance, cells that contain critical infrastructure should be carefully monitored.

3.6 Strom Tracking and Trajectory

In storm tracking, two main processes are involved: a) the identification of cells on a radar image and b) the cell tracking, i.e., the matching of cells in consecutive images. This study follows the flow chart shown in Figure 3-17.
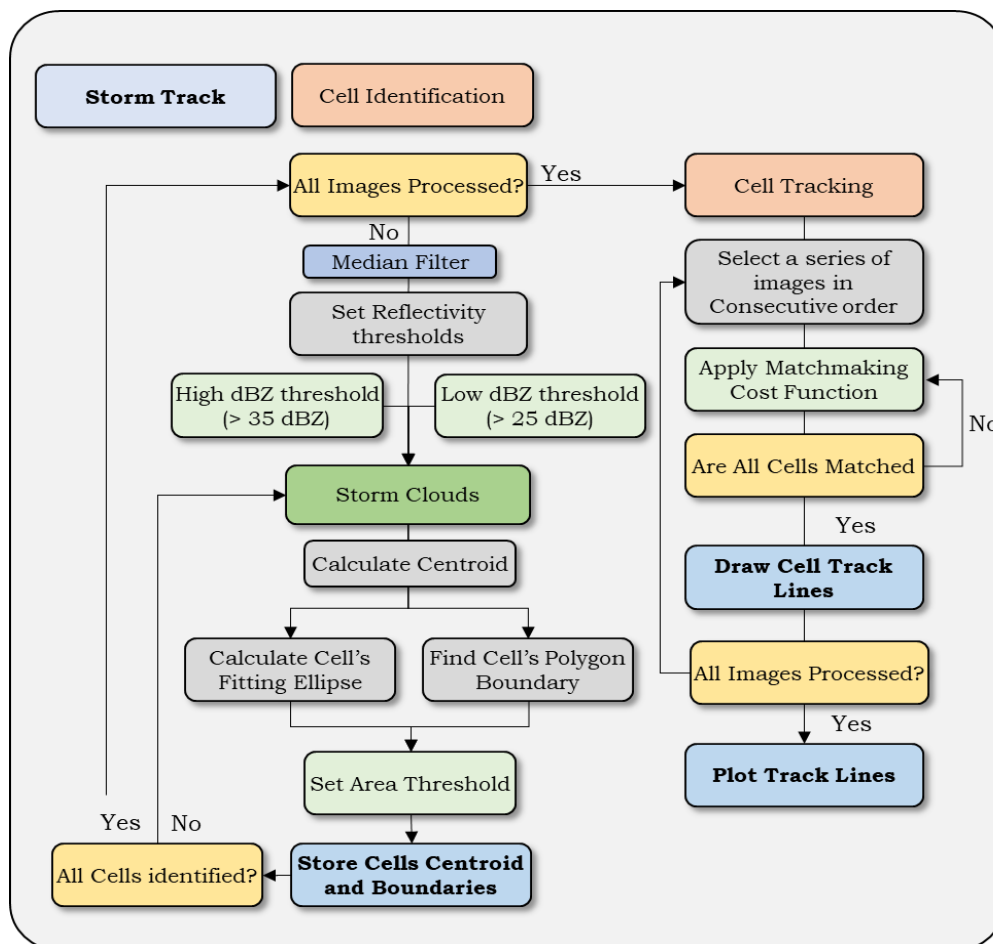
Figure 3-17: Storm Tracking algorithm flow chart

3.6.1 Cell Identification

For each radar image, the cell identification process is first performed. First, the weather image is passed through a 2-D median filter to remove noise. This filter replaces each grid value with the median value of the 3 x 3 neighboring grids. This process assists in "blurring" the image, and therefore, cloud cells that are found to be in near proximity but are not connected due to gaps of a few pixels end up being connected and forming a single cloud entity. Then, the cell identification is performed by applying reflectivity thresholds. A storm cell features the highest rainfall intensity and, thus, the highest reflectivity values in a radar image. A high threshold, i.e., 35 dBZ units, will extract the storm cores, while a lower threshold, i.e., 25 dBZ, will extract the coverage of the storm. Overall, convective events feature high storm cores with small storm coverage, while stratiform events feature

significant coverage but smaller reflectivity cores. In nowcasting systems, the tracking of high rainfall intensity storms is usually the aim; thus, a threshold of over 30 dBZ is preferred, especially if a series of images are used to disaggregate the generated image. However, a multi-threshold approach is better; where multiple thresholds are applied, a tree structure is formed where low storm coverage is first identified and then sub-cells of high reflectivity later. Considering the lower threshold, values of reflectivity below 20 dBZ are usually considered as no part of rainfall storms unless snowfall occurs. In this study, three thresholds are used: one to identify the storm coverage, set for values above 25 dBZ; one to distinguish storm cores, with a dBZ value over 30 dBZ, and finally, one for identifying the most dangerous storms, with a threshold set to 40 dBZ value. An example is shown in Figure 3-18, where by applying a single threshold, the cells with values above the threshold remain, forming the boundaries of the cell cloud. In the featured figure, the values of five storms are identified.

Figure 3-18: Storm Data and cell identification;
Source: (Dixon and Wiener 1993)

Following the identification process, a series of attributes are stored for further use, such as the cell's centroids coordinates, the area of the storm, and the maximum reflectivity value. Moreover, for further cross-correlation calculations, a fitting eclipse is drawn for each polygon, which is an easier-to-handle mathematical shape. The ellipse is drawn with the aim of including all the polygon nodes within its boundaries. The ellipse centroid, eccentricity, and the minor and major axes vectors are stored for further analysis. The process is applied until all storm clouds are processed.

3.6.2 Cell Tracking

Following the identification, the cell tracking algorithm is applied. The method used is based on motion vector and cross-correlation. Specifically, the matching between two consecutive radar images is performed by applying an optimization process between the different cells identified in each image. A cost function is used to find the best fit, which incorporates cell characteristics, such as area and the fitting ellipse properties. All possible entity combinations between two images, Figure 3-19, are assigned to the assessment matrix, which is then solved through a match pair algorithm (Duff and Koster 2001). The linear assignment problem is a way of assigning rows, i.e., storm cells in time *ti*, to columns, storms cells in time *ti+1*, in such a way that the total cost of the assignments is minimized. The algorithm also uses a way to deal with instances that are not matched by adding a further unmatched cost.
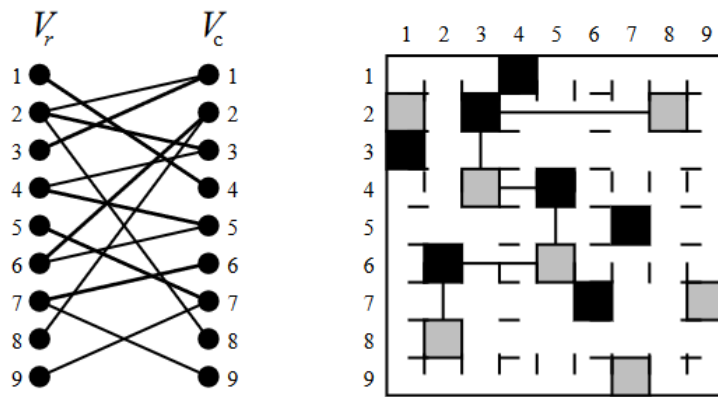
Figure 3-19: Possible cell combinations when using a matchmaking algorithm, where Vr denotes the past cells centroids and Vr the centroids in ti+1.

The Total Cost (TC) of a solution M is the sum of all the costs of all matched pairs added to the cost of all unmatched pairs as follows:

$$TC = \sum_{i=1}^{p} Cost(M(i,1), M(i,2) + costUnmatched * (m + n - 2p) \qquad (3.19)$$

Where TC is the total cost, Cost is an m-by-n matrix, M is a p-by-2 matrix, where M(i,1) and (Mi,2) are the row and column of a matched pair and (m+n-2p) is the total number of unmatched rows and columns.

The cost function can have many forms. The most basic is the Euclidean distance, meaning that the cells are matched based on which one is closer to the cells in the next image. Other cost functions may include other characteristics, such as the area and eccentricity of the cell. The tracking problem has been enhanced to include other elements of tracking, mainly the splitting and merging of cells. A merge is when two cells are merged into a single entity, meaning that only one track should be formed afterward, while a split means that a single

entity will generate two tracks in future predictions. The basic concept is shown in Figure 3-20. In the current implementation, the cost function is applied once, and the best fitting matchmakings are performed. If cells of the previous time image remain unmatched, the matchmaking procedure is re-applied, but with the removal of the cells of the previous image that were matched. This leaves space for unmatched cells to be matched with the new cells and thus results in a merge situation. The splitting situation is performed accordingly but with the removal of the current unmatched cells, this time compared to the previous image cells. The distance threshold in each case dictates whether the cell cloud will be merged or diminished and whether a cell belongs to a splitting cell or is a newly formed cell.
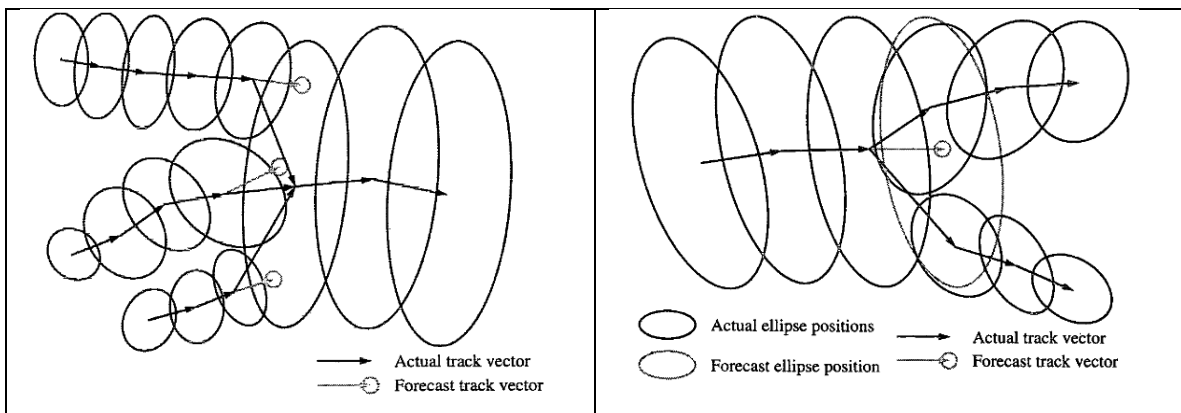
Figure 3-20: Merge (left) and splitting (right) situations
Source: (Dixon and Wiener 1993)

4. Results and Discussion

4.1   Z-R Analysis

The Z-R analysis consists of two sub-processes. First, the correlation analysis is performed, which gives insight into the quality between the Rainscanner and the rain gauge datasets. Following this, the optimization process is performed to derive multiple Z-R relationships using different optimization data groups. Table 4-1 shows the events where both Rainscanner and rain gauge data were available and used for this process. More information about the events can be found in the Appendix A table, where all the Rainscanner events are showcased. The events in Table 4-1 featured the most substantial rainfall among the events where rain gauge datasets were available (up to 2020).

Table 4-1: List of Events used for the Z-R Calibration process

Event	Date	Event	Date
E1	30-09-2018	E20	21-11-2019
E5	16-12-2018	E21	25-11-2019
E6	18-12-2018	E22	30-12-2019
E9	10-01-2019	E31	01-06-2020
E10	07-02-2019	E33	08-08-2020
E12	15-02-2019	E36	04-12-2020
E16	15-04-2019		

4.1.1   Correlation Coefficient Analysis

The correlation analysis is based on the calculation of Pearson's r correlation coefficient index. The calculations are performed at the Station level, meaning a correlation index is calculated for each station per event. The results are showcased in Table 4-2, in descending order of the mean correlation. The color coding stretches a red-to-green color bar of correlation values from -1 to 1. A correlation value of 1 shows a perfect correlation, whereas a -1 shows a negative correlation, i.e., an increase in one timeseries is shown as a decrease in the other. Finally, zero correlation is illustrated with gray, meaning the data are not correlated. Usually, this occurs when data is missing, e.g., the station is located within the Rainscanner clutter area. A correlation threshold is used to distinguish well- and poor-correlated stations to visualize the results better. By applying a 0.6 and a 0.7 threshold, the

number of events in each station features a good correlation, is shown in Figure 4-1, whereas in Figure 4-2, the mean correlation of the stations is illustrated before and after the threshold is used. In the figures, each station is made with its respective ID.

Table 4-2: Stations correlation coefficient per event

| ID	Station	E1	E5	E6	E9	E10	E12	E16	E20	E21	E22	E31	E33	E36
16	Neos Kosmos	0.38	0.82	0.78	0.48	0.86	0.78	0.80	0.63	0.91	0.83	0.01	0.88	1.00
21	Psychico	0.30	0.59	0.84	0.54	0.74	0.83	0.85	0.72	0.72	0.88	0.94	0.90	0.89
31	Agiaparaskevi	0.27	0.64	0.79	0.76	0.81	0.86	-0.39	0.42	0.69	0.80	1.00	0.45	0.92
42	Imittos-dafni	0.23	0.74	0.66	0.22	0.84	0.78	0.87	0.84	0.97	0.78	0.00	0.75	-1.00
35	Vrilissia	0.24	0.81	0.84	0.77	0.69	0.87	-0.35	0.62	0.44	0.81	0.98	-0.17	0.85
39	Nikaia	0.37	0.75	0.62	0.74	0.80	0.79	0.78	0.64	0.15	0.90	0.45	0.86	0.00
52	Delacroix-attiki	0.25	0.67	0.81	0.69	0.93	0.87	0.00	0.29	0.57	0.71	0.98	0.29	0.77
30	Korydallos	0.38	0.97	0.58	0.95	0.84	0.88	0.63	0.86	0.44	0.83	0.45	0.94	-0.31
19	Peristeri	0.50	0.80	0.65	0.81	0.62	0.77	0.64	0.38	0.85	0.80	0.57	0.56	0.00
43	Harokopio-athens	0.40	0.68	0.74	-0.30	0.68	0.66	0.53	0.60	0.79	0.90	0.36	0.93	0.00
51	Anokorydallos	-0.05	0.84	0.66	0.98	0.43	0.91	0.92	0.92	0.43	0.43	0.15	0.87	0.00
46	Pallini-cgs	0.12	0.39	0.31	0.95	0.63	0.66	0.00	0.11	0.58	0.78	0.88	-0.50	0.69
9	Ippokrateios	0.10	0.75	0.44	0.64	0.50	0.03	-1.00	0.86	0.54	0.68	0.95	0.00	-0.50
15	Nea Smyrni	0.31	0.61	0.48	0.25	0.81	0.32	0.63	0.20	0.76	0.85	0.00	0.66	0.00
41	Ska	0.42	0.75	0.83	0.67	0.56	0.00	0.78	0.05	0.36	0.87	0.62	0.84	-0.86
26	Arsakeio-drosia	0.10	0.85	0.50	0.89	0.65	0.63	0.63	0.49	0.39	0.51	0.09	0.65	0.79
8	Faliro	0.31	0.77	0.66	-0.10	0.67	0.63	0.62	0.91	0.32	0.84	0.00	-0.46	0.00
6	Dionysos	0.01	0.51	0.44	0.85	0.00	-0.40	0.32	0.01	0.64	0.35	0.66	0.75	0.75
4	Anoliosia	-0.13	0.75	0.73	0.60	-0.36	0.72	0.73	0.77	0.60	0.24	0.79	0.77	0.00
13	Maroussi	0.22	0.45	0.64	0.45	0.27	0.71	-0.08	0.46	0.21	0.77	0.97	0.96	0.72
17	Patissia	0.43	-0.26	0.65	0.82	0.79	0.71	0.92	0.06	0.00	0.77	0.00	0.91	-1.00
27	Athensmarina	0.40	0.79	0.60	0.74	0.76	0.78	0.40	0.36	0.47	0.88	0.00	0.50	0.00
45	Pireas-pedagogiki	0.36	0.51	0.74	0.35	0.77	0.56	0.35	0.68	0.48	0.84	-0.11	0.80	0.00
28	Tatoi	-0.07	0.58	0.60	0.18	0.36	0.60	0.25	-0.06	0.12	0.81	-0.87	0.76	0.63
5	Athens	0.43	0.68	0.76	0.24	0.55	0.60	-0.13	0.61	0.92	0.88	0.23	0.13	0.00
29	Aspropirgos	0.17	-0.03	0.66	0.53	-0.17	0.64	0.98	0.35	0.43	0.35	0.51	0.45	0.87
48	Pireas	0.16	0.72	0.91	-0.35	0.65	0.66	0.64	0.20	0.13	0.51	0.00	0.00	0.00
32	Alimos	0.28	0.88	0.64	-0.36	0.68	0.50	0.55	0.58	0.45	0.79	0.00	0.00	0.00
2	Ampelokipoi	0.33	0.48	0.38	0.15	0.28	0.64	0.67	0.49	0.25	0.09	0.00	0.34	0.68
50	Malakasa	-0.04	0.06	0.18	0.56	0.75	0.46	1.00	-0.34	0.11	0.51	0.00	0.00	0.71
38	Elefsina	0.04	0.30	0.39	0.77	0.20	-0.09	0.94	0.37	0.28	-0.01	0.41	0.46	0.00
33	Perama	0.38	0.24	0.43	0.01	0.55	-0.15	0.89	0.20	0.46	0.30	0.49	0.71	0.00
47	Chaidari	0.19	0.19	0.43	0.56	0.09	0.63	0.88	0.00	0.18	0.00	0.00	0.48	0.00
34	Petroupoli	0.33	0.00	0.62	0.00	0.00	0.00	0.58	-0.16	0.13	0.21	-0.20	0.67	0.00
14	Neamakri	0.45	0.79	0.00	0.08	0.38	0.01	0.00	-0.39	0.42	0.63	0.00	-0.30	0.59
23	Vari	0.00	0.00	0.00	0.00	0.00	0.00	0.47	-0.21	-0.31	0.00	0.44	1.00	-0.33
37	Kifissia	-0.09	-0.06	-0.19	-0.19	-0.13	0.15	0.00	0.00	0.00	0.22	0.61	0.00	0.07
40	Salamina	0.39	0.48	0.36	-0.13	0.43	0.00	-1.00	-0.19	0.42	0.00	-0.68	1.00	0.00
3	Anavyssos	0.00	0.00	0.00	0.00	0.00	0.00	0.00	0.00	0.00	0.00	0.00	0.00	0.00
7	Ekali	-0.15	-0.34	-0.25	0.45	-0.23	0.00	0.00	0.00	0.00	0.00	0.00	0.00	0.00
10	Kantza	0.00	0.00	0.00	0.00	0.00	0.00	0.00	0.00	0.00	0.00	0.00	0.00	0.00
11	Lavrio	0.00	0.00	0.00	0.00	0.00	0.00	0.00	0.00	0.00	0.00	0.00	0.00	0.00
12	Markopoulo	-0.23	-0.36	-0.21	-0.50	-0.01	0.06	0.00	0.00	0.00	0.00	0.00	-0.46	0.00
18	Penteli	-0.11	-0.40	-0.53	-0.55	-0.37	0.13	0.00	0.00	0.00	0.00	0.00	0.00	0.00
20	Portorafti	0.00	0.00	0.00	0.00	0.00	0.00	0.00	0.00	0.00	0.00	0.00	0.00	0.00
22	Spata	0.00	0.00	0.00	0.00	0.00	0.00	0.00	0.00	0.00	0.00	0.00	0.00	0.00
24	Vilia	0.14	0.00	0.36	0.20	0.00	0.00	0.00	0.08	0.10	0.00	0.48	0.00	0.00
25	Rafina	0.00	0.00	0.00	0.00	0.00	0.00	0.00	0.00	0.00	0.00	0.00	0.00	0.00
36	Pallini	0.00	0.00	0.00	0.00	0.00	0.00	0.00	0.00	0.00	0.00	0.00	0.00	0.00
44	Papagou	0.00	0.00	0.00	0.00	0.00	0.00	0.00	0.00	0.00	0.00	0.00	0.00	0.00
49	Keratea	0.10	0.00	-0.32	-0.41	0.00	0.00	0.00	0.00	0.00	0.00	0.00	0.00	0.00
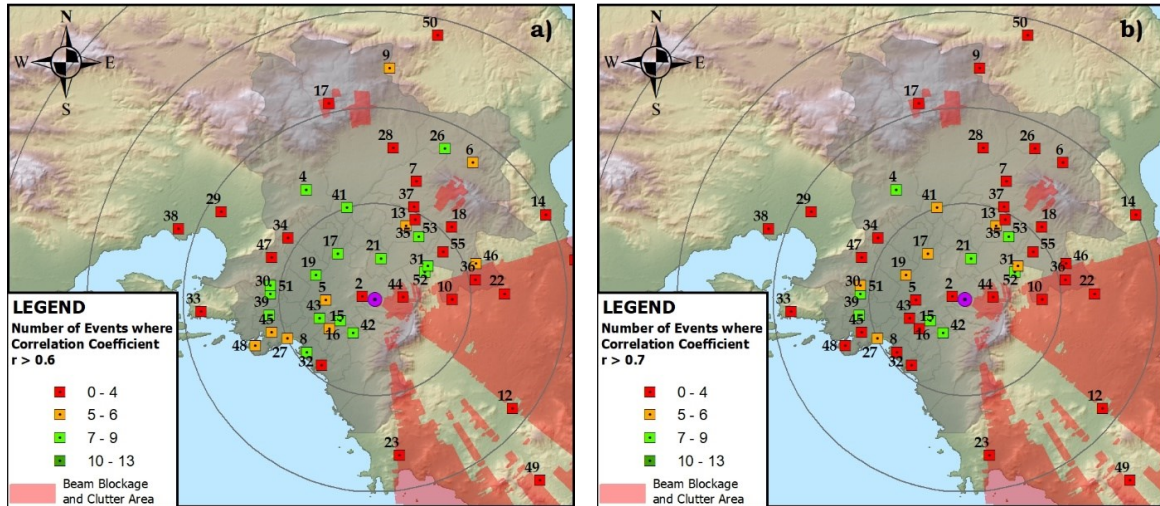
Figure 4-1. The number of events with a correlation coefficient between Rainscanner and rain gauge datasets is higher than a) 0.6 and b) 0.7. Source: (Bournas and Baltas 2022a)
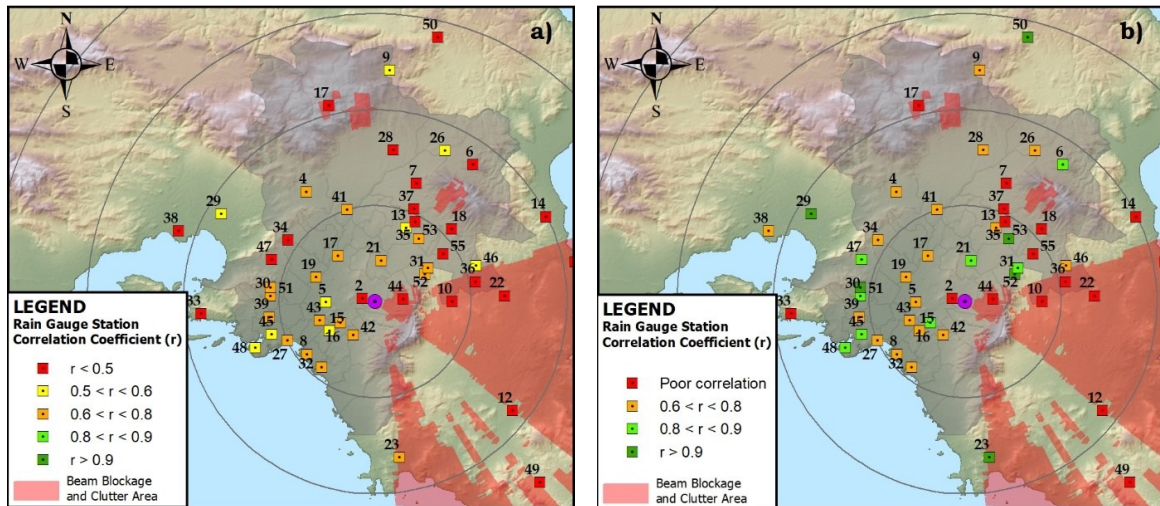

Figure 4-2. The mean correlation coefficient between the Rainscanner and rain gauge stations for a) all available events and b) using events that featured an above 0.6 correlation at each station. Source: (Bournas and Baltas 2022a)

Figure 4-1 highlights the consistency between the Rainscanner and rain-gauge datasets. The number of events with good correlation shows that the two datasets (the Rainscanners and the rain gauges) are consistent at the location of a specific station. The more events with high correlation a station features, the more reliable the station is. Moreover, the figure features the difference between utilizing a different correlation threshold, where in panel a, the threshold is set to 0.6, and in panel b, it is set to 0.7. By comparing the two panels, it is observed that there is a decrease in the number of events that featured good correlation in various stations. For example, station 41, Ska, features seven events with a correlation over 0.6, while only five when the threshold is 0.7. A higher threshold leads to fewer data being

"well-correlated," which is logical since the higher the correlation threshold, the fewer stations will meet this demand among the different events. However, as mentioned in Chapter 3.3.2, choosing a threshold that will remove bad-correlated datasets is critical but still features a significant amount of radar-rain gauge pairs to perform the needed Z-R calibrations. Moreover, the threshold highlights other facts, such as the behavior on the different thresholds set by the station's location.

Considering the location of the poor-correlated stations within the study area, the following findings emerge. Firstly, in both thresholds, it is noticeable that stations located near or within the cluttered area, e.g., stations northeast of the Rainscanner, feature an overall low correlation since only a small number of events, i.e., less than four feature above 0.6 correlation. Secondly, stations located within a 10 km radius of the Rainscanner location tend to feature many well-correlated events in both cases, apart from station 2, Ampelokipoi, which features a low correlation, although it is located near the Rainscanner. Finally, some stations feature a significant decrease in the number of well-correlated events when a different threshold is used, with most stations located in the coastal front. For example, station ID 8, Faliro station, featured seven well-correlated events when a 0.6 threshold is applied, reduced to only four with the 0.7 threshold. However, this behavior is not unique to the coastal areas since station ID 6, Dionysos station, on the northeast, also features a similar behavior. Considering all the above, and after testing several thresholds, the 0.6 threshold was considered the best choice since it filters out bad-correlation data while keeping enough data for the optimization algorithm.

The effect of utilizing only well-correlated datasets is reflected in Figure 4-2, where each station's mean correlation coefficient is compared to the mean correlation coefficient derived when utilizing only the events that featured above 0.6 correlation for each station. A total of 15 stations featured above 0.6 correlation in 7 out of the 13 events, shown in Figure 4-2 panel a, while when considering only events that featured good correlation, shown in panel b of Figure 4, a total of 32 stations featured correlation above 0.6, 29 stations above 0.7, and 15 above 0.8. These results are encouraging, especially for the stations featuring high correlation in multiple events, e.g., stations 21, 42, and 53, as they can be used as control points for future quality control procedures (Bournas and Baltas 2022a).

Finally, it is notable that some stations exhibit a high correlation for only a limited number of rainfall events. For instance, stations 28, 29, and 50, located in the north and southwest, respectively, featured a high correlation in only a few events, less than four, but the correlation in these events was relatively strong, i.e., above 0.8. This finding can be attributed to the fact that the correlation is not dependent only upon the station's location or the data quality, e.g., systematic errors, but also storm-based characteristics. One such characteristic is the amount of rainfall since low rainfall height (light rain) is subject to

factors causing temporal and spatial displacements of the Rainscanner compared to the rain gauge measurements. This behavior was attributed to two factors: first, to the Rainscanner height of measurement, which, depending on the station's distance to the Rainscanner, can be several hundred meters above the ground, and second, to the rain gauge measurement sensitivity.

The first is straightforward since the further a station is located, the more prominent the height problem is. When light rain occurs, the velocity of the hydrometeors is smaller, making them take longer to reach the ground, which leads to temporal displacements between the measurements of the Rainscanner and the rain gauge, i.e., the same hydrometeor is measured in different timesteps in the two instruments. Moreover, the hydrometeor's size and weight make them more subjectable to wind effects, which, in conjunction with the increasing distance to the ground due to the Rainscanner beam angle and earth curvature, may lead to significant spatial displacements, i.e., the hydrometeors fall in a different Rainscanner grid than the one that the station is designated. Spatial and temporal aggregations were performed, with the correlation increasing slightly, mainly when temporal aggregation was performed, but the exact cause is difficult to identify, while the study in coarser scales was not desired.

The second cause that may derail the correlation in low rainfall involves the rain gauge sensitivity. In most instances, and specifically in stations located near the Rainscanner, the Rainscanner featured a higher sensitivity than the respected rain gauge, highlighted by the fact that it measured rainfall when the rain gauge did not, which may be attributed to false Rainscanner readings, but rain gauges are also subject to errors. For instance, the gauge's sensitivity may lead to false readings such as temporal displacement of the rainfall volume, i.e., the amount of rainfall that occurred in a period is measured in the next period or even lost. Although rain gauges are considered the ground truth, the rain gauge device, recorded, or the post-process quality control of the entire rain gauge network can lead to errors. Unfortunately, these cases can only be examined when access to the rain gauge raw datasets and validation procedures are provided. Nevertheless, this study did not focus on this aspect since few stations featured these issues, such as station 2, Ampelokipoi, where the Rainscanner featured in almost all events relatively high reflectivity values, in contrast to the low rainfall height recorded by the rain gauge. The study of poor-correlation stations, whereas nearby stations feature good correlation, is an interesting study for the rain gauge operator to assist in inspecting and maintaining the network.

4.1.2   Event-based Z-R calibration

Following the correlation analysis, the event-based group is the first calibration group for establishing Z-R relationships. A Z-R relationship is determined based on the datasets of the stations that feature a correlation over the 0.6 threshold. Furthermore, as mentioned in

Chapter 3.3, the used data pairs are filtered to remove zero-value pairs. The results are shown in Table 4-3. Two optimizations are performed, one involving optimizing both parameters a and b and one where parameter b is fixed at a default value of 1.6. The second optimization is used to highlight the differences between the two events since parameter b does not vary significantly as parameter a. Furthermore, the table also includes information regarding the date of events, the total number of stations that featured correlation above the threshold, and the correlation coefficient value of the data pairs used.

The results show that there is a high variability between the values of the parameters in each event. The optimization is configured to limit parameter a value from 50 to 2000 and parameter b from 1 to 2.50. Although parameter a never reached the limits, parameter b did, which shows that the optimization would lead to better results should values beyond the limits be explored. However, this would lead to no typical Z-R relationships, leading to the fact that the optimization is not successful. Considering the Z-R relationship, $Z=aR^b$, a high value of parameters a and b translates to the fact that the same amount of reflectivity leads to higher rainfall values, or instead, that a specific amount of rainfall intensity is met when the target omits less reflectivity. Therefore, when parameters are unusually high, it demonstrates that large amounts of reflectivity are recorded against low rainfall measurements by the rain gauge. Furthermore, a second calibration is made by keeping parameter b fixed to the value of 1.60 and optimizing parameter a. By comparing the RMSE; it is seen that it does not change significantly, apart from some cases, which shows that parameter b has little effect on the correlation.

Table 4-3. Z-R Optimization results per rainfall event

Event	Date	Stations Used	Calibration on parameters a and b				Calibration on parameter a with fixed b		
			a	b	RMSE	r	a	b	RMSE
E1	30-09-2018	6	452	2.50	0.130	0.42	343	1.60	0.419
E5	16-12-2018	28	1486	2.50	0.445	0.60	771	1.60	0.169
E6	18-12-2018	31	301	1.95	0.210	0.66	306	1.60	0.450
E9	10-01-2019	23	758	2.42	0.197	0.67	551	1.60	0.237
E10	07-02-2019	26	956	2.50	0.290	0.54	540	1.60	0.225
E12	15-02-2019	27	1628	2.50	0.378	0.25	1070	1.60	0.329
E16	15-04-2019	25	340	1.41	0.304	0.88	292	1.60	0.392
E20	21-11-2019	19	369	2.50	0.308	0.71	402	1.60	0.356
E21	25-11-2019	22	206	1.05	0.216	0.95	118	1.60	0.625
E22	30-12-2019	27	1556	2.50	0.524	0.35	944	1.60	0.258
E31	01-06-2020	19	439	1.05	0.742	0.90	201	1.60	0.744
E33	08-08-2020	25	190	2.28	0.493	0.62	271	1.60	0.768
E36	04-12-2020	14	302	2.50	0.425	0.38	344	1.60	0.550

Considering the parameter a's results, two main event groups are observed: a) events where the parameter is between the typical bounds of 50 to 500 and b) events where the parameter

features larger values of up to 2000. Concerning the latter, it reinstates that snowfall events feature high values of parameter *a*, i.e., over 1000, since all three events that featured these high values, E2, E6, and E10, were indeed snowfall events. Most empirical Z-R relationships opted for snowfall feature high parameter *a* value (Joss and Waldvogel 1970; Austin 1987). In these events, the reflectivity field is usually a uniform low reflectivity field of up to 20 dBZ value. When snowfall is observed, the rainfall intensity measured by the gauging station is usually low, thus requiring a high parameter *a* value to match the relatively high dBZ value into that small rainfall intensity. Since snowfall events require a different approach, they have been excluded from the station-based optimizations.

Finally, although events with parameter *a* values between 50 and 500 are typical rainfall events, more information can be extracted from this optimization. In most empirical Z-R relationships, when the sample consists of convective events, the parameter *a* tends to have a large value, while the opposite occurs in stratiform-based events. Applying a Z-R relationship in large reflectivity values leads to extreme rainfall intensity. For instance, as shown in Figure 1-11, where three different Z-R relationships are used, the Z-R that featured the smallest parameter *a* value, for large reflectivity values resulted in the highest rainfall intensities. Research on the parameter *a* value has shown that when convective events are used, the parameter values are within the 300-500 range, whereas typical values for stratiform events range from 100 in tropical regions up to 250. Therefore, the parameter's value derived from the optimizations can be used to classify storm systems as convective, stratiform, and snowfall events. Although this is convenient, it should not be held as the sole indicator of storm classification since more parameters should be examined, such as vertical profile characteristics (Anagnostou 2004). In the examined case, observing the storm's footprint, identifying high reflectivity cells, and the period the event occurred are deemed sufficient to reach rainfall classification. Overall, the variability of the Z-R relationship, as illustrated in Table 4-3, shows that deriving a Z-R only from data collected from a single event is not optimal, especially in cases with a small coverage, since the storm's trajectory can affect the correlation in some stations, leading to poor results obtained by the optimization (Bournas and Baltas 2022a).

4.1.3 Station-based Z-R calibration

The station-based optimizations are performed utilizing datasets for each station, using the events where the station featured a correlation above 0.6 and excluding snowfall events. The results are shown in Table 4-4. Two optimizations are performed, as in the case of the event-based optimizations, one optimizing both parameters *a* and *b* and the other optimizing only parameter *a* using the average value of the previous optimization for parameter *b*. The results are also displayed in Figure 4-3, where each panel illustrates the spatial distribution of parameters *a* and *b*.

Table 4-4: Z-R Optimization results for each station

Source: (Bournas and Baltas 2022a)

index	Station	a	b	RMSE	r	Events	NMAE %	NMB %
Calibration Stations								
4	Ano Liosia	168	1.79	0.58	0.79	7	57.1	17.0
5	Athens	316	1.68	0.33	0.78	5	40.1	-11.7
17	Patissia	423	2.15	0.23	0.76	4	42.2	-4.1
27	Athens-Marina	430	1.78	0.42	0.65	3	58.2	52.8
28	Tatoi	209	1.52	1.67	0.79	3	54.6	-17.2
30	Korydalos	304	1.57	0.27	0.85	7	41.5	-14.0
32	Alimos	317	1.14	0.38	0.72	2	39.2	28.9
42	Imittos-Dafni	292	1.05	0.58	0.79	6	41.0	-14.0
43	Harokopio-Athens	297	1.98	0.35	0.77	6	44.6	-8.0
45	Pireas-Pedagogiki	192	1.87	0.32	0.81	4	30.7	-9.6
47	Chaidari	257	1.87	0.80	0.87	2	17.8	0.4
48	Pireas	261	1.34	0.34	0.83	4	33.8	-2.2
52	Delacroix-Attiki	448	1.05	0.36	0.87	6	46.5	-16.4
Validation Stations								
6	Dionysos	183	1.86	0.36	0.90	6	35.5	0.8
8	Faliro	433	2.26	0.30	0.75	5	36.4	-1.5
15	Neasmyrni	239	2.18	0.67	0.75	4	56.5	3.0
16	Neos Kosmos	402	1.83	0.39	0.84	8	40.1	-1.6
19	Peristeri	261	1.31	0.21	0.73	5	29.7	-4.1
21	Phychiko	271	1.42	0.45	0.81	8	37.0	-5.1
29	Aspropirgos	310	1.42	0.43	0.92	4	34.6	-10.2
34	Petroupoli	272	1.81	1.12	0.78	3	40.3	-6.8
35	Vrilissia	371	1.23	0.27	0.92	7	31.7	-10.1
38	Elefsina	275	1.05	0.25	0.77	3	41.6	-0.5
39	Nikaia	419	2.42	0.44	0.69	6	46.7	12.5
40	Salamina	490	1.08	0.00	0.83	2	0.1	-0.1
41	Ska	298	1.63	0.32	0.75	7	40.4	-1.4
45	Pireas-Pedagogiki	192	1.87	0.32	0.81	4	30.7	-9.6
51	Ano Korydallos	315	1.84	0.43	0.91	7	32.0	-2.6

Considering the values of the parameters, parameter *a* is calculated within the 168 - 490 range, while parameter b is within the 1.05 - 2.42 range. Figure 4-3 shows that stations found in the coastal front featured high parameter *a* values, while the stations located on the north featured the lowest values. The same is observed with the parameter's *b* values, although the distinction between high and low values seems to follow a west-to-east direction. Parameter *a* value shows higher variability, with the average value being 312, while parameter *b* had an average value of 1.64. As mentioned, these high parameters a and b

values indicate that most rainfall inputs in these locations are more likely to be of the convective rather than the stratiform type.

In order to better comprehend the spatial variability of the Z-R relationship, parameter b is fixed to the average value of 1.64, and the spatial properties of parameter a are analyzed. The results and the stations' names are featured in Figure 4-4. The parameter a's average value is changed slightly from 312 to 293. However, some differences can be noticed at selected stations, especially in stations where the original parameter b differed significantly from the fixed value.
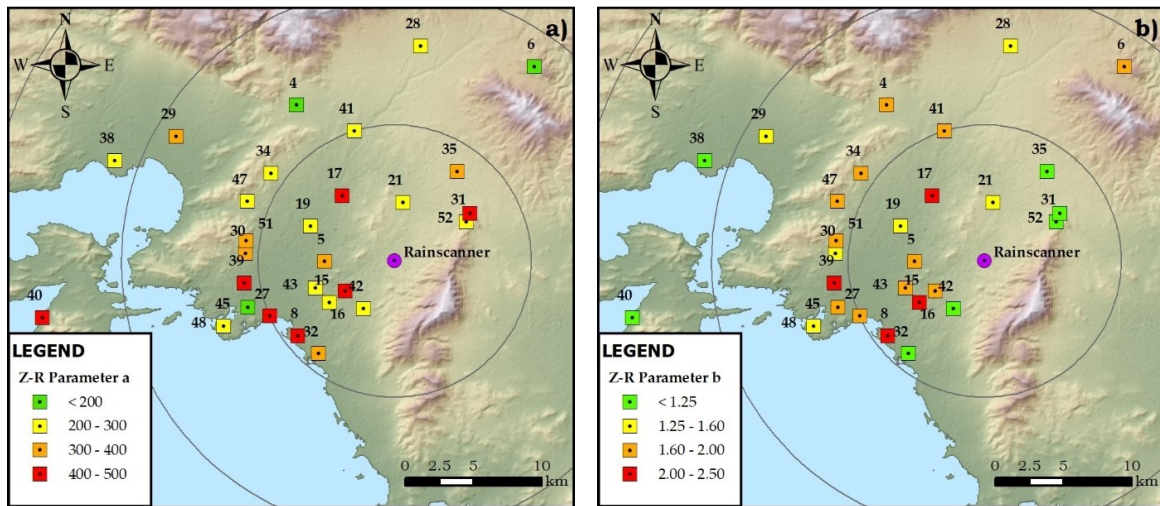
Figure 4-3: Z-R relationship parameters spatial variability, a) parameter a, b) for parameter b, Source: (Bournas and Baltas 2022a)
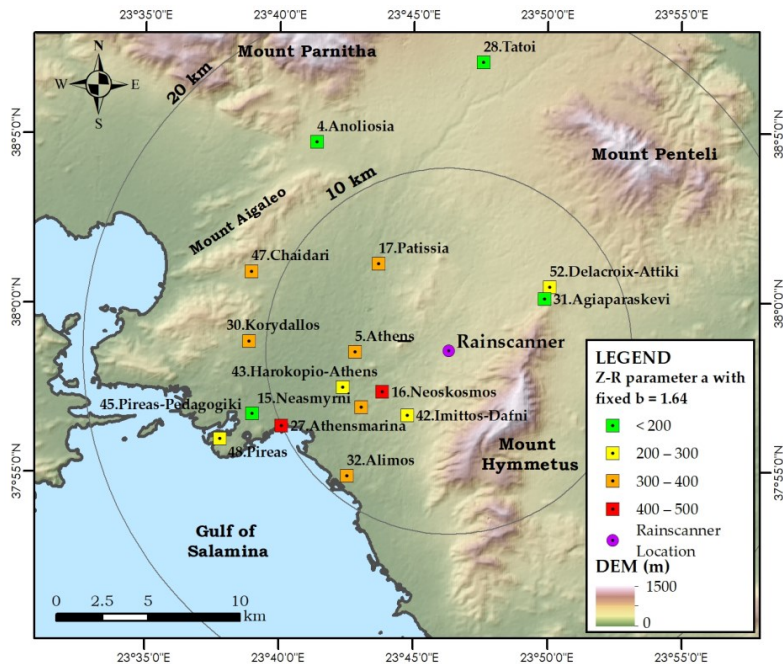
Figure 4-4: Spatial variability of Z-R parameter a, when a fixed parameter b is used, Source: (Bournas and Baltas 2022a)

As previously mentioned and illustrated in Figure 4-4, the highest parameter *a* values are found in the southwest, at the coast front of Athens, while the lowest values are found in the north section. As mentioned, a high parameter a value and a low parameter b are found in Z-R relationships better suited to convective type events. Since the sample includes both convective and stratiform events, this result indicates that higher reflectivity is measured on the coast front and less on the northeast. This finding can also be related to the typical trajectory of rainstorms in Athens. As featured in the studied events, storm cells in Athens tend to have a west-to-east direction. This trajectory usually takes the storm cell above the Gulf of Samalina and towards Mount Aigaleo. Especially in convective events, the storm cell feeds with moisture while it passes the sea, only to discharge when it hits the mainland and the higher elevation that Mount Aigaleo offers. Water discharge, i.e., rainfall, occurs rapidly in the coastal regions, imitating convective-based storm characteristics. From then on, the storm cell keeps discharging until it reaches Athens city center, only to be headed next to the North due to the presence of Hymmetus Mountain on the east. The rainfall intensity drops when it arrives at higher elevation locations, and stratiform-based rainfall intensities are observed. A lower rainfall intensity does not mean less rainfall accumulation since the storm cloud may lose its velocity, thus delaying its departure from these regions. Overall, it is shown that the Z-R relationship does change in space and time. Specifically, the Z-R relationship tends to vary based on the storm cell's proximity to the coastal front, the ground's elevation, and the distance from the Rainscanner.

4.1.4   Single Z-R calibration

This section uses the entire well-correlated dataset to extract a single Z-R relationship. A one-size-fits-all process is performed, where all datasets from multiple stations and events are used. The optimization is performed in two groups, one where a Z-R is derived from all the available data and one where a calibration/validation scheme is used, with the scope of evaluating the robustness of the relationship. In the first case, the derived Z-R relationship is the following:

$$Z = 300R^{1.69} \tag{4.1}$$

The Z-R parameters of the featured equation are similar to the average values of the individual optimizations shown in Table 4-4. In the calibration-validation scheme, a series of stations are selected as the "calibration" stations, and the rest are used as "validation" stations. The "calibration" stations are selected by following two rules. First, the station should feature a high number of well-correlated events. Second, the final selection, out of the pool of the well-correlated stations, is made by selecting stations that provide good coverage and density for both the calibration and validation groups. For instance, if two stations featuring a high number of well-correlated events are in close proximity, only one

is selected to join the calibration group while the other is the validation group. As seen in Figure 4-4, half of the available stations were used for calibration and half for validation, featuring an equal density between each group. The scatter plots of the data pairs used in each group are shown in Figure 4-6, featuring the rainfall intensity [mm/h] as derived from the 10-minute resolution each pair featured. Most measurements are below 5 mm/h, with some exceptions featuring high values of over 15 mm/h. The calibration group features a better correlation between the two pairs, distinctive of the distance of the data pairs to the 1:1 line.
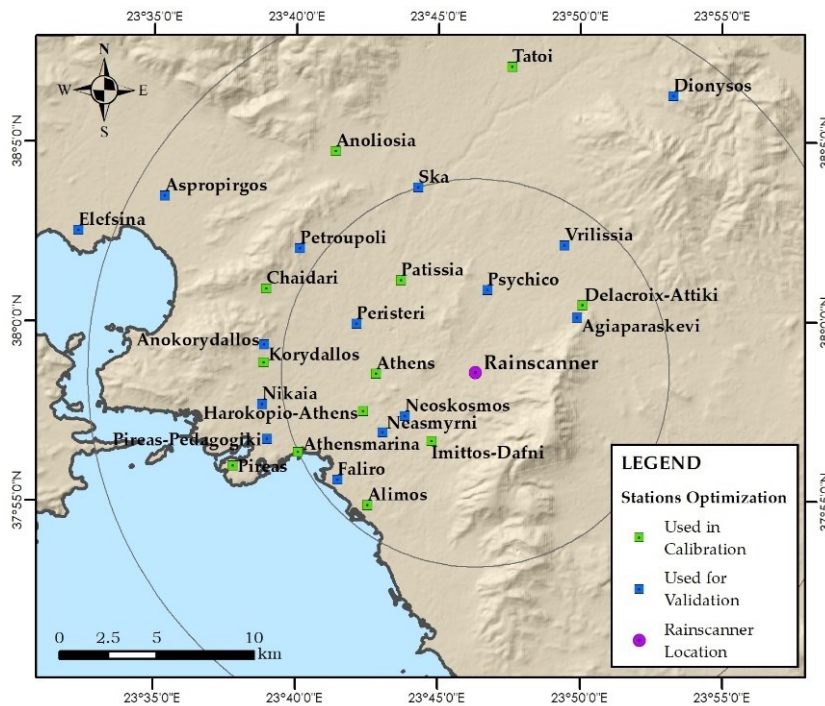
Figure 4-5: Location of stations used in the Calibration and the Validation optimization processes
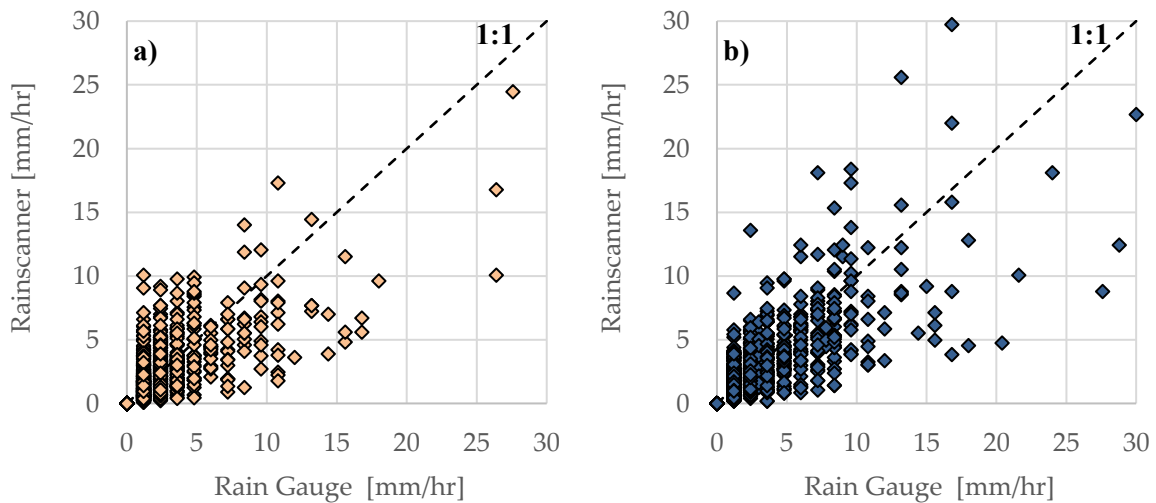
Figure 4-6: Scatter plot of data used in a) Calibration and b) Validation groups.

The derived Z-R relationship is the following:

$$Z = 321R^{1.53}$$

(4.2)

Table 5-5 displays the validation station's RMSE and r correlation coefficient index and compares them with their respective individual optimization. As expected, the correlation index, *r*, is unaffected since it does not alter significantly with the used Z-R. The RMSE values in each case differ slightly but not to a level that may impact the results. Most stations show little changes in the derived indexes.

Table 4-5: Z-R validation station statistics using the $Z = 321R^{1.53}$ relationship.

index	Station	Individual Optimization				Validation	
		a	b	RMSE	r	RMSE	r
6	Dionysos	183	1.86	0.36	0.90	0.45	0.90
8	Faliro	433	2.26	0.30	0.75	0.37	0.75
15	Neasmyrni	239	2.18	0.67	0.75	0.72	0.75
16	Neos Kosmos	402	1.83	0.39	0.84	0.42	0.84
19	Peristeri	261	1.31	0.21	0.73	0.23	0.73
21	Phychiko	271	1.42	0.45	0.81	0.47	0.81
29	Aspropirgos	310	1.42	0.43	0.92	0.46	0.92
31	Agia Paraskevi	290	1.21	0.24	0.95	0.70	0.95
34	Petroupoli	272	1.81	1.12	0.78	1.19	0.78
35	Vrilissia	371	1.23	0.27	0.92	0.30	0.92
38	Elefsina	275	1.05	0.25	0.77	0.28	0.77
39	Nikaia	419	2.42	0.44	0.69	0.46	0.69
40	Salamina	490	1.08	0.30	0.83	0.32	0.83
41	Ska	298	1.63	0.32	0.75	0.32	0.75
45	Pireas-Pedagogiki	192	1.87	0.32	0.81	0.40	0.81
51	Ano Korydallos	315	1.84	0.43	0.91	0.60	0.91

4.1.5 Z-R relationships Comparison

This section compares the derived Z-R relationships based on the precipitation and accumulation timeseries per station. In Figure 4-7 and Figure 4-8, the rainfall and accumulative rainfall timeseries for two validation stations, the Psychiko and Neos Kosmos, and for two rainfall events, E6 and E16, are presented. Blue bars denote the rain gauge measurements within the figures, while the Rainscanner measurements are presented with lines with different coloring based on the Z-R relationship used. Specifically, with green color, the Marshal and Palmar equation, *Z=200R¹·⁶*, with red color the all-data calibration equation 5.2, *Z=321R¹·⁵³*, with purple color the Event-based Z-R, as shown in Table 4-3, and with black color the Station Based Z-R, Table 4-4, and with a blue color the optimized relationship

when the station dataset for the particular event is used. The best-fit result in each plot is the last option from the above since the Z-R parameters are optimized to match the specific data.
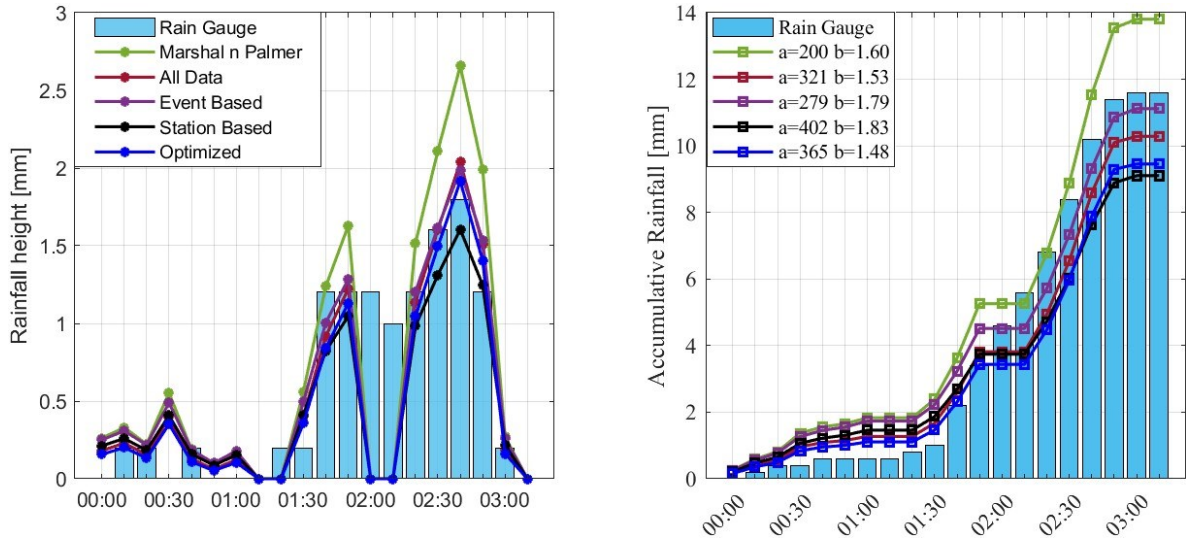
Figure 4-7. Precipitation and accumulative precipitation for Phychiko, on Event 6.
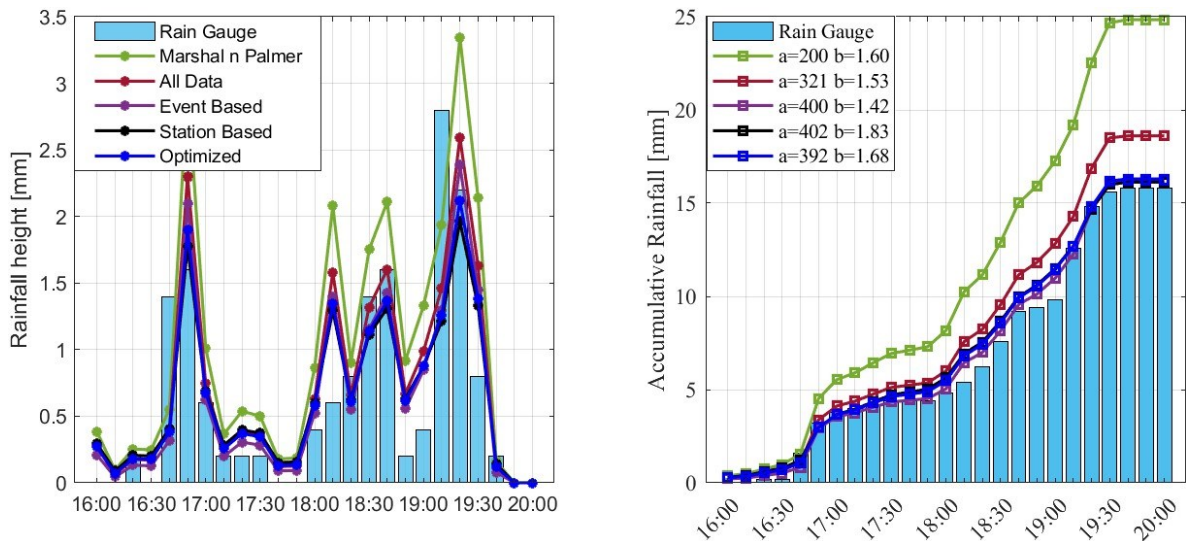
Figure 4-8. Precipitation and accumulative precipitation for Neos Kosmos on Event 16.

In all figures, the Marshal and Palmer equation shows the higher deviations. Specifically, it leads to an overestimation of rainfall compared to the rain gauge datasets. The equation that is closer to the optimized relationship is the station-based equation, followed by the All-data and event-based relationships. In Figure 4-7, Psychiko station event 6, it is observed that while the optimized does the better fitting in each 10 min rainfall height interval, the rainfall accumulation does not feature the best result compared to other relationships. This is caused by the gap of the Rainscanner dataset at 02:00, where no data is recorded, disrupting the accumulation time series graph.

In Figure 4-8, featuring Neos Kosmos station, for event 16, the optimized and Station-based relationships are similar, although the value of parameter b is changed dramatically, from 1.48 to 1.83. This difference showcases that parameter b does not contribute substantially to the Z-R relationship in this case. This is because the time intervals are small. As in the previous case, the Marshal and Palmer equation shows the worst correlation, while the all-data calibration-based is slightly better. The calibrated Z-R shows a good correlation with small biases in the accumulative precipitation diagram, highlighting that it can be used for different stations and events.

Finally, in this section, a comparison is made between the proposed, all-data derived Z-R relationship, $Z=321R^{1.53}$, with relationships that have been derived from past studies, i.e., a) the Marshal and Palmer $Z=200R^{1.6}$, b) the $Z=431R^{1.25}$, and c) the $Z=261R^{1.52}$, the two later derived from distrometer measurements in Athens.

This comparison is performed by calculating the RMSE, BIAS, NMAE, and NMB indexes between the rain gauge measurements and the rainfall heights estimated through each Z-R relationship. The results are presented in Boxplots in Figure 4-9, in which each station's data utilizing only the well-correlated events are shown. The optimum relationship, as in Figure 4-7 and Figure 4-8, includes the optimized result of each station per event, featuring the best results, which the rest of the relationships should reach. All indexes are set to have zero values as their optimum result, while NMAE and BIAS are also allowed to have negative values. Furthermore, apart from the mean value, the red line, which should be found to be close to zero, and the spread of the sample are also essential.

Observing the boxplots, out of the four relationships, the all-data calibrated relationship, $Z=321R^{1.53}$, features the best results, followed by $Z=261R^{1.52}$, $Z=431R^{1.25}$, and last, the Marshal n Palmer $Z=200R^{1.6}$. The Marshal and Palmer relationship has the worst results in all indexes since the median value is the highest, while the spread is significant, which means that it does not apply as well as the other relationships. The convective-based $Z=431R^{1.25}$ shows promising results but tends to underestimate the actual rainfall since the NMB value is negative. This underestimation means that the relationship should be better used only in convective events, i.e., events that feature over 35-40 dBZ reflectivity, since underestimation of rainfall might have an unwanted impact on hydrological applications, such as continuous soil moisture monitoring. Finally, the $Z=261R^{1.52}$ relationship, although featuring a similar parameter b value but a smaller parameter a value than the one proposed, shows promising results. However, the difference in the average BIAS and NMB values in each case signifies how sensitive the rainfall estimation is to parameter a's value.
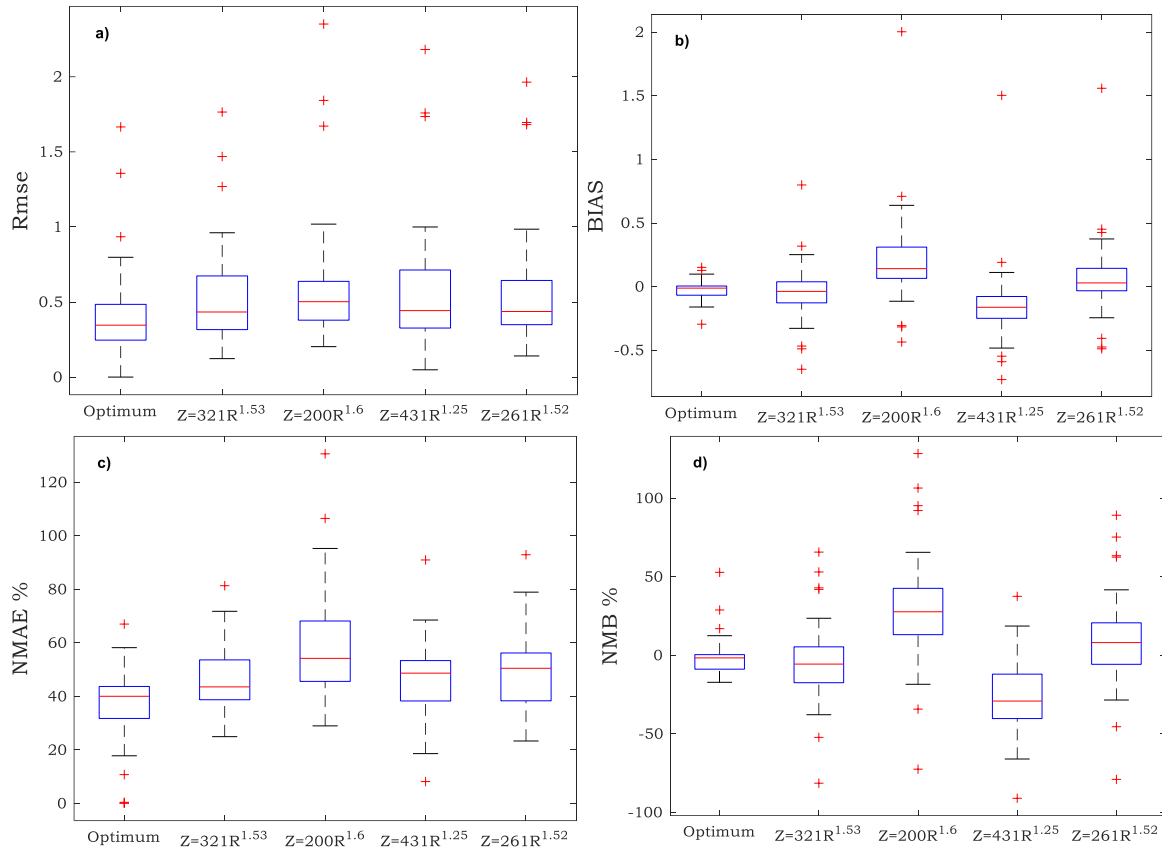
Figure 4-9. Boxplots of the a) RMSE, b) Bias, c) NMAE, and d) NMB per Z-R relationship

4.2 Rainfall-Runoff Model Simulations

4.2.1 Gridded Rainfall-Runoff model calibration

The gridded model used is analyzed in Chapter 3.4. The core element of the model is the construction of the time-area diagram. The model is used in a subbasin of the study area, the rural part of the Sarantapotamos basin, as featured in Figure 4-10. The outlet of the basin is selected at the cross-section of the Sarantapotamos River with the Attiki Odos freeway, totaling an area of 231.50 km². Based on the DEM dataset, the mean elevation of the basin is 491 m, with a maximum elevation of 1270 m and the minimum at the outlet being 40 m. The subbasin lies 25 to 50 km from the Rainscanner location and features an elongated shape governed by two streams, the Sarantapotamos stream on the north and its substream, the Ag. Vlassios stream in the South. Both streams are ephemeral, i.e., substantial flow is only observed during and after rainfall (Bournas and Baltas 2022b).

The time-area diagram is derived in GIS. Considering the spatial resolution of the grid, a 500 m x 500 m grid is used based on the size of the basin. The grid leads to a total of 1021 grids. Following the time-area diagram flow chart in Figure 3-11 while in Figure 4-11, the gridded slope and CN AMC-II values are shown.
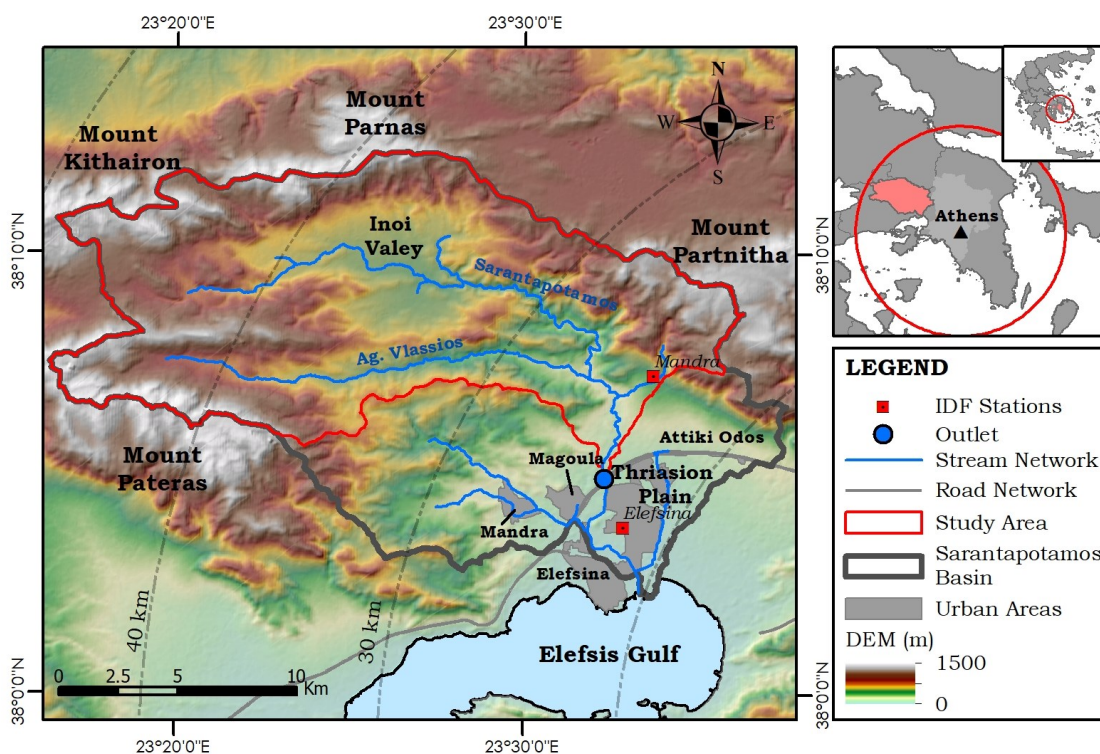
Figure 4-10. The Sarantapotamos basin and its subbasin where the RR model is applied.
Source: (Bournas and Baltas 2022b)
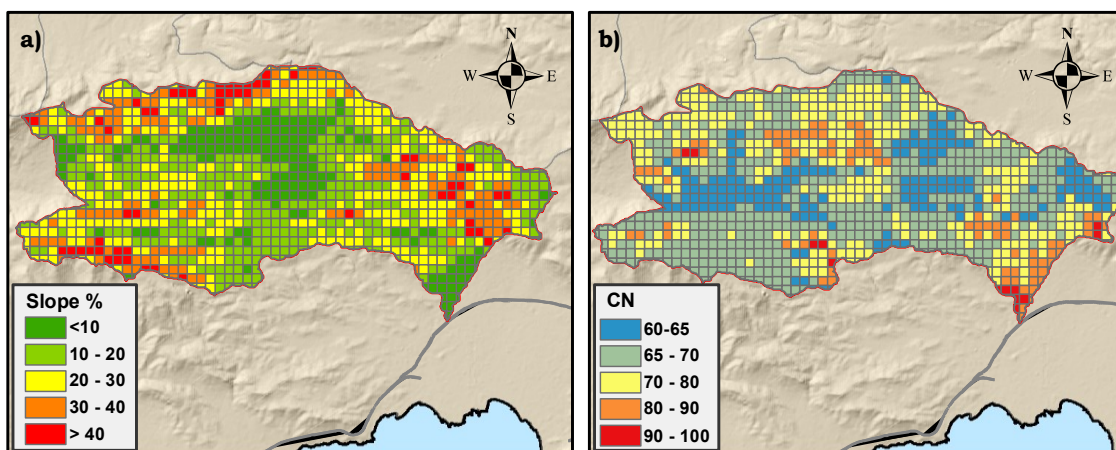
Figure 4-11. Gridded datasets; a) Slope %, b) Curve Number for AMC-II conditions
Source: (Bournas and Baltas 2022b)

Regarding the velocity field, the mean overland velocity over the basin is calculated at 1.2 m/s, while the maximum velocity is four m/s. The maximum travel time is 36 hours. However, as observed in the cumulative time-area graph in Figure 4-12, although the maximum travel time is 36 hours, by the 24-hour mark, most of the basin has reached the outlet, which shows that the actual rate of discharge of the basin is approximately ten km2/h, a considerable value. This rate shows that although the basin has an elongated shape, the

two streams divide the basin into two subbasins that work along each other, resulting in a high runoff potential in the outlet. This characteristic cannot be accounted for when a lumped model is used instead. For instance, if one applies a synthetic UH such as the SCS dimensionless UH, a single concentration time is only calculated, leading to a misinterpretation of the actual basin's discharge rate.
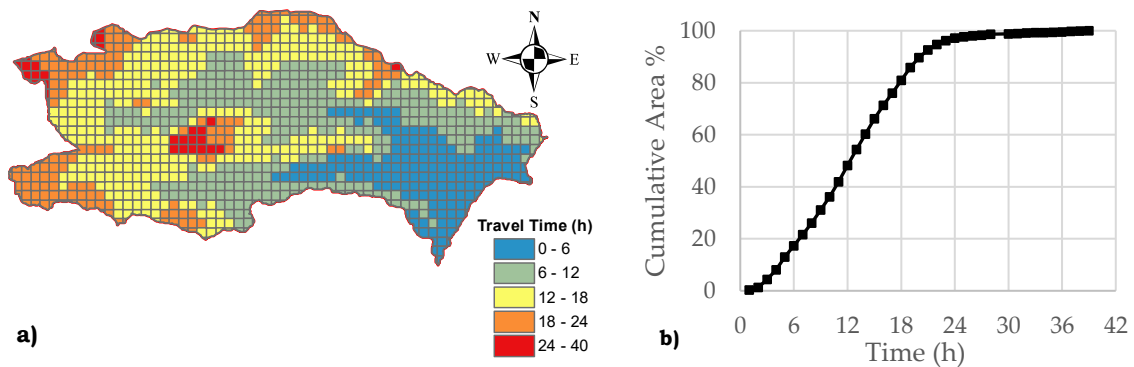
Figure 4-12. Time-area diagram: a) Time travel raster; b) Cumulative area % per hour at the basin outlet. Source: (Bournas and Baltas 2022b)

4.2.2   Rainfall Events Analysis

The model is then applied to a series of rainfall events. The events are showcased in Table 4-6. The events that featured the highest rainfall intensity are used to highlight the application of the model. Table 4-6 also features the event's duration, as well as the 5-day accumulated precipitation, in order to better evaluate the prior soil moisture conditions.

Table 4-6: Simulated events and main characteristics; Source: (Bournas and Baltas 2022b)

Event	Start Datetime	End Datetime	Duration (h)	5-Day API (mm)	Mean Area Cumulative Rainfall (mm)
6	17-12-2018 23:40	18-12-2018 13:50	14.2	13.8	25.8
21	24-11-2019 21:40	25-11-2019 08:30	10.8	37.0	30.4
31	01-06-2020 14:00	01-06-2020 20:00	6.0	0.0	20.5
48	09-06-2021 18:00	10-06-2021 02:44	8.7	0.2	25.0
50	12-06-2021 11:50	12-06-2021 19:00	7.2	32.0	26.0
61	23-11-2021 17:30	24-11-2021 07:40	14.2	2.6	26.4

In Figure 4-13, each event's accumulated rainfall is showcased, highlighting the spatial variability of rainfall. The study area where the RR model is applied is highlighted with a red polygon. In some events, i.e., events 6, 21, and 61, the rainfall coverage is the entire scanning range, while the area on the southeast of the Rainscanner location is within the no-data area of the Rainscanner due to orography.
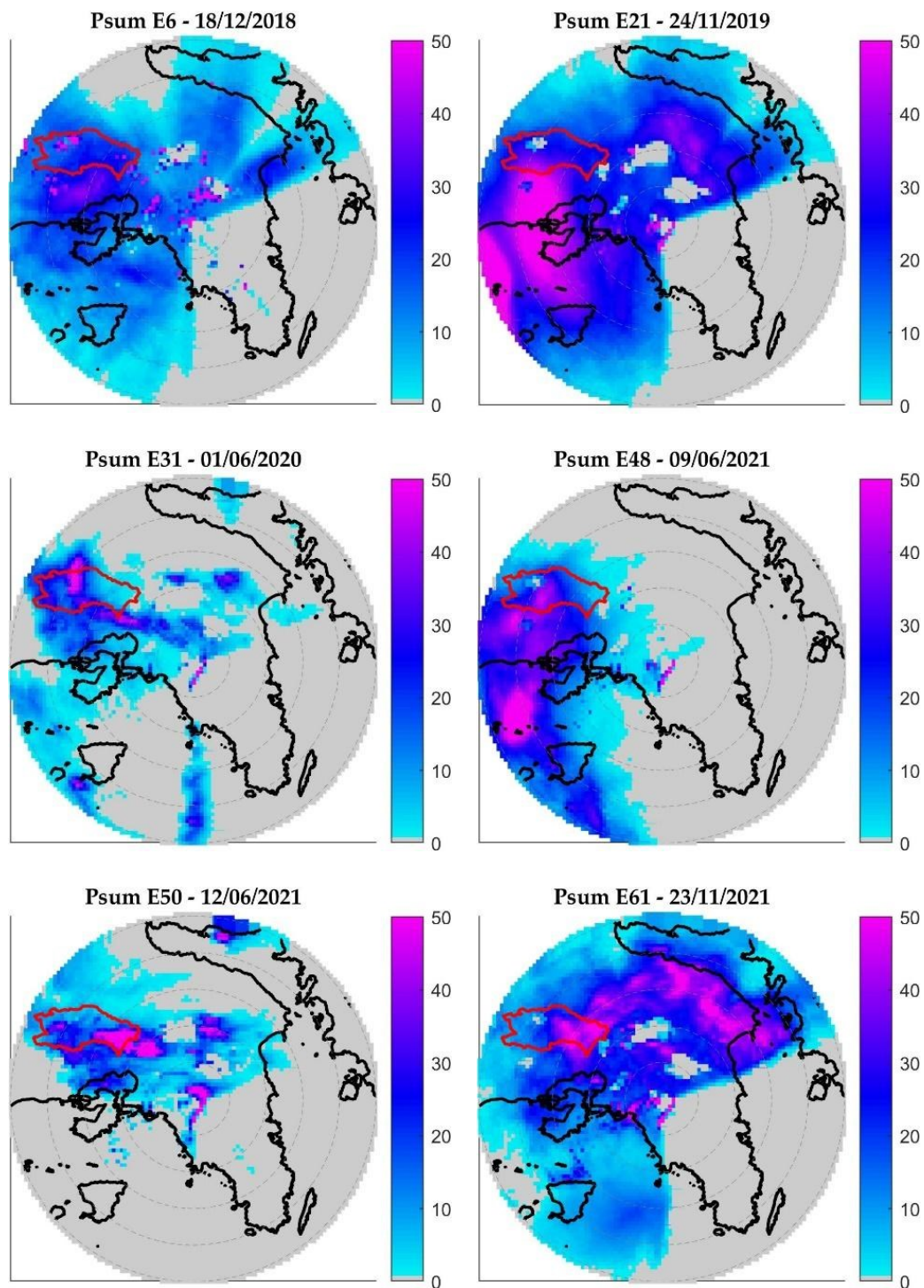
Figure 4-13. Cumulative precipitation per event recorded by the Rainscanner. The study area is highlighted with the red polygon; Source: (Bournas and Baltas 2022b)

The other events, events 31, 48, and 50, feature a smaller coverage, where only a few areas in the west are affected, where the Sarantapotamos basin is located. These events showcase convective-based characteristics since they feature multiple small areas of high rainfall

116

accumulation, a typical characteristic of convective events, and they occur in the summer, with events 31, 48, and 50 occurring in June when convection is favored. Specifically, convective events are formed due to convection when the ground gets heated, and air masses are forced to move up to cool, which leads to unstable conditions and the formation of rainfall. These events usually have a shorter duration than the respective stratiform events but tend to feature high rainfall intensities, i.e., large amounts of rainfall in a small duration. This storm classification can be easily spotted in such a Rainscanner image while highlighting that summertime events in Athens are convective-based.

Runoff potential is not only regulated by the amount of precipitation but also by the soil moisture conditions prior to the event. Summertime events are expected to have dry soil moisture conditions since rainfall is usually absent for several days or even weeks beforehand. Based on the 5-Day API shown in Table 4-6, the AMC for events 6 and 61 is assumed to be medium. In contrast, events 21 and 50 feature conditions close to AMC-III, i.e., wet conditions, since they were the follow-up of other rainfall events. Finally, events 31 and 48 were considered closer to AMC-I, i.e., dry conditions, since no rainfall was observed the prior days. Moreover, in all cases, an assumption is made regarding the actual soil moisture conditions, overcoming the fact that only three conditions can be defined. For the dry events, 20% soil moisture is used, while for the two wet events, 90% is used for event 21 since it occurred in November with substantial prior-days rainfall, and 70% moisture for event 50 since it occurred in June.

In Figure 4-14, the generated hydrographs for each event are shown. Each graph shows the flood hydrograph generated at the outlet when the rainfall field is estimated using the five different Z-R relationships examined. The rainfall timeseries shown in Figure 4-14 are generated through the calculation of the mean areal precipitation over the basin after applying the Marshal and Palmer equation to the Rainscanner fields and are shown only to demonstrate the duration and the scale of the rainfall of each event since the actual rainfall-runoff model used the 10-min, gridded precipitation fields. Table 5-7 shows each event's total accumulated rainfall and estimated peak discharge. Finally, the last two graphs feature the hydrographs generated as above, for events 31 and 50, after removing the $Z=275R^{1.05}$ relationship to visualize better the rest of the hydrographs since it provided out-of-scale peak runoff compared with the other relationships applied.
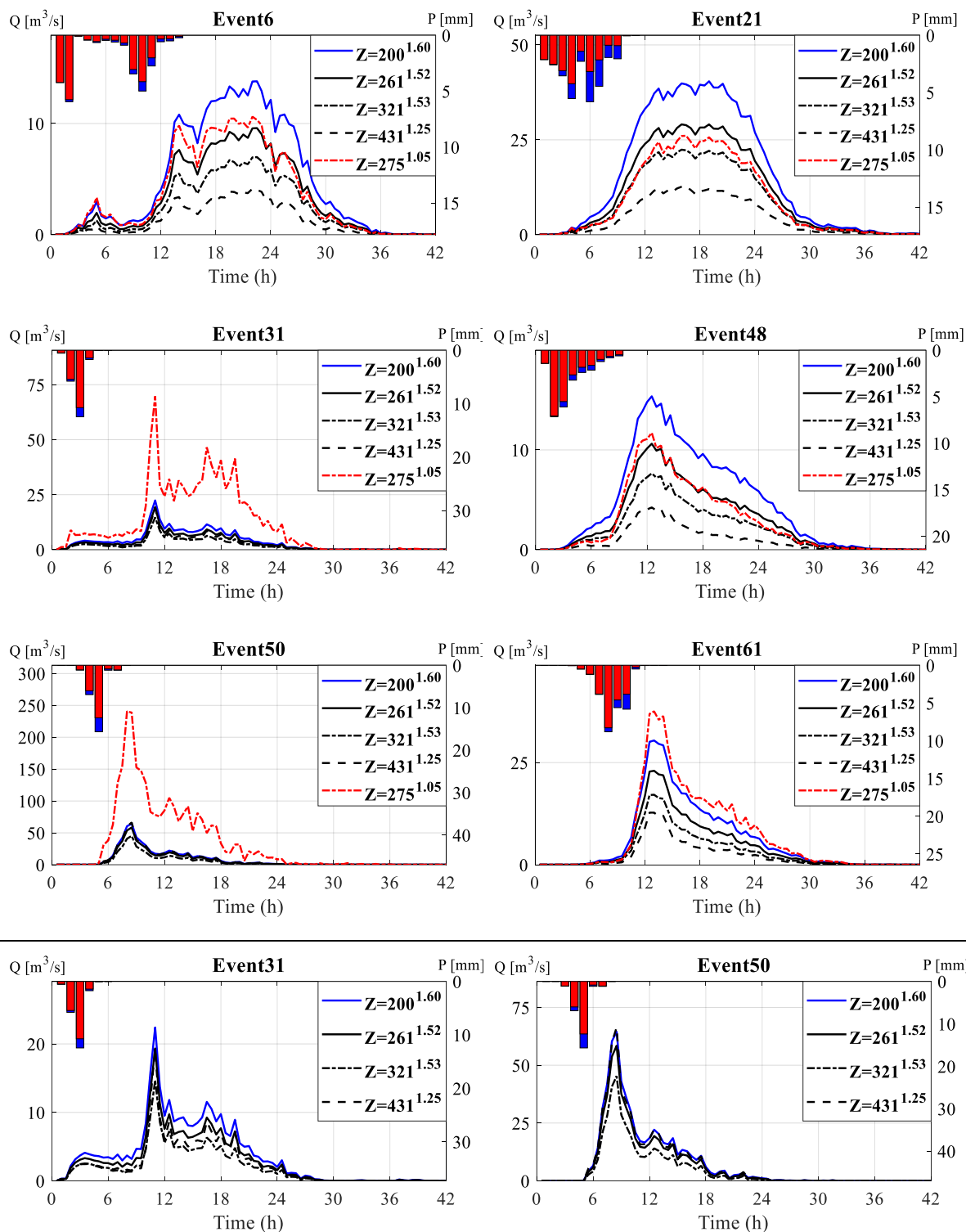
Figure 4-14. Hydrographs of featured events. Blue and red bars denote mean area rainfall and rainfall losses, respectively. The last row graphs for events 31 and 50 are identical with the latter after the removal of the Z=275R $^{1.05}$ results for better comparisons;

Source: (Bournas and Baltas 2022b)

Table 4-7. Hydrograph Results for each Event and Z-R used

Total precipitation (mm)	$Z=200R^{1.6}$	$Z=261R^{1.52}$	$Z=321R^{1.53}$	$Z=431R^{1.25}$	$Z=275R^{1.05}$
E6	25.82	21.95	19.16	15.11	22.59
E21	30.36	25.48	22.28	16.55	23.07
E31	20.51	18.31	15.88	15.85	31.00
E48	25.02	20.97	18.34	13.63	19.22
E50	26.02	24.02	20.74	23.85	53.47
E61	26.37	22.73	19.81	16.67	26.74
Peak Discharge (m^3/s)					
E6	13.80	9.59	6.98	4.13	10.61
E21	40.43	29.07	22.41	12.63	26.06
E31	22.40	19.34	14.71	19.31	69.72
E48	15.37	10.63	7.65	4.23	11.72
E50	78.37	71.43	56.61	79.69	272.79
E61	30.42	23.00	17.13	12.76	37.55

In each hydrograph, what is changed after applying different Z-R relationships is the amount of runoff generated and specifically the peak runoff and runoff volume, while the time to peak and the shape of the hydrograph remain unchanged apart from minor deviations.

The first visible finding is the deviation of the $Z=275R^{1.05}$ equation on the E50 and E61 events. This equation resulted in significant differences in rainfall and peak runoff results. Specifically, the rainfall estimation was 51% and 105% more than the Marshal and Palmer equation, resulting in 211% and 248%, respectively. This equation was derived after analyzing weather radar and rain gauge datasets for the Elefsina rain gauge station, the nearest station with well-correlated Rainscanner-rain gauge datasets from the study area, as shown in Table 4-4. The specific relationship features a stratiform standard parameter *a* value but a very low parameter *b* value, nearly equal to the value of one, denoting a linear relationship between reflectivity and rainfall intensity. Although such relationships might perform within acceptable limits for stratiform events where the reflectivity and rainfall intensity values are low, the rainfall rates calculated in convective events are unacceptable. As shown in Figure 4-15, the Z-R relationship effect on the transformation of reflectivity to rainfall intensity becomes noticeable when the reflectivity values are over 35 dBZ, while substantial differences are noticed only after 45 dBZ. In the case of relationship $Z=275R^{1.05}$, the difference in the rainfall rate is noticeable much earlier, starting from the 35 dBZ value, whereas the difference is increased exponentially, with the 45 dBZ value leading up to four times what a typical relationship calculates. The majority of reflectivity observed in convective events such as E31 and E50 is between 35 and 45 dBZ, in contrast to the stratiform events where reflectivity is usually less than 35 dBZ, making the effect the featured

relationship at its maximum compared to stratiform events, where the change is not noticeable. Therefore, it is deemed that this relationship is unsuitable for such events, as is shown later by calculating the rainfall's return period using the IDF of a nearby station. The derivation of the relationship was probably performed using datasets from stratiform events and generally from events that did not feature such high reflectivity values.
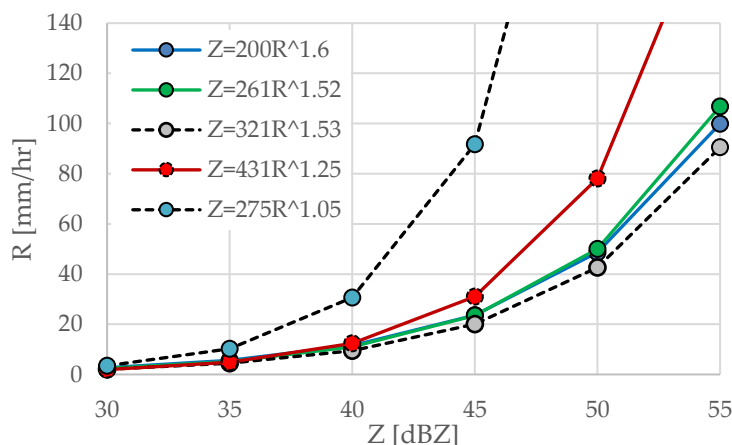

Figure 4-15. Relationship between reflectivity (Z) and Rainfall Rate (R) for the Z-R equations used.

To draw constructive conclusions, since no observed hydrographs are available, the results are compared with the results derived from the Marshal and Palmer (1948) relationship, $Z=200R^{1.60}$. Figure 4-16 shows the absolute percent difference between each Z-R relationship to the Marshal and Palmer equation for total precipitation, while Figure 4-17 shows the peak discharge. The Marshal and Palmer equation led to the largest rainfall fields and runoff values. The equations derived from mixed or stratiform events for Athens, e.g., $Z=261R^{1.52}$ and $Z=321R^{1.53}$, show a steady difference in all events compared with the Marshal and Palmer equation. On the other hand, the convective-based relationship, i.e., $Z=431R^{1.25}$, shows higher differences in the stratiform events than the convective events. Specifically, the difference is slight on the convective events, while the runoff is almost equal to the Marshal and Palmer, at 14% for event 31 and larger by 1% for event 50. In event 50, although the mean accumulated rainfall is slightly higher using the Marshal and Palmer equation, the peak runoff is higher using the $Z=431R^{1.25}$ relationship. This result highlights the importance of using gridded rainfall datasets since this denotes that the rainfall spatial variability impacts the runoff potential. In raw numbers, the precipitation among the used Z-R relationships varied approximately -5 to -10 mm for mean areal precipitation and 10-20 m³/s for peak discharge. For instance, in event 62, a 30 m³/s peak discharge is estimated with the Marshal and Palmer equation, while only 12.76 m³/s for the convective-based $Z=431R^{1.25}$ relationship. Overall, the featured graphs show a strong connection between the type of storm and the Z-R relationship.
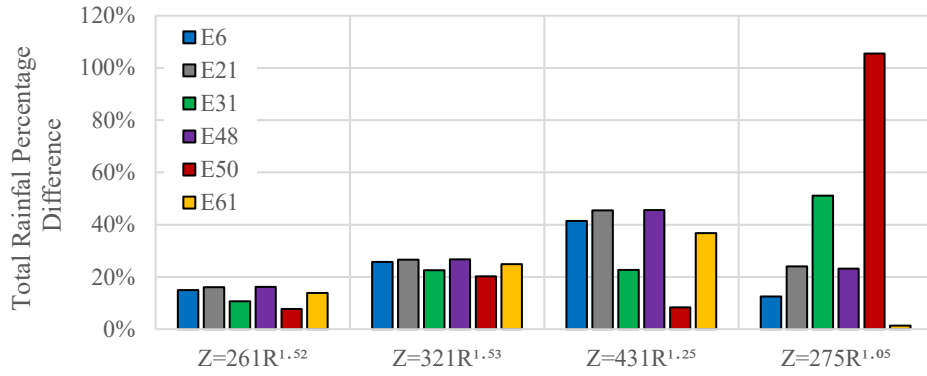
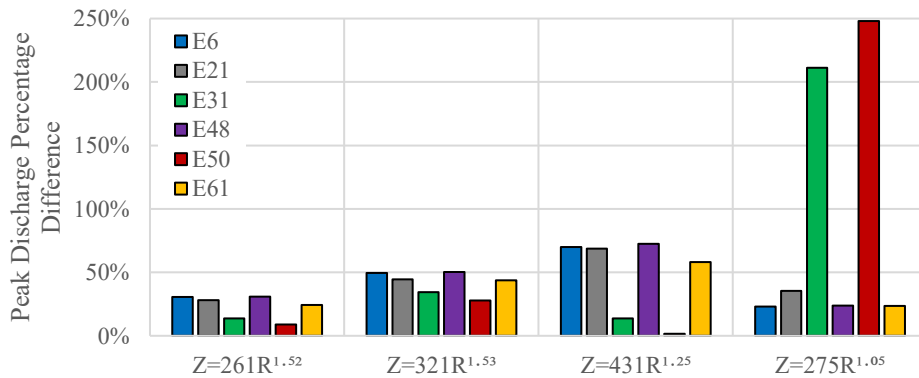Figure 4-16. Total Rainfall percent difference between each Z-R and $Z=200R^{1.6}$

Figure 4-17. Peak Discharge percent difference between each Z-R and $Z=200R^{1.6}$

A final comparison is made by comparing the rainfall fields with rainfall derived from IDF curves of a nearby station. The nearest and most suitable station to the basin is the Mandra station, located northeast of the basin, shown in Figure 4-10, since compared to Elefsina station, it features an elevation closer to the mean elevation of the basin. The IDF curve of the Mandra station is derived from its parameters featured in Table 2-3. Concerning the rainfall events, the IDF curve is constructed by the timeseries of the pixel, which featured the highest total precipitation within the basin. In Figure 4-18, the IDF is plotted per event per Z-R, highlighting the intensity of each event and the differences in the calculated return periods between the different Z-R relationships used. From all the examined events, only events 31 and 50 feature over one-year return periods.
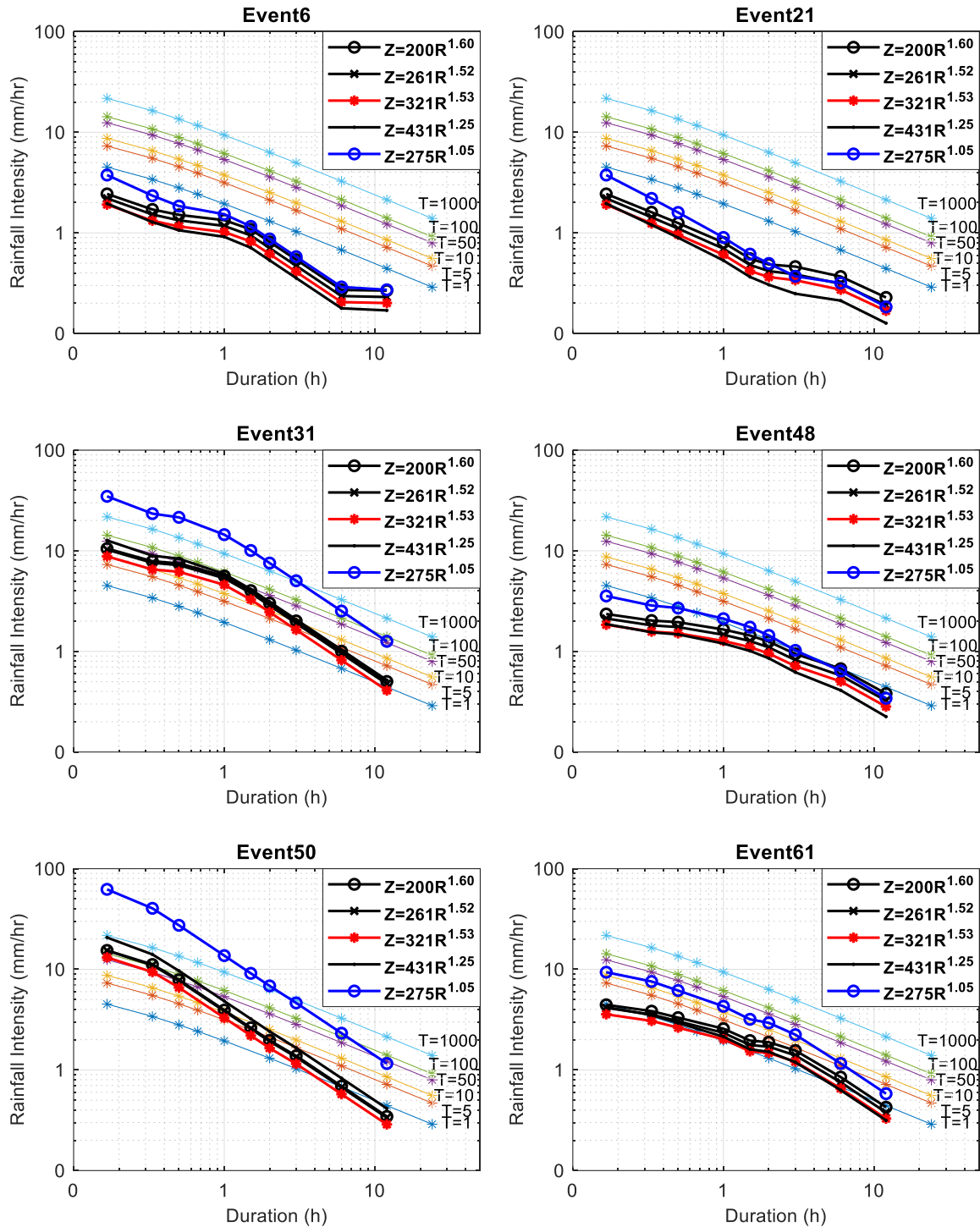
Figure 4-18. IDF curves per event when different Z-R relationships are applied.

Events 6, 21, and 48 featured fewer return periods, below the 1-year mark, while event 61 featured return periods between 1- and 5- years, depending on the Z-R equation used. In these events, the difference between the Z-R relationships in the IDF-derived return period is insignificant, except for slight deviations. On the convective events, the changes are more

significant, highlighted by the difference in the Z=275R$^{1.05}$ relationship. Specifically, when this Z-R equation is used, the IDF plot shows that events 31 and 50 had a returning period of over 1000 years, whereas when applying the rest of the Z-R relationships, a 20-50-year return period is estimated instead. The 1000 value is extreme, given the severity of the specific rainfall event, whereas the 20-to-50-year mark is more in line with the actual severity of the rainfall events. It is vital to notice that these return period values denote the pixel with the highest reflectivity values and might represent the entire event on the basin scale. A basin-wide IDF approach could lead to different results, but this comparison is useful since it can assess a) the Rainscanner datasets and b) the suitability of a Z-R relationship.

Overall, it is highlighted that a proper Z-R relationship should be used in each case. Utilizing a convective type, Z-R ensures that extreme values will most likely be avoided. On the other hand, these relationships tend to underestimate rainfall height in events with medium-sized rainfall intensities and long durations. Therefore, for a properly calibrated weather radar system, a convective/stratiform classification algorithm should be used first to make the best-fitted selection between locally derived Z-R relationships. However, this might always be feasible since classification algorithms require data such as the storm's vertical profile. The required lead time to assess an event might be inappropriate when small-range radars such as an X-Band radar are used instead. Therefore, if classification is not feasible in real-time, seasonal Z-R relationships are advised to be used instead, i.e., a specific Z-R is used for summer and winter. Finally, concerning Attica, a convective-based Z-R is the safest choice since flood events do not occur due to rainfall accumulation over longer periods but rather due to flash floods, i.e., convective events that feature large rainfall rate values.

4.3 Gridded Flash Flood Guidance Application

4.3.1 Derivation of Threshold Maps

The process followed in this section is displayed in the flow chart of Figure 3-14. The process starts with analyzing the study area and the threshold runoff calculation, followed by the FFG values for pre-defined soil moisture conditions. Finally, the system is used on past events to assess the resulting flood threat. The application of the GFFG is first performed at the Sarantapotamos basin, in which the entire process is explained and then applied to the entire Attica region. The Sarantapotamos basin is a rural area of west Attica, whereas the entire Attica region is a large area that includes the Attica metropolitan area, which is highly urbanized. In the first case, the GFFG system is expected to work as intended, while in the second case, uncertainty is expected since the effect of storm sewer networks is not considered to calculate threshold runoff. Nevertheless, the generated results are still valuable since when high rainfall intensity occurs in Athens, the sewer entry points are often

blocked by debris, making the road network act as a typical stream network, while the high percent of urbanization results in high CN values, which favors the runoff potential. In Athens, street flooding occurs rather often due to the poor cleaning of the sewer entry points and, in some cases, the center of Athens, the underperforming design of the sewer network capacity.

First, the Sarantapotamos subbasin is examined. The subbasin has a total area of 231 km² and is divided into square grids of 500 m dimensions in this application. Given the methods used for hydrological processes, the spatial resolution is selected to be as low as possible but retaining a minimum area. A 1 km size grid was also used, providing equal quality results. Following this, the threshold runoff is calculated based on the 5-year rainfall ARI method explained in Chapter 3.5. The nearest stations where the IDF curves are available are the Eleusis, ID #286, and Mandra ID #292 stations shown in Figure 2-9, with the parameters of the IDF equations shown in Table 2-3. Table 4-8 shows the total precipitation for different rainfall durations and return periods, with the 5-year highlighted in bold. Since the system is designed to focus on flash floods, the 1-, 3-, and 6-h periods are used. Concerning the study area, the Mandra station features higher rainfall, attributed to its higher elevation, 258 m against 31 m, and proximity to the mountain peaks. Following this, the "IDF" rainfall for each duration is interpolated to the designated grids using the Inverse Distance Weighting (IDW) algorithm. Unfortunately, both stations are located in the south area of the subbasin, with the nearest station to the west being 50 km away from the basin, which is two times the diagonal of the basin. Stefani station on the north is not suitable since it is not only far away but also located on the other side of the mountain peak, which, due to the effects of orography, can change the rainfall characteristics dramatically. Therefore, it can be said that the Mandra station datasets should correlate better to the area northwest of the basin than the datasets of the Stefani station.

Table 4-8: Eleusis and Mandra accum rainfall derived from IDF curves for different accumulation and return periods. The 5-year return period used in this research is highlighted in bold.

Return Period	Eleusis			Mandra		
T (years)	1-h	3-h	6-h	1-h	3-h	6-h
2	17.2	27.3	36.0	24.3	38.7	50.9
5	**23.0**	**36.5**	**48.0**	**31.5**	**50.1**	**65.9**
10	27.8	44.1	58.1	37.5	59.6	78.4
20	33.0	52.5	69.0	44.0	70.0	92.1

The threshold runoff is then calculated through the methodology mentioned in Chapter 3.5. The two main factors affecting the threshold runoff value, besides rainfall, are the CN and slope values. The CN AMC-II value is calculated through the CORINE Land Use and the

Hydrological Groups maps, while the slope percentage is directly calculated through the DEM, as shown in Figure 4-19. The Slope raster is first calculated in the native DEM resolution, i.e., 5 m x 5 m, and then disaggregated into the 500 m x 500 m grid resolution.
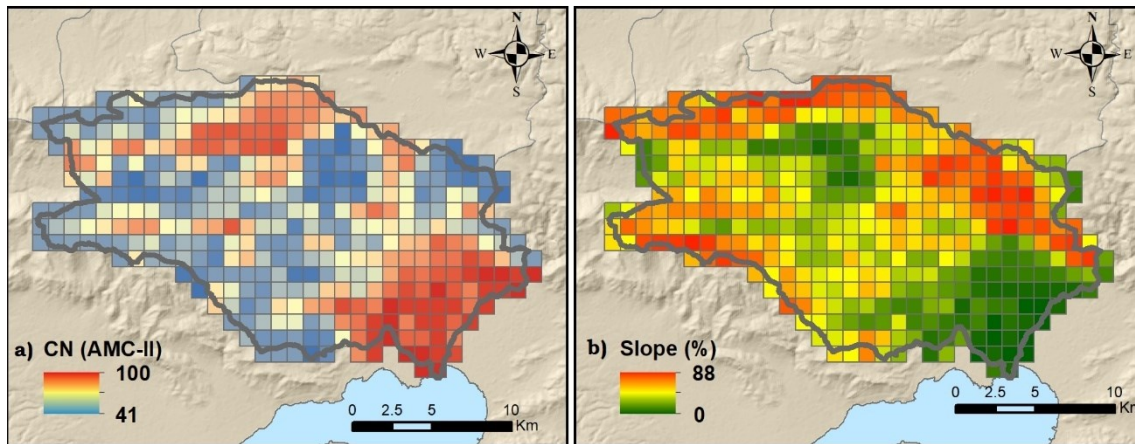

Figure 4-19: Sarantapotamos gridded a) CN values for AMC-II and b) Slope (%)
Source (Bournas and Baltas 2022c)

Besides the CN and slope values, the threshold runoff depends on the soil moisture conditions. In real-time monitoring, the soil moisture is estimated by a hydrological model. In Figure 4-20, the threshold maps are created for the three different rainfall accumulation periods, i.e., 1-, 3- and 6-h, and medium saturated conditions, while in Figure 4-21, for two different soil moisture conditions, medium and saturated for a 3-h accumulated period. In real-time monitoring, each cell's current soil moisture conditions are observed or simulated, resulting in different soil moisture conditions within the same area. When the actual soil moisture is used to derivate the threshold maps, the threshold maps are named the FFG maps, which are used to compare with the forecasted rainfall.

In all generated maps, a low threshold value means that less rainfall is required to reach the threshold, i.e., flooding conditions. Therefore, these maps also act as a flood risk indicator, where a lower threshold indicates a higher risk. Specifically in the study area, low values are observed in the southeast of the Sarantapotamos basin. By comparing the results of these maps with the corresponding CN and Slope maps of Figure 4-19, it is easily observed that areas with high CN values or low Slopes are the ones with the lower threshold. This finding is reasonable since a high CN value denotes a higher runoff potential, i.e., requiring less rainfall to reach flooding conditions. In the generated maps, these areas are located in the southeast area of the basin, mainly the industrial areas, within the Thriasion plain, and in the north, where low slopes indicate the location of the Inoi Valley.
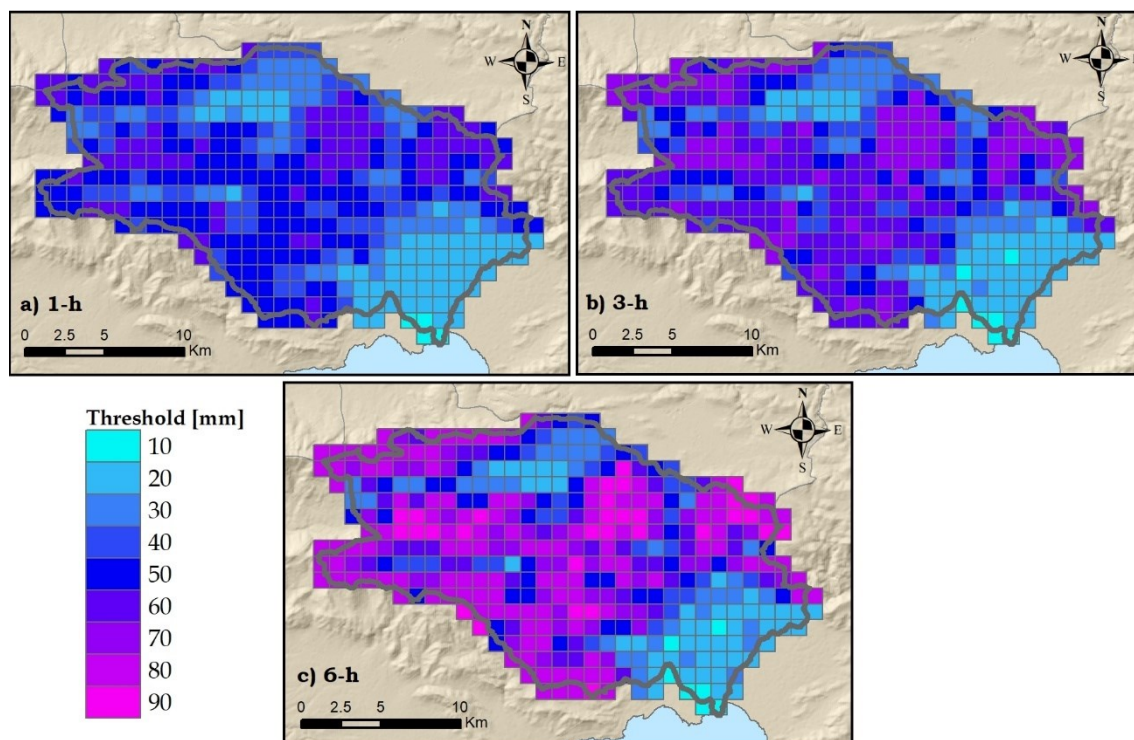
Figure 4-20: Threshold rainfall values for different rainfall duration: a) 1-h, b) 3-h, and c) 6-h.
Source (Bournas and Baltas 2022c)

In Figure 4-20, the difference in the rainfall accumulation period is noticeable in the results. The 6-h maps feature higher precipitation values, indication that more precipitation must fall within six hours than in one or three hours to reach flooding conditions. Within a pre-determined accumulation period, the rainfall rate is considered constant, and therefore, the lower duration limits do not apply in the longer periods. The 6-hour map translates into the phrasing: *"Within the next six hours, if the accumulated rainfall reaches the given threshold, minor flooding will occur."* In the previous statement, it is not known when flooding will occur within the 6-hour periods, but it will eventually occur sometime. Although this includes uncertainty regarding the actual moment within the 6-hour period where flooding may occur, in contrast to the lower durations, it provides an additional lead time and may be more practical for issuing warnings. The 1-h and 3-h maps are generated to provide information in finer temporal resolution, which is helpful for determining the exact moment when the flood will occur. Overall, the products are usually cross-checked with generated maps from previous periods or other derived datasets, e.g., stage monitoring and cameras. In Figure 4-21, the threshold maps are generated for the same accumulation period of 3 hours, but when different soil moisture conditions are met. Specifically, the AMC-II and AMC-III conditions are shown, referring to medium (50%) and wet (100%) soil moisture conditions, respectively. Here, the differences in the threshold values are noticeable since the threshold values are reduced dramatically when saturated conditions are present. This

change indicates that the flooding risk in a designated grid is highly correlated to the soil moisture conditions, which dictate the amount of rainfall subtracted by the soil. This change is noticeable in the grids in the west and northwest of the basin, whereas, in the southeast, the threshold values do not change as dramatically. This fact is attributed to the values of the base CNs, i.e., the medium saturation CN-II values displayed in Figure 4-19. When the grid's CN value is high, indicating urban and impervious areas, the change between dry and saturated conditions does not dramatically change the CN value since an impervious area will have a high dry or wet runoff potential. On the other hand, areas with CN values close to 50, which are found in rural areas, feature the most significant difference between dry and wet conditions, as illustrated in the CN adjustment figure, Figure 3-12, found in section 3.4.4.
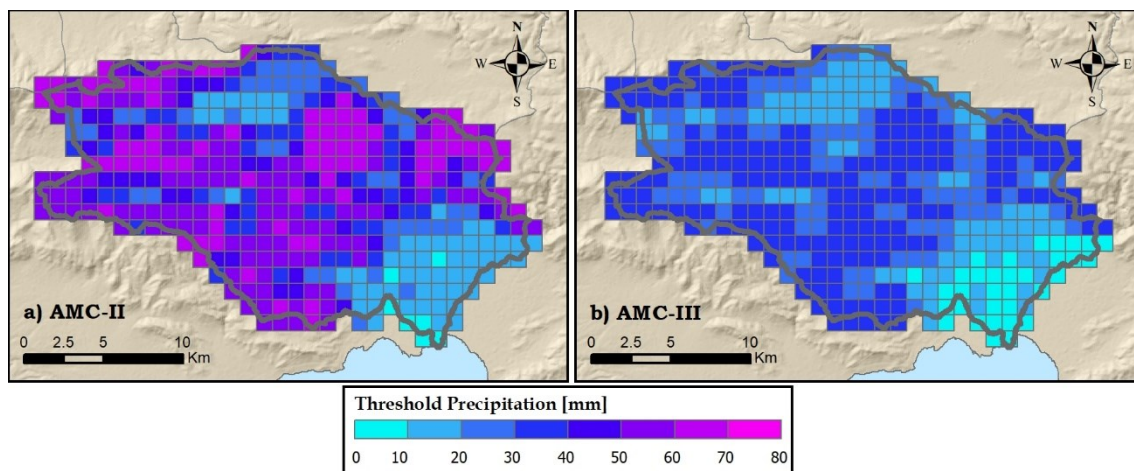
Figure 4-21: Threshold rainfall for a 3-h accumulation period for a) ACM-II and b) AMC-III conditions; Source (Bournas and Baltas 2022c)

Finally, the threshold calculations are performed for each of the three rainfall accumulation periods and soil moisture conditions, i.e., 1-, 3-, 6-h, and the AMC-I, II, and III conditions, and the results are shown in boxplots in Figure 4-22. As mentioned before, the higher variability is calculated when the AMC-I conditions are observed since the variability of the CN values of the grids is at its highest. When wet conditions are found, the CN values tend to limit towards the upper limit, i.e., the 100 value, resulting in less variability across the field. In the specific study area, in all precipitation conditions, an approximately 60 mm difference, 50 to 110 mm, between the lowest and highest threshold value is found when dry conditions are met, whereas this changes to 30 mm and 20 mm for the AMC-II and AMC-III conditions. This result underlines that the uncertainty involved in the threshold runoff, and respectively to the FFG value, is much higher when low soil moisture conditions are present.
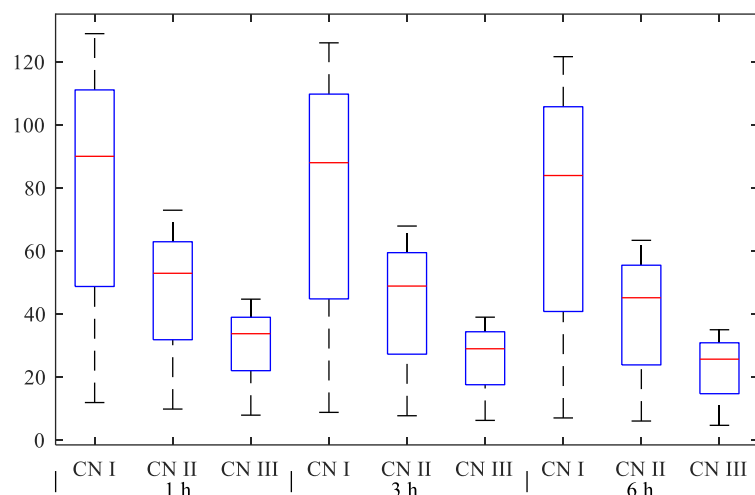
Figure 4-22: Boxplot of threshold runoff values for different soil moisture conditions for Sarantapotamos Basin; Source (Bournas and Baltas 2022c)

Finally, this behavior is met in all accumulative precipitation periods, with the median value decreasing when the accumulation period is increased. Specifically, the median threshold value of all grids drops as wet conditions are met, but not at the same rate. For the 3-h duration, the median threshold value in dry conditions is 75 mm, while for normal and wet conditions, the mean value drops to 40 and 22 mm. Although the results presented are basin-specific, they capture the sensitivity of the threshold runoff to the soil moisture conditions and, consequently, to the calculated FFG values.

Finally, the threshold maps for the entire Attica Region are also generated using the 22 IDF stations featured in Figure 2-9 to calculate the 5-year rainfall ARI. Figure 5-21 shows the threshold runoff in panels a), b), and c) for the three accumulation periods in AMC-II conditions, while panel d) features the threshold for the 3-h period but in AMC-III conditions. The center of Athens, which consists of highly urbanized areas, features a low rainfall threshold with little variability among the soil moisture conditions used since any change between each case is noticeable in rural areas, where the CN varies significantly between the AMC conditions. Finally, comparing panels b) and d), where the same period is illustrated albeit for different soil moisture conditions, it is slightly seen than in the last case, the thresholds are much lower, as the 1-h duration, which indicates that it is much easier to reach flood conditions. Finally, the distribution of the threshold values for each case is shown through the boxplot plots of the same results, shown in Figure 5-24. Specifically, the mean threshold for medium saturated conditions is approximately 18 mm, 20 mm, and 23 mm for 1-, 3- and 6-h durations, respectively, while when fully saturated conditions are present, it is seen that the 3-h threshold mean value not only drops from 20 mm to 15 mm but also the std. Deviation minimizes.
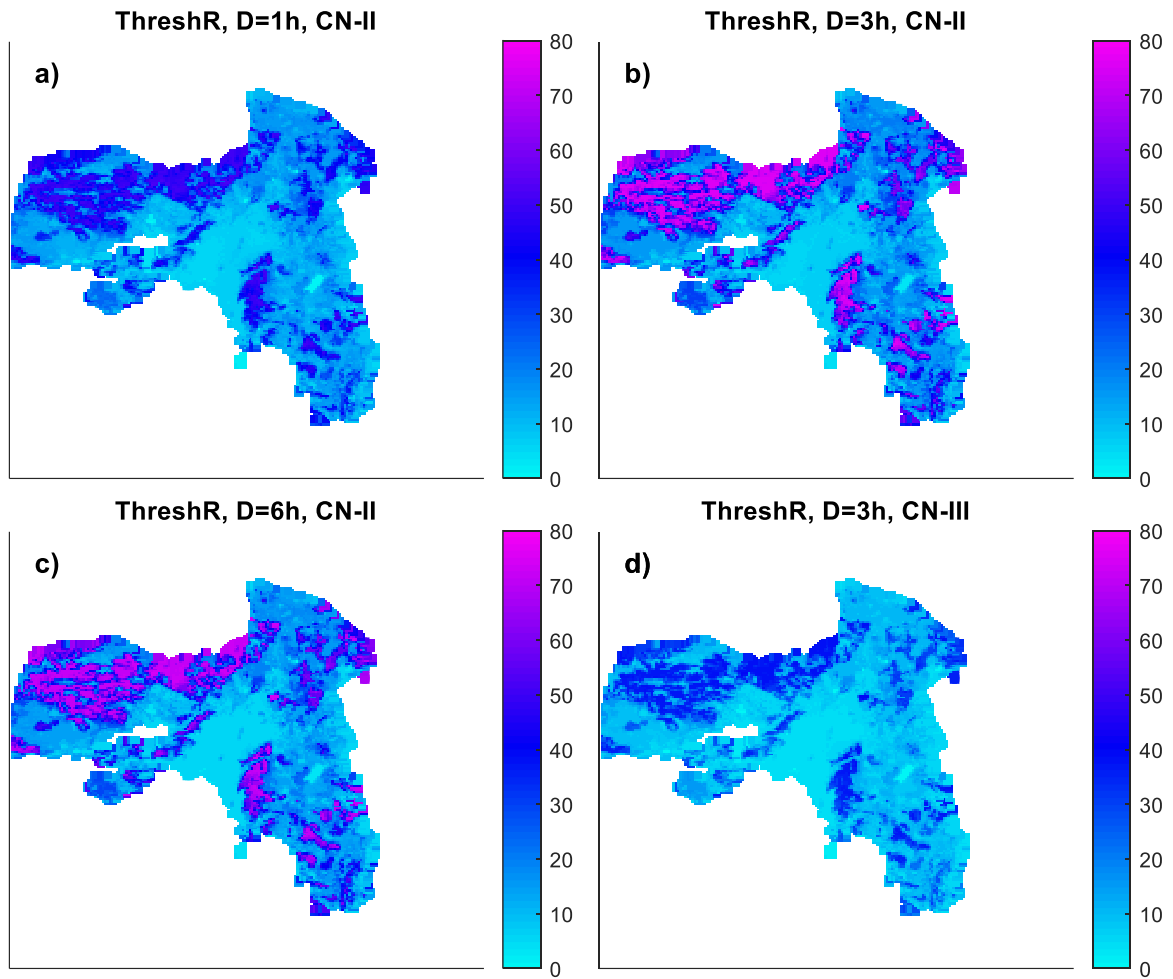
Figure 4-23: Attica region threshold rainfall under four soil moisture conditions, a) 1-h, CN II, b) 3-h CN-II, c) 6-h CN-II, d) 3-h CN-III a 3-h
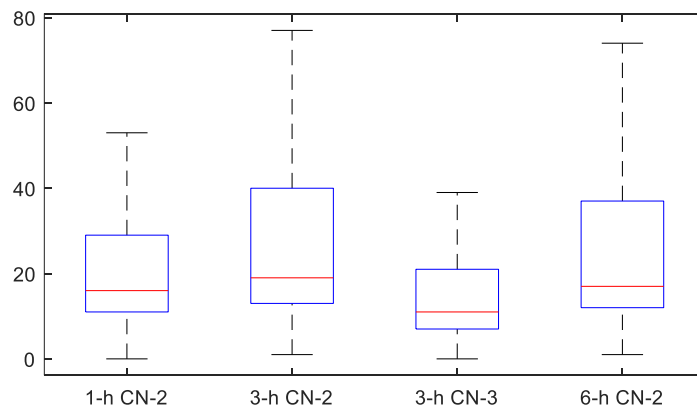

Figure 4-24: Boxplot of threshold runoff values and different soil moisture conditions for the Attica Region

4.3.2 GFFG for selected rainfall events

In this section, the GFFG model is applied to historical events. The application of the GFFG model is performed using a 500 m x 500 m resolution in all three suggested accumulation periods of 1-, 3-, and 6-h. The rainfall estimates for each event are provided after applying the suggested Z-R equation, $Z=321R^{1.53}$ eq. (5.2). For each case, two series of maps are presented. The first consists of the rainfall grid in a time-consecutive order, while the second consists of the result of the GFFG system, i.e., the cells flagged for flooding in each timestep. The flooded cells maps are highlighted by comparing the generated GFFG map with the accumulated rainfall map of the same accumulation period. Cells with a rainfall height higher than their corresponding FFG value are flagged as flooded cells.

Concerning the timesteps, each instance refers to the timestamp shown on each image using the Eastern European Time Zone (UTC+2). For instance, when the 1-h duration results are shown, the timestamp with valid time 13:00 refers to the accumulated rainfall height that was measured between 12:00 and 13:00. In a similar pattern, the 3-h duration products of the same valid timestamp refer to the accumulated period of 10:00-13:00. The benefit of utilizing the longer accumulated periods, lies on the fact that longer lead times are provided. In this application, the observed precipitation by the Rainscanner is used as the forecasted value. In real-time conditions, a 6-h precipitation forecast is expected to feature more uncertainty than the 1-h and 3-h forecasts. To better compare the results, only the results of the 1-h and 3-h forecasts are used since most rainfall events featured a total duration of up to 10 hours, making the 6-hour forecasts impractical. Moreover, after analysis of multiple events, long-range forecasts are not feasible due to the storm's velocities and the Rainscanner range. More extended duration forecasts require more distanced observations to be feasible.

Two different spatial extents are shown in the application area, as previously. The first is the Sarantapotamos basin, and the second is the entire extent of the Attica Region. The first provides better detail of the rainfall and flooded cells results, while the latter encapsulates the application of the system on a broader area. However, caution should be paid to the results for the Attica region since, as mentioned, the effects of the sewer system, found in highly urbanized areas such as the Athens city fabric, have not been examined. Finally, three events are presented, which featured a high amount of rainfall that triggered the GFFG system.

Event 50

The first event examined is event E50, which occurred on 12-06-2021. First, the results for the entire Attica region are presented in Figure 4-25, which shows the 3-hour rainfall fields and the respective flooded cells per timestep. The picture scale is inadequate to extract the high-resolution results but highlights the rainfall's spatial characteristics. Specifically, the

featured event is characterized by its low footprint and high rainfall intensities. The featured event is a convective-based event where visible storm cores can be determined, which results in numerous areas where flooding is expected, especially in high-rainfall areas, at different timesteps. First, flooding is expected in the northern regions of Attica, i.e., the foothills of Penteli mountain, while in the later phases, the storm focuses on west Attica.
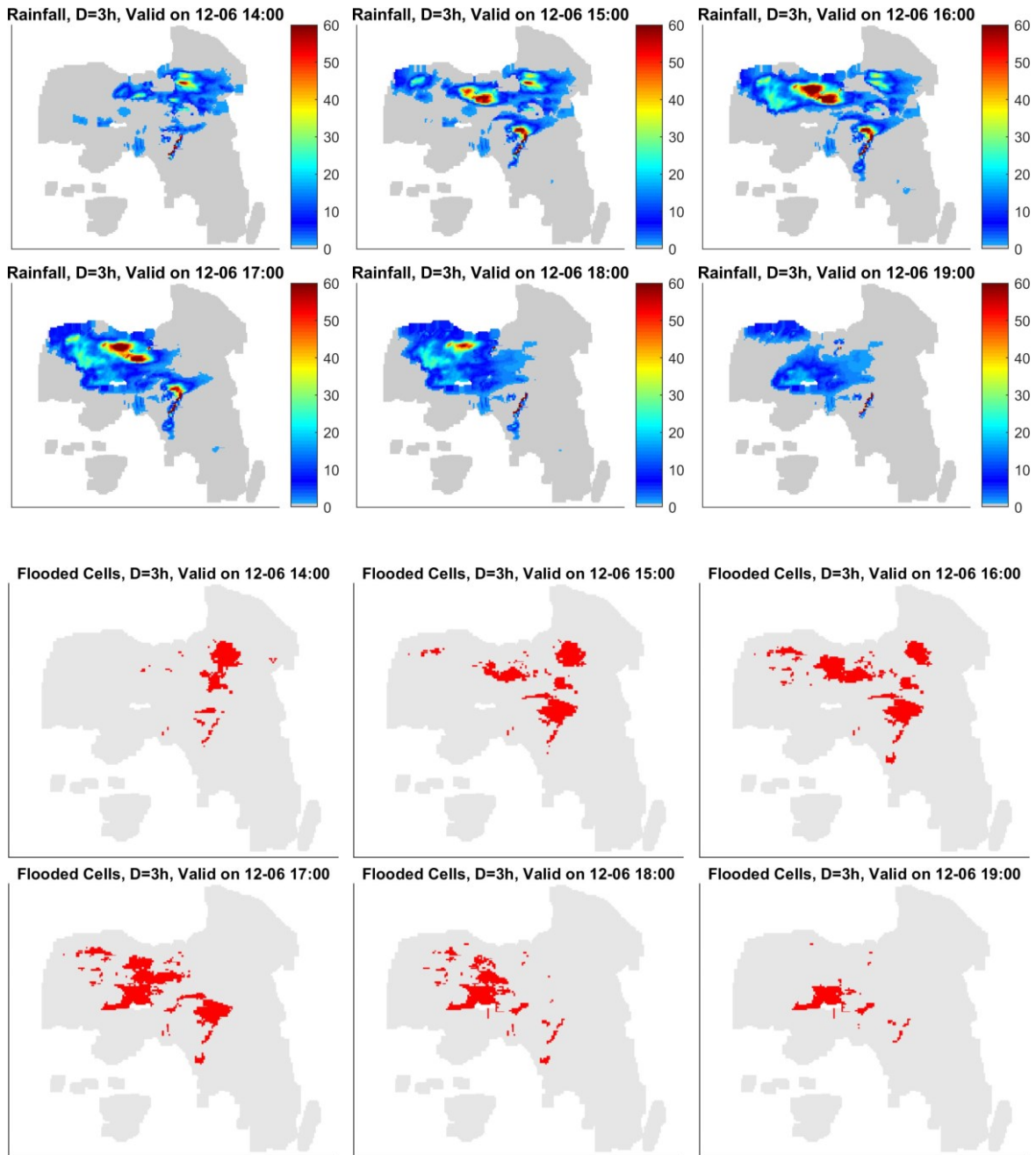

Figure 4-25: 3-hour Gridded Rainfall (above) and Flooded Cells (below with red), valid per timestamp, Event 50, Attica Region.

Figure 4-26 shows the Sarantapotamos precipitation grid and flooded cells for the 1-h rainfall, while Figure 4-27 shows the images of the 3-hour accumulated period.
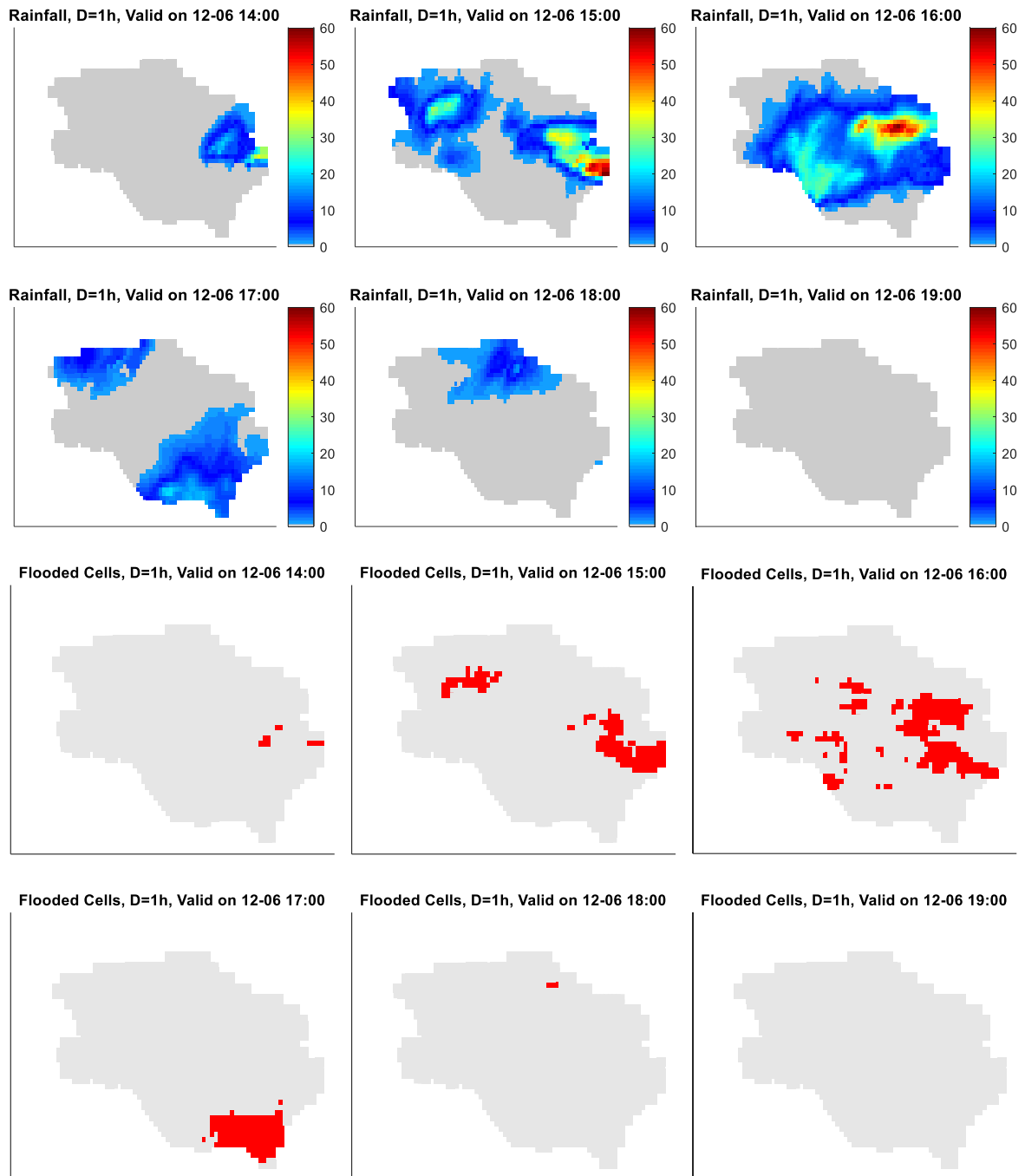
Figure 4-26: 1-hour Gridded Rainfall, valid per timestamp, Event 50, Sarantapotamos subbasin,.
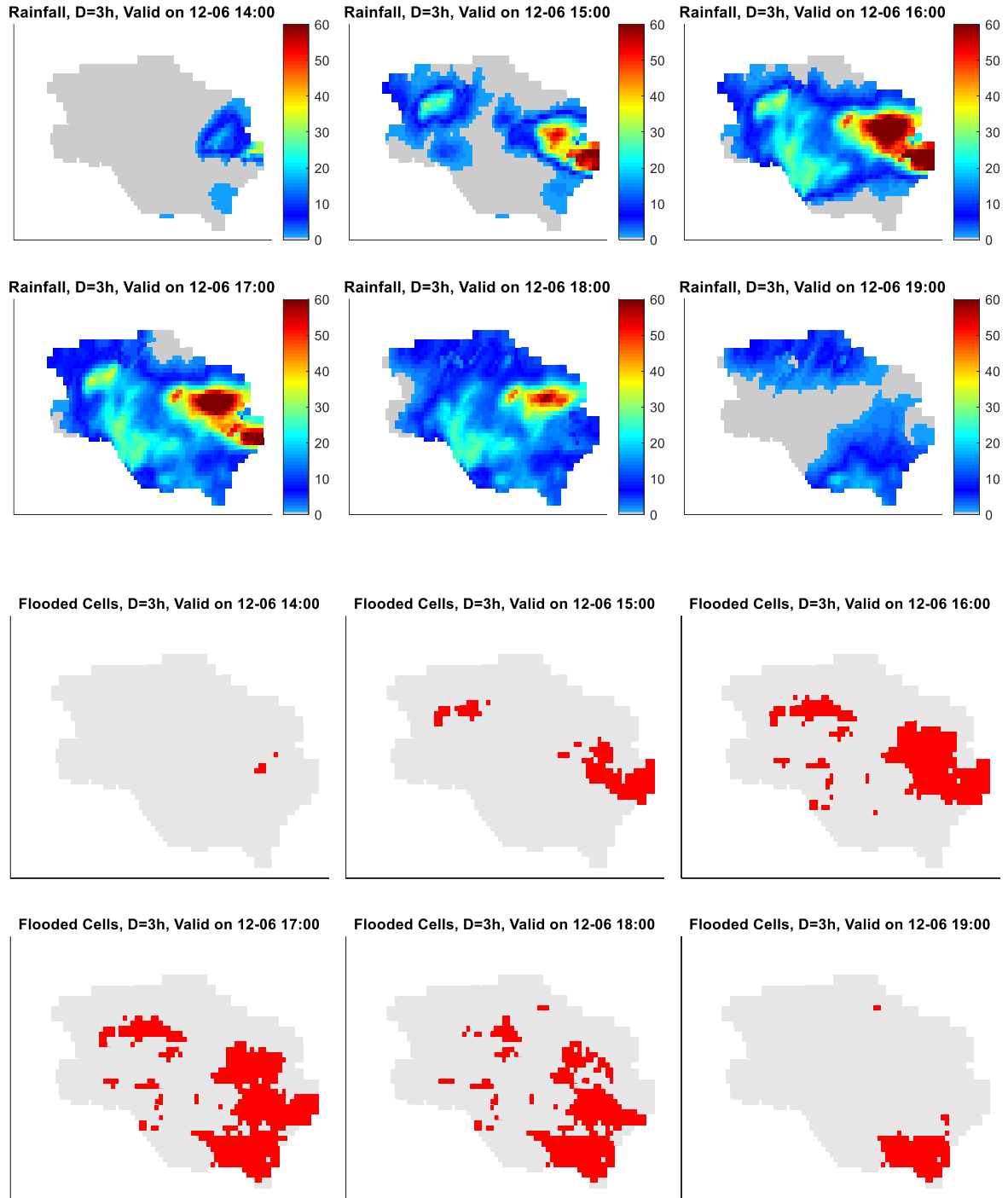
Figure 4-27: 1-hour Flooded Cells (red), valid per timestamp, Event 50, Sarantapotamos subbasin.

The difference between the accumulation periods is visible in the rainfall height and extent of each timestamp feature. The 3-h features higher and more expanded results. The benefit of the 3-h products lies in the fact that it is possible to detect flooding earlier. For instance, observing the 1-hour precipitation maps, the majority of rainfall occurs at the valid time 15:00, meaning between 14:00 and 15:00. In the 1-hour products, the flooded cells are

reported in different timesteps, i.e., first, the western part is flagged for flood, for timesteps 15:00 and 16:00, while at timestep 17:00 only the south part. On the other hand, the 3-hour product shows the same areas being flooded in other timesteps. Specifically, the 16:00 timestep includes rainfall from 14:00 to 16:00, while the 17:00 timestep is the 15:00 to 17:00 time period, where most rainfall occurs. Therefore, the 17:00 timestep features the majority of flooded cells, which is the sum of the flooded cells of the 1-hour product for the 15:00, 16:00, and 17:00 timesteps.

Finally, in Figure 4-28, the total cells flagged for flooding throughout the GFFG system for the different accumulated periods are shown for both the Sarantapotamos and Attica Region, respectively. What is shown is that all accumulation period products end with the flagging of almost the same cells, apart from some slight differences in the longer periods, where more cells are found to feature flooding. The main difference lies in the available lead time each product provides, given the quality of the forecast matching the actual rainfall. Nevertheless, using lower accumulation periods is useful for identifying the exact time when the majority of rainfall occurred, which, in this case, occurred between 15:00 and 17:00.
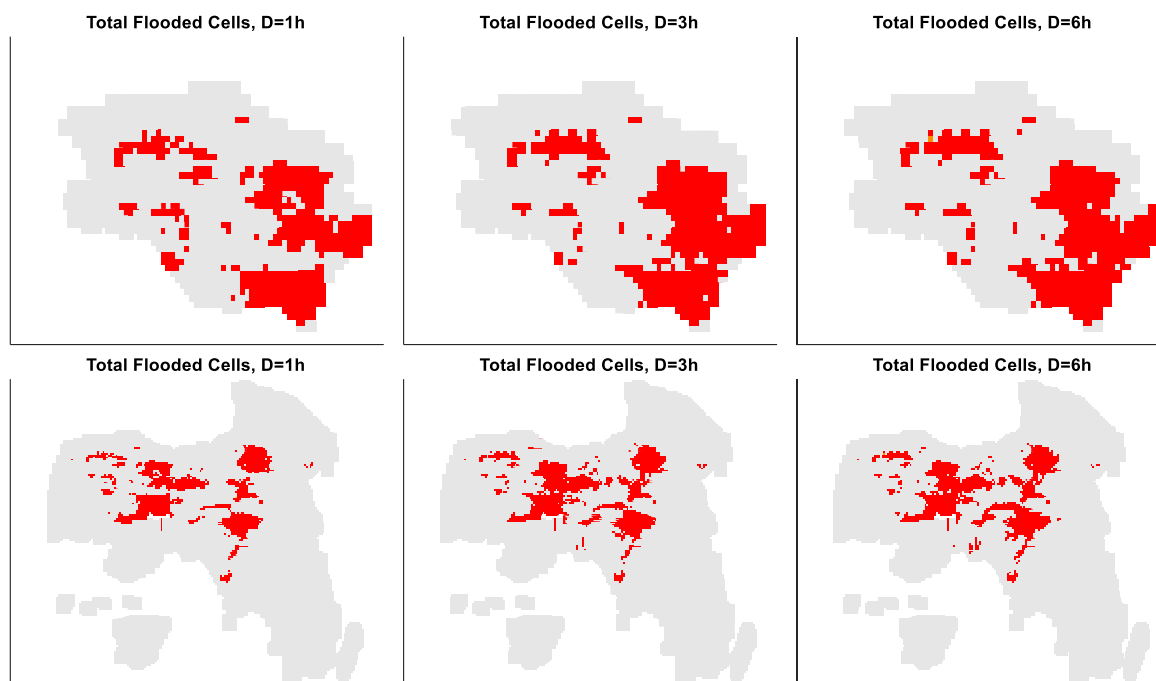
Figure 4-28: Total Cells flagged for flood based on the GFFG system in Event 50, at Sarantapotamos basin and Attica Region.

Event 31

The second event featured is event E31, which occurred on 01-06-2020. Figure 4-29 shows the 3-hour rainfall fields and the estimated flooded cells for the Attica region. The featured event is characterized by its low footprint and high rainfall intensities. The event is also convective-based, where storm cores are highly visible. First, flooding is estimated in the northern regions of Attica, i.e., the foothills of Penteli mountain, while in the later phases, the storm focuses on west Attica. Compared to E50, the intensity is much lower, yet the system is triggered mainly in high urban areas.
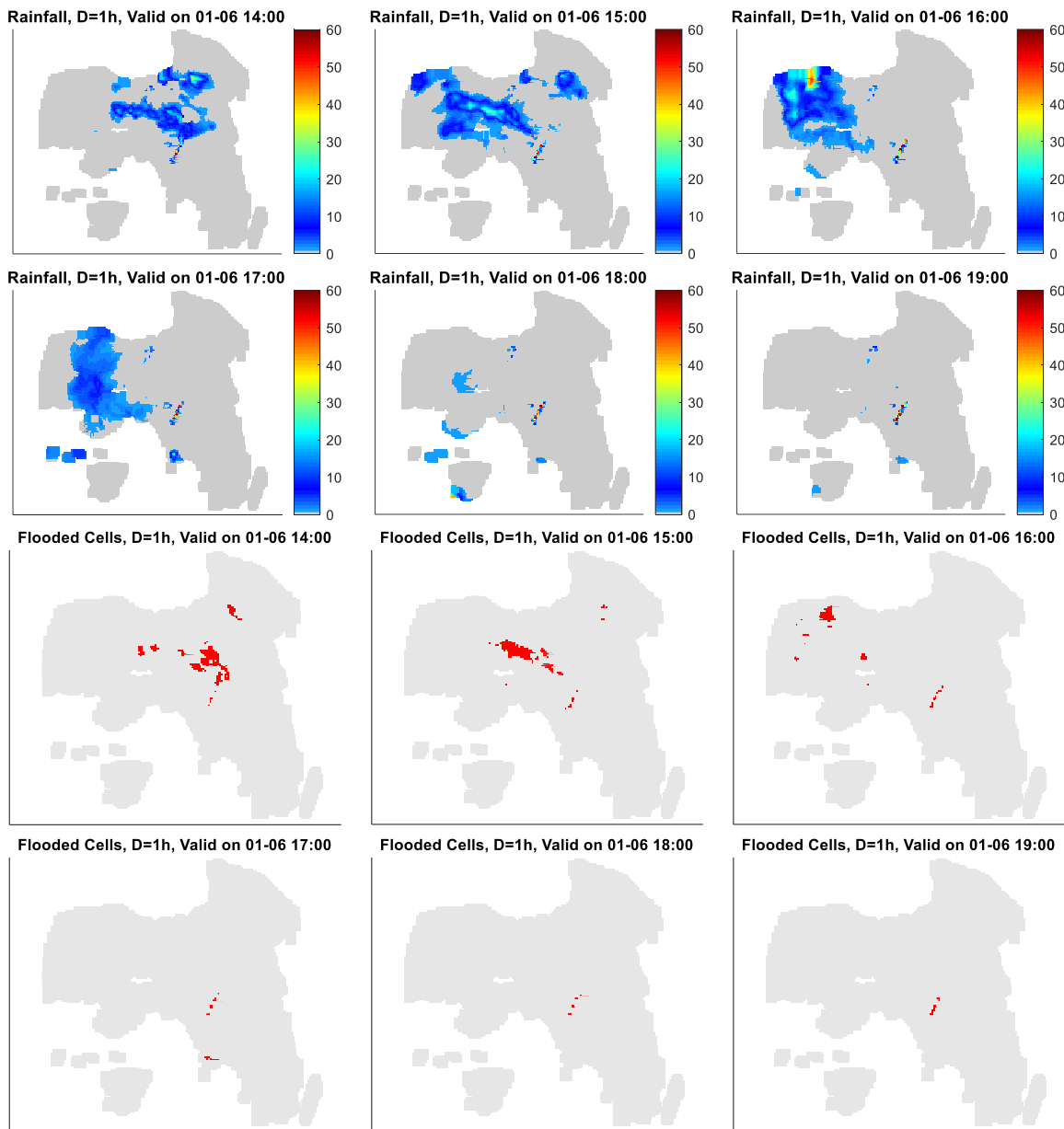
Figure 4-29: 3-hour Gridded Rainfall and Flooded Cells Result, valid per timestamp, Event 31, at Attica Region. Red cells denote cells in which rainfall is over the FFG value.

Figure 4-30 shows the Sarantapotamos precipitation grid and flooded cells for the 3-h rainfall. The southwest areas, where urban areas are found, are flagged for flooding, and the northern area, where increased rainfall occurs. The main difference between the E31 and E50 events lies in the soil moisture conditions, where 70% are set for event 50, whereas near-dry conditions are set for event E31, considering the rainfall that occurred five days before the event, as shown in Table 4-6.
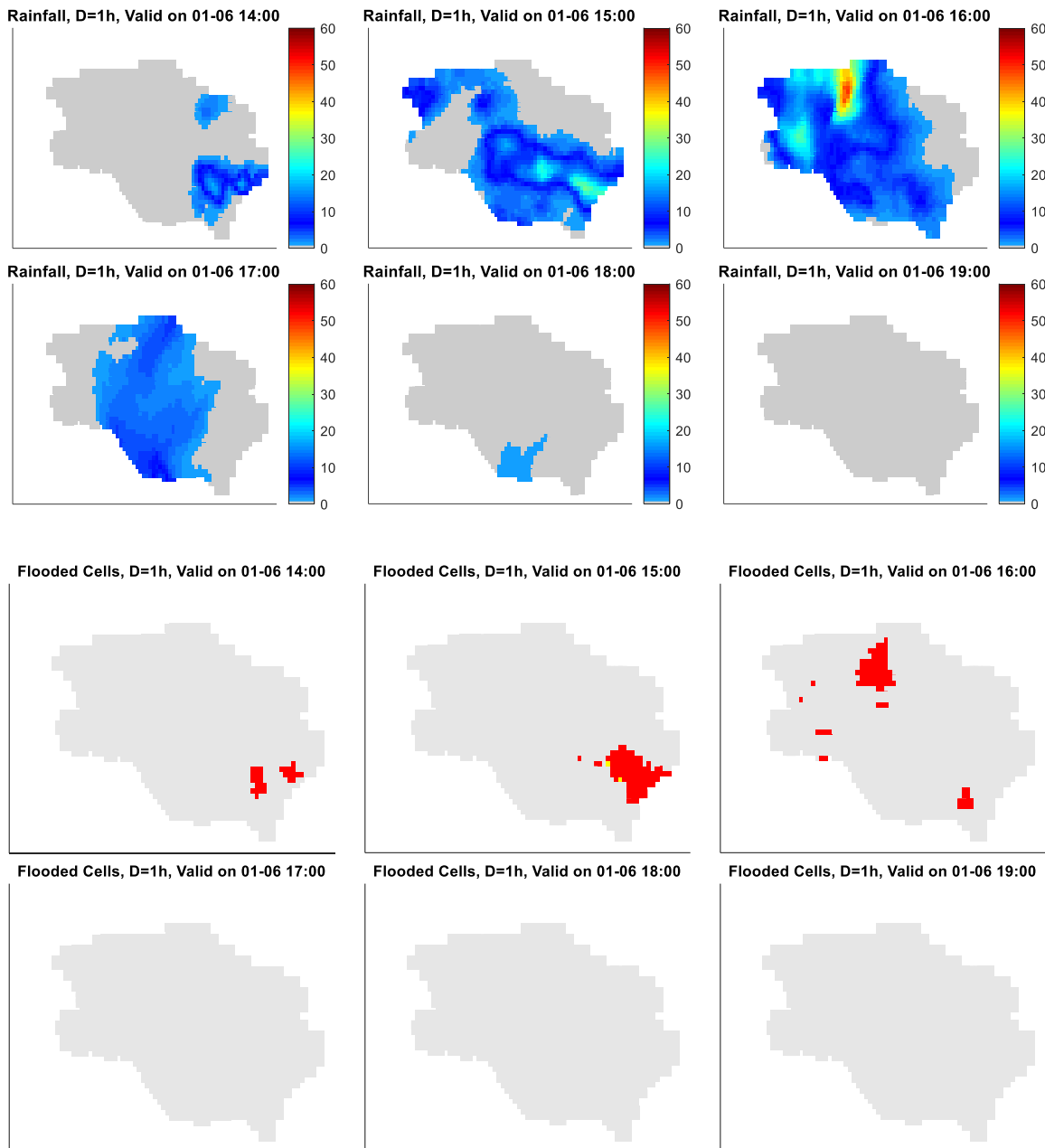
Figure 4-30: 1-hour Gridded Rainfall and Flooded Cells Result, valid per timestamp, Event 31, at Sarantapotamos basin. Red cells denote cells in which rainfall is over the FFG value.
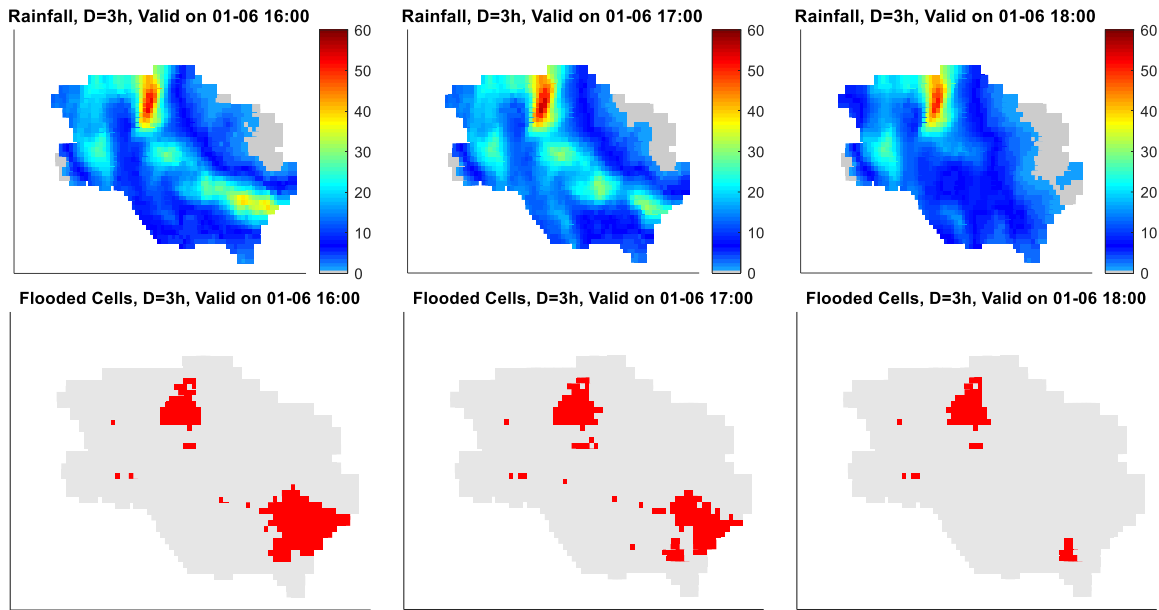
Figure 4-311-hour Gridded Rainfall and Flooded Cells Result, valid per timestamp, Event 31, at Sarantapotamos basin. Red cells denote cells in which rainfall is over the FFG value.

Event 21

The third event examined is event E21, which occurred on 25-11-2019. Figure 4-29 shows the 3-hour rainfall fields and the respected flooded cells for the Attica region. The featured event is characterized by its large footprint and medium-sized rainfall intensities, denoting a stratiform-based event. Nevertheless, since the rainfall event occurred in November and a considerable amount of rainfall occurred the previous days, as shown in Table 4-6, the soil moisture conditions were set to near saturation, i.e., 90, which resulted in high runoff potential. The flooded cells follow the system's trajectory, featuring a west-to-east direction. Although a high number of cells are flagged for flood in the specific event, what is interesting is the progress of flooding, which shows that the system is useful for identifying the timing of when each area is expected to flood or is near flooding conditions.
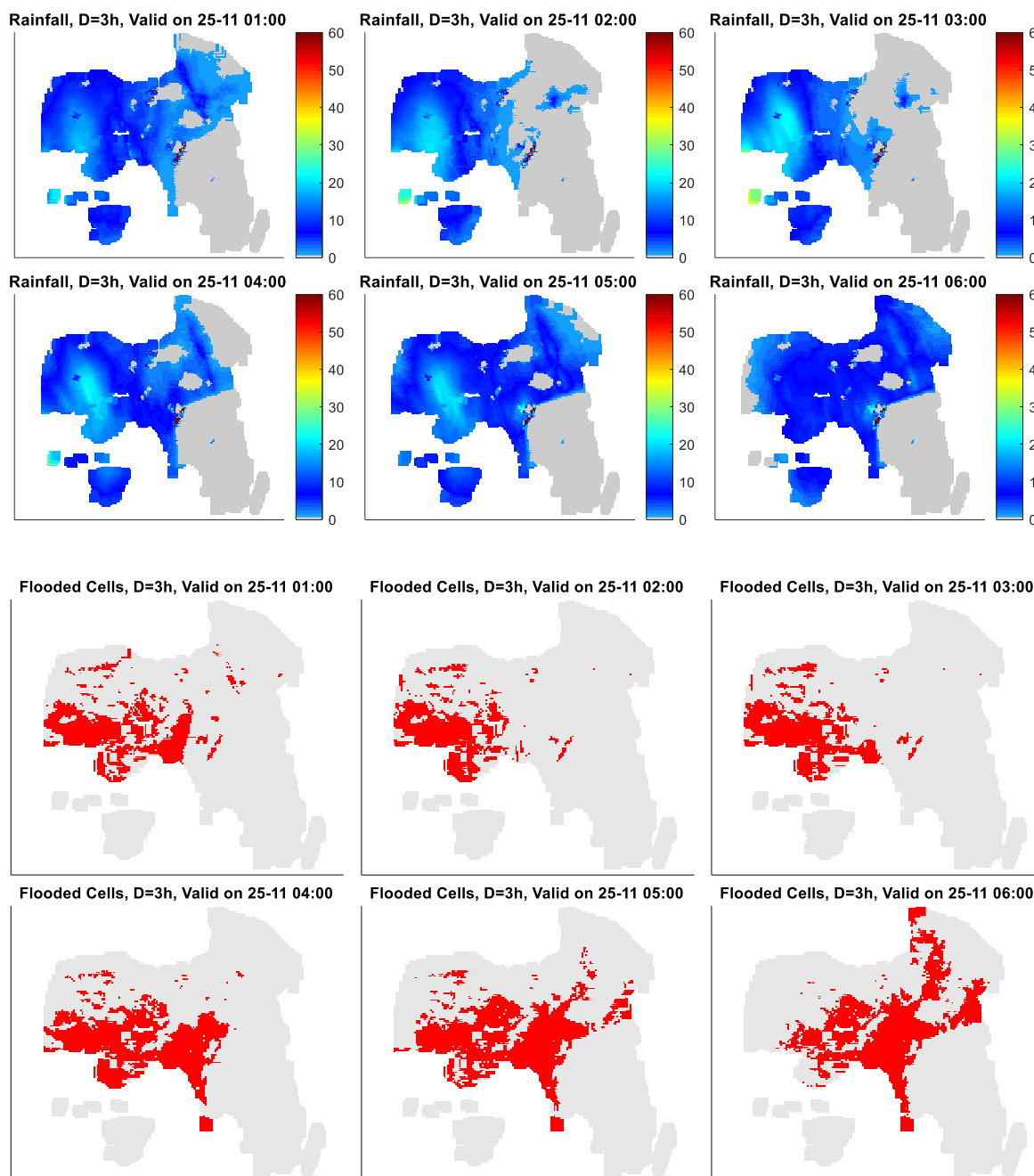
Figure 4-32: 1-hour Gridded Rainfall and Flooded Cells Result, valid per timestamp: Event 31, at Sarantapotamos basin. Red cells denote cells in which rainfall is over the FFG value.

Sensitivity Analysis

In this section, a sensitivity analysis is performed on the generated results. Specifically, the parameters set to the GFFG system, such as the state of the soil moisture conditions and the threshold runoff, are altered. The results of the analysis are presented for the Sarantapotamos basin. In Figure 4-33, the impact of different soil moisture conditions is examined, where the difference in each accumulated period when 70% and 90% soil

moisture are used, while in Figure 4-34, the effect of the rainfall return period used to calculate the threshold runoff is observed, by applying a two- and ten- year return periods.
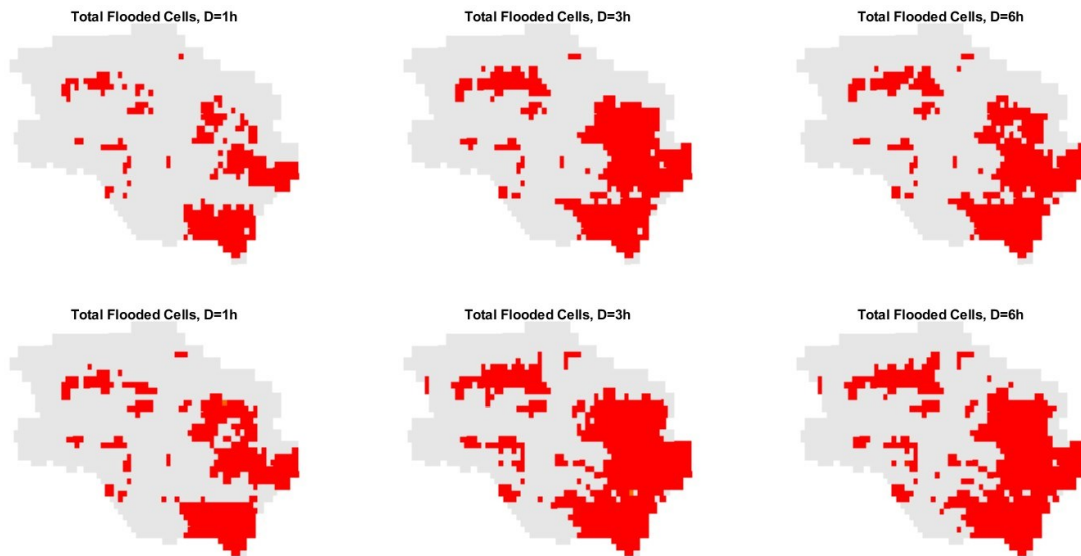
Figure 4-33: Total Flooded Cells difference at Event 50, when a different Soil Moisture percentage is used for each rainfall duration; a) first row 70% Soil moisture, b) second row 90% Soil moisture

As expected, the 90% soil moisture conditions resulted in more cells being flagged for flooding than the 70% case in all durations. However, the difference is not excessive, which is attributed to the fact that if the rainfall height is way above the threshold, as in the case of the featured event, the differences are not noticeable. The same applies to the change of the rainfall return period, since whether using a 2-,5- or 10-year return period, the total flooded cells are almost the same when observed in the basin-wide perspective. The higher the return period, the fewer cells are flagged for flooding since a higher threshold runoff is calculated, meaning that the thresholds are more conservative, aiming for alerts of high return period storms.
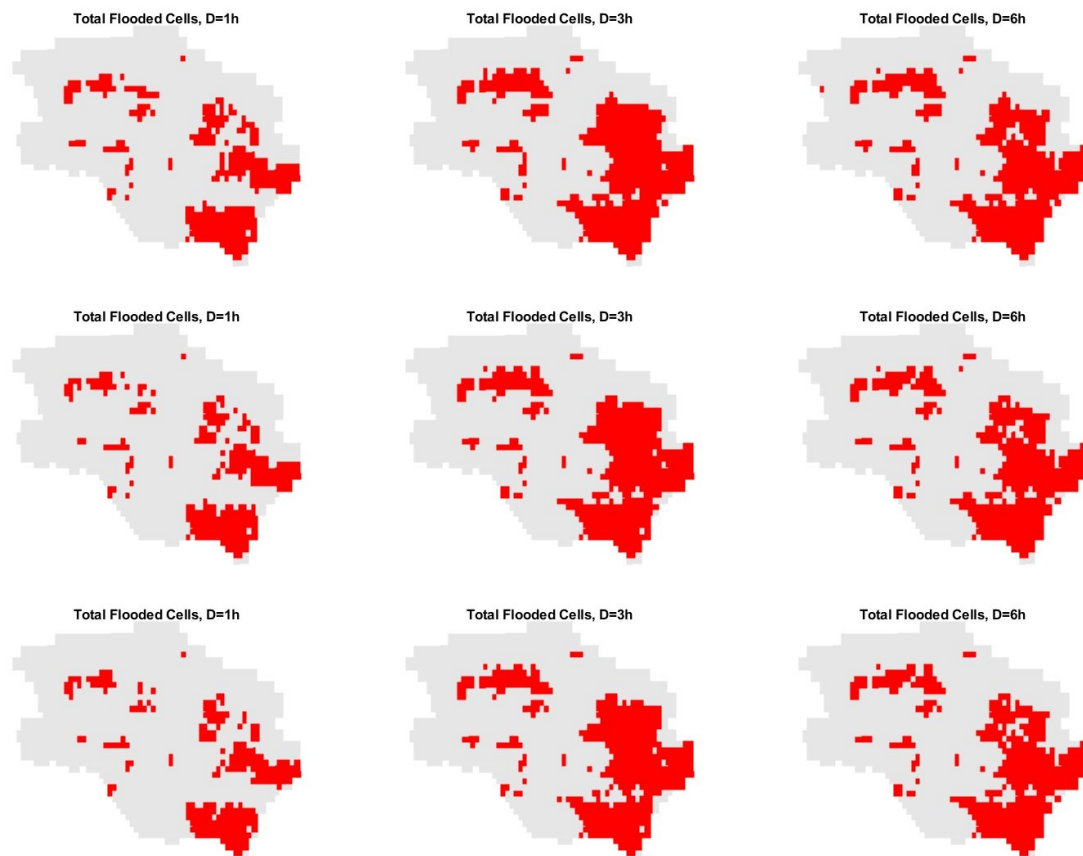
Figure 4-34: Total Flooded Cells difference in Event 50, at Sarantapotamos basin, when a different Period for the estimation of the Threshold runoff is used in each case; rows denote different return periods of 2, 5, and 10 years, while columns to the different duration products of, 1-,3-6h,

Results Discussion

In Figure 4-35, the results of the system on the studied events where the rainfall-runoff simulations were performed, shown in Table 4-6, are presented for all accumulation durations for the Attica region. These maps show that most cells flagged for flooding are usually found in urban areas, specifically in the Athens metropolitan area. However, as discussed earlier, the system does not include the effect of sewer systems, making the cells flagged for flood, not resulting in flooding. Nevertheless, the system was able to identify areas where increased rainfall height would cause potential flood damages, making it a useful tool for providing real-time estimations of flood threat.

Concerning the effect of the system parameters on the results, most of them have an effect when the rainfall height expected is just below or over the calculated threshold. When rainfall is way above the limit, flooding is nevertheless expected. What is evident is that the effect of soil moisture is more important than the set return period for the threshold runoff calculation. This fact is shown when event E21 is examined since although lower rainfall heights were observed, the total number of cells flagged for flooding was high because the

soil moisture conditions were set to near-wet, considering the previous five days' accumulated rainfall.
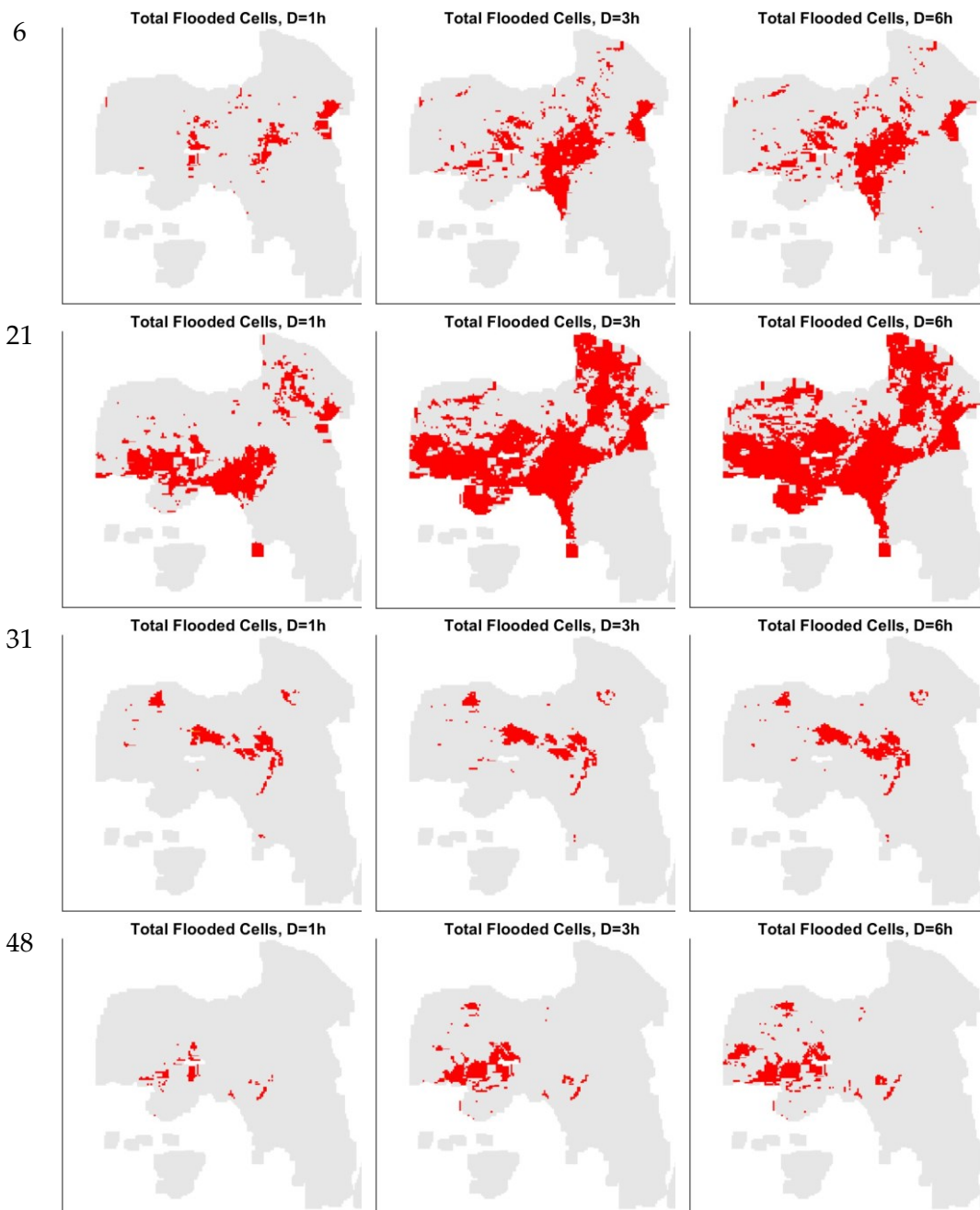

Figure 4-35: Total cells flagged for flood (red cells) for a series of examined events and different accumulation period products; first column 1-h, second column 3-h, and third column 6-h.
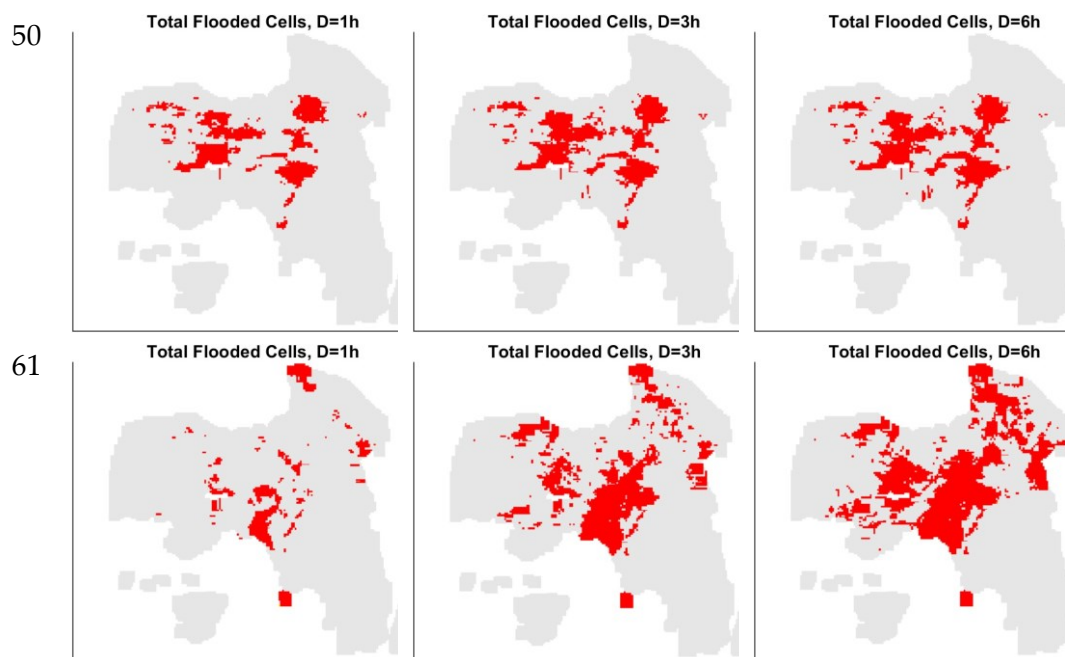
50

61

Figure 4-35 (*continued*)

Another finding after using the GFFG system is that, in most cases, the selected accumulation periods displayed similar results regarding the total cells that flooded. Exceptions are seen in events E6, E48, and E61, where the 3- and 6-h durations resulted in a significantly higher number of cells flooded than in the 1-h case. These cases are attributed not only to the fact that the 1-hour thresholds were more strict than the 3-hour thresholds but also to the rainfall height being just below or over the estimated thresholds. This highlights the need to use multiple-duration products since a better understanding and assessment of the flood risk can be made. Finally, the flood risk threat can be used instead of the deterministic flood or no flood result, where the deficit between the rainfall height and the threshold value is calculated to measure how severe the flood is expected. In this case, a proper decision-making strategy should be applied to determine whether a warning should be issued.

4.4   Storm Trajectory Analysis

4.4.1   Cell Identification Results

The storm tracking algorithm described in Chapter 3.6 and explicitly shown in Figure 3-17 is applied in this section. The first element of the algorithm is the cell identification process. The algorithm is designed to use different thresholds and ways to make the identification. Specifically, reflectivity thresholds are used to define the cells forming a storm entity, followed by either a polygon line or a fitting ellipse to define the storm and calculate its statistics, such as its center and area. Figure 4-36 shows a specific timeframe, where the difference in the storm's size between the three thresholds used, 25, 30, and 35 dBZ, is shown

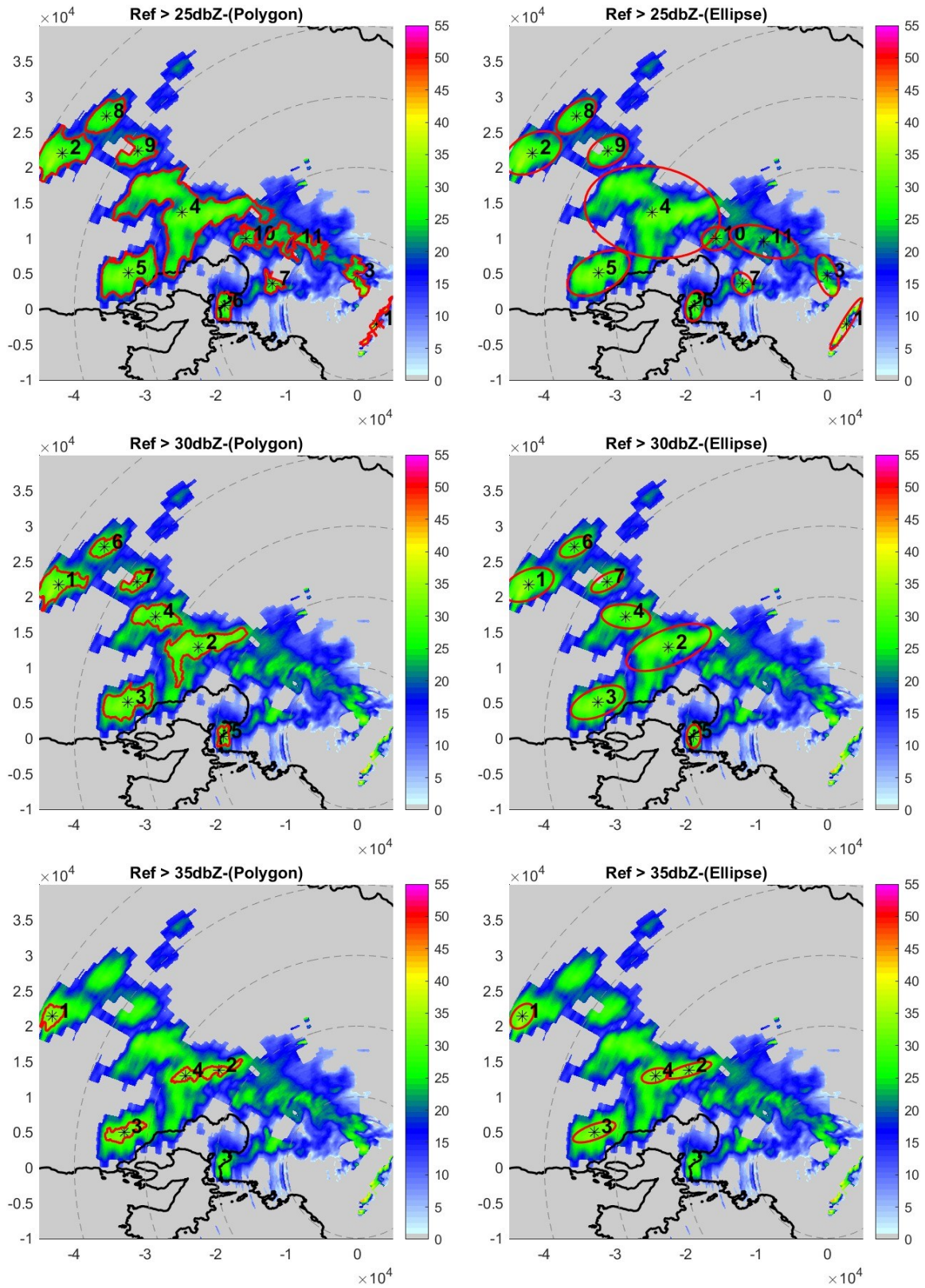in each row, while the result of applying a polygon or a fitting ellipse is shown in each column.

Figure 4-36: Results of the cell algorithm when a different reflectivity threshold is used; 25-, 30- and 35 dBZ shown in each row, and when a polygon or fitting ellipse is used to form the boundaries.

As shown, fewer and smaller cores are identified when the threshold is higher. On the other hand, a lower threshold leads to a better estimation of the cloud's boundaries. In each column of Figure 4-36, the difference between using a polygon or an ellipse is highlighted. A fitting ellipse is a mathematical relationship, making it better for correlation analysis since its eccentricity and rotation can be used in the cell matchmaking algorithm. However, when used with a low threshold, the fitting ellipse lacks the needed accuracy, especially with larger formed clouds. The selected application shows that the optimal use in each case is a fitting ellipse with a 30 dBZ threshold for identifying the cell core, while the 25 dBZ Threshold with a polygon to define the actual boundary of the cloud. Therefore, the 30 dBZ and fitting ellipse are used to identify the core centroids and tracking characteristics, while the 25 dBZ threshold illustrates the storm's footprint.

4.4.2   Cell Tracking Results

Following the identification process, the matchmaking process takes place. In Figure 4-37, six consecutive time frames are shown using a 2-minute timestep equal to the Rainscanner temporal resolution. In the featured images, the 30 dBZ threshold and the fitted ellipse are used to identify the cells illustrated as red when they represent the current time frame and with dashed black lines when they represent the previous time frame. The same color coding applies to the centroids of each cell. The matchmaking process in the first four frames is very successful since the clouds do not change dramatically in only two minutes, making them easier to associate. The last two frames feature slight variability regarding the matchmaking. Specifically, in the 15:48 and 15:50 time frames, a merging occurs, where two past cells are merged to form one larger. Although the merge is acceptable in the 15:48 frame, in the 15:50 time frame, the larger ellipse is not optimal since the cloud features an inverted "V" shape. In order to avoid such matchmaking, it is suggested that more frames be used to define a single image. This results in a coarser temporal resolution, which is calculated with the merge of multiple 2-minute frames. The frames are merged by calculating the average value of the consecutive images. For instance, if two-time frames are merged, the 4-min reflectivity fields are used to perform the matchmaking. In that case, a timestamp of 15:44 would consist of the average reflectivity measured in timeframes 15:42 and 15:44. This results in a more uniform image, where a storm cloud can be easier identified and not divided into multiple smaller clouds, which emphasizes the main storm clouds. Using a coarser resolution is also advantageous since it provides better approximation in nowcasting algorithms, and it generally fits better with other forms of data, such as rain gauges, concerning the used scale. However, it should be mentioned that in such cases, the threshold should be reassessed since when consecutive images are merged, the reflectivity values are normalized, with the minimum and maximum values reduced. Nevertheless, the 30 dBZ threshold used in this application provided acceptable results.
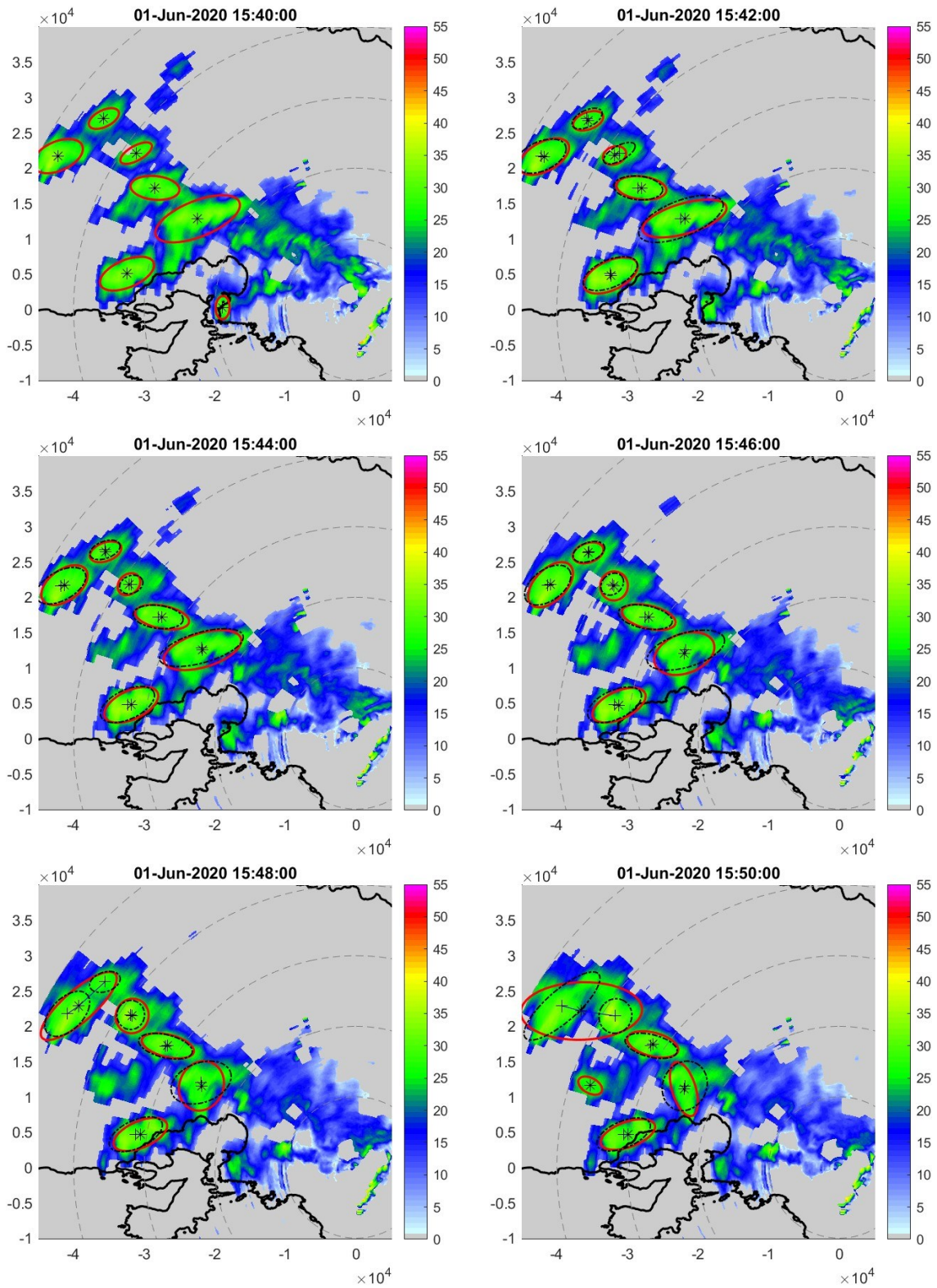
Figure 4-37: The matchmaking procedure between six-time frames with a 2-minute step

In Figure 4-38, the 10-minute reflectivity fields, derived from merging five timeframes, are used with a 2-minute tracking resolution, similar to the tracking performed in Figure 4-37.

145

For simplicity of space, four-time frames are shown, from 15:44 to 15:50. The main differences are highlighted in the last two frames, the 15:48 and 15:50, where a merge is formed from two nearby clouds, where in the 2-min fields, this is not exhibited. Furthermore, in the 15:50 frame, a larger cloud is formed in the 10-min resolution, whereas in the 2-min resolution, they are shown as different cloud cells. In the time frame 15:50, the cells are formed more consistently, making a better cell identification. Specifically, compared with the 2-min resolution, the transition between each timeframe is more natural, yet not less realistic.
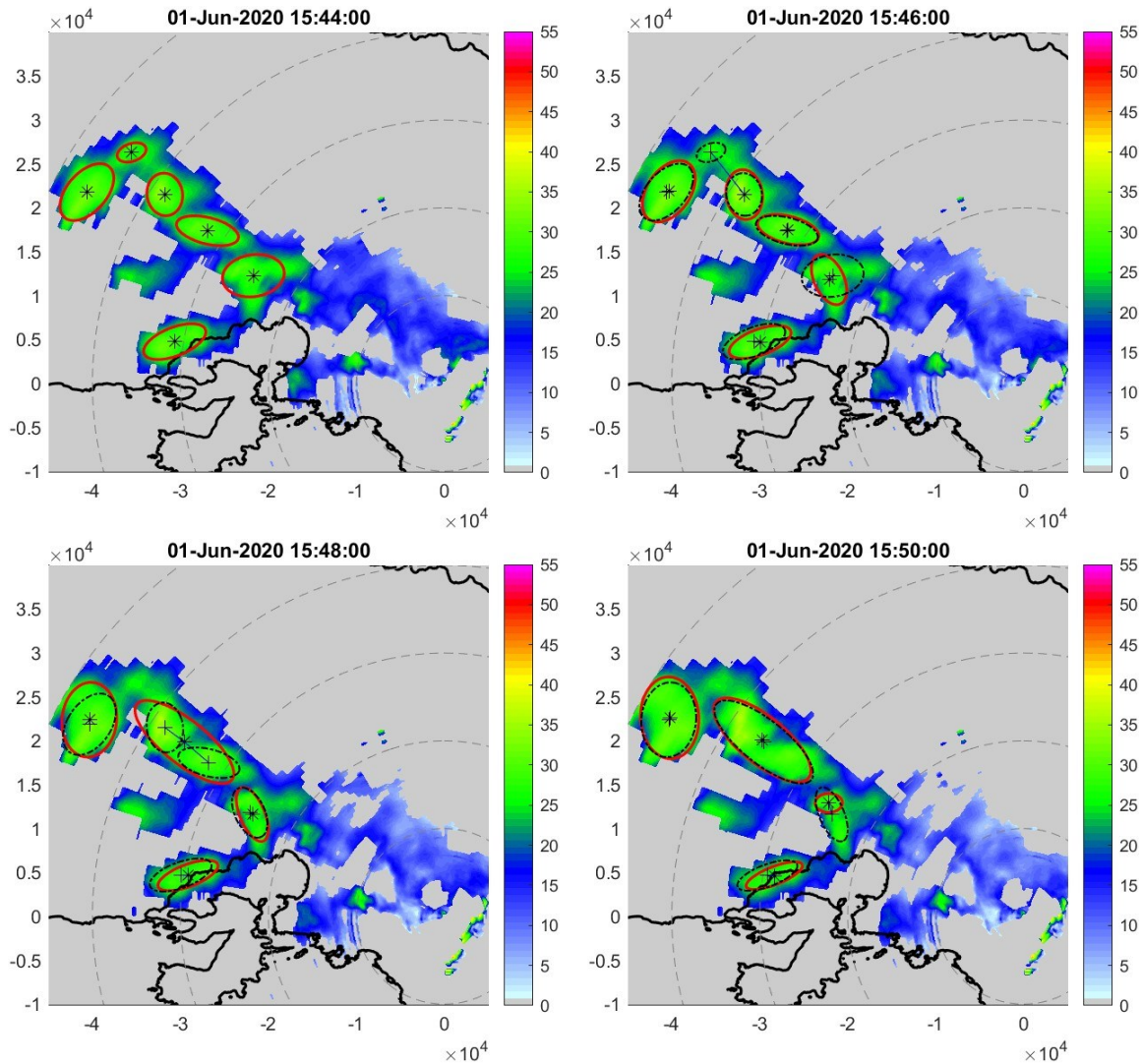

Figure 4-38: The matchmaking procedure between frames time frames with a 2-minute step

The next step lies in using a coarser temporal resolution regarding the period between each image. Specifically, images observed two minutes from each other are logical and would not present significant changes. However, a more extended period is required in nowcasting and forecasting, which would allow adequate lead time. Typical resolutions are in either 5-, 10-, 15- and 30-min resolutions, while more extended periods, such as 1-, 3- and 6- hours,

typically require more data, such as advanced cross-correlation algorithms, dual-frequency Doppler radars, wind velocity, and direction data, and even NWP products. In this application, the 10-minute period is used, and the results are shown in Figure 4-39.
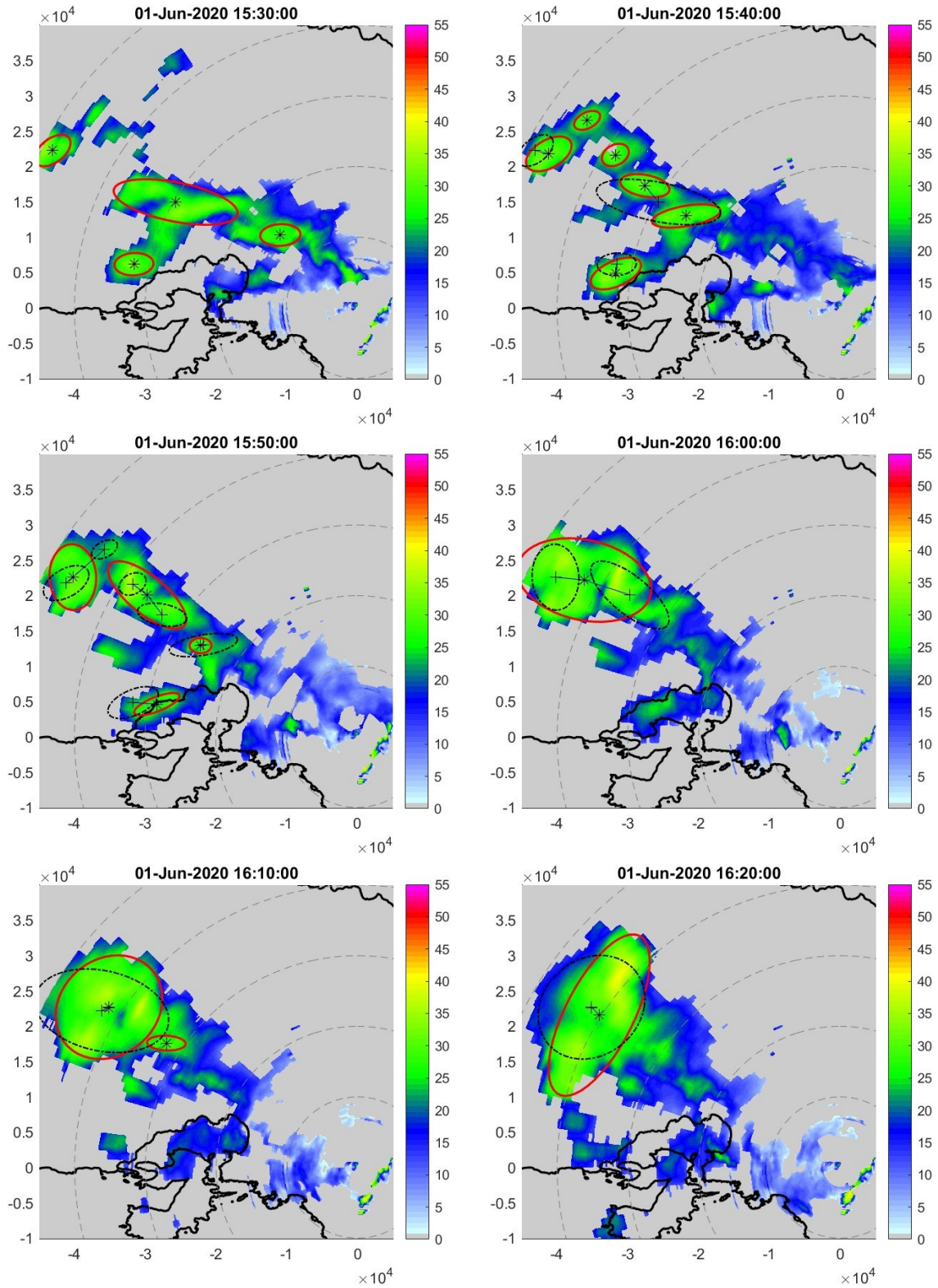

Figure 4-39: The matchmaking procedure between six-time frames with a 5-minute step

In this application, the 10-minute periods show good consistency regarding the storm-tracking algorithm. Specifically, cells were found to be consistent with the used-to-be place and current place. For instance, by comparing the timeframe 15:50 shown in Figure 4-38 and Figure 4-39, it is shown that although in the past cells were calculated using different data, i.e., in the first case, the 15:48 timeframe is used, whereas in the latter case, the 15:40 frame, still the consistency between each period is deemed acceptable.

Finally, the algorithm is applied to the entire event and the areas where the storm's identified cores passed over. These results are useful for identifying areas that were delt with the highest amount of rainfall rate in each event. Figure 4-40 presents the two convective events, 31 and 50, using the 35 dBZ and 40 dBZ thresholds. Similar maps using the 35 dBZ threshold are generated and shown in Appendix B for most events captured by the Rainscanner shown in Appendix A.
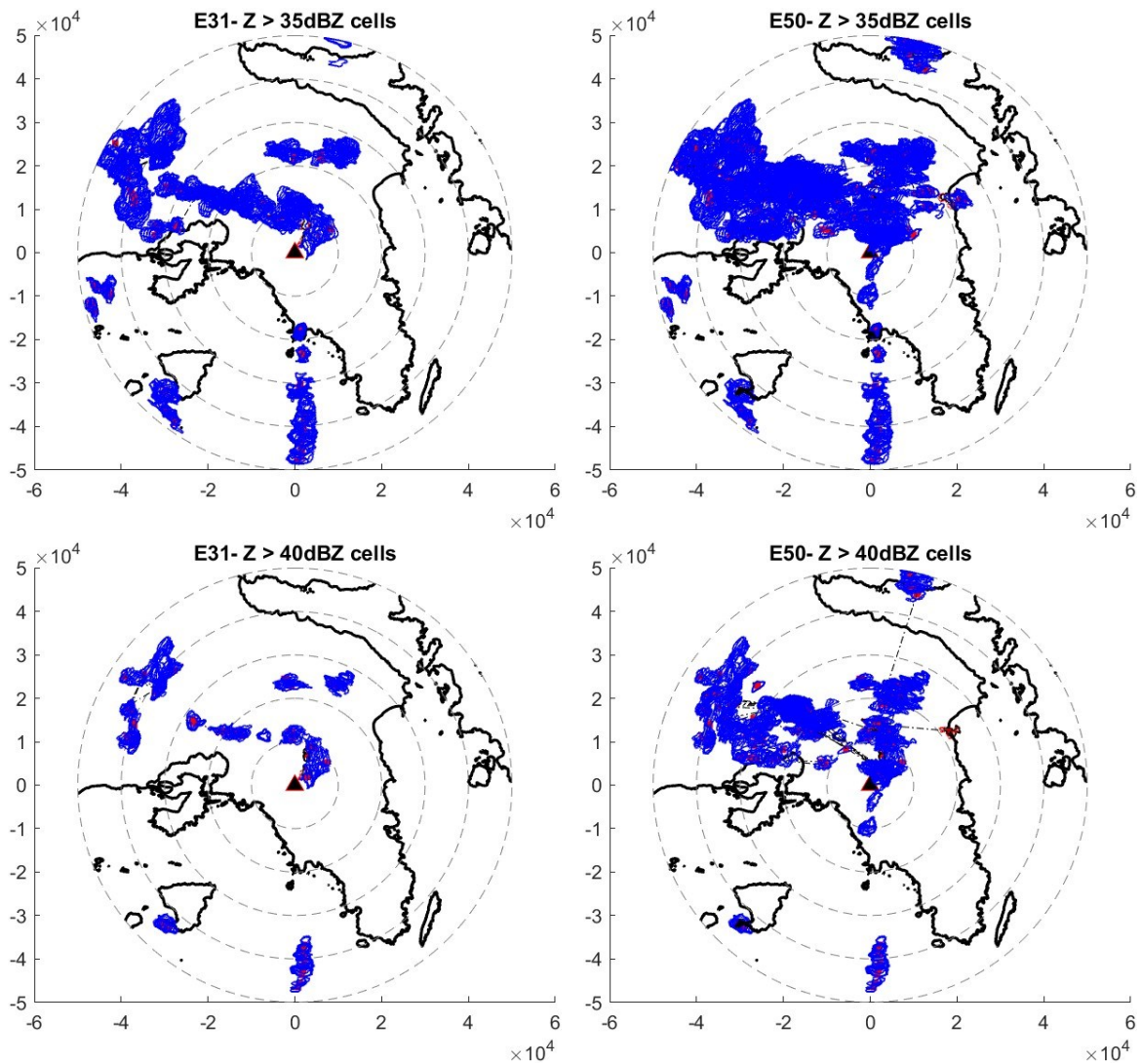

Figure 4-40: Cells borders of events 31 and 50, for two reflectivity thresholds; first row 35 dBZ, second row 40 dBZ

Finally, in Figure 4-41, the 35 dBZ tracking of the six events featured in Table 4-6 is shown, signifying the intensity of the event and the storm directions. Similar results for multiple events in Appendix A are shown in Appendix C.
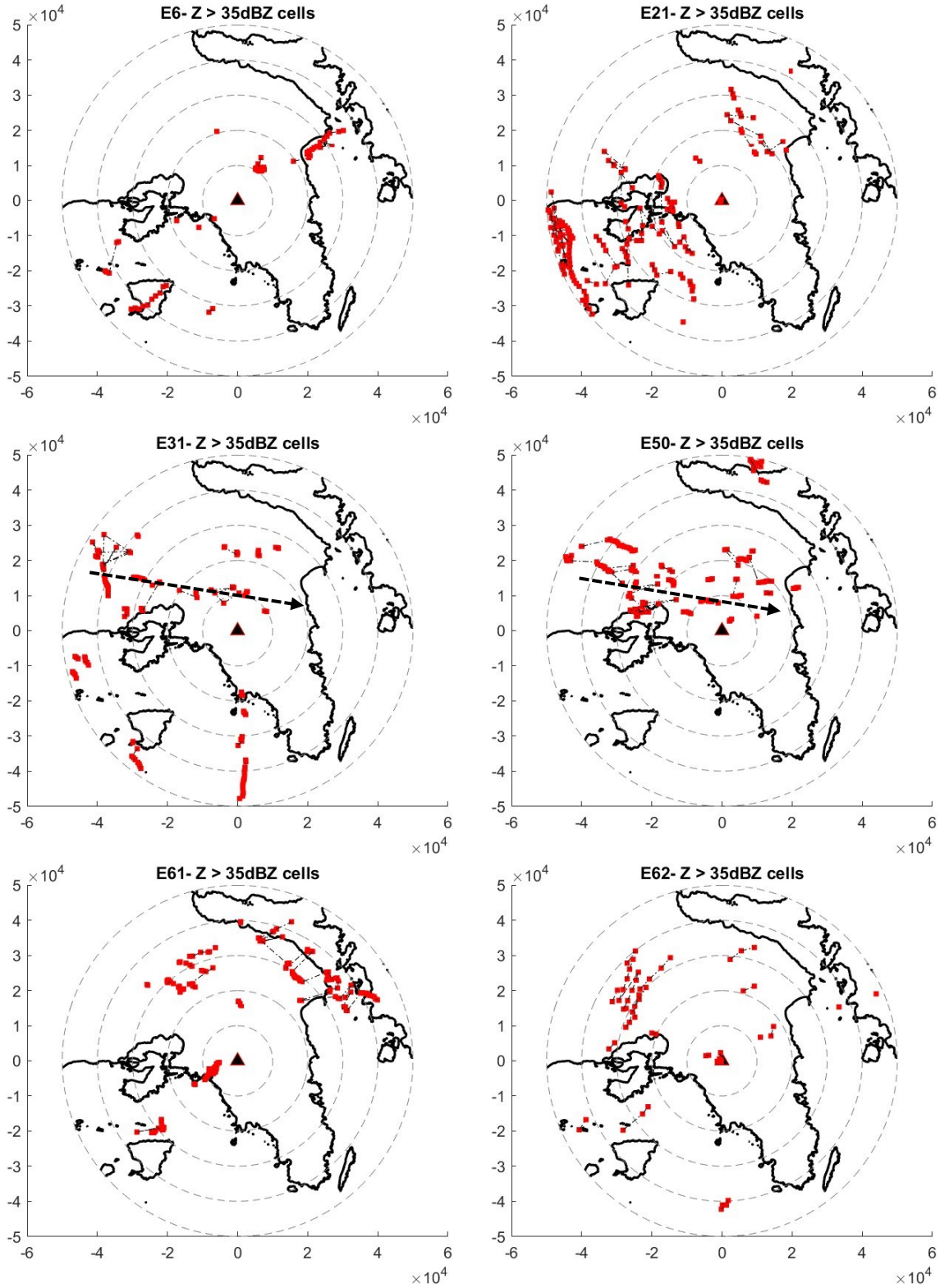

Figure 4-41: Centroids and area covered by storm clouds with a reflectivity threshold > 40 dBZ

The generated maps in Appendix C confirmed the dominant west-to-east direction of storm events in Athens. Figure 4-42 shows the main directions of the storms featured in Attica after analyzing the storm direction of each event. Most storms, 40%, had a southeast to northwest direction, passing over Athens. Following this, a west-to-east and northwest-to-east direction is also featured,20% and 12%, respectively, while some cases of a South to northeast direction, 6%. Finally, North-to-south directions are also featured, 16%, mainly winter events, with stratiform characteristics, low velocity, reflectivity, and snowfall events. Most convective-based events and events that featured high reflectivity values had an east-to-west direction, as seen in events E31 and E50.
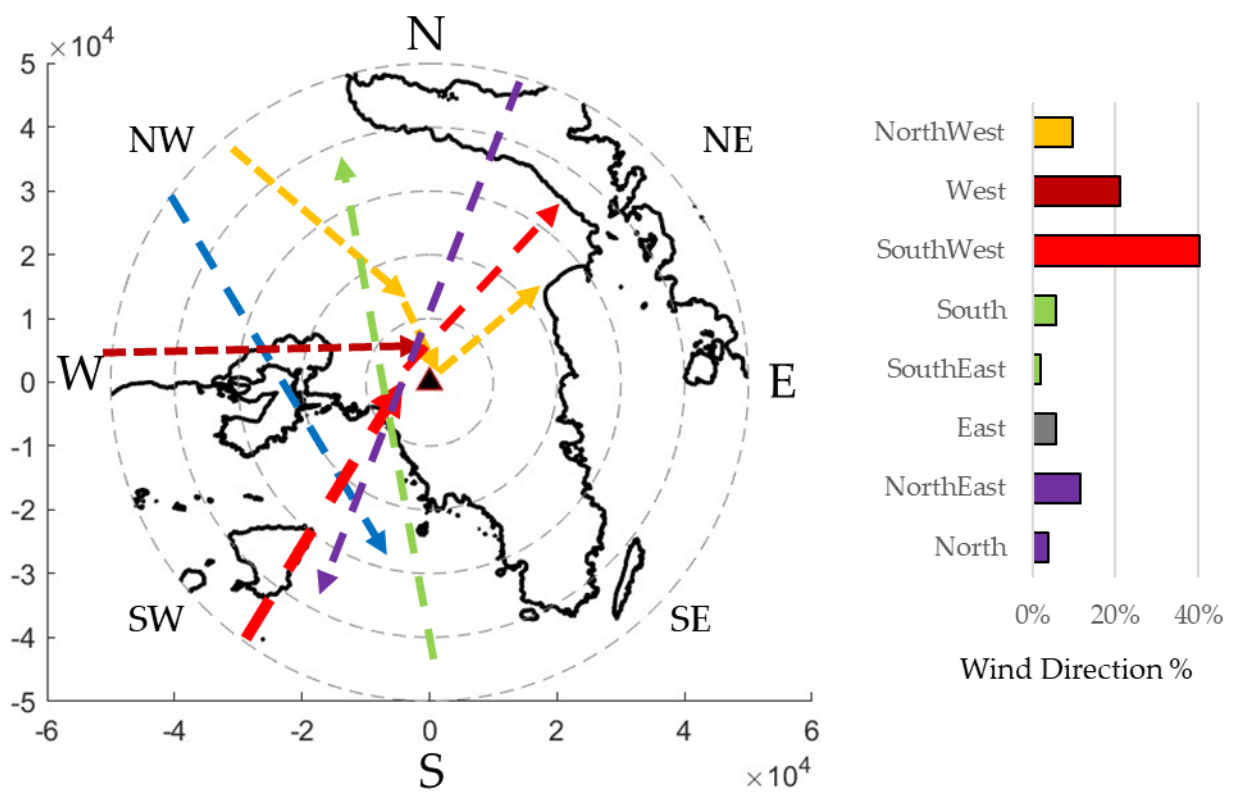

Figure 4-42: Main directions of storm clouds in Attica Region; Red lines are the most reoccurring, followed by blue, yellow, and purple according to the attached chart.

5. Conclusions and Future Research

5.1 Summary

The main scope of this Ph.D. dissertation is the development and implementation of a methodological framework for early warning of intense floods using innovative technologies. The key feature of this research is the collection, analysis, and use of datasets obtained by a newly installed weather radar system, the X-Band Rainscanner system located in Athens, Greece. The Rainscanner system can obtain reflectivity fields of up to two minutes and 100 m x 100 m temporal and spatial scales. These high-resolution datasets provide the necessary knowledge of the rainfall field characteristics required for fine-scaled applications, such as small-basin rainfall-runoff modeling and nowcasting. Furthermore, tools such as Geographical Information Systems (GIS) and code programming were used to quality control and perform the required tasks. These new technologies were utilized to assist in the formulation of an ease-to-use and calibrated Flood Early Warning System (FEWS).

The dissertation is divided into two main sections. The first section includes a review of the weather radar types, formulation, sources of errors, and quality control, while the second section deals with the development of an easy-to-use and applied (FEWS). The system is designed to focus on flash flood events, which are rainfall events characterized by their small duration and intensive rainfall rates. The first main question this thesis answers is stated as follows:

"What are the major factors to consider when utilizing weather radar datasets? Do weather radar datasets provide any benefit compared to rain gauge networks, or are they governed by uncertainty?"

The question refers to the fact that although weather radar datasets provide increased resolution, the uncertainty makes them unattractive. This is a classical dilemma, also set by Berne and Krajewski (2013), with their study of whether radar for hydrology applications is an unfulfilled promise or just unrecognized potential. Their answer "both" also applies to this research's findings. It is acknowledged that the need for high-resolution datasets is expected to increase. Due to satellite imagery, other products used in hydrology, such as

Digital Elevation Models (DEM) and land use maps, are currently obtained in high resolution, making the switch from typical rain gauge network fields to gridded rainfall maps necessary.

On the other hand, with increasing resolution, new models and processes are required to manage these datasets and reduce any model-generated uncertainty. To that end, it is important to address the main sources of uncertainty of weather radar usage. This thesis identifies the following factors that affect the quality of weather radar datasets: a) the type of the weather radar, b) the location of the radar, c) the calibration of the radar's hardware, d) the radar beam geometry settings and scanning strategy, e) the application of signal filtering for eliminating second echoes and ground clutter and g) the Z-R relationship that governs the reflectivity to rainfall intensity transformation. While some factors are to be considered before installing a weather radar system, such as its type, location, and scanning strategy, the latter two are dynamic and cannot be easily pre-determined. Signal filtering is a challenging task, performed in real-time based on pre-arranged clutter filters and gap-filling algorithms. The Z-R relationship is a relationship that controls the reflectivity to rainfall intensity transformation, and therefore, it highly affects the obtained end-product, i.e., the rainfall field. Although there are various factors to consider when utilizing weather radar datasets, there are added benefits compared to rain gauge networks. Urban hydrology and flash flood monitoring systems consider high-resolution datasets essential regarding their true quality. Nevertheless, the potential of weather radar datasets is only challenged by the quality of the data provided. By utilizing the correct tools and processes, the majority of errors generated by the signal can be easily eliminated, especially in short monitoring distances where X-Band weather radars shine. The main issue then rests upon the used Z-R relationship. The following question is raised:

"How does the Z-R relationship vary in time and space? What are the factors that influence the Z-R relationship, and how do they affect it in the case of the Attica Region?"
Is deriving a single Z-R relationship feasible for operational usage, and which Z-R relationship should be used for Athens?"

The variability of the Z-R relationship is well known since it is governed by the hydrometeor's Drop Size Distribution (DSD). Therefore, when different rainfall characteristics are observed, the Z-R relationship changes. To assess this, this study focused on the correlation of radar to rain gauge datasets in multiple events and locations. The findings of this research show that the Z-R parameters are related to the topography of the region. For instance, it is shown that the Z-R parameters vary in space between different events but even within a single event. More detailed findings showed that a location's proximity to specific topographical characteristics, such as the coastline and high-elevation

areas, affects the storm's behavior and, therefore, the Z-R relationship parameters. Another factor to the Z-R variability in space is the storm's movement through the area, specifically its generation and feeding place against the area where it discharges and follows up. For instance, in Athens, the west and areas near the sea featured Z-R parameters related to convective-based characteristics, while the eastern areas featured parameters related to stratiform-based characteristics. This was related to the fact that the western areas are the areas that are near the sea, which tends to enhance a weather system and end to high rainfall intensities measured in areas located on the coast. On the other hand, areas to the east are dealt with lesser rainfall intensities since most rainfall was discharged earlier in the west. This study area-specific behavior highlights the fact that the topography of a region affects the characteristics of rainfall, even within the same rainfall event.

Finally, an attempt was made to extract a single Z-R relationship for further use. Overall, it is shown that uncertainty does exist, and a one-fits-all solution is not optimum. Instead, the quality of weather radar dataset can be maximized only with the combined use of other rainfall products, namely ground rain gauge networks. In such a case, the network is not intended to be compared to the weather radar datasets but to be used as a validation system instead. The derivation of a single Z-R relationship only signifies whether convective or stratiform-based systems affect the specific area. In this research, based on the values of the derived parameters, the derived Z-R relationship signified that Athens is subject to more convective-based events than stratiform-based. However, this finding is strictly based on the used datasets.

The second main question raised in this thesis concerns the FEWS implementation.

What are the necessary components of an integrated flood early warning system (FEWS) based on weather radar datasets? Can such a system be efficient at an operational level, and how can it be implemented?

In this research, a comprehensive methodological framework is devised and applied, which deals with most subjects related to using FEWS. A FEWS complexity is described by the amount and complexity of the data, processes, and models used and contains a series of components divided into technical and non-technical components. The technical components consist of a) the monitoring and datasets quality control system, b) the flood risk estimation, and c) the forecasting systems, while the non-technical components are the warning dissemination and preparedness measures. The technical components define an FEWS complexity and should be configured based on the desired level of flood protection. This research addresses the technical components, focusing on flash flood protection. In such a FEWS, weather radars are deemed the only way forward due to their high resolution as mentioned earlier. Apart from data input, the required processes are also to be addressed.

A hydrometeorological approach is highly favored since integrating the hydrological processes into forecasting provides an improved and holistic approach to the flood generation scheme. Compared to typical fluvial flood monitoring systems, flash flood forecasting requires high temporal resolution datasets and easy-to-assess thresholds to provide adequate warning times, making typical rainfall-runoff modeling and stage monitoring systems impractical. Therefore, apart from high-quality rainfall datasets, the analysis of geomorphological characteristics of the basin, such as its static characteristics size, elevation, slope, land use, time of concertation, as well as its dynamic characteristics, e.g., the soil moisture conditions, are considered crucial for the estimation of the generated runoff. In this research, the FFG concept is implemented and applied into a fully gridded format, the GFFG. In this system, a rainfall threshold, the FFG value, is calculated in real-time based on a given threshold runoff and current soil moisture conditions using reverse rainfall-runoff modeling at the grid level. The gridded implementation aims to provide an easy-to-understand, configure, and use system applicable in areas with data scarcity. Finally, a storm-tracking algorithm is also developed to detect and track storm cells to assess the forecasting component of an FEWS. The algorithm uses reflectivity thresholds and image analysis to identify storm clouds and track their trajectory, providing the basis for future nowcasting products.

The application of the system to a series of events showed that it is robust and applicable for operational usage after proper tuning and user training in interpreting the generated results. The most critical factors defining whether a grid is flagged for flooding are the intensity and current soil moisture conditions. Therefore, the quality of the system implementation depends on the quality of the provided datasets. Unquestionably, the use of weather radar datasets can assist in both cases.

Through this research, the following factors are also to be highlighted, showcasing the importance of this work: a) it is the first time that a holistic approach for the use of weather radar-derived datasets in FEWS implementations in Greece and specifically in Athens is performed; b) it is the first time that a complete research on the spatial and temporal characteristics of the Z-R relationship is analyzed in Athens; c) a comprehensive and easy to follow methodological framework for the integration of weather radar datasets into a FEWS is devised and applied; d) an applicable EWS for flash floods in Greece is presented. Overall, the aim and approach of this thesis centered on a holistic approach for implementing a FEWS. To that end, a complete methodological framework is provided using innovative technologies such as weather radar systems, GIS, and image analysis tools.

5.2   Overview of main findings

This section presents a summary of the findings on each component of the FEWS performed in this Ph.D. dissertation. The main components, as previously stated, are a) the statistical analysis of the Rainscanner – rain gauge correlation to derive the main characteristics of the Z-R relationship, b) the rainfall-runoff model used in the hydrographs estimation, c) the GFFG methodology, and d) the storm tracking algorithm. For each component, the individual summary describes the datasets and the methods used, the results, and the main findings derived.

Z-R Statistical Analysis

The Z-R statistical analysis was performed using the correlation between the rain gauge and the Rainscanner datasets. A series of optimizations were performed utilizing 52 rain gauge stations found within the Rainscanner range. First, a correlation analysis was performed, examining the consistency between the dedicated Rainscanner pixel and each rain gauge timeseries by calculating Pearson's correlation index. The index is irrelevant to the estimated BIAS between the two timeseries but instead highlights whether the same rainfall volume is measured in each timestep, i.e., both instruments observe the same increase and decrease in rainfall height in each timeframe. Results showed that the correlation values are not even between the station's location, even in a single event. After calculation in multiple events, it was found that some stations exhibit a high correlation in many events, others exhibit only in a few, while others exhibit low correlation values in almost all events. The examination of the station's location to the correlation results led to the finding that stations located near ground clutter areas featured the worst correlation, whereas stations located near the coast featured the better correlation. This finding shows that although ground clutter algorithms can be applied, datasets obtained in or close to these areas should be used cautiously and cross-examined with other measurements in the area. Furthermore, the quality of the correlation was also found to be related to the amount of rainfall height measured. Specifically, it was found that when the rainfall height was significant, the correlation was better, while light rain cases, the correlation was considerably lower. This behavior was attributed to two factors: first, to the Rainscanner height of measurement, which, depending on the station's distance to the Rainscanner, can be several hundred meters above the ground, and second, to the rain gauge measurement sensitivity.

In the first case, light rain is subject to the effects of winds, which can relocate a hydrometeor measured with the Rainscanner above the rain gauge station to several hundred meters away, causing spatial displacement. Furthermore, light rain features a lower velocity, leading to a longer time for a hydrometeor to reach the ground. In stations away from the Rainscanner, where the observed elevation is high, this tends to lead to temporal

155

displacements, negatively impacting the correlation between the Rainscanner and the rain gauge. In the second case, the difference between the Rainscanner and rain gauge sensitivity can affect the correlation, especially when a high temporal scale is used. Although, in most cases, poor correlation is attributed to false Rainscanner readings, rain gauges are also subject to errors. For instance, the gauge's sensitivity or even other kinds of errors may lead to false readings such as temporal displacement of the rainfall volume, i.e., the amount of rainfall that occurred in a period is measured in the next period or even lost. Although rain gauges are considered the ground truth, the rain gauge device, recorded, or the post-process quality control of the entire rain gauge network can lead to errors. Unfortunately, these cases can only be examined when access to the rain gauge raw datasets and validation procedures are provided. Nevertheless, the correlation results of this thesis can be used to highlight possible error-prone rain gauge stations, which the rain gauge network operator should examine.

To overcome these errors and avoid low-correlated datasets to be used in the optimization procedures, a correlation threshold is applied per station per event. Two thresholds were examined, with the 0.6 value deemed the most applicable to provide adequate and well-correlated rain gauge – Rainscanner datasets pairs for the optimizations. By applying the threshold, well- and poor-correlated datasets are thus defined.

The findings are then focused on the station's location and the number of well-correlated events that it featured. Specifically, 15 stations featured above 0.60 correlation in 7 out of 13 events. Additionally, when applying the 0.60 correlation limit and excluding the poorly correlated events for each station, it was found that 32 out of 52 stations featured an average correlation of more than 0.60. Finally, it was found that in the majority of convective events, which tend to have a small footprint but with high rainfall intensity, the stations that featured the better correlation were found to be within or near the core of the storm cloud.

The next step of the analysis is the optimization procedures, which were used to shed light on the Z-R variability in time and space. Three optimization groups are formed: the event-based, the station-based, and the entire data-based. The derived Z-R values are then compared to typical parameter values found in either convective or stratiform events. Specifically, small values of parameter a are associated with stratiform events, values between 300 and 500 with convective, while values above 1000 are associated with snow events.

In the event-based optimization, a Z-R is derived by using only the well-correlated stations in a single event, resulting in as many Z-R relationships as the events examined. Results showed good consistency between the derived parameter values and the event's convective, stratiform, or snow event classification. The highlight was the identification of three events with parameter a value above 1000, denoting that they were snow events, which was true.

Moreover, events that featured a smaller footprint and high reflectivity system cores, i.e., typical convective systems, were correctly associated as such by the estimation of a high parameter *a* value. This optimization showed that the Z-R parameters vary in time, making using a single Z-R relationship inappropriate, but also that performing such optimizations is useful for the classification of storm systems. Finally, it is also noted that the majority of the examined events featured convective-based Z-R parameters.

The station-based optimization is performed when the data pairs of multiple events for a specific station are used. This optimization aimed to highlight the spatial variability of the Z-R parameter. The results showed that the variability of the parameters *a* and *b* in space is high since most stations featured a different derived Z-R relationship, but spatial properties can be derived. When parameter *b* was set as static, a pattern was drawn regarding parameter a's value and the station's locations. Specifically, stations near the coastline featured a parameter *a* value above 300, while stations near the high-elevation areas to the east featured a lower parameter *a* value. This led to the finding that coastline areas usually face convective-based rainfall characteristics, i.e., high rainfall rates, while high elevation areas face stratiform-based rainfall characteristics, i.e., low to medium rainfall rates, regardless of the amount of rainfall volume occurring during the event. This finding is justified because stations near the coastline are located in the west area of Athens, which is the first area of the mainland on the way of a typical rainfall system's way paths. In Athens, as highlighted later by the storm tracking algorithm findings, the majority of rainfall events have a west-to-east direction. These rainfall systems are formed in the western areas and, before they reach Athens city, are usually over the Saronic Gulf, thus being enhanced by seawater. When these systems reach the coastline, most rainfall occurs, bearing convective-based characteristics, i.e., intense rainfall rates. The rainfall intensity drops as the storm clouds move inland and to the center of Athens. Finally, these systems follow an east or northeastern direction towards the mountains of Penteli and Hymettus. Due to orography, rainfall volumes are expected to be high in the mountains, but the rainfall intensity is considerably lower. This research finding shows that through the derivation of the Z-R, spatial variability can be used for the required spatially targeted thresholds and mitigation measures since areas near the coast are subject to more intense rainfall rates, whereas the rest areas are subject to more typical rainfall events.

Finally, a calibration and validation procedure produced a single Z-R relationship. The suggested Z-R contains superior metrics than other previously determined Z-R relationships, two of which were derived for Athens by disdrometer measurements, and exhibits strong agreement in many locations. Additionally, it demonstrated good applicability compared to other Z-R relationships established from this study, namely, station- and event-based correlations. The Z-R relationships estimated shows that most

storm events in Athens are of the convective type based on their parameter values. Nevertheless, it is shown that it is extremely important to perform Z-R calibration on a new weather radar system since it is shown that the use of the typical Marshal and Palmer equation is the least appropriate compared to the other equations derived for the specific region.

Rainfall-Runoff Model

The rainfall-runoff model is the heart of the hydrological simulations. In this research, a distributed rainfall-runoff model is developed to assist with the hydrological simulations required in the flood early warning system. The model is designed to be easily configured and applied in small data scare basins. The model is based on the time-area diagram method to derive each grid's time to reach the basin outlet. The model's parameters are calculated through GIS tools using basic raster datasets, such as a digital elevation model and land use cover map, which are easily accessible. The model is then realized in MATLAB, where all the model's hydrological processes are performed. Specifically, the input datasets are the gridded rainfall maps provided by the Rainscanner, a gridded CN map derived using GIS tools, and the time-area diagram, a raster file containing the time of arrival of each grid to the outlet. All datasets are inserted into the model in pre-arranged spatial resolution, which in this application was set to 500 m x 500 m based on the area of the basin to which it was applied. The model uses the SCS CN loss method, with an added soil moisture adjustment factor, to adjust the CN values linearly between dry, medium, and wet conditions.

Apart from its suitability to simulate the rainfall-runoff processes using the Rainscanner datasets, the application of the model also focused on the impact the Z-R relationship has on the generated runoff. Specifically, a series of Z-R relationships were first used to estimate the rainfall fields, and their effect on the generated peak runoff and volume are examined. The comparison is made between the results of each relationship by examining the event's rainfall return period based on the IDF curve of the nearest station.

A total of six events were simulated, featuring both stratiform- and convective-based events. While in the stratiform events, the selection of the Z-R relationship showed minor differences, in the convective events, one Z-R relationship led to unrealistic rainfall and runoff values, highlighted by the fact that the rainfall return period, in that case, was calculated above 100 years whereas the rest relationships estimated 10-20 years return periods. This result shows that caution is required when using a Z-R relationship since this can lead to unrealistic results. Furthermore, between the used relationships, it is shown that the typically used Marshal and Palmer relationship leads to the highest amount of generated runoff. In contrast, the convective-based Z-R relationships feature the least generated runoff in the stratiform-events but the highest in the convective-based among the rest. This result shows that a convective-based relationship is preferable for these events, i.e., events with

high rainfall intensities, while in stratiform events, it will probably underestimate the generated runoff. Therefore, in flash flood early warning system implementations, a convective-based relationship should be desired, whereas in rainfall-runoff continuous monitoring, such as the estimation of soil moisture conditions and hydrological simulations of large river basins, the convective-based Z-R will underestimate runoff significantly.

Gridded Flash Flood Guidance

In this research, the GFFG system is implemented for use not only in rural basins, such as the Sarantapotamos River basin, but also in more significant regions covered by the radar system, such as the entire Attica Prefecture. The system is based on the FFG concept, where a dynamic rainfall threshold is determined, and the FFG value is above the level at which flooding is expected. The system uses a hydrometeorological approach, where the meteorological element, i.e., the current and forecasted rainfall characteristics, and the hydrological element, i.e., the subbasin characteristics and its runoff potential, are used to calculate the rainfall thresholds. The main improvement to the FFG system lies in its gridded approach, where all calculations, parameters, and variables are analyzed in a gridded pattern, in contrast to the original system where the analysis is performed in subbasin units, and the result is disaggregated to grids to match the forecasted rainfall fields resolution. Utilizing a gridded format has the benefit of versatility, as it allows for the adjustment of grid size based on the scale of the rainfall forecast and enables better spatial and temporal resolution. The main components of the system are a) the threshold runoff derivation, b) the current soil moisture conditions, c) the calculation of the FFG value, and d) the comparison of the forecasted values with the respected FFG value.

The threshold runoff is a key parameter of the system. This research uses the five-year return period rainfall to estimate the two-year runoff return period, often used as the threshold for minor floods. Different return periods were also tested, e.g., two- and ten-year rainfall return periods, but only minor differences were noticed. Following this, the rainfall threshold maps, i.e., the FFG values, are calculated for pre-determined rainfall accumulation durations of 1-, 3-, and 6 hours and soil moisture conditions. The use and interpretation of the different accumulation periods are important since the smaller duration may provide a smaller lead time, but less uncertainty is involved. The longer duration provides a longer lead time but increases uncertainty due to a) the uncertainty provided by the more extended forecast and b) the uncertainty regarding the exact moment flooding will occur within the designated period. Specifically, the system does not reply to the exact timing of flooding occurring within the accumulation period but that it will eventually occur. Following this, the research focuses on the parameters that affect the threshold value, namely the basin characteristics and the soil moisture conditions. Areas with a high percentage of imperviousness and low slope feature the smaller FFG values, denoting that less rainfall is

required to accumulate to form flooding conditions. The effect of soil moisture is at its maximum in permeable land cover since the CN value changes dramatically between dry and wet conditions. In contrast, highly impervious areas are less dependent on soil moisture conditions since the runoff potential is already high. Overall, these findings showcase a study area's flood threat, highlighting the need for a hydrometeorological FEWS approach. The system is finally applied in six events. Results show the dependency of the system's sensitivity to the basin's hydrological characteristics and rainfall intensity. Most areas flagged for flooding were areas featuring high CN values, i.e., urban areas, in conjunction with the increased rainfall accumulation over the examined durations. The system performed as intended in all events, considering the rainfall field examined in each case. Finally, despite the parameters set, the most important factors are the soil moisture conditions before the event and the amount of rainfall that occurs over a designated grid. Therefore, using high-resolution weather radar datasets is the only way to provide equal-resolution early warnings.

Storm Tracking

The storm-tracking algorithm developed in this research focused on cell identification and tracking procedures. In the first case, the algorithm's ability to track cloud cells using different reflectivity thresholds and shapes. It is acknowledged that applying multiple thresholds is favored since the centroid of the cell and its actual boundaries are better identified. Specifically, the 25 dBZ threshold works well when identifying polygon boundaries, while the 30 dBZ threshold is for identifying primary cells. Considering the above, the 30 dBZ was used in the matchmaking algorithm, along with a fitting ellipse of a minimum area of 4 km², since it provided the best results for identifying primary cells. A fitting ellipse is also favored since, as a mathematical representation, it applies better to the matchmaking algorithms used.

Following this, cell tracking is performed by applying the matchmaking algorithm. In this application, the algorithm provides cell tracking using different temporal scales. Specifically, the Rainscanner features 2-min temporal resolution products of reflectivity. Since a 2-min tracking is impractical, 10-min resolution reflectivity fields are first determined, each by merging five images in a consecutive order. The matchmaking using more data per tracking period was deemed more successful. Furthermore, the algorithm was tested in a 10-minute tracking period, which performed well, considering the number of tracked, merged, disappeared, or created cells.

Finally, the tracking algorithm is applied to all available Rainscanner events, over 80 events, to address the main directions of storms in Attica. As expected, most storms had a southwest-west to east direction, 40% of the events, followed by northwest-to-east and south-to-north directions. Moreover, North and Northeast to West directions were also

found in high amounts, but these events featured stratiform-based rainfall, i.e., smaller velocity storms, with little to medium rainfall rates. In contrast, most convective events had a west-to-east direction while showcasing an increased velocity. These results are deemed necessary regarding the storm's characteristics in Athens, while the usage of the algorithm is considered an essential and valuable step for following nowcasting systems that could be applied to assist with the FEWS.

5.3 Future Research

The main recommendations for future research lie in the limitations of this research. The first recommendations deal with the finalization of the FEWS since the number of required components involved in such a system is vast. Other recommendations concern various aspects of the processes used in this thesis. A list of future research recommendations is listed below:

- Regarding the weather radar datasets, apart from the use of rain gauge datasets, the use of disdrometer datasets could be used to validate the findings of this research. Furthermore, a disdrometer network can be used to compare the generated results with those from the rain gauge network and/or the Rainscanner.

- Regarding radar technology, radar composites should be examined to minimize the errors a single weather radar generates. Furthermore, more advanced radar systems, such as dual-frequency and phased-array systems, can be used to assess the results generated by the FEWS. Finally, the analysis of the vertical profile of the storms or the observation of different beam angles should also be investigated.

- A bias correction procedure to weather radar datasets using rain gauge measurements should be applied to further quality control the weather radar rainfall fields. In this research, the biases were mitigated by optimizing the Z-R relationship. Instead, a bias-driven correction algorithm using geostatistical interpolation methods may be applied to perform corrections in real-time regardless of the Z-R relationship used. Ongoing research makes such an analysis, using the calibration and validation stations featured in this research as the control points for real-time adjustments.

- An in-detail convective–stratiform classification method may be applied based on weather radar observations. Ongoing research in this field incorporates existing classification algorithms with weather radar observations.

- Concerning the rainfall-runoff model, a comprehensive analysis can be performed to calibrate the model parameters using in-situ stage-level and runoff observations. To that end, regional relationships concerning the runoff generation and the grid's characteristics can be identified, aiding the estimation of the GFFG parameters.

- Concerning the GFFG model, incorporating satellite-derived products to estimate current soil moisture conditions can provide a better applicable system that does not rely upon further rainfall-runoff simulations. Moreover, the generated uncertainty of the system can be assessed by providing uncertainty estimates to the datasets and methods used in each case.

- A comprehensive nowcasting system should be provided regarding the storm tracking algorithm to validate the system's performance in real-time applications. The nowcasting system can rely on the provided tracking algorithm, but more assumptions and models should be used to estimate the actual forecasted reflectivity and, consequently, rainfall fields. Ongoing research also focuses on ensemble forecasting fields, which can be used and validated through the current models provided in this research.

- Finally, after completing the Ph.D. dissertation, it is planned to develop a software application with a user-friendly interface that can perform rainfall field analysis, GFFG calculations, and flood estimations.

References

Alfieri L, Claps P, Laio F (2010) Time-dependent ZR relationships for estimating rainfall fields from radar measurements. Nat Hazards Earth Syst Sci 10:149–158. https://doi.org/10.5194/nhess-10-149-2010

Alfieri L, Salamon P, Pappenberger F, Wetterhall F, Thielen J (2012) Operational early warning systems for water-related hazards in Europe. Environmental Science & Policy 21:35–49. https://doi.org/10.1016/j.envsci.2012.01.008

Alfieri L, Thielen J (2015) A European precipitation index for extreme rain-storm and flash flood early warning. Meteorological Applications 22:3–13. https://doi.org/10.1002/met.1328

Alqudah A, Chandrasekar V, Le M (2013) Investigating rainfall estimation from radar measurements using neural networks. Natural Hazards and Earth System Sciences 13:535–544

Anagnostou EN (2004) A convective/stratiform precipitation classification algorithm for volume scanning weather radar observations. Meteorological Applications 11:291–300. https://doi.org/10.1017/S1350482704001409

Anagnostou EN, Krajewski WF (1999) Real-Time Radar Rainfall Estimation. Part I: Algorithm Formulation. Journal of Atmospheric and Oceanic Technology 16:189–197. https://doi.org/10.1175/1520-0426(1999)016<0189:RTRREP>2.0.CO;2

Anagnostou M, Nikolopoulos E, Kalogiros J, Anagnostou E, Marra F, Mair E, Bertoldi G, Tappeiner U, Borga M (2018) Advancing Precipitation Estimation and Streamflow Simulations in Complex Terrain with X-Band Dual-Polarization Radar Observations. Remote Sensing 10:1258. https://doi.org/10.3390/rs10081258

Anagnostou MN, Kalogiros J, Anagnostou EN, Tarolli M, Papadopoulos A, Borga M (2010) Performance evaluation of high-resolution rainfall estimation by X-band dual-polarization radar for flash flood applications in mountainous basins. Journal of Hydrology 394:4–16. https://doi.org/10.1016/j.jhydrol.2010.06.026

Anagnostou MN, Kalogiros J, Nikolopoulos E, Derin Y, Anagnostou EN, Borga M (2017) Satellite rainfall error analysis with the use of high-resolution X-band dual-polarization radar observations over the Italian Alps. In: Perspectives on Atmospheric Sciences. Springer, pp 279–286

Anderson EA (2002) Calibration of conceptual hydrologic models for use in river forecasting. Office of Hydrologic Development, US National Weather Service, Silver Spring, MD

Anderson RM, Koren VI, Reed SM (2006) Using SSURGO data to improve Sacramento Model a priori parameter estimates. Journal of Hydrology 320:103–116. https://doi.org/10.1016/j.jhydrol.2005.07.020

Aouissi J, Benabdallah S, Chabaâne ZL, Cudennec C (2018) Valuing scarce observation of rainfall variability with flexible semi-distributed hydrological modelling–Mountainous Mediterranean context. Science of the Total Environment 643:346–356

Atlas D, Ulbrich CW (1977) Path- and Area-Integrated Rainfall Measurement by Microwave Attenuation in the 1–3 cm Band. Journal of Applied Meteorology and Climatology 16:1322–1331. https://doi.org/10.1175/1520-0450(1977)016<1322:PAAIRM>2.0.CO;2

Auipong N, Trivej P (2018) Study of Z-R relationship among different topographies in Northern Thailand. J Phys: Conf Ser 1144:012098. https://doi.org/10.1088/1742-6596/1144/1/012098

Austin PM (1987) Relation between measured radar reflectivity and surface rainfall. Monthly Weather Review 115:1053–1070

Baltas EA (2008) Climatic Conditions and Availability of Water Resources in Greece. International Journal of Water Resources Development 24:635–649. https://doi.org/10.1080/07900620802230129

Baltas EA, Dervos NA, Mimikou MA (2007) Research on the initial abstraction – storage ratio and its effect on hydrograph simulation at a watershed in Greece. 36

Baltas EA, Mimikou MA (2002a) Considerations for the optimum location of a C-band weather radar in the Athens area. In: Proceedings of ERAD

Baltas EA, Mimikou MA (2002b) The use of the Joss-type disdrometer for the derivation of ZR relationships. In: 2nd European Conference on Radar in Meteorology and Hydrology (ERAD). Delft, Netherlands

Baltas EA, Panagos DS, Mimikou MA (2015) An Approach for the Estimation of Hydrometeorological Variables Towards the Determination of Z-R Coefficients. Environ Process 2:751–759. https://doi.org/10.1007/s40710-015-0119-x

Berenguer M, Corral C, Sánchez-Diezma R, Sempere-Torres D (2005) Hydrological Validation of a Radar-Based Nowcasting Technique. J Hydrometeor 6:532–549. https://doi.org/10.1175/JHM433.1

Berenguer M, Park S, Sempere-Torres D, Didszun J, Pool M, Pfeifer M (2012) RAINSCANNER@ Barcelona: an experiment to assess the hydrological value of a portable X-band radar. In: Conference Proceedings of the Seventh European Conference on Radar in Meteorology and Hydrology (ERAD). Toulouse, France

Berne A, Delrieu G, Creutin J-D, Obled C (2004) Temporal and spatial resolution of rainfall measurements required for urban hydrology. Journal of Hydrology 299:166–179. https://doi.org/10.1016/j.jhydrol.2004.08.002

Berne A, Krajewski WF (2013) Radar for hydrology: Unfulfilled promise or unrecognized potential? Advances in Water Resources 51:357–366. https://doi.org/10.1016/j.advwatres.2012.05.005

Borga M (2002) Accuracy of radar rainfall estimates for streamflow simulation. Journal of Hydrology 267:26–39. https://doi.org/10.1016/S0022-1694(02)00137-3

Borga M, Anagnostou EN, Blöschl G, Creutin J-D (2011) Flash flood forecasting, warning and risk management: the HYDRATE project. Environmental Science & Policy 14:834–844. https://doi.org/10.1016/j.envsci.2011.05.017

Borga M, Anagnostou EN, Frank E (2000) On the use of real-time radar rainfall estimates for flood prediction in mountainous basins. Journal of Geophysical Research: Atmospheres 105:2269–2280. https://doi.org/10.1029/1999JD900270

Bournas A, Baltas E (2020) Application of a Rainscanner system for quantitative precipitation estimates in the region of Attica. In: Sixth International Symposium on Green Chemistry, Sustainable Development and Circular Economy Conference on Environmental Science and Technology, Thessaloniki, Greece. p 8

Bournas A, Baltas E (2021a) Increasing the Efficiency of the Sacramento Model on Event Basis in a Mountainous River Basin. Environ Process 8:943–958. https://doi.org/10.1007/s40710-021-00504-4

Bournas A, Baltas E (2022a) Determination of the Z-R Relationship through Spatial Analysis of X-Band Weather Radar and Rain Gauge Data. Hydrology 9:137. https://doi.org/10.3390/hydrology9080137

Bournas A, Baltas E (2022b) Analysis of Weather Radar Datasets through the Implementation of a Gridded Rainfall-Runoff Model. Environ Process

Bournas A, Baltas E (2022c) Investigation of the gridded flash flood Guidance in a Peri-Urban basin in greater Athens area, Greece. Journal of Hydrology 610:127820. https://doi.org/10.1016/j.jhydrol.2022.127820

Bournas A, Baltas E (2021b) Comparative Analysis of Rain Gauge and Radar Precipitation Estimates towards Rainfall-Runoff Modelling in a Peri-Urban Basin in Attica, Greece. Hydrology 8:29. https://doi.org/10.3390/hydrology8010029

Boyle DP, Gupta HV, Sorooshian S, Koren V, Zhang Z, Smith M (2001) Toward improved streamflow forecasts: value of semidistributed modeling. Water Resour Res 37:2749–2759. https://doi.org/10.1029/2000WR000207

Bruen M, O'Loughlin F (2014) Towards a nonlinear radar-gauge adjustment of radar via a piece-wise method. Meteorological Applications 21:675–683. https://doi.org/10.1002/met.1390

Burnash RJC (1995) The NWS river forecast system-catchment modeling. In: Singh VP (ed) Computer models of watershed hydrology. Water Resources Publications, Highlands Ranch, Colorado, pp 311–366

Burnash RJC, Ferral RL, McGuire RA (1973) A Generalized Streamflow Simulation System: Conceptual Modeling for Digital Computers. Joint Federal-State River Forecast Center, U.S. National Weather Service and California Department of Water Resources, Sacramento, CA, USA

Caloiero T, Coscarelli R, Ferrari E, Sirangelo B (2017) Temporal Analysis of Rainfall Categories in Southern Italy (Calabria Region). Environ Process 4:113–124. https://doi.org/10.1007/s40710-017-0215-1

Carpenter TM, Sperfslage JA, Georgakakos KP, Sweeney T, Fread DL (1999) National threshold runoff estimation utilizing GIS in support of operational flash flood warning systems. Journal of Hydrology 224:21–44

Cheng Z, Georgakakos KP, Spencer CR, Banks R (2022) Numerical Modeling of Flash Flood Risk Mitigation and Operational Warning in Urban Areas. Water 14:2494. https://doi.org/10.3390/w14162494

Cho Y, Engel BA, Merwade VM (2018) A spatially distributed Clark's unit hydrograph based hybrid hydrologic model (Distributed-Clark). Hydrological Sciences Journal 63:1519–1539

Ciach GJ, Krajewski WF (1999) Radar–rain gauge comparisons under observational uncertainties. Journal of Applied Meteorology and Climatology 38:1519–1525

Clark RA, Gourley JJ, Flamig ZL, Hong Y, Clark E (2014) CONUS-Wide Evaluation of National Weather Service Flash Flood Guidance Products. Weather and Forecasting 29:377–392. https://doi.org/10.1175/WAF-D-12-00124.1

Colli M, Lanza LG, La Barbera P (2013) Performance of a weighing rain gauge under laboratory simulated time-varying reference rainfall rates. Atmospheric research 131:3–12

Collier CG (1996) Applications of weather radar systems: a guide to uses of radar data in meteorology and hydrology, 2nd ed. Wiley, Chichester ; New York

Collier CG (2009) On the propagation of uncertainty in weather radar estimates of rainfall through hydrological models. Meteorological Applications 16:35–40. https://doi.org/10.1002/met.120

Cordery I (1970) Antecedent wetness for design flood estimation. Civ Eng Trans, Inst Eng Aust, CE12 2:181–184

Corral C, Berenguer M, Sempere-Torres D, Poletti L, Silvestro F, Rebora N (2019) Comparison of two early warning systems for regional flash flood hazard forecasting. Journal of Hydrology 572:603–619. https://doi.org/10.1016/j.jhydrol.2019.03.026

CRED - Centre for Research on the Epidemiology of Disasters (2022). https://www.cred.be

Cristiano E, ten Veldhuis M-C, van de Giesen N (2017) Spatial and temporal variability of rainfall and their effects on hydrological response in urban areas – a review. Hydrology and Earth System Sciences 21:3859–3878. https://doi.org/10.5194/hess-21-3859-2017

Cunha LK, Smith JA, Krajewski WF, Baeck ML, Seo B-C (2015) NEXRAD NWS polarimetric precipitation product evaluation for IFloodS. Journal of Hydrometeorology 16:1676–1699

Di Baldassarre G, Montanari A (2009) Uncertainty in river discharge observations: a quantitative analysis. Hydrology and Earth System Sciences 13:913–921

Diakakis M, Andreadakis E, Nikolopoulos EI, Spyrou NI, Gogou ME, Deligiannakis G, Katsetsiadou NK, Antoniadis Z, Melaki M, Georgakopoulos A, Tsaprouni K, Kalogiros J, Lekkas E (2019) An integrated approach of ground and aerial observations in flash flood disaster investigations. The case of the 2017 Mandra flash flood in Greece. International Journal of Disaster Risk Reduction 33:290–309. https://doi.org/10.1016/j.ijdrr.2018.10.015

Diakakis M, Mavroulis S, Deligiannakis G (2012) Floods in Greece, a statistical and spatial approach. Natural Hazards 62:485–500. https://doi.org/10.1007/s11069-012-0090-z

Diakakis M, Skordoulis M, Kyriakopoulos P (2022) Public Perceptions of Flood and Extreme Weather Early Warnings in Greece. Sustainability 14:10199. https://doi.org/10.3390/su141610199

Dieulin C, Boyer J-F, Ardoin-Bardin S, Dezetter A (2006) The contribution of GIS to hydrological modelling. IAHS publication 308:68

Directorate-General for Environment (European Commission) (2021) Assessment of Second Cycle Preliminary Flood Risk Assessments and Identification of Areas of Potential Significant Flood Risk under the Floods Directive: Member State : Greece. Publications Office of the European Union, LU

Dixon M, Wiener G (1993) TITAN: Thunderstorm Identification, Tracking, Analysis, and Nowcasting—A Radar-based Methodology. J Atmos Oceanic Technol 10:785–797. https://doi.org/10.1175/1520-0426(1993)010<0785:TTITAA>2.0.CO;2

Douinot A, Roux H, Garambois P-A, Larnier K, Labat D, Dartus D (2016) Accounting for rainfall systematic spatial variability in flash flood forecasting. Journal of Hydrology 541:359–370. https://doi.org/10.1016/j.jhydrol.2015.08.024

Doviak RJ, Zrnić DS (1993) Doppler radar and weather observations, 2nd ed. Academic Press, San Diego

Duff IS, Koster J (2001) On Algorithms For Permuting Large Entries to the Diagonal of a Sparse Matrix. SIAM J Matrix Anal Appl 22:973–996. https://doi.org/10.1137/S0895479899358443

Einfalt T, Arnbjerg-Nielsen K, Golz C, Jensen N-E, Quirmbach M, Vaes G, Vieux B (2004) Towards a roadmap for use of radar rainfall data in urban drainage. Journal of Hydrology 299:186–202. https://doi.org/10.1016/j.jhydrol.2004.08.004

Erlingis JM, Gourley JJ, Hong Y (2013) Relationships between Return Period and Flash Flooding in the United States. 2013:H51Q-04

European Union (2007) Directive 2007/60/EC of the European Parliament and of the Council of 23 October 2007 on the assessment and management of flood risks. European Union

European Union (2021) The 6th Water Framework Directive and Floods Directive Implementation Report

Feloni E (2019) Assessment of flood induced by heavy rainfall using advanced methodologies, as a premise for an integrated flood early warning system: the case of Attica region. PhD Thesis, National Technical University of Athens

Feloni E, Kotsifakis K, Dervos N, Giavis G, Baltas E (2017) Analysis of Joss-Waldvogel disdrometer measurements in rainfall events. In: Papadavid G, Hadjimitsis DG, Michaelides S, Ambrosia V, Themistocleous K, Schreier G (eds) Fifth International Conference on Remote Sensing and Geoinformation of the Environment (RSCy2017). SPIE, Paphos, Cyprus, p 60

Feloni E, Mousadis I, Baltas E (2020) Flood vulnerability assessment using a GIS-based multi-criteria approach—The case of Attica region. Journal of Flood Risk Management 13:e12563. https://doi.org/10.1111/jfr3.12563

Finnerty BD, Smith MB, Seo D-J, Koren V, Moglen GE (1997) Space-time scale sensitivity of the Sacramento model to radar-gage precipitation inputs. Journal of Hydrology 203:21–38

Gabella M, Amitai E (2000) Radar rainfall estimates in an alpine environment using different gage-adjustment techniques. Physics and Chemistry of the Earth, Part B: Hydrology, Oceans and Atmosphere 25:927–931. https://doi.org/10.1016/S1464-1909(00)00127-1

Gaur A, Simonovic SP (2015) Towards Reducing Climate Change Impact Assessment Process Uncertainty. Environ Process 2:275–290. https://doi.org/10.1007/s40710-015-0070-x

Gauthreaux S, Diehl R (2020) Discrimination of biological scatterers in polarimetric weather radar data: Opportunities and challenges. Remote Sensing 12:545

Gekat F, Meischner P, Friedrich K, Hagen M, Koistinen J, Michelson DB, Huuskonen A (2004) The state of weather radar operations, networks and products. Weather radar: Principles and advanced applications 1–51

Georgakakos KP (2006) Analytical results for operational flash flood guidance. Journal of Hydrology 317:81–103. https://doi.org/10.1016/j.jhydrol.2005.05.009

Georgakakos KP (1986) A generalized stochastic hydrometeorological model for flood and flash-flood forecasting: 2. Case studies. Water Resour Res 22:2096–2106. https://doi.org/10.1029/WR022i013p02096

Georgakakos KP, Modrick TM, Shamir E, Campbell R, Cheng Z, Jubach R, Sperfslage JA, Spencer CR, Banks R (2022) The Flash Flood Guidance System Implementation Worldwide: A Successful Multidecadal Research-to-Operations Effort. Bulletin of the American Meteorological Society 103:E665–E679. https://doi.org/10.1175/BAMS-D-20-0241.1

Georgakakos KP, Modrick TM, Shamir E, Campbell R, Cheng Z, Jubach R, Sperfslage JA, Spencer CR, Banks R (2021) The Flash Flood Guidance System Implementation Worldwide: A Successful Multidecadal Research-To-Operations Effort. Bulletin of the American Meteorological Society 1–35. https://doi.org/10.1175/BAMS-D-20-0241.1

Germann U, Galli G, Boscacci M, Bolliger M (2006) Radar precipitation measurement in a mountainous region. Quarterly Journal of the Royal Meteorological Society: A journal of the atmospheric sciences, applied meteorology and physical oceanography 132:1669–1692

Ghimire GR, Krajewski WF, Ayalew TB, Goska R (2022) Hydrologic investigations of radar-rainfall error propagation to rainfall-runoff model hydrographs. Advances in Water Resources 161:104145. https://doi.org/10.1016/j.advwatres.2022.104145

Gilewski P, Nawalany M (2018) Inter-comparison of rain-gauge, radar, and satellite (IMERG GPM) precipitation estimates performance for rainfall-runoff modeling in a mountainous catchment in Poland. Water 10:1665

Gires A, Tchiguirinskaia I, Schertzer D, Schellart A, Berne A, Lovejoy S (2014) Influence of small scale rainfall variability on standard comparison tools between radar and rain gauge data. Atmospheric Research 138:125–138. https://doi.org/10.1016/j.atmosres.2013.11.008

Gossard EE, Strauch RG, Welsh DC, Matrosov SY (1992) Cloud layers, particle identification, and rain-rate profiles from ZRV f measurements by clear-air Doppler radars. Journal of Atmospheric and Oceanic Technology 9:108–119

Goudenhoofdt E, Delobbe L (2009) Evaluation of radar-gauge merging methods for quantitative precipitation estimates. Hydrol Earth Syst Sci 9

Grek E, Zhuravlev S (2020) Simulation of Rainfall-Induced Floods in Small Catchments (the Polomet'River, North-West Russia) Using Rain Gauge and Radar Data. Hydrology 7:92

Gupta HV, Sorooshian S, Yapo PO (1998) Toward improved calibration of hydrologic models: Multiple and noncommensurable measures of information. Water Resour Res 34:751–763. https://doi.org/10.1029/97WR03495

Hapuarachchi H a. P, Wang QJ, Pagano TC (2011) A review of advances in flash flood forecasting. Hydrol Process 25:2771–2784. https://doi.org/10.1002/hyp.8040

Hasan MM, Sharma A, Mariethoz G, Johnson F, Seed A (2016) Improving radar rainfall estimation by merging point rainfall measurements within a model combination framework. Advances in Water Resources 97:205–218. https://doi.org/10.1016/j.advwatres.2016.09.011

Hellenic Statistical Authority (ELSTAT) (2023) Greece in Figures (April to June 2023). https://www.statistics.gr/documents/20181/18074233/GreeceinFigures_2023Q2_EN.pdf. Accessed 14 Aug 2023

Hill PI, Graszkiewicz Z, Taylor M, Nathan RJ (2014) ARR Revision Project 6 Loss models for catchment simulation. Stage 4 Analysis of rural catchments

Hogue TS, Sorooshian S, Gupta H, Holz A, Braatz D (2000) A multistep automatic calibration scheme for river forecasting models. Journal of Hydrometeorology 1:524–542

Houze Jr. RA, Rasmussen KL, Zuluaga MD, Brodzik SR (2015) The variable nature of convection in the tropics and subtropics: A legacy of 16 years of the Tropical Rainfall Measuring Mission satellite. Reviews of Geophysics 53:994–1021. https://doi.org/10.1002/2015RG000488

Huuskonen A, Saltikoff E, Holleman I (2014) The Operational Weather Radar Network in Europe. Bulletin of the American Meteorological Society 95:897–907. https://doi.org/10.1175/BAMS-D-12-00216.1

Joss J, Schram K, Thams JC, Waldvogel A (1970) On the Quantitative Determination of Precipitation by a Radar. Osservatorio Ticinese DellaCentrale Meteorologica Svizzera Locarno-Monti

Joss J, Waldvogel A (1970) A Method to Improve the Accuracy of Radar Measured Amounts of Precipitation. In: 14th Radar Meteorology Conf. Amer. Meteor. Soc, Tucson, p 776

K. Ajami N, Gupta H, Wagener T, Sorooshian S (2004) Calibration of a semi-distributed hydrologic model for streamflow estimation along a river system. Journal of Hydrology 298:112–135. https://doi.org/10.1016/j.jhydrol.2004.03.033

Kalogiros J, Anagnostou MN, Anagnostou EN, Montopoli M, Picciotti E, Marzano FS (2013) Correction of Polarimetric Radar Reflectivity Measurements and Rainfall Estimates for Apparent Vertical Profile in Stratiform Rain. Journal of Applied Meteorology and Climatology 52:1170–1186. https://doi.org/10.1175/JAMC-D-12-0140.1

Kaltenberger R (2022) The Needs of Re-users of Authoritative Hydromet Warnings-Lessons Learned from Meteoalarm. Copernicus Meetings

Kammer A (1991a) Hydrological Applications of Weather Radar. Hydrological Applications of Weather Radar 250

Kammer A (1991b) An integrated X-band radar system for short-range measurements of rain rates in HERP. Ellis Horwood, Chichester, West Sussex, UK

Karagiannidis A, Lagouvardos K, Kotroni V (2016) The use of lightning data and Meteosat infrared imagery for the nowcasting of lightning activity. Atmospheric Research 168:57–69. https://doi.org/10.1016/j.atmosres.2015.08.011

Kim J-H, Bae D-H (2006) Estimation or Threshold Runoff on Han River Watershed. Journal of Korea Water Resources Association 39:151–160. https://doi.org/10.3741/JKWRA.2006.39.2.151

Kohler MA, Linsley RK (1951) Predicting the runoff from storm rainfall. US Department of Commerce, Weather Bureau

Kohn M, Galanti E, Price C, Lagouvardos K, Kotroni V (2011) Nowcasting thunderstorms in the Mediterranean region using lightning data. Atmospheric Research 100:489–502. https://doi.org/10.1016/j.atmosres.2010.08.010

Kollias P, Potiriadis G, Alexakis G, Serpetzoglou E (2007) THE HELLENIC WEATHER RADAR NETWORK–UPGRADES, DESCRIPTION AND FUTURE PLANS. In: 33 rd Conference on Radar Meteorology, Caims, Australia

Kolydas T (2023) ΣΤΟΝ ΑΠΟΗΧΟ ΤΗΣ ΚΑΚΟΚΑΙΡΙΑΣ EVA. https://kolydas.gr/content/%CF%83%CF%84%CE%BF%CE%BD-%CE%B1%CF%80%CF%8C%CE%B7%CF%87%CE%BF-%CF%84%CE%B7%CF%82-%CE%BA%CE%B1%CE%BA%CE%BF%CE%BA%CE%B1%CE%B9%CF%81%CE%AF%CE%B1%CF%82-eva-0. Accessed 20 Jul 2023

Koren V, Smith M, Duan Q (2003) Use of a Priori Parameter Estimates in the Derivation of Spatially Consistent Parameter Sets of Rainfall-Runoff Models. In: Duan Q, Gupta HV, Sorooshian S, Rousseau AN, Turcotte R (eds) Calibration of Watershed Models. American Geophysical Union, pp 239–254

Koren VI, Smith M, Wang D, Zhang Z (2000) Use Of Soil Property Data In The Derivation Of Conceptual Rainfall-Runoff Model Parameters. Presented at 15th Conference on Hydrology, AMS, January 9-14, 2000, Long Beach, CA

Krajewski WF, Smith JA (2002) Radar hydrology: rainfall estimation. Advances in Water Resources 25:1387–1394. https://doi.org/10.1016/S0309-1708(02)00062-3

Kull DW, Feldman AD (1998) Evolution of Clark's unit graph method to spatially distributed runoff. Journal of Hydrologic engineering 3:9–19

La Barbera P, Lanza LG, Stagi L (2002) Tipping bucket mechanical errors and their influence on rainfall statistics and extremes. Water Science and Technology 45:1–9. https://doi.org/10.2166/wst.2002.0020

Lagouvardos K, Kotroni V, Bezes A, Koletsis I, Kopania T, Lykoudis S, Mazarakis N, Papagiannaki K, Vougioukas S (2017) The automatic weather stations NOANN network of the National Observatory of Athens: operation and database. Geoscience Data Journal 4:4–16

Lagouvardos K, Kotroni V, Koussis A, Feidas H, Buzzi A, Malguzzi P (2003) The Meteorological Model BOLAM at the National Observatory of Athens: Assessment of Two-Year Operational Use. Journal of Applied Meteorology and Climatology 42:1667–1678. https://doi.org/10.1175/1520-0450(2003)042<1667:TMMBAT>2.0.CO;2

Lagouvardos K, Papavasileiou G, Kotroni V, Papagiannaki K, Dafis S, Galanaki E (2022) Regional Precipitation Index: ranking storms in Greece. Copernicus Meetings

Leaning J, Guha-Sapir D (2013) Natural disasters, armed conflict, and public health. New England journal of medicine 369:1836–1842

Legates DR (2000) Real-Time Calibration of Radar Precipitation Estimates. The Professional Geographer 52:235–246. https://doi.org/10.1111/0033-0124.00221

Li Z, Yang D, Hong Y, Qi Y, Cao Q (2015) Evaluation of radar-based precipitation estimates for flash flood forecasting in the Three Gorges Region. Proceedings of the International Association of Hydrological Sciences 368:89–95. https://doi.org/10.5194/piahs-368-89-2015

Libertino A, Allamano P, Claps P, Cremonini R, Laio F (2015) Radar Estimation of Intense Rainfall Rates through Adaptive Calibration of the Z-R Relation. Atmosphere 6:1559–1577. https://doi.org/10.3390/atmos6101559

Liu C, Guo L, Ye L, Zhang S, Zhao Y, Song T (2018) A review of advances in China's flash flood early-warning system. Nat Hazards 92:619–634. https://doi.org/10.1007/s11069-018-3173-7

Marchi L, Borga M, Preciso E, Gaume E (2010) Characterisation of selected extreme flash floods in Europe and implications for flood risk management. Journal of Hydrology 394:118–133. https://doi.org/10.1016/j.jhydrol.2010.07.017

Mariani S, Casaioli M, Coraci E, Malguzzi P (2015) A new high-resolution BOLAM-MOLOCH suite for the SIMM forecasting system: assessment over two HyMeX intense observation periods. Natural Hazards and Earth System Sciences 15:1–24. https://doi.org/10.5194/nhess-15-1-2015

Marshall JS, Palmer WMK (1948) The distribution of raindrops with size. Journal of meteorology 5:165–166

Mattheus S, Dupuy P, Scovell R, Kergomard A, Urban B, Huuskonen A (2012) EUMETNET OPERA Radar Data Centre: providing operational, homogeneous European radar rainfall composites. IAHS-AISH publication 9–14

Merz R, Blöschl G (2003) A process typology of regional floods. Water resources research 39:

Michaelides S, Levizzani V, Anagnostou E, Bauer P, Kasparis T, Lane JE (2009) Precipitation: Measurement, remote sensing, climatology and modeling. Atmospheric Research 94:512–533. https://doi.org/10.1016/j.atmosres.2009.08.017

Mimikou MA, Baltas EA (1996) Flood Forecasting Based on Radar Rainfall Measurements. Journal of Water Resources Planning and Management 122:151–156. https://doi.org/10.1061/(ASCE)0733-9496(1996)122:3(151)

Mockus V (1961) Watershed lag. U.S. Dept. of Agri- culture, Soil Conservation Service, ES-105, Washington, DC.

Nanding N, Rico-Ramirez MA, Han D (2015) Comparison of different radar-raingauge rainfall merging techniques. Journal of Hydroinformatics 17:422–445. https://doi.org/10.2166/hydro.2015.001

Norbiato D, Borga M, Degli Esposti S, Gaume E, Anquetin S (2008) Flash flood warning based on rainfall thresholds and soil moisture conditions: An assessment for gauged and ungauged basins. Journal of Hydrology 362:274–290. https://doi.org/10.1016/j.jhydrol.2008.08.023

Norbiato D, Borga M, Dinale R (2009) Flash flood warning in ungauged basins by use of the flash flood guidance and model-based runoff thresholds. Met Apps 16:65–75. https://doi.org/10.1002/met.126

NRSC USDA (2009) Part 614 Stream Visual Assessment Protocol Version 2. In: National Biology Handbook. NRSC

Oliver-Smith A, Alcántara-Ayala I, Burton I, Lavell A (2017) The social construction of disaster risk: Seeking root causes. International Journal of Disaster Risk Reduction 22:469–474. https://doi.org/10.1016/j.ijdrr.2016.10.006

Orellana-Alvear J, Célleri R, Rollenbeck R, Bendix J (2019) Optimization of X-band radar rainfall retrieval in the southern Andes of Ecuador using a random forest model. Remote Sensing 11:1632

Papadopoulos A, Katsafados P, Kallos G, Nickovic S (2002) The Weather Forecasting System for Poseidon - an Overview. Journal of Atmospheric & Ocean Science 8:219–237. https://doi.org/10.1080/1023673029000003543

Pappa A, Bournas A, Lagouvardos K, Baltas E (2021) Analysis of the Z-R relationship using X-Band weather radar measurements in the area of Athens. Acta Geophys. https://doi.org/10.1007/s11600-021-00622-5

Pappenberger F, Cloke HL, Parker DJ, Wetterhall F, Richardson DS, Thielen J (2015) The monetary benefit of early flood warnings in Europe. Environmental Science & Policy 51:278–291

Park S, Berenguer M, Sempere-Torres D (2019) Long-term analysis of gauge-adjusted radar rainfall accumulations at European scale. Journal of Hydrology 573:768–777. https://doi.org/10.1016/j.jhydrol.2019.03.093

Park S, Berenguer M, Sempere-Torres D, Baugh C, Smith P (2017) Toward seamless high-resolution flash flood forecasting over Europe based on radar nowcasting and NWP: An evaluation with case studies. 12158

Park S-G, Bringi VN, Chandrasekar V, Maki M, Iwanami K (2005) Correction of Radar Reflectivity and Differential Reflectivity for Rain Attenuation at X Band. Part I: Theoretical and Empirical Basis. Journal of Atmospheric and Oceanic Technology 22:1621–1632. https://doi.org/10.1175/JTECH1803.1

Paschalis A, Molnar P, Fatichi S, Burlando P (2013) A stochastic model for high-resolution space-time precipitation simulation. Water Resources Research 49:8400–8417. https://doi.org/10.1002/2013WR014437

Pathak C, Curtis D, Kitzmiller D, Vieux B (2013) Identifying and Resolving the Barriers and Issues in Using Radar-Derived Rainfall Estimating Technology. Journal of Hydrologic Engineering 18:1193–1199

Patsinghasanee S, Laonamsai J, Suwanprasert K, Pracheepchai J (2017) Evaluation of MRC Flash Flood Guidance System for the Southern Thailand: Case study from 28th November to 4th December 2017. Weather

Paz I, Willinger B, Gires A, Alves de Souza B, Monier L, Cardinal H, Tisserand B, Tchiguirinskaia I, Schertzer D (2019) Small-Scale Rainfall Variability Impacts Analyzed by Fully-Distributed Model Using C-Band and X-Band Radar Data. Water 11:1273. https://doi.org/10.3390/w11061273

Pereira S, Diakakis M, Deligiannakis G, Zêzere JL (2017) Comparing flood mortality in Portugal and Greece (Western and Eastern Mediterranean). International Journal of Disaster Risk Reduction 22:147–157. https://doi.org/10.1016/j.ijdrr.2017.03.007

Perera D, Agnihotri J, Seidou O, Djalante R (2020) Identifying societal challenges in flood early warning systems. International Journal of Disaster Risk Reduction 51:101794. https://doi.org/10.1016/j.ijdrr.2020.101794

Perera D, Seidou O, Agnihotri J, Rasmy M, Smakhtin V, Coulibaly P, Mehmood H (2019) Flood Early Warning Systems: A Review Of Benefits, Challenges And Prospects. United Nations University Institute for Water, Environment and Health

Picciotti E, Marzano FS, Anagnostou EN, Kalogiros J, Fessas Y, Volpi A, Cazac V, Pace R, Cinque G, Bernardini L, De Sanctis K, Di Fabio S, Montopoli M, Anagnostou MN, Telleschi A, Dimitriou E, Stella J (2013) Coupling X-band dual-polarized mini-radars and hydro-meteorological forecast models: the HYDRORAD project. Natural Hazards and Earth System Sciences 13:1229–1241. https://doi.org/10.5194/nhess-13-1229-2013

Posner AJ, Georgakakos KP (2015) Soil moisture and precipitation thresholds for real-time landslide prediction in El Salvador. Landslides 12:1179–1196. https://doi.org/10.1007/s10346-015-0618-x

Price K, Purucker ST, Kraemer SR, Babendreier JE, Knightes CD (2014) Comparison of radar and gauge precipitation data in watershed models across varying spatial and temporal scales. Hydrological Processes 28:3505–3520. https://doi.org/10.1002/hyp.9890

Probert-Jones JR (1990) A history of radar meteorology in the United Kingdom. In: Radar in Meteorology: Battan Memorial and 40th Anniversary Radar Meteorology Conference. Springer, pp 54–60

Qiu Q, Liu J, Tian J, Jiao Y, Li C, Wang W, Yu F (2020) Evaluation of the Radar QPE and Rain Gauge Data Merging Methods in Northern China. Remote Sensing 12:363

Raynaud D, Thielen J, Salamon P, Burek P, Anquetin S, Alfieri L (2015) A dynamic runoff co-efficient to improve flash flood early warning in Europe: evaluation on the 2013 central European floods in Germany: Dynamic runoff co-efficient for flash flood early warning in Europe. Met Apps 22:410–418. https://doi.org/10.1002/met.1469

Reed S, Johnson D, Sweeney T (2002) Application and National Geographic Information System Database to Support Two-Year Flood and Threshold Runoff Estimates.

Journal of Hydrologic Engineering 7:209–219. https://doi.org/10.1061/(ASCE)1084-0699(2002)7:3(209)

Reed S, Schaake J, Zhang Z (2007) A distributed hydrologic model and threshold frequency-based method for flash flood forecasting at ungauged locations. Journal of Hydrology 337:402–420. https://doi.org/10.1016/j.jhydrol.2007.02.015

Robbins GL, Collier CG (2005) Assessing error in hydrological and hydraulic model output flows. Atmospheric Science Letters 6:47–53. https://doi.org/10.1002/asl.90

Rogger M, Agnoletti M, Alaoui A, Bathurst JC, Bodner G, Borga M, Chaplot V, Gallart F, Glatzel G, Hall J, Holden J, Holko L, Horn R, Kiss A, Kohnová S, Leitinger G, Lennartz B, Parajka J, Perdigão R, Peth S, Plavcová L, Quinton JN, Robinson M, Salinas JL, Santoro A, Szolgay J, Tron S, van den Akker JJH, Viglione A, Blöschl G (2017) Land use change impacts on floods at the catchment scale: Challenges and opportunities for future research. Water Resour Res 53:5209–5219. https://doi.org/10.1002/2017WR020723

Ryde JW (1946) The attenuation and radar echoes produced at centimeter wavelengths by various meteorological phenomena. Meteorological Factors in Radio Wave Propagation, London 169–189

Sadeghi SHR, Mostafazadeh R, Sadoddin A (2015) Changeability of simulated hydrograph from a steep watershed resulted from applying Clark's IUH and different time–area histograms. Environ Earth Sci 74:3629–3643. https://doi.org/10.1007/s12665-015-4426-3

Sahlaoui Z, Mordane S (2019) Radar rainfall estimation in Morocco: quality control and gauge adjustment. Hydrology 6:41

Saltikoff E, Cho JYN, Tristant P, Huuskonen A, Allmon L, Cook R, Becker E, Joe P (2016) The threat to weather radars by wireless technology, B. Am. Meteorol. Soc., 97, 1159–1167

Saltikoff E, Friedrich K, Soderholm J, Lengfeld K, Nelson B, Becker A, Hollmann R, Urban B, Heistermann M, Tassone C (2019a) An Overview of Using Weather Radar for Climatological Studies: Successes, Challenges, and Potential. Bulletin of the American Meteorological Society 100:1739–1752. https://doi.org/10.1175/BAMS-D-18-0166.1

Saltikoff E, Haase G, Delobbe L, Gaussiat N, Martet M, Idziorek D, Leijnse H, Novák P, Lukach M, Stephan K (2019b) OPERA the Radar Project. Atmosphere 10:320. https://doi.org/10.3390/atmos10060320

Sayama T, Yamada M, Sugawara Y, Yamazaki D (2020) Ensemble flash flood predictions using a high-resolution nationwide distributed rainfall-runoff model: case study of the heavy rain event of July 2018 and Typhoon Hagibis in 2019. Progress in Earth and Planetary Science 7:75. https://doi.org/10.1186/s40645-020-00391-7

Schleiss M, Olsson J, Berg P, Niemi T, Kokkonen T, Thorndahl S, Nielsen R, Ellerbæk Nielsen J, Bozhinova D, Pulkkinen S (2020) The accuracy of weather radar in heavy rain: a comparative study for Denmark, the Netherlands, Finland and Sweden. Hydrology and Earth System Sciences 24:3157–3188. https://doi.org/10.5194/hess-24-3157-2020

Schmidt JA, Anderson AJ, Paul JH (2007) Spatially-variable, physically-derived flash flood guidance. In: Preprints, 21st Conf. on Hydrology, San Antonio, TX, Amer. Meteor. Soc. B

Selex ES (2014) Instruction Manual RainView Analyzer® User Guide

Selex ES GmbH (2014) Software Manual - Rainbow® 5 File Format

Sene K (2008) Flood warning, forecasting and emergency response. Springer, New York

Seo B-C, Dolan B, Krajewski WF, Rutledge SA, Petersen W (2015a) Comparison of single- and dual-polarization–based rainfall estimates using NEXRAD data for the NASA Iowa Flood Studies project. Journal of Hydrometeorology 16:1658–1675

Seo D, Lakhankar T, Mejia J, Cosgrove B, Khanbilvardi R (2013) Evaluation of Operational National Weather Service Gridded Flash Flood Guidance over the Arkansas Red River Basin. JAWRA Journal of the American Water Resources Association 49:1296–1307. https://doi.org/10.1111/jawr.12087

Seo D-J, Breidenbach JP (2002) Real-Time Correction of Spatially Nonuniform Bias in Radar Rainfall Data Using Rain Gauge Measurements. Journal of Hydrometeorology 3:93–111. https://doi.org/10.1175/1525-7541(2002)003<0093:RTCOSN>2.0.CO;2

Seo D-J, Habib E, Andrieu H, Morin E (2015b) Hydrologic applications of weather radar. Journal of Hydrology 531:231–233. https://doi.org/10.1016/j.jhydrol.2015.11.010

Sitterson J, Knightes C, Parmar R, Wolfe K, Avant B, Muche M (2018) An overview of rainfall-runoff model types

Smith G (2003) Flash flood potential: Determining the hydrologic response of FFMP basins to heavy rain by analyzing their physiographic characteristics. A white paper available from the NWS Colorado Basin River Forecast Center web site at http://www cbrfc noaa gov/papers/ffp_wpap pdf

Smith MB, Seo D-J, Koren VI, Reed SM, Zhang Z, Duan Q, Moreda F, Cong S (2004) The distributed model intercomparison project (DMIP): motivation and experiment design. Journal of Hydrology 298:4–26. https://doi.org/10.1016/j.jhydrol.2004.03.040

Sokol Z, Szturc J, Orellana-Alvear J, Popová J, Jurczyk A, Célleri R (2021) The Role of Weather Radar in Rainfall Estimation and Its Application in Meteorological and Hydrological Modelling—A Review. Remote Sensing 13:351. https://doi.org/10.3390/rs13030351

Spyrou C, Varlas G, Pappa A, Mentzafou A, Katsafados P, Papadopoulos A, Anagnostou MN, Kalogiros J (2020) Implementation of a Nowcasting Hydrometeorological System for Studying Flash Flood Events: The Case of Mandra, Greece. Remote Sensing 12:2784. https://doi.org/10.3390/rs12172784

SSW-MEECC (2017) Flood risk Management Plan. Stage I, Phase 1st, Deliverable 2. Intensity-Duration-Frequency Curves. Special Secretariat for Water, Ministry of Environment and Energy, Athens

Staudinger M, Koppe C, Heikinheimo M, Kroonenberg F (2009) Meteoalarm-Latest developments for weather warnings in Europe. In: 9th EMS Annual Meeting. pp EMS2009-102

Suhardi, Hidayah E, Halik G (2020) Flash flood modeling using the artificial neural network (Case study: Welang Watershed, Pasuruan District, Indonesia. IOP Conf Ser: Earth Environ Sci 419:012123. https://doi.org/10.1088/1755-1315/419/1/012123

Sweeney TL (1992) Modernized areal flash flood guidance

Theochari A-P, Feloni E, Bournas A, Baltas E (2021) Hydrometeorological - Hydrometric Station Network Design Using Multicriteria Decision Analysis and GIS Techniques. Environ Process. https://doi.org/10.1007/s40710-021-00527-x

Thielen J, Bartholmes J, Ramos M-H, Roo A de (2009) The European flood alert system–Part 1: concept and development. Hydrology and Earth System Sciences 13:125–140

Thielen-del Pozo J, Thiemig V, Pappenberger F, Revilla-Romero B, Salamon P, De Groeve T, Hirpa F (2015) The benefit of continental flood early warning systems to reduce the impact of flood disasters. EUR 27533: https://doi.org/10.2788/46941

Thorndahl S, Einfalt T, Willems P, Nielsen JE, ten Veldhuis M-C, Arnbjerg-Nielsen K, Rasmussen MR, Molnar P (2017) Weather radar rainfall data in urban hydrology. Hydrology and Earth System Sciences 21:1359–1380

Todini E (2001) A Bayesian technique for conditioning radar precipitation estimates to rain-gauge measurements. Hydrology and Earth System Sciences 5:187–199. https://doi.org/10.5194/hess-5-187-2001

Uijlenhoet R, Andrieu H, Austin GL, Baltas E, Borga M, Brilly M, Cluckie ID, Creutin JD, Delrieu G, Deshons P (1999) HYDROMET Integrated Radar Experiment (HIRE): Experimental setup and first results. In: 29th International Conference on Radar Meteorology. American Meteorological Society. pp 926–930

United Nations Office for Disaster Risk Reduction (UNDRR) (2017) Report of the Open-Ended Intergovernmental Expert Working Group on Indicators and Terminology Relating to Disaster Risk Reduction,. United Nations Office for Disaster Risk Reduction (UNDRR)

United Nations Office for Disaster Risk Reduction (UNDRR) (2003) Early Warning as a Matter of Policy. Germany

US Department of Agriculture (1986) Urban hydrology for small watersheds. US Department of Agriculture Tech Release 55 164

Van Der Knijff JM, Younis J, De Roo APJ (2010) LISFLOOD: a GIS-based distributed model for river basin scale water balance and flood simulation. International Journal of Geographical Information Science 24:189–212

Varlas G, Anagnostou MN, Spyrou C, Papadopoulos A, Kalogiros J, Mentzafou A, Michaelides S, Baltas E, Karymbalis E, Katsafados P (2019) A Multi-Platform Hydrometeorological Analysis of the Flash Flood Event of 15 November 2017 in Attica, Greece. Remote Sensing 11:45. https://doi.org/10.3390/rs11010045

Varlas G, Papadopoulos A, Papaioannou G, Dimitriou E (2021) Evaluating the Forecast Skill of a Hydrometeorological Modelling System in Greece. Atmosphere 12:902. https://doi.org/10.3390/atmos12070902

Varlas G, Spyrou C, Papadopoulos A, Korres G, Katsafados P (2020) One-year assessment of the CHAOS two-way coupled atmosphere-ocean wave modelling system over the Mediterranean and Black Seas. Mediterranean Marine Science 21:372–385. https://doi.org/10.12681/mms.21344

Velásquez N, Hoyos CD, Vélez JI, Zapata E (2020) Reconstructing the 2015 Salgar flash flood using radar retrievals and a conceptual modeling framework in an ungauged basin. Hydrol Earth Syst Sci 24:1367–1392. https://doi.org/10.5194/hess-24-1367-2020

Villarini G, Krajewski WF (2010) Review of the Different Sources of Uncertainty in Single Polarization Radar-Based Estimates of Rainfall. Surveys in Geophysics 31:107–129. https://doi.org/10.1007/s10712-009-9079-x

Wang G, Liu L, Ding Y (2012) Improvement of radar quantitative precipitation estimation based on real-time adjustments to Z-R relationships and inverse distance weighting correction schemes. Adv Atmos Sci 29:575–584. https://doi.org/10.1007/s00376-011-1139-8

Wasko C, Westra S, Nathan R, Orr HG, Villarini G, Villalobos Herrera R, Fowler HJ (2021) Incorporating climate change in flood estimation guidance. Philosophical Transactions of the Royal Society A: Mathematical, Physical and Engineering Sciences 379:20190548. https://doi.org/10.1098/rsta.2019.0548

Whiton RC, Smith PL, Bigler SG, Wilk KE, Harbuck AC (1998) History of Operational Use of Weather Radar by U.S. Weather Services. Part I: The Pre-NEXRAD Era. Weather and Forecasting 13:219–243. https://doi.org/10.1175/1520-0434(1998)013<0219:HOOUOW>2.0.CO;2

World Meteorological Organization (WMO) (2013a) Integrated flood management tools series: Flood Forecasting and Early Warning

World Meteorological Organization (WMO) (2023) WMO Radar Database. http://wrd.mgm.gov.tr. Accessed 11 Jul 2023

World Meteorological Organization (WMO) (2013b) Workshop on regional & global exchange of weather Radar data. Exeter, UK

Wu S-J, Lien H-C, Chang C-H (2012) Calibration of a conceptual rainfall–runoff model using a genetic algorithm integrated with runoff estimation sensitivity to parameters. Journal of Hydroinformatics 14:497. https://doi.org/10.2166/hydro.2011.010

You C-H, Suh S-H, Jung W, Kim H-J, Lee D-I (2022) Dual-Polarization Radar-Based Quantitative Precipitation Estimation of Mountain Terrain Using Multi-Disdrometer Data. Remote Sensing 14:2290. https://doi.org/10.3390/rs14102290

Zeng Z, Tang G, Long D, Zeng C, Ma M, Hong Y, Xu H, Xu J (2016) A cascading flash flood guidance system: development and application in Yunnan Province, China. Nat Hazards 84:2071–2093. https://doi.org/10.1007/s11069-016-2535-2

Zhang X, Srinivasan R (2010) GIS-based spatial precipitation estimation using next generation radar and raingauge data. Environmental Modelling & Software 25:1781–1788. https://doi.org/10.1016/j.envsoft.2010.05.012

Zhang Y, Zhang Z, Reed S, Koren V (2011) An enhanced and automated approach for deriving a priori SAC-SMA parameters from the soil survey geographic database. Computers & Geosciences 37:219–231. https://doi.org/10.1016/j.cageo.2010.05.016

Appendix A

Log of event datasets acquired by the Rainscanner during the period end of 10/2018-12/2022.

Event	Event Start (UTC+2)	Event End (UTC+2)	Duration (hour)	Total Event Duration (Hour)
2018				
1	**30-09-18 | 03:08**	**01-10-18 | 02:58**	**23.83**	
	01-10-18 | 03:08	**01-10-18 | 09:20**	**6.20**	**30.03**
2	30-11-18 | 14:22	30-11-18 | 16:10	1.80	1.80
3	11-12-18 | 23:00	12-12-18 | 01:58	2.97	
	12-12-18 | 02:08	13-12-18 | 01:58	23.83	
	13-12-18 | 02:08	13-12-18 | 09:12	7.07	33.87
4	13-12-18 | 12:16	13-12-18 | 14:54	2.63	2.63
5	16-12-18 | 02:08	16-12-18 | 09:24	7.27	7.27
6	**17-12-18 | 23:44**	**18-12-18 | 01:58**	**2.23**	
	18-12-18 | 02:08	**18-12-18 | 13:56**	**11.80**	**14.03**
7	27-12-18 | 05:16	27-12-18 | 11:22	6.10	6.10

Event	Event Start (UTC+2)	Event End (UTC+2)	Duration (hour)	Total Event Duration (Hour)
2019				
8	08-01-19 | 00:38	08-01-19 | 01:58	1.33	
	08-01-19 | 02:08	08-01-19 | 08:02	5.90	7.23
9	09-01-19 | 15:22	10-01-19 | 01:58	10.60	
	10-01-19 | 02:08	10-01-19 | 08:06	5.97	16.57
10	06-02-19 | 19:52	07-02-19 | 01:58	6.10	
	07-02-19 | 02:08	07-02-19 | 06:56	4.80	10.90
12	15-02-19 | 11:46	15-02-19 | 19:58	8.20	8.20
13	23-02-19 | 07:56	23-02-19 | 10:30	2.57	2.57
14	12-03-19 | 23:48	13-03-19 | 01:44	1.93	1.93
15	08-04-19 | 10:48	08-04-19 | 14:42	3.90	3.90
16	15-04-19 | 15:40	15-04-19 | 21:40	6.00	6.00
17	17-04-19 | 15:44	17-04-19 | 19:58	4.23	4.23
18	18-11-19 | 23:08	19-11-19 | 01:58	2.83	
	19-11-19 | 02:08	19-11-19 | 07:12	5.07	7.90
19	20-11-19 | 16:00	20-11-19 | 16:00	0.00	0.00
20	21-11-19 | 17:36	21-11-19 | 19:56	2.33	2.33
21	**24-11-19 | 21:36**	**25-11-19 | 01:58**	**4.37**	
	25-11-19 | 02:08	**25-11-19 | 08:32**	**6.40**	**10.77**
22	30-12-19 | 19:24	31-12-19 | 01:58	6.57	
	31-12-19 | 02:08	31-12-19 | 05:04	2.93	9.50

| Event	Event Start (UTC+2)	Event End (UTC+2)	Duration (hour)	Total Event Duration (Hour)
2020				
23	05-01-20 ǀ 19:06	05-01-20 ǀ 20:50	1.73	1.73
24	22-01-20 ǀ 02:08	22-01-20 ǀ 02:12	0.07	0.07
25	27-01-20 ǀ 14:34	27-01-20 ǀ 15:12	0.63	0.63
26	06-02-20 ǀ 11:48	06-02-20 ǀ 14:52	3.07	3.07
27	14-02-20 ǀ 20:42	14-02-20 ǀ 21:42	1.00	1.00
28	28-05-20 ǀ 20:22	28-05-20 ǀ 20:26	0.07	0.07
29	29-05-20 ǀ 17:04	29-05-20 ǀ 22:34	5.50	5.50
30	31-05-20 ǀ 15:16	31-05-20 ǀ 17:18	2.03	2.03
31	**01-06-20 ǀ 13:58**	**01-06-20 ǀ 20:04**	**6.10**	**6.10**
32	22-06-20 ǀ 15:46	22-06-20 ǀ 16:40	0.90	0.90
33	08-08-20 ǀ 12:50	08-08-20 ǀ 20:12	7.37	7.37
34	09-08-20 ǀ 09:38	09-08-20 ǀ 13:36	3.97	3.97
35	04-12-20 ǀ 15:44	04-12-20 ǀ 16:32	0.80	0.80
36	**04-12-20 ǀ 23:36**	**05-12-20 ǀ 01:58**	**2.37**	
	05-12-20 ǀ 02:10	**05-12-20 ǀ 03:08**	**0.97**	**3.33**
37	07-12-20 ǀ 02:36	07-12-20 ǀ 10:58	8.37	8.37
38	14-12-20 ǀ 14:58	15-12-20 ǀ 01:58	11.00	
	15-12-20 ǀ 02:08	15-12-20 ǀ 09:18	7.17	18.17

Event	Event Start (UTC+2)	Event End (UTC+2)	Duration (hour)	Total Event Duration (Hour)
2021				
39	00-01-00 ǀ 00:00	00-01-00 ǀ 00:00	0.00	0.00
40	26-01-21 ǀ 19:14	27-01-21 ǀ 01:58	6.73	
	27-01-21 ǀ 02:08	27-01-21 ǀ 08:48	6.67	13.40
41	30-01-21 ǀ 14:36	30-01-21 ǀ 14:52	0.27	0.27
42	01-02-21 ǀ 13:50	01-02-21 ǀ 13:54	0.07	0.07
43	15-02-21 ǀ 20:34	16-02-21 ǀ 01:58	5.40	
	16-02-21 ǀ 02:08	16-02-21 ǀ 22:34	20.43	25.83
44	19-03-21 ǀ 23:36	20-03-21 ǀ 01:58	2.37	
	20-03-21 ǀ 02:08	20-03-21 ǀ 13:02	10.90	10.90
45	20-03-21 ǀ 19:54	21-03-21 ǀ 01:58	6.07	
	21-03-21 ǀ 02:08	21-03-21 ǀ 03:14	1.10	7.17
46	31-03-21 ǀ 12:22	31-03-21 ǀ 19:30	7.13	7.13
47	24-04-21 ǀ 06:04	25-04-21 ǀ 02:46	20.70	
	25-04-21 ǀ 03:08	25-04-21 ǀ 05:38	2.50	23.20
48	09-06-21 ǀ 18:00	10-06-21 ǀ 02:44	8.74	8.74
49	11-06-21 ǀ 14:02	11-06-21 ǀ 19:00	4.97	4.97
50	**12-06-21 ǀ 11:48**	**12-06-21 ǀ 19:02**	**7.23**	**7.23**
51	13-06-21 ǀ 13:36	13-06-21 ǀ 18:04	4.47	4.47

52	08-10-21 ǀ 11:04	08-10-21 ǀ 21:04	10.00	10.00
53	08-10-21 ǀ 16:58	09-10-21 ǀ 02:58	10.00	
	09-10-21 ǀ 03:08	09-10-21 ǀ 09:20	6.20	16.20
54	10-10-21 ǀ 11:08	10-10-21 ǀ 17:02	5.90	5.90
55	10-10-21 ǀ 20:34	11-10-21 ǀ 02:58	6.40	
	11-10-21 ǀ 03:08	11-10-21 ǀ 08:56	5.80	12.20
58	15-10-21 ǀ 00:08	15-10-21 ǀ 02:58	2.83	
	15-10-21 ǀ 03:08	15-10-21 ǀ 08:34	5.43	8.27
59	15-10-21 ǀ 10:20	16-10-21 ǀ 02:58	16.63	
	15-10-21 ǀ 03:08	15-10-21 ǀ 08:48	5.67	22.30
60	22-11-21 ǀ 21:22	23-11-21 ǀ 01:58	4.60	
	23-11-21 ǀ 02:08	23-11-21 ǀ 02:50	0.70	5.30
61	**23-11-21 ǀ 17:34**	**24-11-21 ǀ 01:58**	**8.40**	
	24-11-21 ǀ 02:08	**24-11-21 ǀ 07:44**	**5.60**	**14.00**
62	26-11-21 ǀ 11:46	26-11-21 ǀ 17:20	5.57	5.57
63	04-12-21 ǀ 02:08	04-12-21 ǀ 08:12	6.07	6.07
64	04-12-21 ǀ 13:32	04-12-21 ǀ 19:14	5.70	5.70
65	06-12-21 ǀ 20:18	07-12-21 ǀ 01:58	5.67	
	07-12-21 ǀ 02:08	07-12-21 ǀ 10:58	8.83	14.50
66	10-12-21 ǀ 23:34	11-12-21 ǀ 01:58	2.40	
	11-12-21 ǀ 02:08	12-12-21 ǀ 01:58	23.83	
	12-12-21 ǀ 02:08	12-12-21 ǀ 09:10	7.03	33.27
67	14-12-21 ǀ 15:24	15-12-21 ǀ 01:58	10.57	
	15-12-21 ǀ 02:08	15-12-21 ǀ 07:58	5.83	16.40
68	18-12-21 ǀ 09:26	18-12-21 ǀ 09:26	-	-

| Event	Event Start (UTC+2)	Event End (UTC+2)	Duration (hour)	Total Event Duration (Hour)
2022				
69	10-01-22 ǀ 19:38	11-01-22 ǀ 01:58	6.33	
	11-01-22 ǀ 02:08	11-01-22 ǀ 07:48	5.67	12.00
70	11-01-22 ǀ 12:14	12-01-22 ǀ 01:58	13.73	
	12-01-22 ǀ 02:08	12-01-22 ǀ 08:48	6.67	20.40
71	23-01-22 ǀ 19:16	23-01-22 ǀ 20:20	1.07	1.07
72	24-01-22 ǀ 08:28	25-01-22 ǀ 01:58	17.50	
	25-01-22 ǀ 02:08	26-01-22 ǀ 01:58	23.83	
	26-01-22 ǀ 02:08	27-01-22 ǀ 01:58	23.83	
	27-01-22 ǀ 02:08	27-01-22 ǀ 16:28	14.33	79.50
73	29-01-22 ǀ 11:04	30-01-22 ǀ 01:58	14.90	
	30-01-22 ǀ 02:08	30-01-22 ǀ 17:02	14.90	14.90
74	01-02-22 ǀ 16:16	02-02-22 ǀ 01:58	9.70	
	02-02-22 ǀ 02:08	02-02-22 ǀ 10:33	8.42	18.12
75	02-02-22 ǀ 13:26	03-02-22 ǀ 01:58	12.53	
	03-02-22 ǀ 02:08	03-02-22 ǀ 10:10	8.03	20.57

| 76	03-02-22 | 18:30	03-02-22 | 20:16	1.77	1.77
77	09-03-22 | 18:40	10-03-22 | 01:58	7.30	
	10-03-22 | 02:08	10-03-22 | 18:26	16.30	23.60
78	11-03-22 | 08:12	11-03-22 | 10:54	2.70	2.70
79	12-03-22 | 14:42	12-03-22 | 23:22	8.67	8.67
80	18-05-22 | 21:54	19-05-22 | 02:58	5.07	
	19-05-22 | 03:08	19-05-22 | 07:44	4.60	9.67
81	25-05-22 | 10:32	25-05-22 | 10:42	0.17	0.17
82	06-06-22 | 14:32	07-06-22 | 02:50	12.30	12.30
83	10-06-22 | 23:36	11-06-22 | 02:58	3.37	
	11-06-22 | 03:08	11-06-22 | 22:12	19.07	22.43
84	12-06-22 | 09:54	12-06-22 | 14:48	4.90	4.90
85	22-08-22 | 16:00	22-08-22 | 19:48	3.80	3.80
86	23-08-22 | 08:34	23-08-22 | 23:52	15.30	15.30
87	24-08-22 | 12:02	25-08-22 | 02:58	14.93	
	25-08-22 | 03:08	26-08-22 | 02:58	23.83	
	26-08-22 | 03:08	26-08-22 | 17:42	14.57	53.33
88	01-09-22 | 16:14	01-09-22 | 21:42	5.47	5.47
89	02-09-22 | 12:28	02-09-22 | 22:30	10.03	10.03
90	03-09-22 | 14:22	03-09-22 | 17:08	2.77	2.77
91	05-11-22 | 19:00	06-11-22 | 01:58	6.97	6.97
	07-11-22 | 02:08	07-11-22 | 12:22	10.23	41.03
92	23-11-22 | 07:58	23-11-22 | 10:36	2.63	2.63
93	28-11-22 | 14:10	28-11-22 | 19:52	5.70	5.70
94	30-11-22 | 08:00	01-12-22 | 01:58	17.97	17.97
95	01-12-22 | 02:08	01-12-22 | 08:26	6.30	24.27

Appendix B

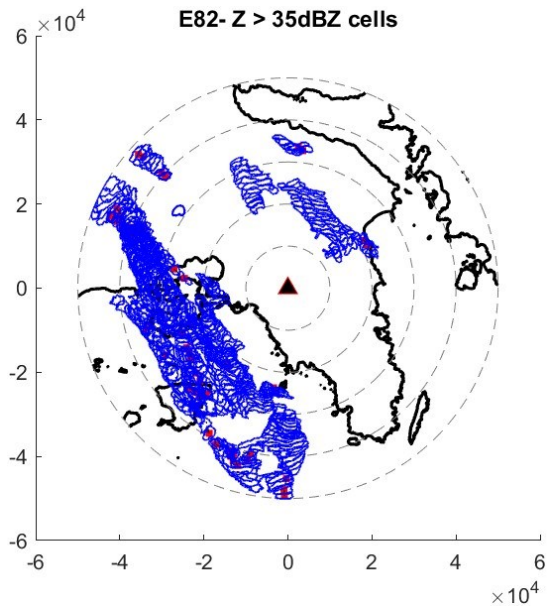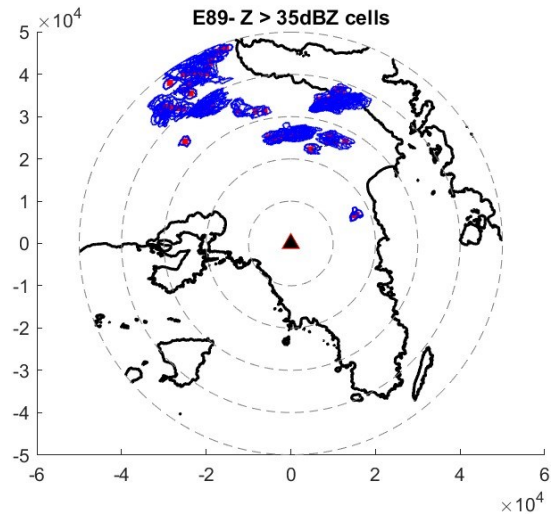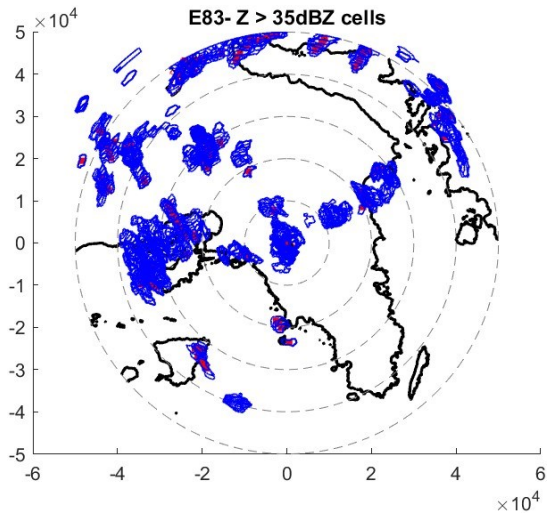**Results of Storm Tracking Algorithm with cell Borders (Selected Events).**
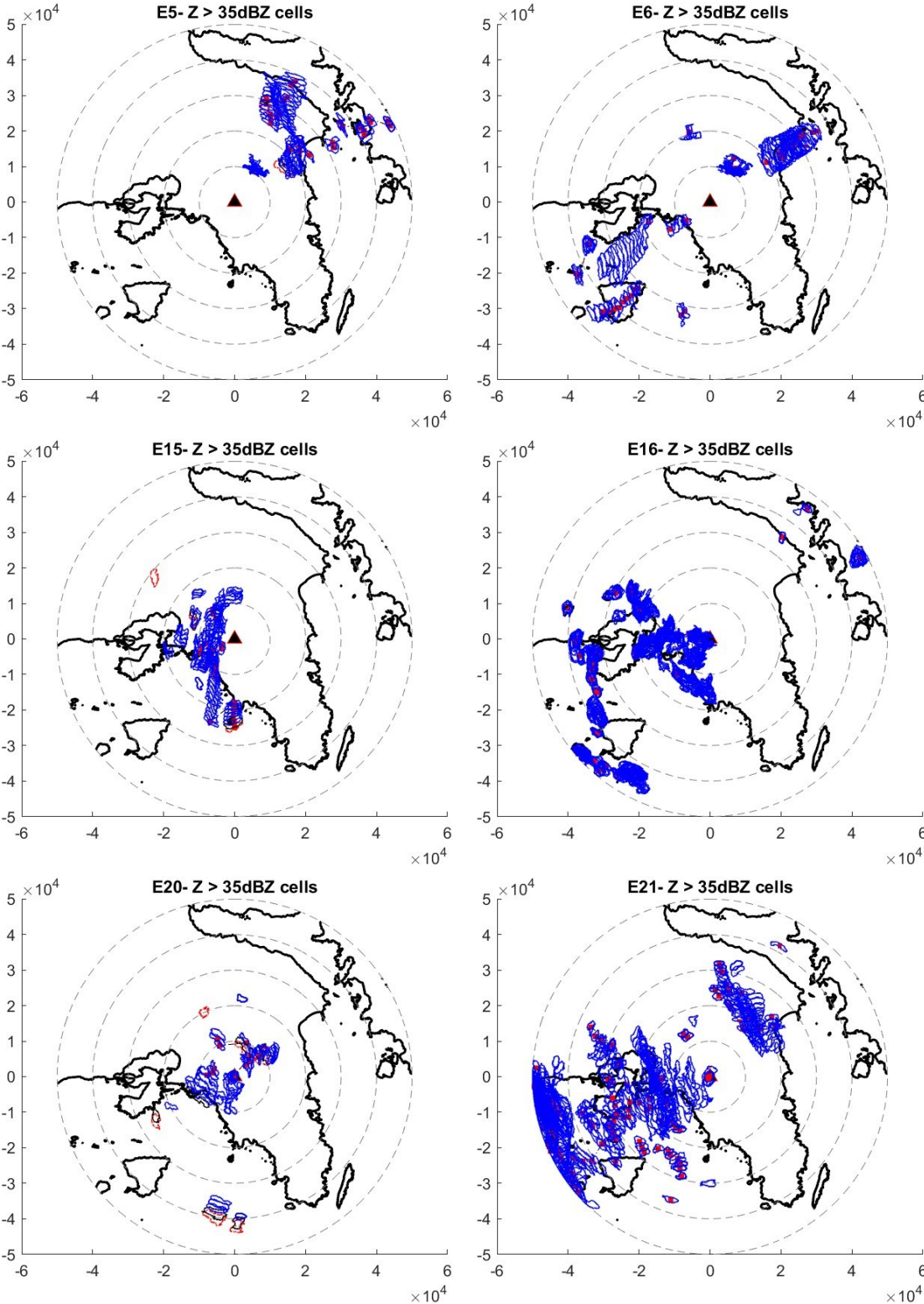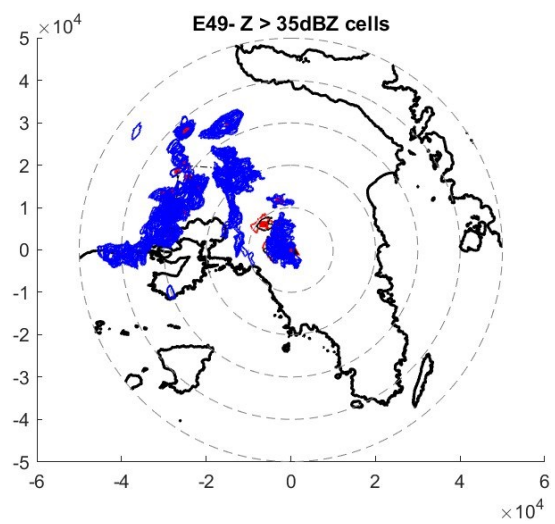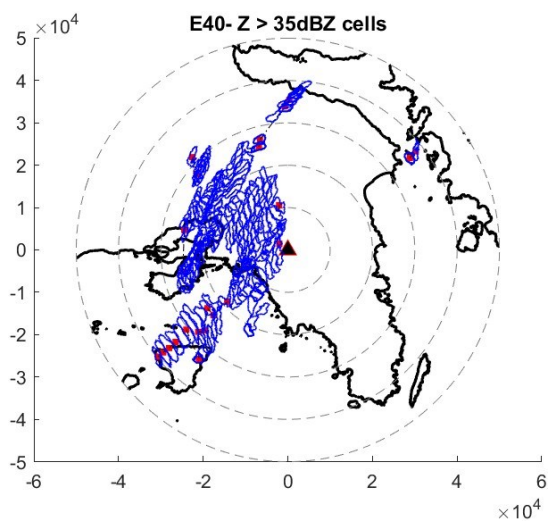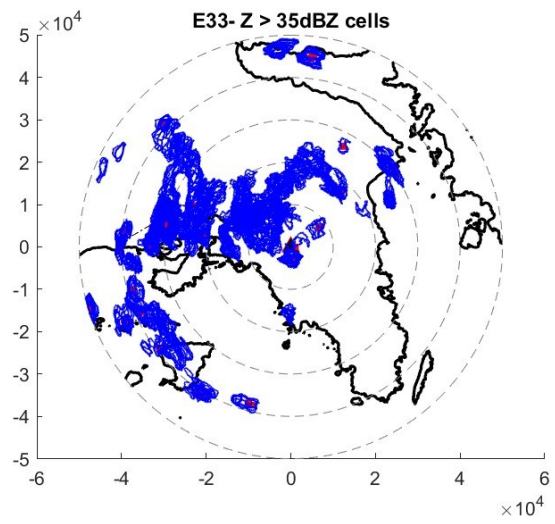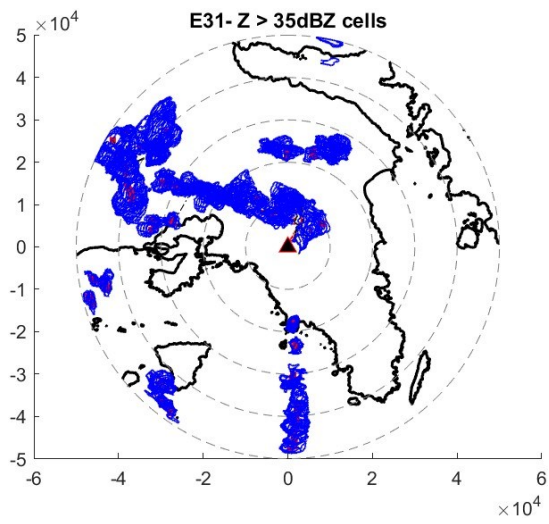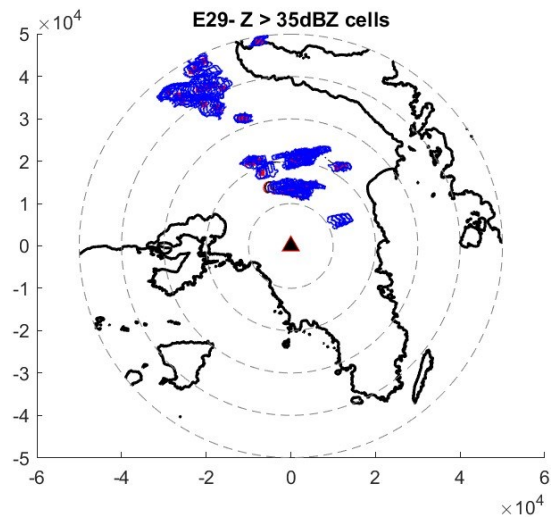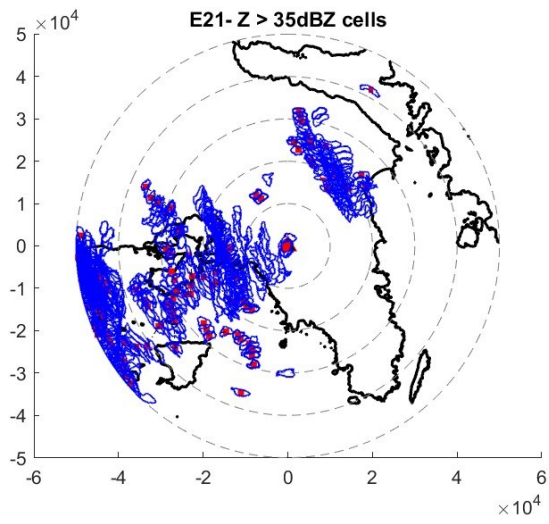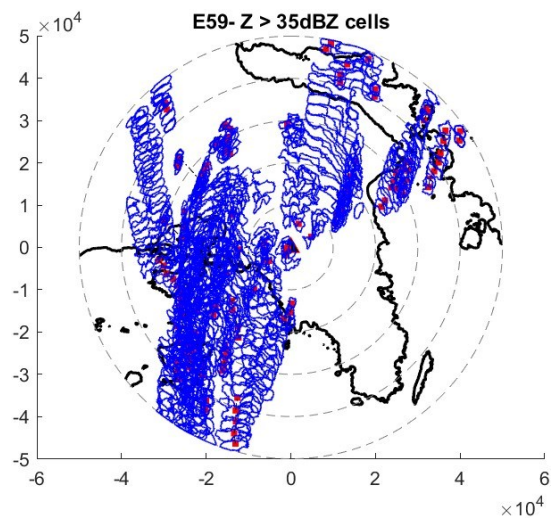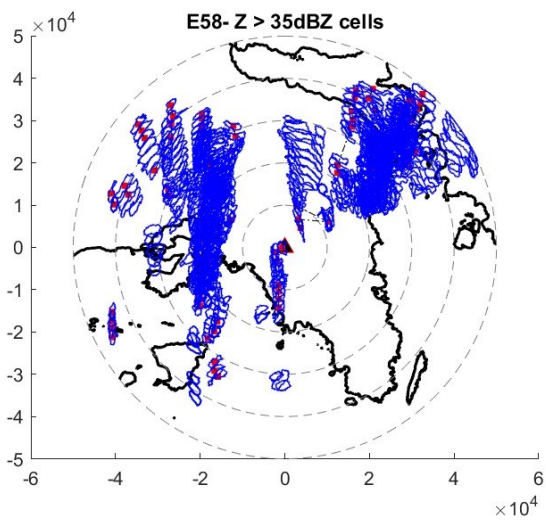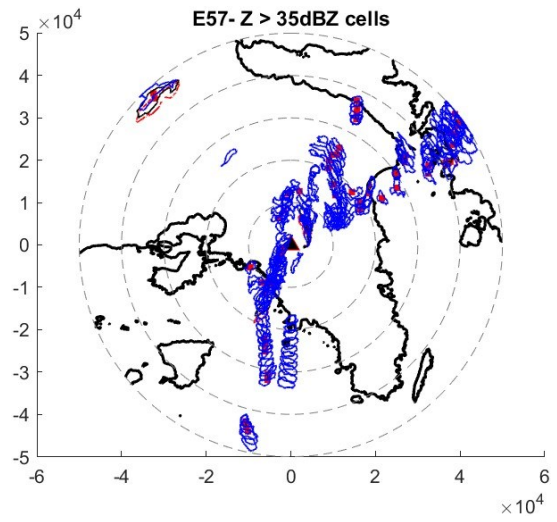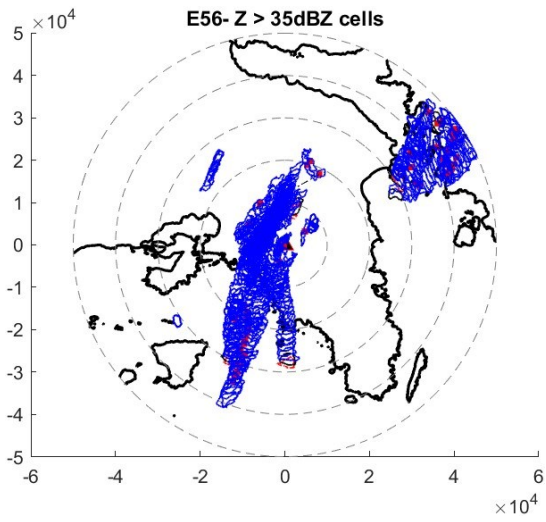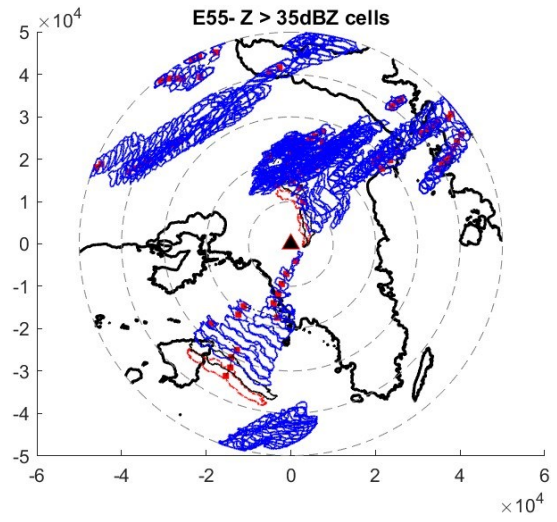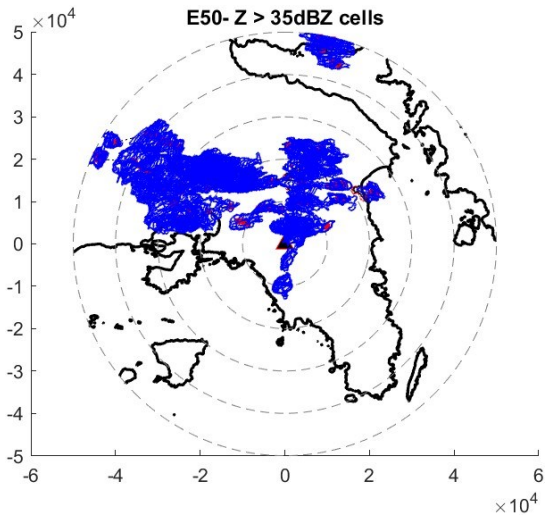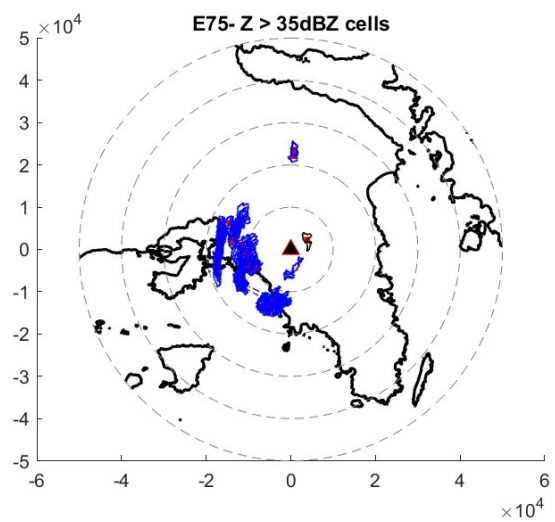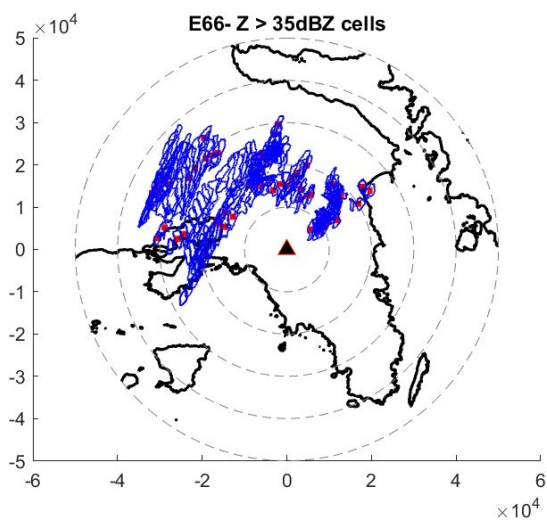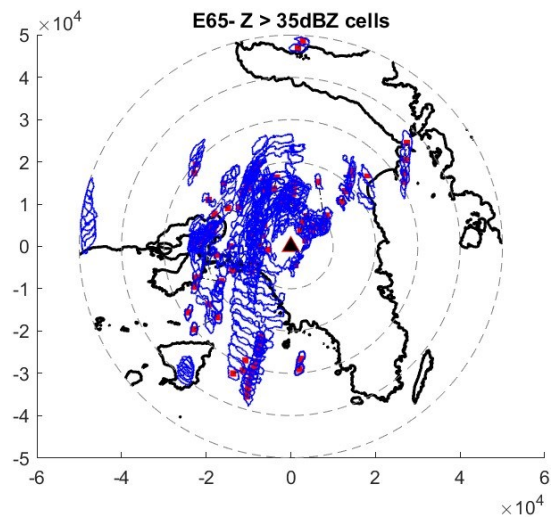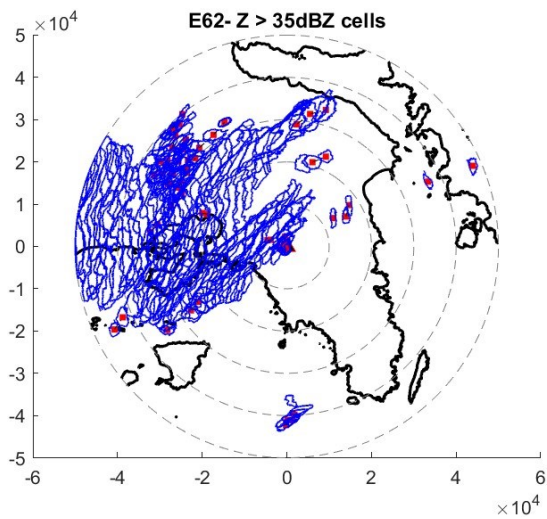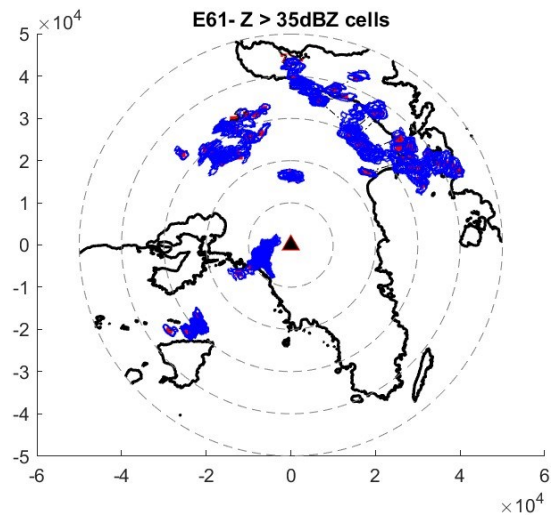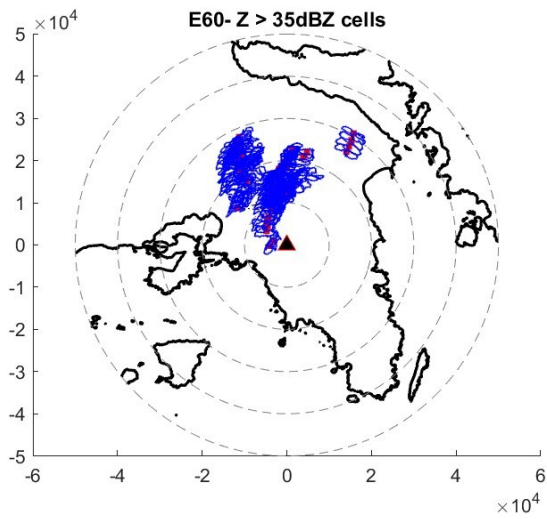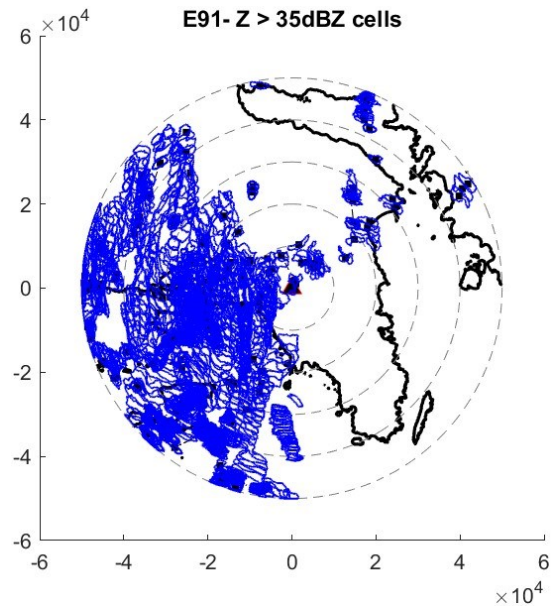
Appendix C

Results of Storm Tracking Algorithm (Selected Events).